Structure-Processing-Property Relationships in Molecular Assembly Across Length Scales: From Semicrystalline Polymers to Small Molecule Surfactants

by

James Robert Brown

A Dissertation Presented in Partial Fulfillment
of the Requirements for the Degree
Doctor of Philosophy

Approved June 2023 by the
Graduate Supervisory Committee:

Timothy E. Long, Chair
Michael J. Bortner
Kailong Jin
Kyle F. Biegasiewicz

ARIZONA STATE UNIVERSITY

August 2023

ABSTRACT

Both molecular structure of macromolecular materials and subsequent processing of these materials dictate resulting material properties. In this work novel synthetic strategies combined with detailed analytical methodology reveal fundamental structure-processing-property relationships in thermoplastic polyesters, thermoplastic polyurethanes, covalently crosslinked acetal functionalized networks, and small molecule surfactants. 4,4' dimethyloxybisbenzoate afforded a series of novel polyester structures, and the incorporation of this monomer both increased the T_g and decreased the crystallinity in cyclohexane dimethanol based polyesters. Solubility and dynamic light scattering experiments combined with oscillatory rheology techniques provided methodology to validate polyurethane extrusion in commercial polyurethanes. Acid catalyzed hydroxyl addition to vinyl ethers provided two families of acetal functionalized poly(ethylene glycol hydrogels). Stoichiometric control of binary thiol-acrylate polymerizations afforded hydrogels with both tunable mechanical properties and predictable degradation profiles. Following this work, a photoacid generator catalyzed cationic catalysis provided acetal functionalized organogels whose mechanical properties were predicted by excess vinyl ether monomers which underwent cationic polymerization under the same reaction conditions that yielded acetal functionalization. Time resolved FT-IR spectroscopy provided new understanding in hydroxyl vinyl ether reactions, where both hydroxyl addition to a vinyl ether and vinyl ether cationic polymerization occur concurrently. This work inspired research into new reactive systems for photobase generator applications. However, current photobase generator technologies proved incompatible for carbon-Michael reactions between acetoacetate and acrylate functionalities as a result of uncontrollable acrylate free radical polymerization. The fundamental knowledge and synthetic strategies afforded by these investigations were applied to small molecule surfactant systems for fire-fighting applications. Triethylsilyl-containing zwitterionic and cationic surfactants displayed surface tensions lower than hydrocarbon surfactants, but larger than siloxane-containing surfactants. For the first time, oscillatory rheology and polarized optical light imagine rheology highlighted shear-induced micelle alignment in triethylsilyl surfactants, which provided more stable foams than zwitterionic analogues. The knowledge gained from these investigations provided fundamental structure-processing-property relationships in small molecule surfactant solutions applied as fire-fighting foams. This discovery regarding the effect of self-assembled structures in foam solutions informs the design and analysis of next generation surfactants to replace fluorocarbon surfactants in fire-fighting foam applications.

DEDICATION

This work is dedicated to my future wife, Amelia, my parents, Connie and Jim, and all those I have learned from throughout my academic journey.

ACKNOWLEDGMENTS

I humbly acknowledge many in my life whose love, support, encouragement, and at times challenges inspired me to pursue my doctorate in chemistry. First, I would like to thank my parents Connie and Jim Brown. They inspired and supported my deep sense of curiosity from a very young age by providing me with educational resources and science kits, which garnered my love and passion for intellectual creativity and expression. I would like to further thank my mother Connie for demonstrating her own selfless commitment to education and learning throughout my life. I also thank my siblings Daniel and Tori. Tori led our shared path in the field of chemistry and our loving sibling rivalry and competition played a role in my decision to continue my educational journey after college. My brother Daniel continues to provide support and a sense of grounding to our shared values, shared friends, and shared love for literature and story-telling. I thank my other childhood and lifelong friends JT Maynard, Hunter Blumer, Scott Furman, Chancellor Ramsey, and Kent Wilkinson who grew up with me in the small town of Coudersport. I thank them for their continued understanding and support for my prolonged absence in the friend group over the previous five years. I thank all my educators throughout life including my high school math and science teachers Eric Zaun, Michael Davis, and Chris Fink. Most importantly, I would like to thank my high school chemistry teacher Robert Anderson for letting me turn study halls into extra lab periods and providing me opportunities to test-run experiments. I also thank the entirety of the St. Bonaventure University Chemistry faculty, David Hilmey, Donna Brestensky, Larry Weir, Scott Simpson, and Peter Schneider for their guidance in and out of the classroom and for the fun, engaging, and supportive community they fostered within the department. I am very fortunate to have received my graduate education in macromolecular science and engineering from the great professors at Virginia tech including Professors Robert Moore, Michael Schulz, John Matson, Kevin Edgar, and Michael Bortner. They deepened my understanding and appreciation for the multifaceted scientific discipline I pursued while providing incredible perspectives within their specializations. I am honored to contribute to the academic legacy of my graduate school advisor Timothy Long. I am forever grateful for his support, guidance, and motivation over the last five years. I cherish the opportunities he granted, which allowed me to explore my academic curiosities through access to state of the art instrumentation and a dedicated and driven research group. This leads me to thank my graduate school peers and mentors Jana Herzberger, Emily Wilts, Chris Kasprzak, Clay Arrington, Josh Wolfgang, Tyler White, Jack Bryant, Glenn Spiering, and Boer Liu. I owe a special debt of gratitude to my lab /roommates: Cody Weyhrich, Ren Bean, and Jose Sintas for pursuing our academic journeys together in such a supportive, brotherly, and understanding way. I thank them for becoming a family during our time in Arizona and I will never forget all they have done for me in the lab, but most importantly at home. Finally, I would like to thank the love of my life and my soulmate, Amelia Porter for her constant support, continued love, and perpetual understanding for our time apart during our academic pursuits.

TABLE OF CONTENTS

Page

10.1 Triethylsilyl and Trisiloxane Gemini Surfactants for Enhanced Foam Stability

APPENDIX

LIST OF TABLES

LIST OF FIGURES

Figure Page

Figure Page

Figure Page

CHAPTER 1

INTRODUCTION AND DISSERTATION OVERVIEW

1.1 Fundamentals of Structure-Processing-Property Relationships

Within the fields of chemistry and material science, molecular design and its subsequent processing dictate the resulting physical and thermomechanical properties. Molecular level structural understanding, such as chemical composition, molecular weight, molecular microstructure, supramolecular interactions, and reactivity inform potential the design of next generation materials to address emerging material needs across the fields of adhesives, packaging, medicine, transportation, water treatment, and fire-fighting in addition to many other research areas across multiple disciplines.[1–4] Newly developed materials often require subsequent processing techniques such as annealing, extrusion, selective reactivity, and stimuli response to meet specific needs of emerging applications. Comprehensive analytical strategies ranging from spectroscopy, chromatography, light scattering, calorimetry, thermomechanical analysis, and rheology provide deeper understanding of the interplay between molecular structure, its response under certain processing conditions, and the resulting mechanical properties.[5–7] This dissertation provides examples of both synthetic and analytical understanding of molecular design, processing, and mechanical properties of novel materials including amorphous and semicrystalline thermoplastic polymers, polymer solutions, covalently crosslinked polymer networks, and small molecule self-assemblies in solution. Pervasive analytical strategies demonstrate the effects of reactivity, supramolecular interactions, thermal history, and shear history on the mechanical properties of films, gels, and foams.

1.2 Thermoplastic Polymers

Thermoplastic polymers find use in industrial spaces such as adhesives, packaging, barriers, textiles, biomedical devices, and elastomers.[8,9] Linear and branched polymer microstructures provide ease in thermal processing by leveraging thermal transitions such as glass transition temperature, crystallite melting, crystallization, and phase separation to process flowing materials into robust materials upon cooling. Chapters 3 and 4 detail processing effects in two families of thermoplastic polymers: polyesters, and polyurethanes respectively. Synthesis of a family of novel polyesters based on 4,4' dimethyloxybisbenzoate highlighted this monomers effect on the glass transition temperature, crystallizability, and sub T_g relaxations in cyclohexane dimethanol based polyesters. This monomer accessed polyesters with tunable glass transition temperatures exceeding 100 °C and tunable crystallizability. Chapter 4 expanded on these fundamental thermoplastic properties in a series of polyurethanes whose processing was complicated by not only molecular structure, but also on changes in polymer microstructure imparted by inherent side reactions in polyurethane polymerization, chemical reactions at processing temperatures, and non-crystalline polymer assembly under shear. This work demonstrated analytical methodology to correlate polymer size in solution to its viscoelastic properties during processing, which affected extrusion performance and the ultimate mechanical properties. These chapters yielded fundamental understanding of molecular structure, chemical reactivity, and processing on morphology and the resulting viscoelastic properties. These fundamental trends inform the design, processing, and appropriate analytical methodology in the development of novel materials presented in subsequent chapters.

1.3 Covalent Polymer Networks

Covalent polymer networks differ from thermoplastic polymers in that these network materials are entirely covalently crosslinked in to one macromolecular material.[10,11] Whereas thermoplastics demonstrate facile reprocessing, covalently crosslinked networks are not amenable to thermal reprocessing or mechanical recycling. However, many emerging advance manufacturing processes such as photo-assisted additive manufacturing utilize low viscosity mixtures of reactive multifunctional monomers and oligomers to achieve solid and robust crosslinked networks. Chapters 5, 6, 7, and 8 present material design and analytical methodology to develop and understand photo-process specific reactivity effects on network morphology and the resulting chemical and physical properties crosslinked covalent polymer networks.

Chapter 5 introduces polymerization strategies to impart degradable acetal functionalization in hydrophilic telechelic pol(ethylene glycol) oligomers with vinyl ether chain ends suitable for subsequent photo-initiated thiol-ene polymerization. This provided covalently crosslinked hydrogels designed with selectively degradable functionality. Chapter 6 expanded on this acetal functionalized chemistry in the design of binary thiol-acrylate hydrogels. Whereas prior work in chapter 5 was limited to exclusively photo-initiated thiol-ene crosslinking, an acetal functionalized acrylate oligomer provided two photo-initiated polymerization pathways during photo-processing: thiol-ene addition and acrylate homopolymerization. This binary reaction platform provided covalently crosslinked networks with both high and low crosslink density domains. The incorporation of these highly crosslinked domains tuned hydrogel mechanical properties and degradation rates in addition to inspiring research in other photo-processing platforms with competing reaction pathways.

Chapter 7 and 8 leverage less common photoacid generator and photobase generator photo-catalysts to develop platforms for reactive systems, which tune crosslinked network mechanical properties through stoichiometric variation of each reactive pathway. Chapter 7 harnesses a photoacid generator as a catalyst for both acetal forming hydroxyl addition to a vinyl ether and cationic vinyl ether homopolymerization. This platform provided degradable organogels with tunable plateau storage moduli dictated by the ratio of these competing reaction kinetics. Similarly, chapter 8 sought to apply this crosslinking strategy to base catalyzed carbon-Michael addition between acetoacetate and acrylate functionalities with the use of a photobase generator. While both carbon-Michael addition and acrylate homopolymerization were possible reaction strategies, the much faster acrylate homopolymerization pathway dominated acrylate consumption prior to any detectable carbon-Michael additions.

1.4 Self-Assembly in Solution

Fundamental principles of macromolecular science and engineering expand beyond polymeric materials and provide additional perspectives to address interdisciplinary problems in non-polymeric material systems.[12,13] Chapter 9 applies fundamental understanding of molecular structure effects on supramolecular interactions, molecular assembly, and shear-induced morphological changes to the development and understanding of small molecule surfactants in fire-fighting foams. The presented surfactants formed short wormlike micelles in aqueous solution which historically perform similarly to polymer chains in solution. However, while polymeric solutions achieve these solution properties from covalently bound repeat units, wormlike micelles form macromolecular assemblies formed exclusively through physical interactions between hydrophilic and hydrophobic domains. This work demonstrated shear-induced micelle assembly akin to shear-induced crystallization in polymeric materials, and for the first time the viscoelastic properties of these shear-induced assemblies at representative shear rates informed surfactant structure and processing relationships in aqueous foam stability.

1.5 References

1. Nunes, R. W.; Martin, J. R.; Johnson, J. F. Influence of Molecular Weight and Molecular Weight Distribution on Mechanical Properties of Polymers. *Polym Eng Sci* **1982**, *22* (4), 205–228. https://doi.org/10.1002/PEN.760220402.

2. Wilts, E. M.; Herzberger, J.; Long, T. E. Addressing Water Scarcity: Cationic Polyelectrolytes in Water Treatment and Purification. *Polym Int* **2018**, *67* (7), 799–814. https://doi.org/10.1002/PI.5569.

3. Rabnawaz, M.; Wyman, I.; Auras, R.; Cheng, S. A Roadmap towards Green Packaging: The Current Status and Future Outlook for Polyesters in the Packaging Industry. *Green Chemistry* **2017**, *19* (20), 4737–4753. https://doi.org/10.1039/C7GC02521A.

4. Mapari, S.; Mestry, S.; Mhaske, S. T. Developments in Pressure-Sensitive Adhesives: A Review. *Polymer Bulletin 2020 78:7* **2020**, *78* (7), 4075–4108. https://doi.org/10.1007/S00289-020-03305-1.

5. Li, T.; Senesi, A. J.; Lee, B. Small Angle X-Ray Scattering for Nanoparticle Research. *Chem Rev* **2016**, *116* (18), 11128–11180. https://doi.org/10.1021/ACS.CHEMREV.5B00690/ASSET/IMAGES/CR-2015-00690Z_M061.GIF.

6. Carvalho, P. M.; Felício, M. R.; Santos, N. C.; Gonçalves, S.; Domingues, M. M. Application of Light Scattering Techniques to Nanoparticle Characterization and Development. *Front Chem* **2018**, *6*, 237. https://doi.org/10.3389/FCHEM.2018.00237/BIBTEX.

7. Saba, N.; Jawaid, M. A Review on Thermomechanical Properties of Polymers and Fibers Reinforced Polymer Composites. *Journal of Industrial and Engineering Chemistry* **2018**, *67*, 1–11. https://doi.org/10.1016/J.JIEC.2018.06.018.

8. Tjong, S. C. Structure, Morphology, Mechanical and Thermal Characteristics of the in Situ Composites Based on Liquid Crystalline Polymers and Thermoplastics. *Materials Science and Engineering: R: Reports* **2003**, *41* (1–2), 1–60. https://doi.org/10.1016/S0927-796X(03)00035-4.

9. Wang, W.; Lu, W.; Goodwin, A.; Wang, H.; Yin, P.; Kang, N. G.; Hong, K.; Mays, J. W. Recent Advances in Thermoplastic Elastomers from Living Polymerizations: Macromolecular Architectures and Supramolecular Chemistry. *Prog Polym Sci* **2019**, *95*, 1–31. https://doi.org/10.1016/J.PROGPOLYMSCI.2019.04.002.

10. Rizwan, M.; Baker, A. E. G.; Shoichet, M. S. Designing Hydrogels for 3D Cell Culture Using Dynamic Covalent Crosslinking. *Adv Healthc Mater* **2021**, *10* (12), 2100234. https://doi.org/10.1002/ADHM.202100234.

11. Rodin, M.; Li, J.; Kuckling, D. Dually Cross-Linked Single Networks: Structures and Applications. *Chem Soc Rev* **2021**, *50* (14), 8147–8177. https://doi.org/10.1039/D0CS01585G.

12. Svenson, S. Controlling Surfactant Self-Assembly. *Curr Opin Colloid Interface Sci* **2004**, *9* (3–4), 201–212. https://doi.org/10.1016/J.COCIS.2004.06.008.

13. Romsted, L. S. Introduction to Surfactant Self-Assembly. *Supramol Chem* **2012**. https://doi.org/10.1002/9780470661345.SMC013.

CHAPTER 2
DESIGNING ADHESIVES FOR SUSTAINABILITY

2.1 Adhesives from sustainable sources

From a chemical and manufacturing perspective, sustainability refers to approaches that leverage renewable and naturally sourced monomers to need application needs while providing a closed-loop material economy.[1] As the earth is a circular system with limited assimilative capacity, the practice of circular economy is key to sustainable development.[2,3] Under a circular economy, the input for production comes from renewable natural resources, and consumption serves as restorative and regenerative sources. This approach seeks to reduce dependence on petroleum-sourced monomers in addition to designing polymers with end-of-life considerations in mind.

Adhesives play a critical role in nearly every aspect of modern life, where the market size exceeds $70 billion across medical, automotive, construction, packaging, furniture, footwear, and pressure-sensitive applications.[4] Automotive manufacturers desire weight reduction for vehicles to increase fuel efficiency and reduce greenhouse gas emissions. Adhesives serve as replacements for the historical use of bolts and welding to manufacture cars without a reduction in performance. Another major adhesive market includes packaging, which continues to expand as more and more transactions occur online.[5] Flexible packaging requires new and efficient adhesive applications to ensure rapid manufacturing times and user satisfaction. A push to reduce volatile organic compounds (VOC) emissions historically caused water-based adhesive technologies to capture the largest revenue share. This indicates the consumer initiative to use greener and more sustainable types of adhesives. Trends in both the industrial and academic worlds push the desire for more sustainable technologies. Researchers are harnessing both new and old naturally and sustainably sourced chemicals to design and improve upon the adhesives of the past.

2.2 Urea

Urea, also called carbamide, is a nitrogen-rich molecule naturally occurring in the urine of mammals.[6] Depicted in **Figure 2.1**, urea contains two primary amines connected through a carbonyl functional group. Urea is water-soluble, non-toxic, and colorless solid, where 90 % of the world's supply serves the fertilizer industry.[7] Containing the highest nitrogen content (46.7 %) of solid, commercially available fertilizers enables urea to act as an excellent plant nutrient. In soil, urea hydrolyzes into ammonia and CO_2. Bacteria convert ammonia into nitrates, which plants subsequently absorb.[8,9] Another popular use of urea includes creating urea-formaldehyde-based polymers for adhesives.[10] Urea-formaldehyde thermosets provide high modulus adhesives and high substrate reactivity, thus affording leading adhesives for wood. However, the reversible aminomethylene linkage within the network is susceptible to hydrolysis, and therefore researchers explored adding melamine to the mixture.[11] Even though melamine increased gelation speed due to buffering effects of the triazole ring and increased cost, a decrease in water sorption significantly increased the lifetime of the adhesive.[12,13] While urea is already used in successful adhesives, its hydrogen bonding capabilities and dynamic covalent bonds render it a great candidate for further reversible and recyclable adhesive research.

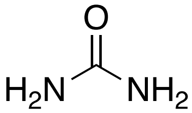

Figure 2.1. Chemical structure of urea.

Reactions between ammonia and CO_2 produce the majority of the world's urea supply, but isolation from urine remains a viable source. Feedstock natural gas provides the raw material source, and production price depends directly on natural gas prices. While the world works to eliminate fossil fuel dependency, other feedstocks for urea must be considered.[14] The catabolic route of urea synthesis in mammals produces up to 30 g of urea per liter of urine depending on dietary choices, such as protein consumption.[15] Even though mammals produce an abundance of urea daily, challenges arise in isolating urea from other disposed materials, and urea stability decreases after exiting a sterile environment. Researchers estimated urea completely hydrolyzes in one day in the presence of urease-containing bacteria, and therefore the development of urease inhibitors may resolve this problem.[16] One example includes lowering the pH to 5 with acetic acid, which denatures microbial urease and stabilizes the urea for up to 100 days.[17,18]

Polyureas are commonly used in coatings, foams, and self-healing materials owing to their superior mechanical and adhesive properties.[19,20] Compared to polyurethanes, polyureas contain bidentate hydrogen bonding enabling increased adhesive and mechanical properties. Unfortunately, commercial production of polyurethanes and polyureas requires highly toxic isocyanates derived from phosgene.[21] Efforts to avoid isocyanates include using cyclic diamines, carbonates, carbonyldiimidazole, and CO_2 as starting materials.[22–24] Other examples describe synthesizing polyureas utilizing urea as a monomer in a solvent-free, catalysts-free step-growth polymerization through the decomposition of urea into reactive isocyanic acid and ammonia, depicted in **Figure 2.2**2.2.[25,26] Amines subsequently react and form preferred 1,3-dialkylurea linkages, which produce linear polymers. Achievement of the 1,3-substitution requires a regimented heating ramp exceeding 200 °C and a stoichiometric excess of diamine vs. urea to prevent 1,1-dialkylurea, biurets, or imidazolidone cycles.[26,27]

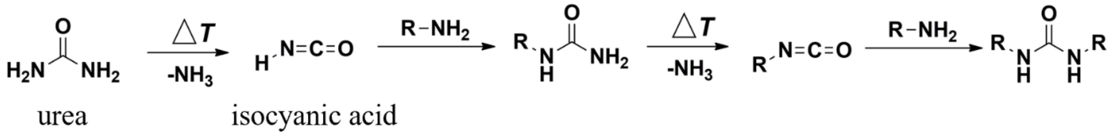

Figure 2.2. Heat enables urea to form reactive isocyanic acid, leading to a 1,3- dialkylurea addition of substitutes and polymer formation.

Polyureas provide hydrogen bonding for adhesive abilities and degrade in the presence of urease. Long *et al*.[26] synthesized polyureas with urea, diethyleneoxide diamine, and diaminoctane copolymers and monitored ammonia release in water in the presence of urease. They found decomposition was related to the hydrophobicity of the polymer backbone. Another example described copolymerizing urea with 3.2 to 30.6 kg mol^{-1} poly(dimethyl siloxane)-diamine to create low T_g polymers (-124 – 18 °C). Low T_gs combined with polyurea hydrogen bonding formed effective pressure-sensitive adhesions.[25] Finally, Long *et al.* copolymerized urea with poly(tetramethylene oxide), which afforded low T_g polymers (-76 to 21 °C) and strain at break values of 340 and 770 %.[27] Urea is a sustainable and renewable monomer choice, and its demonstrated use as a monomer encourages urea incorporation in future adhesive design.

2.3 CO_2

2.3.1 CO_2-based polyols

CO_2 is an abundant naturally produced chemical and accounts for 400 parts per million of earth's atmosphere. Humans generate vast amounts of this material every day and upwards of 10 billion tons annually.[28] Increases in greenhouse gases such as CO_2 have resulted in climate change and increased air pollution. However, this abundant "waste" material has been heavily investigated as a chemical feedstock for the synthesis of polymeric materials. CO_2 is a potential primary carbon or "C1" source and serves as a more sustainable addition to polymer designs. These emerging polymerizations effectively remove an amount of CO_2 from the atmosphere and convert it into a durable material.[29] CO_2-based polymerizations serve two key roles: reduction of annual net CO_2 emissions and reduction of the dependency on fossil fuel feedstocks by acting as a renewable primary carbon source. Such materials show promise in many polymer applications but notably for the scope of this review, in adhesives.[30–32] Polycarbonates are the most notable polymeric materials sourced from CO_2 through the catalyzed polymerization of CO_2 and epoxides, as shown in **Figure 2.3**.[33] While these processes remain in their infancy, recent advances more efficiently harnessed CO_2 from the atmosphere, utilized it as a primary carbon source in polymerizations and ultimately incorporated these materials into industrially applicable adhesive precursors.

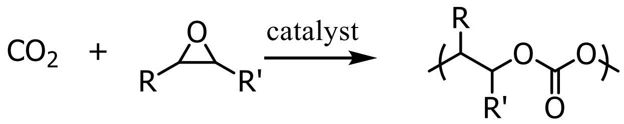

Figure 2.3. Metal-catalyzed copolymerization of CO_2 and epoxides yields polycarbonates.

2.3.2 CO_2-based polycarbonates

Polycarbonate materials contain hydrogen bonds accepting carbonate bonds in each repeat unit. This hydrogen bond acceptor makes polycarbonate materials attractive for incorporation into many adhesive applications, primarily in polyurethane design. Traditionally the reaction between diol monomers and toxic phosgene gas established the vast polycarbonate catalog. However, as the world moves in a more sustainable direction, researchers have developed more environmentally friendly synthetic pathways. CO_2 serves as a C1 source for polycarbonate materials, most notably through copolymerization with epoxide monomers. As CO_2 is a chemically stable molecule, these reactions involve using metal catalysts and elevated conditions to afford the CO_2-derived polycarbonates. Zinc catalysts remain the most common catalytic platform for these polymerizations through the coordination of the epoxide oxygen to the metal center of the catalyst.[34] Researchers continue to study new catalysts for CO_2 polymerizations; cobalt-based homogenous catalyst systems emerged as the most efficient catalysts in recent years.[35] **Figure 2.4** shows two industrially relevant polycarbonates derived from this sustainable process, which are poly(propylene carbonate) and poly(cyclohexene carbonate) from propylene oxide and cyclohexene oxide, respectively. Williams *et al.* reported molecular weight and end group control through a dizinc catalyst system yielding hydroxy-terminated poly(cyclohexene carbonate) polyols that served as soft blocks in elastomeric block copolymer systems alongside sustainably sourced poly(lactic acid).[36] Similar polycarbonate polyols have been incorporated into polyurethane hot melt and water-born adhesive systems as sustainably sourced replacements for historic polyether polyols.[37,38] Aside from the sustainable advantage of a CO_2-sourced material, these alkyl polycarbonates served to establish more rigid polyurethanes compared to polyether polyol systems due to the improved hydrogen bonding introduced by the carbonate bond.[39]

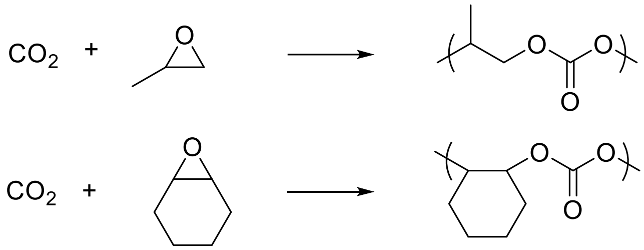

Figure 2.4. CO_2 serves as a primary carbon source for the polymerization of poly(propylene carbonate) (top) and poly(cyclohexene carbonate) (bottom).

Catalyst design remains the largest barrier to establishing novel CO_2-sourced polycarbonates with advantageous properties. The demand for more robust and durable materials inspired researchers to develop more stable catalysts, propelling sustainable polycarbonates to the forefront. Notably, Chen *et al.* established a one-pot polymerization of poly(cyclohexene carbonate-*b*-ε-decalactone-*b*-cyclohexene carbonate) and achieved competitive adhesive properties through the tuning of copolymer structure.[40] Implementation of a highly active organometallic heterodinuclear Zn(II)/Mg(II) catalyst afforded copolymers with CO_2 incorporations upwards of 23% and moderate T_gs ranging from 50-118 °C. Novel polymers achieved through this process displayed adhesive properties (180° peel and tack) on par with or exceeding leading copolymers in pressure-sensitive applications.[41] These materials are readily degraded in slightly acidic conditions at low temperatures (60 °C), making them ideal for renewable applications.

Epoxides represent the most common and effective route to CO_2-based polycarbonates, but oxy-carbonylation of alcohols has also demonstrated viability as a path to CO_2-derived polycarbonates. This process leverages the propylene carbonate byproduct in epoxide ring-opening polycarbonate synthesis with CO_2. This propylene carbonate, when reacted with alkyl alcohols, yielded dialkyl carbonates.[42] Transcarbonation of dialkyl carbonates with diol monomers provided a green route to a catalog of polycarbonate materials by using byproducts from previously discussed epoxide/CO_2 reactions.[43] These soft polycarbonate materials demonstrated suitability for pressure-sensitive applications. Grinstaff *et al.* recently reported on a sustainably derived polycarbonate-based PSA system.[44] Their copolymer series displayed tunable T_gs from -5 to 28 °C, and all copolymers demonstrated competitive peel strengths compared to leading industry standards such as Duct-Tape®.

2.3.3. CO_2 as a urea feedstock

CO_2 also provides a pl Reaction of CO_2 and ammonia first establish an ammonium carbamate intermediate, which subsequent dehydrates to yield urea and water.[45] Previously mentioned in this review, urea serves as a monomer in step-growth polymerization of low T_g polymers suitable for pressure-sensitive, hot melt, and biodegradable adhesive applications. Polycondensation reactions yielded polyureas by removing ammonia, which drove the reaction forward. Similar techniques utilized diol monomers to yield polycarbonates from urea.[46] Both these techniques share the urea monomer and ammonia condensate. These two sustainable processes show potential for use in a closed-loop ammonia recycling process, as shown in **Figure 2.5**, to remove CO_2 from the atmosphere while establishing new materials from CO_2 through urea.[43]

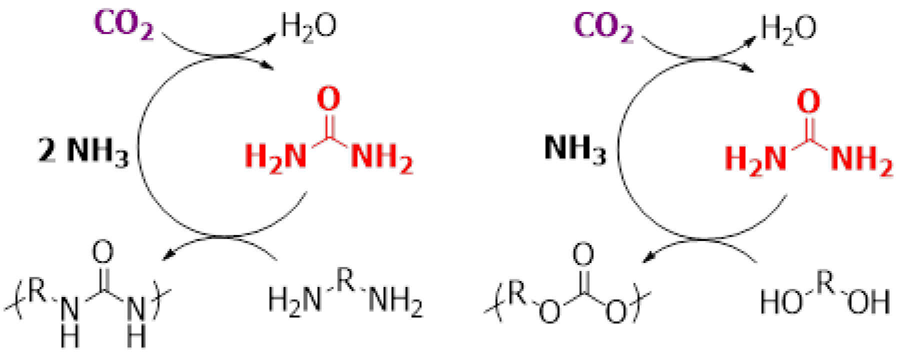

Figure 2.5. Ammonia serves as a recyclable condensate and CO_2 fixator in forming polyureas (left) and polycarbonates.[47]

2.4 Plant oil-based adhesives

Oils acquired from petroleum sources remain the most prevalent chemical feedstocks in all aspects of polymer chemistry. The finite and diminishing amount of fossil fuels on earth requires new and sustainable feedstocks for chemical synthesis.[48] Fortunately, abundant flora around the globe produce oils, which are harnessed in numerous chemical applications and provide renewable and sustainable sources for adhesive syntheses. Polymerization of oils refined from biomass yields high molecular weight aliphatic polyesters and epoxides, which show promise as thermoplastics and potential precursor polyols for adhesive manufacturing.[49,50] Polyols incorporated into traditional polyurethane formulations achieve properties comparable to petrochemical sources. [30,32,51–54] Two-part epoxy resins are a commercial and consumer commodity that build strength and hardness through covalent crosslinking of the epoxide functional group. Soybean oil is the most prevalently used plant oil as an epoxide precursor, but canola, linseed, vegetable, Karanja, and grapeseed oils have also been utilized as epoxide precursors.[55] Plant oil isolation first produces a mixture of triglycerides with varying aliphatic chain lengths and levels of unsaturation. Further isolation through ester hydrolysis provides glycerol and an array of fatty acid molecules, as shown in **Figure 2.6**.

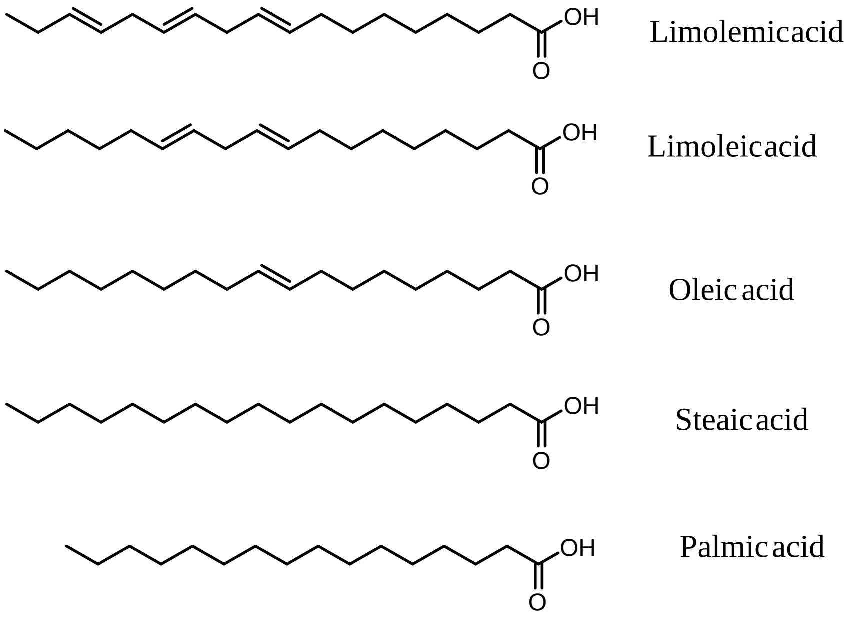

Figure 2.6. Common fatty acids derived from plant oil triglycerides with varying degrees of unsaturation.

2.4.1 Common functionalization of plant oils

Unsaturation in plant oil-derived fatty acids presents a highly malleable reactive site for various functionalization reactions, shown in **Figure 2.7**. These naturally sourced polyols are easily incorporated into many adhesive systems, such as hot melts, waterborne adhesives, and PSA.[56–58] The most well-understood post-isolation functionalization of plant oil fatty acids are epoxidation/ring opening, transesterification, amidation, hydroformylation/hydrolysis, and thiol-ene coupling.[59] Epoxidation/ring opening of the unsaturated fatty acids is the most common functionalization method.[60,61] This technique establishes secondary alcohol functionality to the fatty acids for further use as polyols. Transesterification and amidation of the carboxylic acid end of fatty acids yield polyols after reactions with other polyols and hydroxyl-functionalized amines.[62] This process is less attractive from a sustainability perspective as it requires using other chemical feedstocks containing hydroxyl functionality, and the fatty acid derivative itself does not contain hydroxyl functionality. Hydroformylation/hydrolysis describes alkene conversion to an aldehyde in the presence of a metal catalyst, such as rhodium.[63] Rhodium-based catalysts demonstrate leading alkene conversions to aldehydes. Subsequent reduction of the generated aldehyde produces primary hydroxyl functionalization, which is more reactive than secondary alcohols generated through epoxidation techniques.[64] Thiol-ene coupling to fatty acid alkenes is a promising route to establishing a variety of plant oil-derived polyols with primary hydroxyl functionality. Hong *et al.* reported carbon-carbon double bond consumption upwards of 99% utilizing a facile photo-catalyzed thiol-ene coupling with mercaptoethanol. This work achieved plant oil polyols with hydroxyl numbers reaching 105 mg KOH/g by titration.[65]

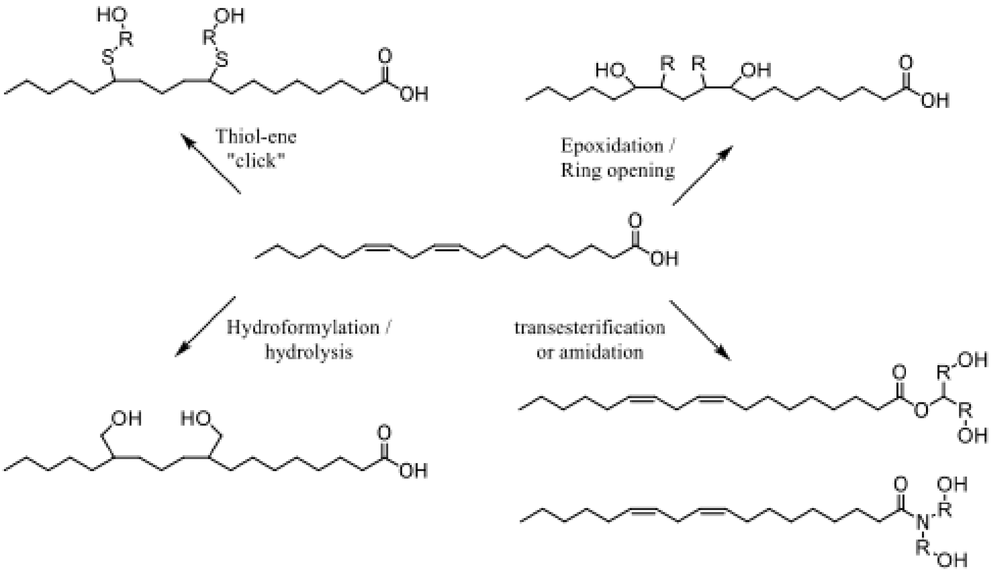

Figure 2.7. Common techniques to impart OH functionality to unsaturated plant oils.

2.4.2 Plant oil polyols in adhesives

Vegetable oil-sourced polyols are attractive additives to many polyurethane adhesive systems as a sustainably sourced and multifunctional component with selective hydroxyl numbers. Long *et al.* discovered crosslinked triglyceride-based polyols as tack-free coatings using air oxidation of soybean oil.[66] Hong *et al.* reported thermoplastic elastomers with properties advantageous to adhesive applications through the thiol-ene coupling functionalization strategy.[67] The researchers achieved full functionalization of the vegetable oil double bonds to primary alcohols through facile radical thiol-ene functionalization. Polyurethanes derived from this bio-sourced material achieved T_gs of 24 °C and displayed tensile strengths on the order of 13 MPa with 800% strain at break, which are ideal properties for incorporating in elastomeric polyurethane adhesives and sealants.[67]

Epoxidation of vegetable oils establishes multifunctional epoxide molecules that have attracted much attention in thermoset applications.[68,69] Ring-opening of the oxirane groups on epoxidized natural material with unique nucleophiles developed sustainably sourced adhesives with additionally advantageous properties. Wang *et al.* established flame retardant functionality in a vegetable oil-based pressure-sensitive by functionalizing the material with flame retardant monomers 9,10-dihydro-10-[2,3-di(hydroxycarbonyl)propyl]-10-phosphaphenanthrene-10-oxide (DDP) and 2-(6-oxido-6*H*-dibenzoxaphosphorin-6-yl)-1,4-hydroxyethoxyphenylene (DOPO-HQ-HE).[69] The PSA improved thermal stability and adhesive strength while meeting the criteria for flame resistance determined by limiting oxygen index and UL-94 tests.

Hydroformylation provides leading vegetable oil derivatives as it produces more reactive primary hydroxyl functionalization. This strategy established more efficient reaction times and faster cure rates when compared to secondary hydroxyl groups.[70] Petrović *et al.* reported these superior properties in the development of wood adhesives sourced from hydroformylation functionalized rubber oil.[71]Primary hydroxyl groups established polyurethane wood adhesives with T_gs of 40-50 °C. Lap shear tests of the adhesives highlighted oak substrate failure in all cases following ASTM D 2339-98 testing procedures. This novel adhesive system presents an excellent example of the progress in using sustainably sourced polyols in wood-wood applications.

While many plant oils sourced from triglycerides require subsequent functionalization to serve as polyol precursors, some plant oils naturally contain hydroxyl functionality, such as castor oil, which has an average of 2.7 hydroxyl groups per triglyceride.[71] These natural hydroxyl-containing plant oil polyols are incredibly attractive for many polyurethane applications, including those in the design of reactive adhesive systems.[72,73] Barros-Timmons *et al.* investigated the curing times and ultimate bond strength of the reactive hot melt polyurethanes derived from castor oil. Sustainably sourced materials displayed bond strengths comparable to petroleum-sourced polyols while subsequently curing process leading to more efficient bond formation.[72] Without the need for post-isolation functionalization, castor oil polyols are one of the most exciting avenues for sustainable polyols in adhesive design.

2.5 Biomass

2.5.1 Lactone copolymers as emerging PSA

PSAs remain large commercial and industrial products accounting for a multimillion-dollar global industry.[74] The leading subsection of PSA relies on ABA copolymers with relatively high T_g A sections and low T_g B sections. Petroleum-based copolymer systems account for the majority of the PSAs produced annually.[75] Many studies introduced sustainably sourced hard segments such as poly(lactic acid), which displays T_g of 60-65 °C and T_m approaching 180 °C as the A block in these ABA copolymers. Poly(lactic acid) is a well-known and heavily researched biodegradable polyester and is easily sustainably sourced. [76,77] For many years, fully sustainable ABA copolymer PSAs have been limited by the lack of non-competitive sustainably sourced rubbery B blocks compared to poly(isoprene) or poly(butadiene).[78] Recent research has developed new methodologies for obtaining such sustainably sourced PSAs from lactone monomers. Ring-opening polymerization of renewably sourced lactones afforded aliphatic polyester copolymers, whose thermal and mechanical properties were altered through aliphatic chain length and the addition of side groups.[79] Other strategies addressed lacking adhesive properties of sustainably sourced PSAs with the addition of tackifiers.[80] Recently, Hillmyer *et al*. established a sustainably sourced rubbery B block from monomers derived from cashew nut shells.[81] Palladium-catalyzed hydrogenation and subsequent Baeyer–Villiger oxidation of naturally derived cardanol established a regioisomeric mixture of 5-pentadecyl caprolactone and 3-pentadecyl caprolactone, displayed in **Figure 2.8**. Ring-opening polymerization of caprolactone formed polyesters with 15-carbon long branches along the backbone. This synthetic approach significantly raised the critical entanglement molecular weight and thus the adhesive properties when the polymers were utilized as the B block alongside PLA A blocks in an ABA copolymer PSA competitive with commercial standards.[82]

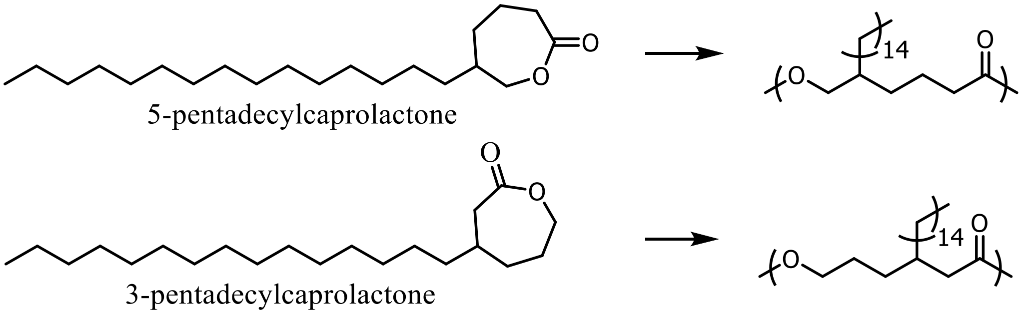

Figure 2.8. Ring-opening polymerization of long alkyl chain containing caprolactones yields polyesters with high entanglement molecular weights. (Hillmyer *et al*.[81])

2.6 Polysaccharides in adhesive design

Cellulose is the most abundant bio-sourced macromolecule and a popular sustainable reactive component in pressure-sensitive, self-healing, and nanocomposite adhesives. Using cellulose as an adhesive filler replaces the mass of nonrenewable materials in adhesive formulations, which enables the production of adhesives in a more sustainable and economically competitive way. Furthermore, cellulose holds promising routes to improved adhesive properties. Dubé *et al.* discovered that in-situ cellulose nanocrystals (CNCs) seeded polymerization of PSA poly(*n*-butyl acrylate-co-methyl acrylate) improved tack, peel strength, and ultimate shear strength as the CNCs achieved optimal incorporation into the latex network.[83] Hydroxyl functionality of cellulose enables post-isolation modification strategies for inoculant-establish reactive functionality in adhesive applications.[84] Isocyanate functionalization of naturally derived cellulose acetate created competitive bonds in wood-to-wood bonding applications when combined with castor oil-sourced polyols in a thermoplastic polyurethane adhesive network.[85]

Aside from cellulose, many other naturally occurring polysaccharides are naturally abundant and serve as primary polymer components in adhesive dispersions and waterborne applications. The most promising polysaccharides for adhesive applications are starches, gums, glucomannans, and chitosans.[86] The chemical similarities between many natural polysaccharides and the polysaccharides present in wood, such as cellulose and hemicellulose, render polysaccharide adhesives ideal for wood applications due to the improved interactions between substrate and adhesive. This property, combined with the moderate water solubility of many starches, has enabled the development of some of the earliest forms of adhesives. Native starch is an exceptional binder and low-strength adhesive for many consumer and non-demanding industrial applications. However, its viability as a reactive component in more durable adhesives has only been thoroughly investigated recently, as it serves as a sustainable replacement for existing adhesive technologies. Recently, Zhang *et al.* researched starch as a replacement for formaldehyde in formaldehyde/urea-containing adhesives to reduce the harmful emissions of formaldehyde.[87] The oxidation of starch yields aldehyde functionality, which can react with urea to form crosslinked adhesives with faster curing times, greater final bond strength, and significantly improved uncured bond strength compared to a urea/formaldehyde system at the cost of a moderate increase of viscosity. Another new starch-based adhesive utilized silane functionalized starch with trimethoxy silane to develop wood-wood adhesives with improved lap shear strength dependent on crosslink density.[88]

Chitosan is a derivative of chitin, which is an abundant polysaccharide found most often in shellfish. Bass catalyzed hydrolysis of the N-acetyl group of native chitin yields chitosan, a β-(1,4)-linked 2-acetamido-2-deoxy-D-glucopyranose and 2-amino-2-deoxy-D-glucopyranose. The amine functionality enables pH-dependent adhesive properties upon protonation and changes in hydrogen bonding behavior.[89] Chitosan displays antimicrobial properties, which have inspired its use in many biomedical adhesive and antifouling applications.[90] The Maillard reaction between glucose and chitosan provides a fully sustainable route to crosslinked polysaccharide adhesives for wood-wood applications. Kawai *et al.* thoroughly investigated this reaction kinetics and the effects of processing parameters on bond strength.[89] They reported improvements in tensile strength for low molecular weight chitosan after crosslinking with up to 10 wt. % glucose. Combinatory systems utilizing chitosan and oxidized starch showed potential for producing reactive crosslinking adhesives with low toxicity, biodegradability, and sustainable sourcing.[91]

2.7 Nucleobase-containing adhesives

Nucleobase pairs, including adenine/thymine (A/T) and cytosine/guanine (C/G), have unique molecular recognition to form complementary hydrogen bonding. The G/C bond exhibits greater strength due to triple hydrogen bonds, whereas the A/T bond only contains double hydrogen bonds. Chain copolymerization of the nucleobase-containing monomer and a low T_g acrylate, such as *n*-butyl acrylate, affords tacky substances as polymeric adhesives. The hydrogen bonding interaction, which is stronger than van der Waals interaction, affords sufficient cohesive strength for these copolymers used as PSA.[92–96] Long *et al*.[97] previously designed novel acetyl-protected cytosine and guanine-containing random copolymers as supramolecular adhesives. The designed adhesives realized tunable thermo-property of T_g ranging from -46 to -10 °C and tunable *G'* via varying the content of hydrogen bonding units. As illustrated before, the Dahlquist criterion requires *G'* of an adhesive to be lower than room temperature for effective surface wetting. The copolymers containing 5 *mol*. % acetyl-cytosine and 3 *mol*. % acetyl-guanine met the Dahlquist criterion that exhibited effective surface wetting for potential PSAs. In addition, the 180 °C peel test indicated the protected guanine and cytosine-containing copolymers demonstrated peel strength 3× and 2× higher than the Scotch® tape control, respectively. Besides nucleobase pairs, multiple hydrogen bonding-containing functional groups such as 2-ureido-4[1H]-pyrimidinone (UPy) and ureido-cytosine (UCy) are candidates for improved adhesions.[97–108] Additionally, those functional groups possess reactive sites, such as primary and secondary amine, which can readily synthesize vinyl and acrylate monomers. Long *et al.* demonstrated that UCy-functionalized supramolecular polymer exhibited ideal rheological properties used as acrylate adhesives.[102] Highly directional quadruple hydrogen bonding between UCy enhanced thermomechanical resistance compared to the cytosine analog, which formed dimeric hydrogen bonds. Thermomechanical analysis suggested a plateau window for copolymers with higher content UCy. Copolymers containing 9 *mol.* % and 11 *mol.* % UCy functional group met the Dahlquist criterion and demonstrated the potential application of UCy-containing acrylate copolymers as PSA.

2.8 Biodegradable polymeric adhesives

Biodegradable polymers are effective strategies for reducing or eliminating harmful waste plastic accumulated in the eco-system environment. Through bacteria or enzyme treatment, polymer backbones break down and decompose to non-toxic small molecules such as CO_2, water, and natural gas, eventually entering into environmental systems without creating burdens to the earth.[109] biodegradable adhesives include chitosan, collagen, lignosulfonate, chitosan, and dextran. [110–113] The structure of synthetic biodegradable polymers typically consists of aliphatic ester, ether, carbamate, and amide groups. Aliphatic polyesters and poly(alkylene glycol)s, such as poly(ethylene glycol) (PEG), poly(propylene glycol) (PPG), poly(lactic acid) (PLA), and poly(ε-caprolactone) (PCL), biodegrade through aliphatic ester and ether groups, which degrade in aqueous environments, during exposure to UV or enzymes.[114,115] The rate and extent of degradation highly depend on polymer molecular weight. Kawai and Moriya demonstrated that PEGs with number average of molecular weight over 20 kDa are biodegradable.[116] However, an increase in molecular weight increased the difficulty for bacteria and enzymes to attack the terminal free hydroxyl group, leading to poor biodegradability.[117]

Besides biodegradability, poly(alkylene glycol)s and aliphatic polyesters are non-toxic and nonantigenic, displaying ideal immunologic tolerance in aqueous environments. Researchers recognized these polymers as a potential option for tissue adhesive and wound healing applications due to their biocompatibility *in vivo*.[118] Kofinas *et al*. presented a straightforward system of low and high-molecular distribution polyester blend that offers biodegradability and sufficient adhesion.[119] Further study of this group fabricated wound adhesives using poly(lactic-*co*-glycolic acid) and poly(ethylene glycol) (PLGA/PEG) blend fibers with silver salt incorporated.[120] Solution block spinning (SBS) provided a method that afforded a high porosity and intrinsically adhesive polymer fibers. The authors demonstrated the efficiency of wound dressing using PLGA/PEG/AgNO3 adhesive on the porcine excisional wound model, with comparable healing rates as the clinical control (Tegaderm ™). The antimicrobial and healing function correlated to the addition of $AgNO_3$ without compromising cell viability and wound closure strength. Other efforts on biodegradable polymers for sustainable adhesives include polyaspartic acid, polylactide, and PCL.[121–123]

Another aspect of improving biodegradability is using monomers from renewable sources.[53,118] Orgilés-Calpena and coworkers selected a soybean oil-derived monomer and modified it to a polyol through transesterification.[124] The use of bio-derived monomers improved the biocompatibility and biodegradability of the polyurethane adhesives, highlighting the benefit of bio-sourced monomers over petroleum-derived monomers. Another strategy for biodegradable adhesives is to use a hybrid of bio-based adhesives and biodegradable polymers. Recently, Ciannamea *et al.* combined PCL with several natural polymers, including soybean protein isolate, castor oil, and pine rosin, for a potentially biodegradable HMA.[125] Employing the blend of PCL and castor oil, Ferreira *et al*. developed a photocrosslinkable tissue adhesive.[126] Other combinations of polymers and natural products for biodegradable adhesives include polyvinyl acetate/PMMA/starch.[127]

2.10 Conclusions and perspectives

Adhesives have been and will remain a critical aspect of all industries, and thus the need for innovations in adhesive design will prevail. As sustainable feedstocks for adhesives continue to develop, the field will move towards larger implementation of these green materials and become less reliant on fossil fuels. Researchers have harnessed abundant and sustainable natural resources for the synthesis of new adhesive precursors. Catalytic conversion of CO_2 yields polycarbonate materials promising for inclusion in hot melt and pressure-sensitive applications. Plant-oil chemical feedstocks enable sustainable polyols in polyurethane manufacturing and establish epoxide thermosets competitive with the current state-of-the-art materials. Biomass sources materials ranging from lactone precursors to polysaccharide additives, both of which serve many roles in the design of new pressure-sensitive and waterborne adhesives.

Biomedical adhesion is an interdisciplinary research topic that spans chemistry, biology, and material science. Safety is the primary consideration of designing biomedical adhesives and strongly directs the chemical avenues to ensure biocompatibility, eliminate leachable molecules, and lower cytotoxicity. Preferably, tissue adhesives should be biodegradable to avoid the requirement of removal while exhibiting no long-term side effects after degradation. One major challenge for polymeric biomedical adhesives is cell affinity. In response, coating, functionalization (on backbone or side chain), and hybridization of polymer with natural adhesive provides strategies to improve adhesion properties. Concurrently, polymeric adhesives should also exhibit low interfacial tension and have comparable mechanical properties, such as modulus and toughness, with targets. Finally, a novel biomedical adhesive requires multifunction (self-healable, antibacterial, and tissue-regenerative) and environmental response (temperature, acidity, and humidity), providing modularity and adaptivity to dynamic biological environments. Addressing these challenges transcends material design alone. Innovative applications of sustainably sourced adhesives harness the natural power of wood, allowing for robust, novel engineered materials such as cross-laminated timber. Advanced processing techniques, such as additive manufacturing, may help to introduce the next generation of customized personal biomedical adhesives.

2.9 References

1. *Sustainable chemistry – OECD*. https://www.oecd.org/chemicalsafety/risk-management/sustainable-chemistry/ (accessed 2023-04-12).

2. Geng, Y.; Doberstein, B. Developing the Circular Economy in China: Challenges and Opportunities for Achieving "Leapfrog Development." *International Journal of Sustainable Development & World Ecology* **2008**, *15* (3), 231–239. https://doi.org/10.3843/SusDev.15.3:6.

3. Webster, K. *The Circular Economy: A Wealth of Flows*; Ellen MacArthur Foundation Publishing, 2017.

4. *Global Adhesives And Sealants Market Size Report, 2023-2030*. https://www.grandviewresearch.com/industry-analysis/adhesives-and-sealants-market (accessed 2023-04-12).

5. Dahlbo, H.; Poliakova, V.; Mylläri, V.; Sahimaa, O.; Anderson, R. Recycling Potential of Post-Consumer Plastic Packaging Waste in Finland. *Waste management* **2018**, *71*, 52–61.

6. Klein, J. D.; Blount, M. A.; Sands, J. M. Urea Transport in the Kidney. *Compr Physiol* **2011**, *1*, 699–729. https://doi.org/10.1002/cphy.c100030.

7. Loeser, E.; Delacruz, M.; Madappalli, V. Solubility of Urea in Acetonitrile-Water Mixtures and Liquid-Liquid Phase Separation of Urea-Saturated Acetonitrile-Water Mixtures. *J Chem Eng Data* **2011**, *56*, 2909–2913. https://doi.org/10.1021/je200122b.

8. Greenan, N. S.; Mulvaney, R. L.; Sims, G. K. A Microscale Method for Colorimetric Determination of Urea in Soil Extracts. *Commun Soil Sci Plant Anal* **1995**, *26*, 2519–2529. https://doi.org/10.1080/00103629509369465.

9. Marsh, K. L.; Sims, G. K.; Mulvaney, R. L. Availability of Urea to Autotrophic Ammonia-Oxidizing Bacteria as Related to the Fate of 14C- and 15N-Labeled Urea Added to Soil. *Biol Fertil Soils* **2005**, *42*, 137–145. https://doi.org/10.1007/s00374-005-0004-2.

10. Dunky, M. Urea-Formaldehyde (UF) Adhesive Resins for Wood. *Int J Adhes Adhes* **1998**, *18*, 95–107. https://doi.org/10.1016/S0143-7496(97)00054-7.

11. Zhou, J.; Yue, K.; Lu, W.; Chen, Z.; Cheng, X.; Liu, W.; Jia, C.; Tang, L. Bonding Performance of Melamine-Urea-Formaldehyde and Phenol-Resorcinol-Formaldehyde Adhesives in Interior Grade Glulam. *J Adhes Sci Technol* **2017**, *31*, 2630–2639. https://doi.org/10.1080/01694243.2017.1313185.

12. Paiva, N. T.; Ferra, J. M.; Pereira, J.; Martins, J.; Carvalho, L.; Magalhães, F. D.

Production of Water Tolerant Melamine–Urea–Formaldehyde Resin by Incorporation of Sodium Metabisulphite. *Int J Adhes Adhes* **2016**, *70*, 160–166. https://doi.org/10.1016/j.ijadhadh.2016.06.005.

13. Jeong, B.; Park, B.-D. Practical Relationship between Apparent Viscosity and Molecular Weight of Urea-Formaldehyde Resin Adhesives. *J Adhes Sci Technol* **2019**, *33*, 209–216. https://doi.org/10.1080/01694243.2018.1529282.

14. Rollinson, A. N.; Jones, J.; Dupont, V.; Twigg, M. V. Urea as a Hydrogen Carrier: A Perspective on Its Potential for Safe, Sustainable and Long-Term Energy Supply. *Energy Environ Sci* **2011**, *4*, 1216–1224. https://doi.org/10.1039/c0ee00705f.

15. Macpherson, G. Black's Student Medical Dictionary. **2004**.

16. Maurer, M.; Muncke, J.; … T. A. L.-R. and R.; 2002, undefined. Technologies for Nitrogen Recovery and Reuse. *IWA Publishing London*.

17. Udert, K. M.; Larsen, T. A.; Biebow, M.; Gujer, W. Urea Hydrolysis and Precipitation Dynamics in a Urine-Collecting System. *Water Res* **2003**, *37*, 2571–2582. https://doi.org/10.1016/S0043-1354(03)00065-4.

18. Hellström, D.; Johansson, E.; Grennberg, K. Storage of Human Urine: Acidification as a Method to Inhibit Decomposition of Urea. *Ecol Eng* **1999**, *12*, 253–269. https://doi.org/10.1016/S0925-8574(98)00074-3.

19. Montarnal, D.; Cordier, P.; Soulié-Ziakovic, C.; Tournilhac, F.; Leibler, L. Synthesis of Self-Healing Supramolecular Rubbers from Fatty Acid Derivatives, Diethylene Triamine, and Urea. *J Polym Sci A Polym Chem* **2008**, *46*, 7925–7936. https://doi.org/10.1002/pola.23094.

20. Wang, P.; Ma, X.; Li, Q.; Yang, B.; Shang, J.; Deng, Y. Green Synthesis of Polyureas from CO2 and Diamines with a Functional Ionic Liquid as the Catalyst. *RSC Adv* **2016**, *6*, 54013–54019. https://doi.org/10.1039/c6ra07452a.

21. Redlich, C. A.; Karol, M. H. Diisocyanate Asthma: Clinical Aspects and Immunopathogenesis. *Int Immunopharmacol* **2002**, *2*, 213–224. https://doi.org/10.1016/S1567-5769(01)00174-6.

22. Ma, S.; Liu, C.; Sablong, R. J.; Noordover, B. A. J.; Hensen, E. J. M.; Van Benthem, R. A. T. M.; Koning, C. E. Catalysts for Isocyanate-Free Polyurea Synthesis: Mechanism and Application. *ACS Catal* **2016**, *6*, 6883–6891. https://doi.org/10.1021/acscatal.6b01673.

23. Sintas, J. I.; Wolfgang, J. D.; Long, T. E. Carbamate Thermal Decarboxylation for the Design of Non-Isocyanate Polyurethane Foams. *Polym Chem* **2023**, *14* (13), 1497–1506. https://doi.org/10.1039/D3PY00096F.

24. Wolfgang, J. D.; White, B. T.; Long, T. E. Non-Isocyanate Polyurethanes from 1,1′-Carbonyldiimidazole: A Polycondensation Approach. *Macromol Rapid Commun* **2021**, *42* (13), 2100163. https://doi.org/10.1002/MARC.202100163.

25. Sirrine, J. M.; Schexnayder, S. A.; Dennis, J. M.; Long, T. E. Urea as a Monomer for Isocyanate-Free Synthesis of Segmented Poly(Dimethyl Siloxane) Polyureas. *Polymer (Guildf)* **2018**, *154*, 225–232. https://doi.org/https://doi.org/10.1016/j.polymer.2018.09.003.

26. Dennis, J. M.; Steinberg, L. I.; Pekkanen, A. M.; Maiz, J.; Hegde, M.; Müller, A. J.; Long, T. E. Synthesis and Characterization of Isocyanate-Free Polyureas. *Green Chemistry* **2018**, *20* (1), 243–249. https://doi.org/10.1039/C7GC02996A.

27. White, B. T.; Migliore, J. M.; Mapesa, E. U.; Wolfgang, J. D.; Sangoro, J.; Long, T. E. Isocyanate- and Solvent-Free Synthesis of Melt Processible Polyurea Elastomers Derived from Urea as a Monomer. *RSC Adv* **2020**, *10*, 18760–18768. https://doi.org/10.1039/D0RA02369H.

28. Dlugokencky, E. J. Atmospheric Composition [in State of the Climate in 2018, Chapter 2: Global Climate]. *Bull Am Meteorol Soc* **2019**, *100* (9), S48–S50.

29. Scharfenberg, M.; Hilf, J.; Frey, H. Functional Polycarbonates from Carbon Dioxide and Tailored Epoxide Monomers: Degradable Materials and Their Application Potential. *Adv Funct Mater* **2018**, *28* (10), 1704302. https://doi.org/10.1002/adfm.201704302.

30. Orgilés-Calpena, E.; Arán-Aís, F.; Torró-Palau, A. M.; Orgilés-Barceló, C. Novel Polyurethane Reactive Hot Melt Adhesives Based on Polycarbonate Polyols Derived from CO2 for the Footwear Industry. *Int J Adhes Adhes* **2016**, *70*, 218–224. https://doi.org/https://doi.org/10.1016/j.ijadhadh.2016.07.009.

31. Samanta, S.; Selvakumar, S.; Bahr, J.; Wickramaratne, D. S.; Sibi, M.; Chisholm, B. J. Synthesis and Characterization of Polyurethane Networks Derived from Soybean-Oil-Based Cyclic Carbonates and Bioderivable Diamines. *ACS Sustain Chem Eng* **2016**, *4* (12), 6551–6561. https://doi.org/10.1021/acssuschemeng.6b01409.

32. Poussard, L.; Mariage, J.; Grignard, B.; Detrembleur, C.; Jérôme, C.; Calberg, C.; Heinrichs, B.; De Winter, J.; Gerbaux, P.; Raquez, J. M.; Bonnaud, L.; Dubois, P. Non-Isocyanate Polyurethanes from Carbonated Soybean Oil Using Monomeric or Oligomeric Diamines To Achieve Thermosets or Thermoplastics. *Macromolecules* **2016**, *49* (6), 2162–2171. https://doi.org/10.1021/acs.macromol.5b02467.

33. Wang, Y.; Darensbourg, D. J. Carbon Dioxide-Based Functional Polycarbonates: Metal Catalyzed Copolymerization of CO2 and Epoxides. *Coord Chem Rev* **2018**, *372*, 85–100. https://doi.org/https://doi.org/10.1016/j.ccr.2018.06.004.

34. Aida, T.; Ishikawa, M.; Inoue, S. Alternating Copolymerization of Carbon Dioxide and

Epoxide Catalyzed by the Aluminum Porphyrin-Quaternary Organic Salt or -Triphenylphosphine System. Synthesis of Polycarbonate with Well-Controlled Molecular Weight. *Macromolecules* **1986**, *19* (1), 8–13. https://doi.org/10.1021/ma00155a002.

35. Trott, G.; Saini, P. K.; Williams, C. K. Catalysts for CO2/Epoxide Ring-Opening Copolymerization. *Philosophical Transactions of the Royal Society A: Mathematical, Physical and Engineering Sciences* **2016**, *374* (2061), 20150085. https://doi.org/doi:10.1098/rsta.2015.0085.

36. Kember, M. R.; Copley, J.; Buchard, A.; Williams, C. K. Triblock Copolymers from Lactide and Telechelic Poly(Cyclohexene Carbonate). *Polym Chem* **2012**, *3* (5), 1196–1201. https://doi.org/10.1039/C2PY00543C.

37. Ren, G.; Sheng, X.; Qin, Y.; Chen, X.; Wang, X.; Wang, F. Toughening of Poly(Propylene Carbonate) Using Rubbery Non-Isocyanate Polyurethane: Transition from Brittle to Marginally Tough. *Polymer (Guildf)* **2014**, *55* (21), 5460–5468. https://doi.org/https://doi.org/10.1016/j.polymer.2014.08.052.

38. Han, D.; Chen, G.; Xiao, M.; Wang, S.; Chen, S.; Peng, X.; Meng, Y. Biodegradable and Toughened Composite of Poly(Propylene Carbonate)/Thermoplastic Polyurethane (PPC/TPU): Effect of Hydrogen Bonding. *Int J Mol Sci* **2018**, *19* (7), 2032.

39. Ma, L.; Song, L.; Wang, H.; Fan, L.; Liu, B. Synthesis and Characterization of Poly(Propylene Carbonate) Glycol-Based Waterborne Polyurethane with a High Solid Content. *Prog Org Coat* **2018**, *122*, 38–44. https://doi.org/https://doi.org/10.1016/j.porgcoat.2018.05.003.

40. Sulley, G. S.; Gregory, G. L.; Chen, T. T. D.; Peña Carrodeguas, L.; Trott, G.; Santmarti, A.; Lee, K.-Y.; Terrill, N. J.; Williams, C. K. Switchable Catalysis Improves the Properties of CO2-Derived Polymers: Poly(Cyclohexene Carbonate-b-ε-Decalactone-b-Cyclohexene Carbonate) Adhesives, Elastomers, and Toughened Plastics. *J Am Chem Soc* **2020**, *142* (9), 4367–4378. https://doi.org/10.1021/jacs.9b13106.

41. Jenkins, C. L.; Siebert, H. M.; Wilker, J. J. Integrating Mussel Chemistry into a Bio-Based Polymer to Create Degradable Adhesives. *Macromolecules* **2017**, *50* (2), 561–568. https://doi.org/10.1021/acs.macromol.6b02213.

42. Chung, H. U.; Kim, B. H.; Lee, J. Y.; Lee, J.; Xie, Z.; Ibler, E. M.; Lee, K.; Banks, A.; Jeong, J. Y.; Kim, J.; Ogle, C.; Grande, D.; Yu, Y.; Jang, H.; Assem, P.; Ryu, D.; Kwak, J. W.; Namkoong, M.; Park, J. Bin; Lee, Y.; Kim, D. H.; Ryu, A.; Jeong, J.; You, K.; Ji, B.; Liu, Z.; Huo, Q.; Feng, X.; Deng, Y.; Xu, Y.; Jang, K.-I.; Kim, J.; Zhang, Y.; Ghaffari, R.; Rand, C. M.; Schau, M.; Hamvas, A.; Weese-Mayer, D. E.; Huang, Y.; Lee, S. M.; Lee, C. H.; Shanbhag, N. R.; Paller, A. S.; Xu, S.; Rogers, J. A. Binodal, Wireless Epidermal Electronic Systems with in-Sensor Analytics for Neonatal Intensive Care. *Science* **2019**, *363* (6430), eaau0780–eaau0780.

https://doi.org/10.1126/science.aau0780.

43. Shukla, K.; Srivastava, V. C. Synthesis of Organic Carbonates from Alcoholysis of Urea: A Review. *Catalysis Reviews* **2017**, *59* (1), 1–43. https://doi.org/10.1080/01614940.2016.1263088.

44. Beharaj, A.; McCaslin, E. Z.; Blessing, W. A.; Grinstaff, M. W. Sustainable Polycarbonate Adhesives for Dry and Aqueous Conditions with Thermoresponsive Properties. *Nat Commun* **2019**, *10* (1), 5478. https://doi.org/10.1038/s41467-019-13449-y.

45. Krase, N. W.; Gaddy, V. L. Synthesis of Urea from Ammonia and Carbon Dioxide. *Journal of Industrial & Engineering Chemistry* **1922**, *14* (7), 611–615. https://doi.org/10.1021/ie50151a009.

46. Du, Z.; Chen, F.; Lin, Z.; Li, X.; Yuan, H.; Wu, Y. Effect of MgO on the Catalytic Performance of MgTiO3 in Urea Alcoholysis to Propylene Carbonate. *Chemical Engineering Journal* **2015**, *278*, 79–84. https://doi.org/https://doi.org/10.1016/j.cej.2014.12.033.

47. Woodcock, J. W.; Wright, R. A. E.; Jiang, X.; O'Lenick, T. G.; Zhao, B. Dually Responsive Aqueous Gels from Thermo- and Light-Sensitive Hydrophilic ABA Triblock Copolymers. *Soft Matter* **2010**, *6* (14), 3325–3336. https://doi.org/10.1039/C000450B.

48. Bender, T. A.; Dabrowski, J. A.; Gagné, M. R. Homogeneous Catalysis for the Production of Low-Volume, High-Value Chemicals from Biomass. *Nat Rev Chem* **2018**, *2* (5), 35–46. https://doi.org/10.1038/s41570-018-0005-y.

49. Stemmelen, M.; Lapinte, V.; Habas, J.-P.; Robin, J.-J. Plant Oil-Based Epoxy Resins from Fatty Diamines and Epoxidized Vegetable Oil. *Eur Polym J* **2015**, *68*, 536–545. https://doi.org/https://doi.org/10.1016/j.eurpolymj.2015.03.062.

50. Farhadian, A.; Gol Afshani, M. B.; Babaei Miyardan, A.; Nabid, M. R.; Safari, N. A Facile and Green Route for Conversion of Bifunctional Epoxide and Vegetable Oils to Cyclic Carbonate: A Green Route to CO2 Fixation. *ChemistrySelect* **2017**, *2* (4), 1431–1435. https://doi.org/10.1002/slct.201601891.

51. Orgilés-Calpena, E.; Arán-Aís, F.; Torró-Palau, A. M.; Montiel-Parreño, E.; Orgilés-Barceló, C. Synthesis of Polyurethanes from CO2-Based Polyols: A Challenge for Sustainable Adhesives. *Int J Adhes Adhes* **2016**, *67*, 63–68. https://doi.org/https://doi.org/10.1016/j.ijadhadh.2015.12.027.

52. Delebecq, E.; Pascault, J.-P.; Boutevin, B.; Ganachaud, F. On the Versatility of Urethane/Urea Bonds: Reversibility, Blocked Isocyanate, and Non-Isocyanate Polyurethane. *Chem Rev* **2013**, *113* (1), 80–118. https://doi.org/10.1021/cr300195n.

53. Heinrich, L. A. Future Opportunities for Bio-Based Adhesives – Advantages beyond Renewability. *Green Chemistry* **2019**, *21* (8), 1866–1888. https://doi.org/10.1039/C8GC03746A.

54. Janvier, M.; Ducrot, P.-H.; Allais, F. Isocyanate-Free Synthesis and Characterization of Renewable Poly(Hydroxy)Urethanes from Syringaresinol. *ACS Sustain Chem Eng* **2017**, *5* (10), 8648–8656. https://doi.org/10.1021/acssuschemeng.7b01271.

55. Wai, P. T.; Jiang, P.; Shen, Y.; Zhang, P.; Gu, Q.; Leng, Y. Catalytic Developments in the Epoxidation of Vegetable Oils and the Analysis Methods of Epoxidized Products. *RSC Adv* **2019**, *9* (65), 38119–38136. https://doi.org/10.1039/C9RA05943A.

56. Li, Y.; Sun, X. S. Polyols from Epoxidized Soybean Oil and Alpha Hydroxyl Acids and Their Adhesion Properties from UV Polymerization. *Int J Adhes Adhes* **2015**, *63*, 1–8. https://doi.org/https://doi.org/10.1016/j.ijadhadh.2015.07.013.

57. Li, Y.; Chou, S.-H.; Qian, W.; Sung, J.; Chang, S. I.; Sun, X. S. Optimization of Soybean Oil Based Pressure-Sensitive Adhesives Using a Full Factorial Design. *J Am Oil Chem Soc* **2017**, *94* (5), 713–721. https://doi.org/10.1007/s11746-017-2966-2.

58. Liu, X. Synthesis and Properties of Bio-Based Adhesives Derived from Plant Oil Residues. *American Journal of Modern Energy* **2019**, *5* (6), 94–99. https://doi.org/10.11648/j.ajme.20190506.12.

59. Sawpan, M. A. Polyurethanes from Vegetable Oils and Applications: A Review. *Journal of Polymer Research* **2018**, *25* (8), 184. https://doi.org/10.1007/s10965-018-1578-3.

60. Vanags, E.; Kirpluks, M.; Cabulis, U.; Walterova, Z. Highly Functional Polyol Synthesis from Epoxidized Tall Oil Fatty Acids. *J Renew Mater* **2018**, *6* (7), 764–771. https://doi.org/10.7569/JRM.2018.634111.

61. Kurańska, M.; Banaś, J.; Polaczek, K.; Banaś, M.; Prociak, A.; Kuc, J.; Uram, K.; Lubera, T. Evaluation of Application Potential of Used Cooking Oils in the Synthesis of Polyol Compounds. *J Environ Chem Eng* **2019**, *7* (6), 103506. https://doi.org/https://doi.org/10.1016/j.jece.2019.103506.

62. Goudarzi, F.; Izadbakhsh, A. Evaluation of K/SnO2 Performance as a Solid Catalyst in the Trans-Esterification of a Mixed Plant Oil. *Reaction Kinetics, Mechanisms and Catalysis* **2017**, *121* (2), 539–553. https://doi.org/10.1007/s11144-017-1176-0.

63. Li, C.; Wang, W.; Yan, L.; Ding, Y. A Mini Review on Strategies for Heterogenization of Rhodium-Based Hydroformylation Catalysts. *Front Chem Sci Eng* **2018**, *12* (1), 113–123. https://doi.org/10.1007/S11705-017-1672-9/METRICS.

64. Pandey, S.; Chikkali, S. H. Highly Regioselective Isomerizing Hydroformylation of Long-Chain Internal Olefins Catalyzed by a Rhodium Bis(Phosphite) Complex.

ChemCatChem **2015**, *7* (21), 3468–3471. https://doi.org/10.1002/cctc.201500743.

65. Alagi, P.; Ghorpade, R.; Jang, J. H.; Patil, C.; Jirimali, H.; Gite, V.; Hong, S. C. Functional Soybean Oil-Based Polyols as Sustainable Feedstocks for Polyurethane Coatings. *Ind Crops Prod* **2018**, *113*, 249–258. https://doi.org/https://doi.org/10.1016/j.indcrop.2018.01.041.

66. Pechar, T. W.; Sohn, S.; Wilkes, G. L.; Ghosh, S.; Frazier, C. E.; Fornof, A.; Long, T. E. Characterization and Comparison of Polyurethane Networks Prepared Using Soybean-Based Polyols with Varying Hydroxyl Content and Their Blends with Petroleum-Based Polyols. *J Appl Polym Sci* **2006**, *101* (3), 1432–1443. https://doi.org/10.1002/app.23625.

67. Alagi, P.; Choi, Y. J.; Seog, J.; Hong, S. C. Efficient and Quantitative Chemical Transformation of Vegetable Oils to Polyols through a Thiol-Ene Reaction for Thermoplastic Polyurethanes. *Ind Crops Prod* **2016**, *87*, 78–88. https://doi.org/https://doi.org/10.1016/j.indcrop.2016.04.027.

68. Teacă, C.-A.; Roşu, D.; Tanasă, F.; Zănoagă, M.; Mustaţă, F. Epoxidized Vegetable Oils for Thermosetting Resins and Their Potential Applications. In *Functional Biopolymers*; Thakur, V. K., Thakur, M. K., Eds.; Springer International Publishing: Cham, 2018; pp 217–238. https://doi.org/10.1007/978-3-319-66417-0_8.

69. Wang, X.-L.; Chen, L.; Wu, J.-N.; Fu, T.; Wang, Y.-Z. Flame-Retardant Pressure-Sensitive Adhesives Derived from Epoxidized Soybean Oil and Phosphorus-Containing Dicarboxylic Acids. *ACS Sustain Chem Eng* **2017**, *5* (4), 3353–3361. https://doi.org/10.1021/acssuschemeng.6b03201.

70. Tenorio-Alfonso, A.; Sánchez, M. C.; Franco, J. M. A Review of the Sustainable Approaches in the Production of Bio-Based Polyurethanes and Their Applications in the Adhesive Field. *J Polym Environ* **2020**, *28* (3), 749–774. https://doi.org/10.1007/s10924-020-01659-1.

71. Hong, J.; Radojčić, D.; Yang, X.-Q.; Wan, X.; Petrović, Z. S. Tough Thermosetting Polyurethanes and Adhesives from Rubber Seed Oil by Hydroformylation. *J Appl Polym Sci* **2020**, *137* (13), 48509. https://doi.org/10.1002/app.48509.

72. Gama, N.; Ferreira, A.; Barros-Timmons, A. Cure and Performance of Castor Oil Polyurethane Adhesive. *Int J Adhes Adhes* **2019**, *95*, 102413. https://doi.org/https://doi.org/10.1016/j.ijadhadh.2019.102413.

73. Faria, D. L.; Lopes, T. A.; Scatolino, M. V.; Protásio, T. D. P.; Nascimento, M. F. do; Lahr, F. A. R.; Mendes, L. M.; Guimarães Júnior, J. B. STUDYING THE GRAMMAGE IN LVL PANELS GLUED WITH CASTOR OIL-BASED POLYURETHANE ADHESIVE: A POSSIBLE ALTERNATIVE TO FORMALDEHYDE RELEASING ADHESIVES. *CERNE* **2020**, No. 1, 140-149%V 26.

74. Mapari, S.; Mestry, S.; Mhaske, S. T. Developments in Pressure-Sensitive Adhesives: A Review. *Polymer Bulletin 2020 78:7* **2020**, *78* (7), 4075–4108. https://doi.org/10.1007/S00289-020-03305-1.

75. Ewert, T. R.; Mannion, A. M.; Coughlin, M. L.; Macosko, C. W.; Bates, F. S. Influence of Rheology on Renewable Pressure-Sensitive Adhesives from a Triblock Copolymer. *J Rheol (N Y N Y)* **2018**, *62* (1), 161–170. https://doi.org/10.1122/1.5009194.

76. Sodergard, A.; Stolt, M. Properties of Lactic Acid Based Polymers and Their Correlation with Composition. *Progress in Polymer Science – PROG POLYM SCI* **2002**, *27*, 1123–1163. https://doi.org/10.1016/S0079-6700(02)00012-6.

77. De Hoe, G. X.; Zumstein, M. T.; Tiegs, B. J.; Brutman, J. P.; McNeill, K.; Sander, M.; Coates, G. W.; Hillmyer, M. A. Sustainable Polyester Elastomers from Lactones: Synthesis, Properties, and Enzymatic Hydrolyzability. *J Am Chem Soc* **2018**, *140* (3), 963–973. https://doi.org/10.1021/jacs.7b10173.

78. Martello, M. T.; Schneiderman, D. K.; Hillmyer, M. A. Synthesis and Melt Processing of Sustainable Poly(ε-Decalactone)-Block-Poly(Lactide) Multiblock Thermoplastic Elastomers. *ACS Sustain Chem Eng* **2014**, *2* (11), 2519–2526. https://doi.org/10.1021/sc500412a.

79. Wu, S. Chain Structure and Entanglement. *J Polym Sci B Polym Phys* **1989**, *27* (4), 723–741. https://doi.org/10.1002/polb.1989.090270401.

80. Nasiri, M.; Reineke, T. M. Sustainable Glucose-Based Block Copolymers Exhibit Elastomeric and Adhesive Behavior. *Polym Chem* **2016**, *7* (33), 5233–5240. https://doi.org/10.1039/C6PY00700G.

81. Kim, H. J.; Jin, K.; Shim, J.; Dean, W.; Hillmyer, M. A.; Ellison, C. J. Sustainable Triblock Copolymers as Tunable and Degradable Pressure Sensitive Adhesives. *ACS Sustain Chem Eng* **2020**. https://doi.org/10.1021/acssuschemeng.0c03158.

82. Kim, H. J. Sustainable Triblock Copolymers as Tunable and Degradable Pressure Sensitive Adhesives. *ACS Sustain Chem Eng* **2020**.

83. Dastjerdi, Z.; Cranston, E. D.; Dubé, M. A. Pressure Sensitive Adhesive Property Modification Using Cellulose Nanocrystals. *Int J Adhes Adhes* **2018**, *81*, 36–42. https://doi.org/https://doi.org/10.1016/j.ijadhadh.2017.11.009.

84. Yang, X.; Li, N.; Constantinesco, I.; Yu, K.; Kizhakkedathu, J. N.; Brooks, D. E. Choline Phosphate Functionalized Cellulose Membrane: A Potential Hemostatic Dressing Based on a Unique Bioadhesion Mechanism. *Acta Biomater* **2016**, *40*, 212–225. https://doi.org/https://doi.org/10.1016/j.actbio.2016.06.030.

85. Abd el-sayed, E.; El-Sakhawy, M.; Kamel, S.; El-Gendy, A.; Abouzeid, R. Eco-Friendly Mimosa Tannin Adhesive System for Bagasse Particleboard Fabrication.

Egypt J Chem **2018**. https://doi.org/10.21608/ejchem.2018.5413.1479.

86. Patel, A. K.; Mathias, J.-D.; Michaud, P. Polysaccharides as Adhesives. *Reviews of Adhesion and Adhesives* **2013**, *1* (3), 312–345. https://doi.org/10.7569/RAA.2013.097310.

87. Zhao, X.; Peng, L.; Wang, H.; Wang, Y.; Zhang, H. Environment-Friendly Urea-Oxidized Starch Adhesive with Zero Formaldehyde-Emission. *Carbohydr Polym* **2018**, *181*, 1112–1118. https://doi.org/https://doi.org/10.1016/j.carbpol.2017.11.035.

88. Chen, L.; Wang, Y.; Zia ud, D.; Fei, P.; Jin, W.; Xiong, H.; Wang, Z. Enhancing the Performance of Starch-Based Wood Adhesive by Silane Coupling Agent(KH570). *Int J Biol Macromol* **2017**, *104*, 137–144. https://doi.org/https://doi.org/10.1016/j.ijbiomac.2017.05.182.

89. Umemura, K.; Mihara, A.; Kawai, S. Development of New Natural Polymer-Based Wood Adhesives III: Effects of Glucose Addition on Properties of Chitosan. *Journal of Wood Science* **2010**, *56* (5), 387–394. https://doi.org/10.1007/s10086-010-1117-2.

90. Park, E.; Lee, J.; Huh, K. M.; Lee, S. H.; Lee, H. Toxicity-Attenuated Glycol Chitosan Adhesive Inspired by Mussel Adhesion Mechanisms. *Adv Healthc Mater* **2019**, *8* (14), 1900275. https://doi.org/10.1002/adhm.201900275.

91. Nourmohammadi, J.; Ghaee, A.; Liavali, S. H. Preparation and Characterization of Bioactive Composite Scaffolds from Polycaprolactone Nanofibers-Chitosan-Oxidized Starch for Bone Regeneration. *Carbohydr Polym* **2016**, *138*, 172–179. https://doi.org/https://doi.org/10.1016/j.carbpol.2015.11.055.

92. Benedek, I. *Pressure-Sensitive Adhesives and Applications*; CRC Press, 2004.

93. Griehl, W.; Ruestem, D. Nylon-12-Preparation, Properties, and Applications. *Ind Eng Chem* **1970**, *62* (3), 16–22.

94. Lundberg, R. D. Structure and Properties of Ionomers'(Eds M. Pineri and A. Eisenberg), D. Reidel Publishing Company, Boston 1987.

95. Boval'dinova, K. A.; Sherstneva, N. E.; Fel'dshtein, M. M.; Moskalets, A. P.; Khokhlov, A. R. Pressure-Sensitive Adhesives with Tunable Tackiness. *Polymer Science, Series B* **2019**, *61* (4), 458–470.

96. Wang, W.; Liu, S.; Chen, B.; Yan, X.; Li, S.; Ma, X.; Yu, X. DNA-Inspired Adhesive Hydrogels Based on the Biodegradable Polyphosphoesters Tackified by a Nucleobase. *Biomacromolecules* **2019**, *20* (10), 3672–3683. https://doi.org/10.1021/acs.biomac.9b00642.

97. Zhang, K.; Fahs, G. B.; Margaretta, E.; Hudson, A. G.; Moore, R. B.; Long, T. E. Acetyl-Protected Cytosine and Guanine Containing Acrylics as Supramolecular

Adhesives. *J Adhes* **2019**, *95* (2), 146–167.

98. Chen, X.; Zhang, K.; Talley, S. J.; Orsino, C. M.; Moore, R. B.; Long, T. E. Quadruple Hydrogen Bonding Containing Supramolecular Thermoplastic Elastomers: Mechanical and Morphological Correlations. *J. Polym. Sci. Part A: Polym. Chem.* **2019**, *57* (1), 13–23. https://doi.org/doi:10.1002/pola.29272.

99. Tamami, M.; Zhang, K.; Dixit, N.; Moore, R. B.; Long, T. E. Association of Nucleobase-Containing Ammonium Ionenes. *Macromol Chem Phys* **2014**, *215* (23), 2337–2344.

100. Zhang, K.; Fahs, G. B.; Aiba, M.; Moore, R. B.; Long, T. E. Nucleobase-Functionalized ABC Triblock Copolymers: Self-Assembly of Supramolecular Architectures. *Chemical Communications* **2014**, *50* (65), 9145–9148. https://doi.org/10.1039/C4CC03363A.

101. Tamami, M.; Hemp, S. T.; Zhang, K.; Zhang, M.; Moore, R. B.; Long, T. E. Poly(Ethylene Glycol)-Based Ammonium Ionenes Containing Nucleobases. *Polymer (Guildf)* **2013**, *54* (6), 1588–1595. https://doi.org/10.1016/J.POLYMER.2013.01.040.

102. Zhang, K.; Chen, M.; Drummey, K. J.; Talley, S. J.; Anderson, L. J.; Moore, R. B.; Long, T. E. Ureido Cytosine and Cytosine-Containing Acrylic Copolymers. *Polym. Chem.* **2016**, *7* (43), 6671–6681.

103. Zhang, K.; Aiba, M.; Fahs, G. B.; Hudson, A. G.; Chiang, W. D.; Moore, R. B.; Ueda, M.; Long, T. E. Nucleobase-Functionalized Acrylic ABA Triblock Copolymers and Supramolecular Blends. *Polym Chem* **2015**, *6* (13), 2434–2444.

104. Cashion, M. P.; Park, T.; Long, T. E. Influence of Hydrogen Bonding on the Adhesive Properties of Photo-Curable Acrylics. *J Adhes* **2009**, *85* (1), 1–17.

105. Karikari, A. S.; Mather, B. D.; Long, T. E. Association of Star-Shaped Poly (D, L-Lactide) s Containing Nucleobase Multiple Hydrogen Bonding. *Biomacromolecules* **2007**, *8* (1), 302–308.

106. Yamauchi, K.; Lizotte, J. R.; Long, T. E. Thermoreversible Poly (Alkyl Acrylates) Consisting of Self-Complementary Multiple Hydrogen Bonding. *Macromolecules* **2003**, *36* (4), 1083–1088.

107. Chen, X.; Zawaski, C. E.; Spiering, G. A.; Liu, B.; Orsino, C. M.; Moore, R. B.; Williams, C. B.; Long, T. E. Quadruple Hydrogen Bonding Supramolecular Elastomers for Melt Extrusion Additive Manufacturing. *ACS Appl Mater Interfaces* **2020**, *12* (28), 32006–32016. https://doi.org/10.1021/acsami.0c08958.

108. Liu, B.; Chen, X.; Spiering, G. A.; Moore, R. B.; Long, T. E. Quadruple Hydrogen Bond-Containing A-AB-A Triblock Copolymers: Probing the Influence of Hydrogen Bonding in the Central Block. *Molecules 2021, Vol. 26, Page 4705* **2021**, *26* (15), 4705.

https://doi.org/10.3390/MOLECULES26154705.

109. Domb, A. J.; Kost, J.; Wiseman, D. *Handbook of Biodegradable Polymers*; CRC press, 1998.

110. Du, X.; Liu, Y.; Yan, H.; Rafique, M.; Li, S.; Shan, X.; Wu, L.; Qiao, M.; Kong, D.; Wang, L. Anti-Infective and Pro-Coagulant Chitosan-Based Hydrogel Tissue Adhesive for Sutureless Wound Closure. *Biomacromolecules* **2020**, *21* (3), 1243–1253. https://doi.org/10.1021/acs.biomac.9b01707.

111. Takeoka, Y.; Yurube, T.; Morimoto, K.; Kunii, S.; Kanda, Y.; Tsujimoto, R.; Kawakami, Y.; Fukase, N.; Takemori, T.; Omae, K.; Kakiuchi, Y.; Miyazaki, S.; Kakutani, K.; Takada, T.; Nishida, K.; Fukushima, M.; Kuroda, R. Reduced Nucleotomy-Induced Intervertebral Disc Disruption through Spontaneous Spheroid Formation by the Low Adhesive Scaffold Collagen (LASCol). *Biomaterials* **2020**, *235*, 119781. https://doi.org/https://doi.org/10.1016/j.biomaterials.2020.119781.

112. Ushimaru, K.; Morita, T.; Fukuoka, T. A Bio-Based Adhesive Composed of Polyelectrolyte Complexes of Lignosulfonate and Cationic Polyelectrolytes. *Journal of Wood Chemistry and Technology* **2020**, *40* (3), 172–177. https://doi.org/10.1080/02773813.2020.1722701.

113. Vargas Villanueva, J. G.; Sarmiento Huertas, P. A.; Galan, F. S.; Esteban Rueda, R. J.; Briceño Triana, J. C.; Casas Rodriguez, J. P. Bio-Adhesion Evaluation of a Chitosan-Based Bone Bio-Adhesive. *Int J Adhes Adhes* **2019**, *92*, 80–88. https://doi.org/https://doi.org/10.1016/j.ijadhadh.2019.04.009.

114. Giroto, J. A.; Teixeira, A. C. S. C.; Nascimento, C. A. O.; Guardani, R. Degradation of Poly(Ethylene Glycol) in Aqueous Solution by Photo-Fenton and H2O2/UV Processes. *Ind Eng Chem Res* **2010**, *49* (7), 3200–3206. https://doi.org/10.1021/ie9015792.

115. Banerjee, A.; Chatterjee, K.; Madras, G. Enzymatic Degradation of Polymers: A Brief Review. *Materials Science and Technology* **2014**, *30* (5), 567–573.

116. Kawai, F.; Moriya, F. Bacterial Assimilation of Polytetramethylene Glycol. *J Ferment Bioeng* **1991**, *71* (1), 1–5. https://doi.org/https://doi.org/10.1016/0922-338X(91)90294-Q.

117. Kawai, F. Biodegradation of Polyethers (Polyethylene Glycol, Polypropylene Glycol, Polytetramethylene Glycol, and Others). *Biopolymers Online: Biology• Chemistry• Biotechnology• Applications* **2005**, *9*.

118. Cernadas, T. M.; Gonçalves, F. A. M. M.; Alves, P.; Miguel, S. P.; Cabral, C.; Correia, I. J.; Ferreira, P. Preparation of Biodegradable Functionalized Polyesters Aimed to Be Used as Surgical Adhesives. *Eur Polym J* **2019**, *117*, 442–454. https://doi.org/https://doi.org/10.1016/j.eurpolymj.2019.05.019.

119. Daristotle, J. L.; Zaki, S. T.; Lau, L. W.; Ayyub, O. B.; Djouini, M.; Srinivasan, P.; Erdi, M.; Sandler, A. D.; Kofinas, P. Pressure-Sensitive Tissue Adhesion and Biodegradation of Viscoelastic Polymer Blends. *ACS Appl Mater Interfaces* **2020**, *12* (14), 16050–16057. https://doi.org/10.1021/acsami.0c00497.

120. Daristotle, J. L.; Lau, L. W.; Erdi, M.; Hunter, J.; Djoum Jr., A.; Srinivasan, P.; Wu, X.; Basu, M.; Ayyub, O. B.; Sandler, A. D.; Kofinas, P. Sprayable and Biodegradable, Intrinsically Adhesive Wound Dressing with Antimicrobial Properties. *Bioeng Transl Med* **2020**, *5* (1), e10149. https://doi.org/10.1002/btm2.10149.

121. Yang, Z.; Wang, F.; Liu, H. Dual Responsive Spiropyran-Ended Poly(N-Vinyl Caprolactam) for Reversible Complexation with Metal Ions. *Journal of Polymer Research* **2019**, *26* (4). https://doi.org/10.1007/s10965-019-1747-z.

122. Wang, X.; Chen, D.; Zhang, M.; Hu, H. Biodegradable Polylactide/TiO2 Composite Fiber Scaffolds with Superhydrophobic and Superadhesive Porous Surfaces for Water Immobilization, Antibacterial Performance, and Deodorization. *Polymers (Basel)* **2019**, *11* (11), 1860.

123. Bou-Francis, A.; Piercey, M.; Al-Qatami, O.; Mazzanti, G.; Khattab, R.; Ghanem, A. Polycaprolactone Blends for Fracture Fixation in Low Load-Bearing Applications. *J Appl Polym Sci* **2020**, *137* (32), 48940. https://doi.org/10.1002/app.48940.

124. Orgilés-Calpena, E.; Arán-Aís, F.; Torró-Palau, A.; Orgilés-Barceló, C. Biodegradable Polyurethane Adhesives Based on Polyols Derived from Renewable Resources. *Proceedings of the Institution of Mechanical Engineers, Part L: Journal of Materials: Design and Applications* **2014**, *228* (2), 125–136. https://doi.org/10.1177/1464420713517674.

125. Tous, L.; Ruseckaite, R. A.; Ciannamea, E. M. Sustainable Hot-Melt Adhesives Based on Soybean Protein Isolate and Polycaprolactone. *Ind Crops Prod* **2019**, *135*, 153–158. https://doi.org/https://doi.org/10.1016/j.indcrop.2019.04.043.

126. Cernadas, T.; Morgado, S.; Alves, P.; Gonçalves, F. A. M. M.; Correia, T. R.; Correia, I. J.; Ferreira, P. Preparation of Functionalized Poly(Caprolactone Diol)/Castor Oils Blends to Be Applied as Photocrosslinkable Tissue Adhesives. *J Appl Polym Sci* **2020**, *n/a* (n/a), 49092. https://doi.org/10.1002/app.49092.

127. Gu, Y.; Cheng, L.; Gu, Z.; Hong, Y.; Li, Z.; Li, C. Preparation, Characterization and Properties of Starch-Based Adhesive for Wood-Based Panels. *Int J Biol Macromol* **2019**, *134*, 247–254. https://doi.org/https://doi.org/10.1016/j.ijbiomac.2019.04.088.

CHAPTER 3

4,4’ DIMETHYL OXYBISBENZOATE AS A MONOMER FOR FULLY AMORPHOUS HIGH TG POLYESTERS

3.1 Introduction

Polyesters demonstrate an extensive family of thermoplastics and thermosets, which find use across all industries from adhesive design to covalent adaptive networks to high performance materials.[1–4] Most notably, the most ubiquitous polyester, poly(ethylene terephthalate) PET finds extensive use in single use plastics and current estimates predict that 30 million tons of PET is manufactured annually.[5] This massive production and consumption of PET prompted many scientists to optimize recycling strategies for PET to enable a circular economy. Whereas many polymer families are limited to mechanical recycling, recent catalytic efforts, such as VolCat and others, demonstrated efficient and scalable chemical recycling strategies for PET.[6,7] These processes leverage facile hydrolysis of the ester bond to return to polymerizable monomers. This work inspired ester incorporation into polyolefins to promote chemical recycling to monomers.[8] While PET is limited to select applications, the chemical recyclability of polyesters encourages the design of novel polyester structures to serve other applications which require higher glass transition temperatures and differing morphological properties.

Structure-property relationships in polyesters is a largely studied field where the unique combinations of diol and diester monomers provide innumerable polymers, copolymers, terpolymers, networks, etc. This enables precise tailoring of thermal properties and morphology through simple monomer selection. For example, linear aliphatic diols lower glass transition temperatures as the diol length increases.[9,10] Also, cycloaliphatic polyesters such as poly(cyclohexamethylene terephthalate) impart improved impact resistance by introducing ring relaxations at high frequency deformations.[11,12] Furthermore, variations in aromatic diesters enabled liquid crystalline polymers, improved thermal resistance, and changes in glass transition temperature.[13–15] Continued exploration of novel polyesters with previously unexplored monomers provides deeper fundamental understanding of structure-property relationships, and also provides industry and academia with a more expansive toolbox for the design of future polyesters for specific applications.

Thermal transitions of polyesters encompass sub T_g relaxations such as ring flipping, the T_g, which is the onset of cooperative long-range segmental motion, and the T_m associated with crystalline phases in the polyester.[16] Depending on the chemical composition, a polyester contains all these thermal transitions or only the glass transition temperature in fully amorphous polymers with no sub T_g relaxations. Polyesters often also contain more than one T_m associated with either different sizes of crystallites or different types of crystallites such as the smectic and nematic phases in liquid crystalline polymers.[17,18] Quantitative structure-property relationships, such as the Fox equation (**Equation 3.1**), provide predictability based on the mass incorporation of specific monomers.[19] The Fox equation predicts the glass transition temperature of copolymers based on the weight percent incorporation of each monomer and the glass transition temperature of their respective homopolymers.

(**Equation 3.1**)

$$\frac{1}{T_{gab}} = \frac{w_a}{T_{ga}} + \frac{w_b}{T_{gb}}$$

4, 4’ dimethyloxybisbenzoate (DMOB) is an aromatic diester monomer containing two para-substituted phenyl rings joined together through an aryl ether bond. Little research has been conducted on this monomer in polyester applications, and prior investigations have been limited to polyesters for liquid-crystalline applications where only one copolymer composition was investigated.[20,21] These findings found DMOB incorporation to provide advantageous properties such as increased load-bearing and elevated glass transition temperatures. These advantageous properties attributed to DMOB incorporation warrant continued investigation of DMOB polyesters in other application spaces. For instance, cyclohexane dimethanol (CHDM) based polymers provide high glass transition temperature and improved impact resistance. However, in semicrystalline polymers such as poly(cyclohexamethylene terephthalate), embrittlement caused by crystallization distracts from the impact resistance properties imparted from CHDM. Thus, investigating new dimethyl ester monomers for CHDM polyesters will provide more understanding towards the structure-property relationships dictating the high degree of crystallinity in other CHDM based polyesters.

In this work, we present a family of novel polyesters incorporating both DMOB and CHDM. Structure-property relationships regarding changes in T_g and T_m are discussed. DMOB both increased glass transition temperatures and decreased crystallinity in comparison to a synthesized poly(cyclohexamethylene terephthalate) control. This monomer demonstrates promise in the future design of fully amorphous polyesters with glass transition temperatures greater than 100 °C.

3.2 Experimental

3.2.1 Materials

Butane diol (BD) (Sigma Aldrich ≥ 99%), dimethyl terephthalate (DMT) (Tokyo Chemical Industries ≥ 99%), cyclohexanedimethanol (CHDM) (Sigma Aldrich ≥ 99%), dibutyltin oxide (Sigma Aldrich), chloroform-*d* ($CDCl_3$) (Cambridge Isotope Laboratories, 99.8% atom D), and dimethyl sulfoxide-d6 (DMSO-d6) (Cambridge Isotope Laboratories, 99.9% atom D) were used as received. 4,4’ dimethyloxybisbenzoate (DMOB) was supplied by Eastman Chemical Company and used as received. Optima^{TM} grade chloroform ($CHCl_3$) and tetrahydrofuran (THF) (Fischer Scientific) were used as received.

3.2.2 Synthesis of 4, 4’ Dimethyloxybisbenzoate homopolyesters and copolyesters

Polyesters were synthesized via melt transesterification and polycondensation following procedures previously implemented within our research group.[22] The selected diol (BD or CHDM) (1.2 eq), the selected combination of dimethyl ester monomers (DMT or DMOB) (1.0 eq), and dibutyltin oxide (200ppm) were charged to a 100 mL round-bottomed flask equipped with a t-neck adaptor, overhead stirrer, nitrogen inlet, and distillation arm connected to a 100 mL collection flask. Monomer amounts were calculated to achieve a total mass loading of 25 g. Prior to the start of the reaction, the reaction setup was evacuated under reduced pressure and backfilled with N_2 over three cycles to ensure inert reaction conditions during polymerization. The reaction flask was lowered into a bismuth tin alloy metal bath heated to 180 °C. Every 30 min, the bath temperature was raised to 20 °C. After 3 h, from the reaction start, the reaction was held at 280 °C and the pressure was reduced to 30 mmHg for 2 hours. Following the reaction, a clear viscous polymer melt wrapped the stir bar. The polymers were used after cooling without any further purification.

3.2.3 Analytical Methods

^{1}H NMR and ^{13}C NMR spectra were recorded using a Bruker Avance NEO 500 MHz NMR equipped with a 5mm iProbe. A Waters e2695 Separations Module Size Exclusion Chromatography system (SEC) with two Shodex KF-806M Columns and one Shodex K-G Guard Column connected to both a Waters 2414 refractive index detector and a Wyatt TREOS II light scattering detector afforded molecular weight information of the polymers. Polymers were dissolved at a concentration of 3 mg/mL in either $CHCl_3$ or THF and sampled into the SEC at a flow rate of 1 mL/min at a temperature of 35 °C. Online dn/dc values were determined from the dRI data assuming a 100% mass retention. Solubility of the polymers was confirmed prior to SEC analysis using a Malvern Zetasizer Nano ZS dynamic light scattering instrument. Prior to thermal analysis all polymer samples were melt pressed at 295°C, quench cooled in a water bath, and finally dried at 25 °C under a reduced pressure of 30 mmHg. A TA Instruments TGA5500 thermogravimetric analyzer (TGA) afforded weight loss profiles for polymers from 25 to 650 °C, under constant N2 flow at a heating rate of 10 °C/min. A TA Instruments DSC2500 differential scanning calorimeter (DSC) revealed the thermal transitions for the novel polymer under N2 flow. Initial DSC experiments followed a heat/cool/heat cycle from 25 °C to 300 °C to -80 °C to 300 °C at rates of 10/100/10 °C/min to remove the thermal history of the samples. In subsequent DSC annealing studies, samples were held 100 °C above their T_g for 1 h to facilitate crystallization prior to cooling and reheating. T_ms were determined by the peak of the melting endotherm and integration of the endothermic peak determined ΔH_m. Calibration of the instrument with indium (T_m = 156.60 °C) and zinc (T_m = 419.47 °C) standards occurred prior to analysis. Dynamic mechanical analysis (DMA) on a TA instruments Q800 with a static force of 0.01 N, amplitude of 0.1% strain, frequency of 1 Hz, and a heating rate of 3 °C/min provided storage and loss modulus from -100-175 °C. The polymers discussed will be identified using the abbreviation for the diol and diester monomeric starting materials. For example, BD DMOB refers to the polyester synthesized from butane diol and 4,4' dimethyloxybisbenzoate. Copolymers synthesized from both DMOB and DMT monomers will be referred to as CHDM DMOBX-DMTY) where X and Y refer to the wt.% incorporation of each dimethyl ester monomer respectively.

3.3 Results and Discussion

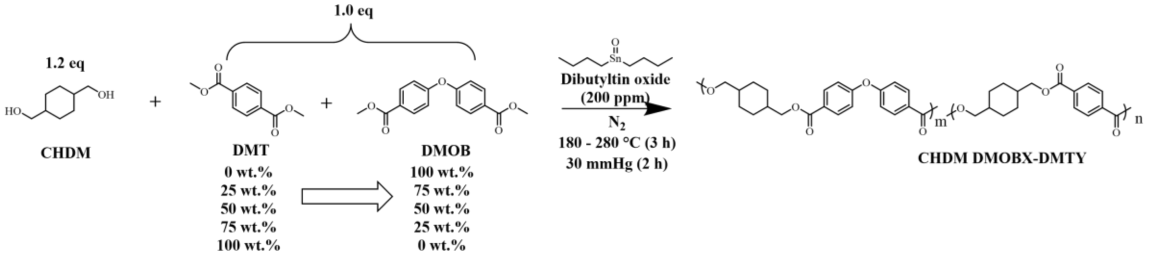

Scheme 3.1. Synthesis of dimethyloxybisbenzoate (DMOB) copolymers with cyclohexanedimethanol and dimethyl terephthalate.

Traditional melt polycondensation reactions provided both linear and cyclic aliphatic polyesters with DMOB incorporation as shown in **Scheme 3.1**. 1.2 equivalents of diol initially established low molecular weight oligomers prior to the final transesterification step under reduced pressure, which drove the reaction to yield high molecular weight polymer through distillation of the diol. Size exclusion chromatography in $CHCl_3$ or THF equipped with multi-angle light scattering detector determined absolute molecular weight values for only 3 of the 6 synthesized polyesters. CHDM DMOB DMT copolyesters remained insoluble in both THF and $CHCl_3$ when DMT incorporation was 75 wt.% or greater. Additionally, when the DMOB incorporation was 75 wt. % or greater, the polymers displayed UCST behavior in $CHCl_3$ and THF. Additionally, only the CHDM DMOB homopolymer and BD DMOB homopolymer were fully soluble in THF. **Table 3.1** provides the absolute molecular weight data from the soluble polymers, which demonstrated number average molecular weights around 20 kg/mol, which is a typical molecular weight for polycondensation polymers.[23] Furthermore, all quench-cooled polymer films were easily creased, which indicated all polymers had sufficiently large molecular weights for further characterization.

Table 3.1. Absolute molecular weight data for DMOB polymers and copolymers determined from online dn/dc measurements and light scattering data. Insoluble polymers noted with N/A.

Sample	**dn/dc**	**M_n (kg/mol)**	**M_w (kg/mol)**	**Đ**
BD DMOB	0.1590[a]	20.3	34.3	1.69
CHDM DMOB	0.157[b]	18.3	35.1	1.92
CHDM DMOB75-DMT25	N/A			
CHDM DMOB50-DMT50	0.1198[a]	22.4	41.6	1.86

CHDM DMOB25-DMT75	N/A			
CHDM DMT	N/A			

[a] $CHCl_3$ eluent, [b] THF eluent

Polymer insolubility prevented ^{1}H NMR analysis to confirm monomer incorporation across the CHDM DMOB-DMT copolymer series. However, FT-IR analysis, shown in **Figure 3.1**, confirmed DMOB and DMT incorporation, which matched the wt.% loadings in the reaction. Notably, DMOB incorporation systematically increased IR absorbance at 1595 cm^{-1}, 1500 cm^{-1}, 1160 cm^{-1}, and 765 cm^{-1} attributed to the symmetric aryl-O-aryl stretch, asymmetric aryl-O-aryl stretch, aryl-O stretch, and in plane ester bending respectively.[24] The in-plane ester bending of DMOB is blue-shifted in comparison to the in-plane ester bending of DMT.

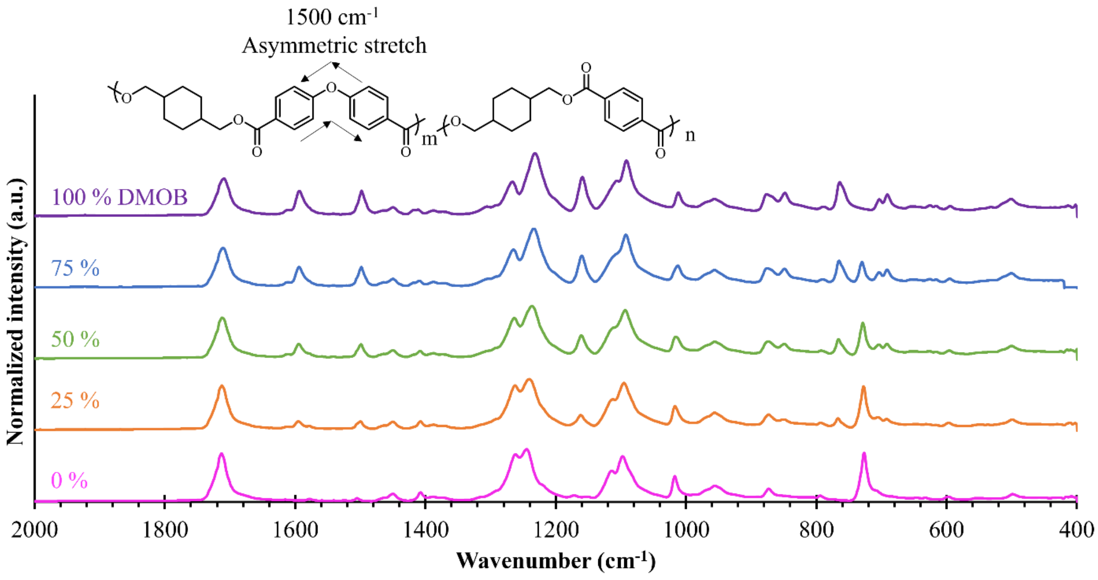

Figure 3.1. FTIR confirmed DMOB incorporation across copolymer series, which is demonstrated by the increased absorbance of the asymmetric aryl-O-aryl stretching vibrational mode at 1500 cm^{-1}.

TGA, shown in **Figure 3.2**. revealed thermal weight loss profiles for all six DMOB polymers. BD sentence. Furthermore, all polymers across the CHDM DMOB DMT copolymer series displayed $T_{d5\%}$ Values between 395 and 405 °C, which is consistent with many families of polyesters owing to the degradation of ester bonds in the polymer backbone.[25] Thus, DMOB incorporation did not impact the thermal degradation profiles in comparison to DMT. Additionally, char yield at 650 °C increased upon DMOB incorporation as a result of the higher percentage of aromatic groups in the homopolymers and copolymers.[26]

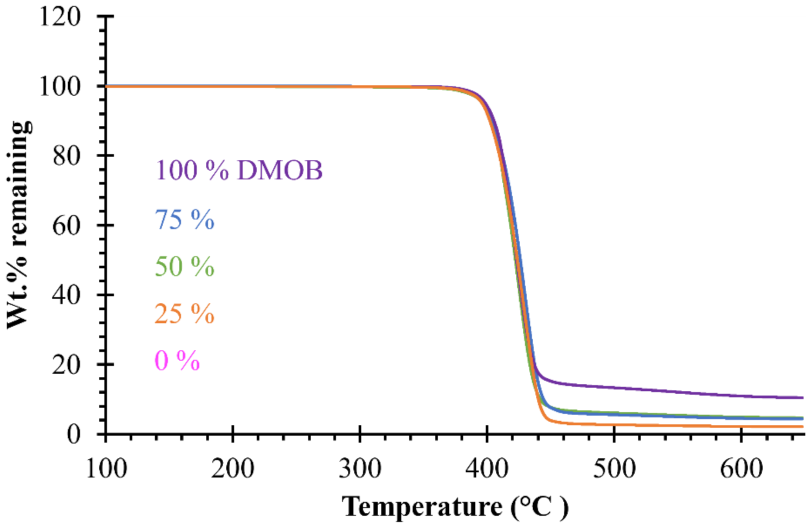

Figure 3.2. TGA shows consistent $T_{d5\%}$ across the copolymer series and shows that char yield increases with DMOB incorporation.

CHDM DMOB DMT copolyesters demonstrated predicable control over the glass transition temperature. DSC measurements, shown in **Figure 3.3** informed glass transition temperatures across the copolymer series ranging from 86-105 °C. All samples except for CHDM 25DMOB-75DMT agreed with T_g values predicted from the Fox equation. This deviation likely resulted from physical crosslinking caused by crystallites in the sample, which is known to increase the glass transition temperature of semicrystalline polymers.[27] However, general agreement with the Fox equation demonstrated random incorporation of each dimethyl ester monomer and highlighted elevated glass transition temperatures caused by increased DMOB incorporation. It should also be noted that no transitions indicative of liquid crystalline properties were observed in this copolyester series.

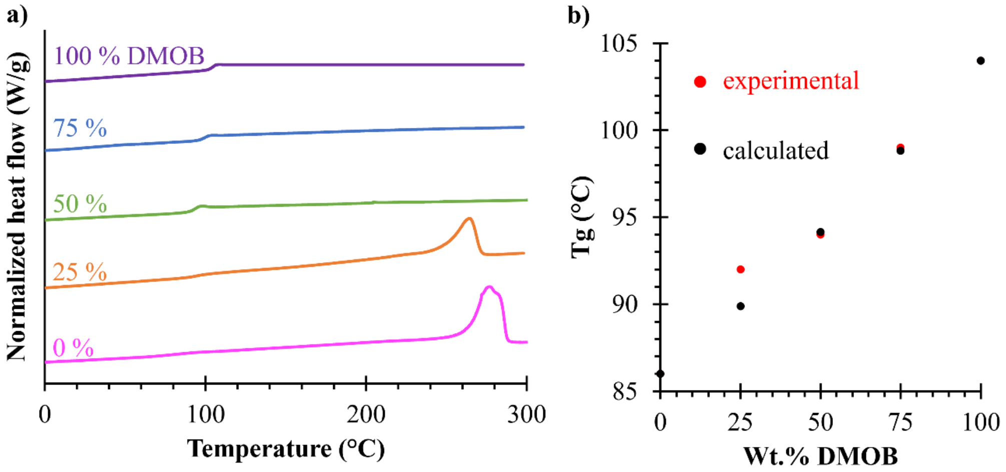

Figure 3.3. a) Differential scanning calorimetry shows changes in thermal transitions as DMOB incorporation increases. B) The copolymer series closely follows the T_g predictions from the fox equation (right).

In addition to providing predictable control of the glass transition temperature of polymer samples, incorporation of DMOB in copolyesters impacted polymer morphology.

Notably, DMOB incorporation suppressed crystallizability in copolyesters resulting in transparent films as seen in **Figure 3.4**. Integration of T_m peaks present in DSC measurements of annealed copolyesters, plotted in **Figure 3.4**, quantified this decrease in crystallinity. Melting enthalpy (ΔH_m) decreased from 40 j/g to 30 j/g with the addition of 25 wt.% DMOB in CHDM DMOB DMT copolyesters. DSC did not reveal a distinguishable T_m in copolyesters with at least 50 wt.% DMOB incorporation. This result demonstrated that the kinked DMOB structure disrupted regularity in the polymer chain, which prevented crystallization and ultimately provided fully amorphous polyesters with glass transition temperatures greater than 100 °C.

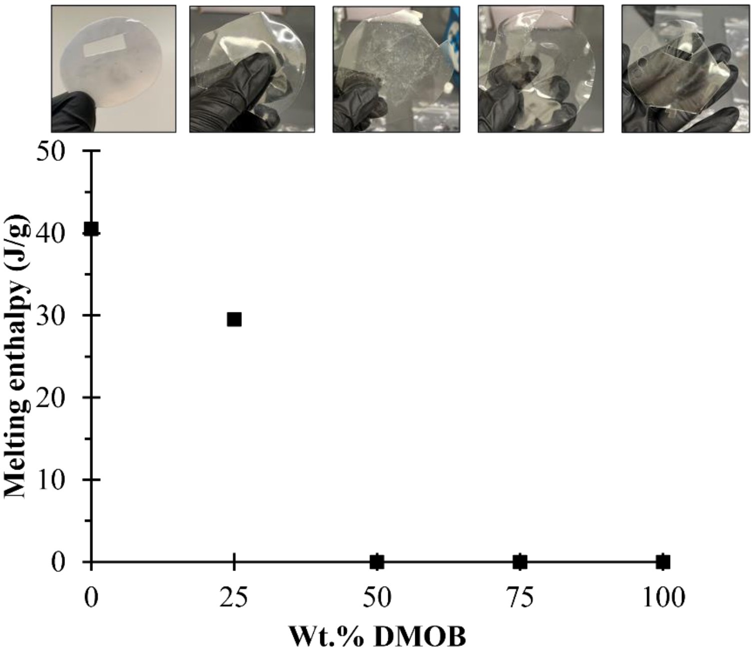

Figure 3.4. Melting enthalpy decreases as DMOB incorporation increases revealing a loss of crystillinity at 50 wt % DMOB.

Dynamic mechanical analysis, shown in **Figure 3.5**, explored polymer viscoelasticity across a wide temperature window from -10 to 170 °C, which confirmed glass transition trends measured by DSC. Furthermore, low temperature DMA measurements revealed the presence of sub-T_g relaxations in CHDM containing polymers at -60 °C. This relaxation is attributed to ring flipping in the CHDM segments of the polyesters. This feature is often attributed to increased impact resistance and is a known advantage of CHDM polyesters.[11,12] This relaxation remained in the CHDM DMOB homopolymer, which showed that DMOB incorporation did not impact this critical feature of CHDM containing polyesters. Thus, DMOB is an attractive monomer in high T_g amorphous polyester design for impact resistant applications.

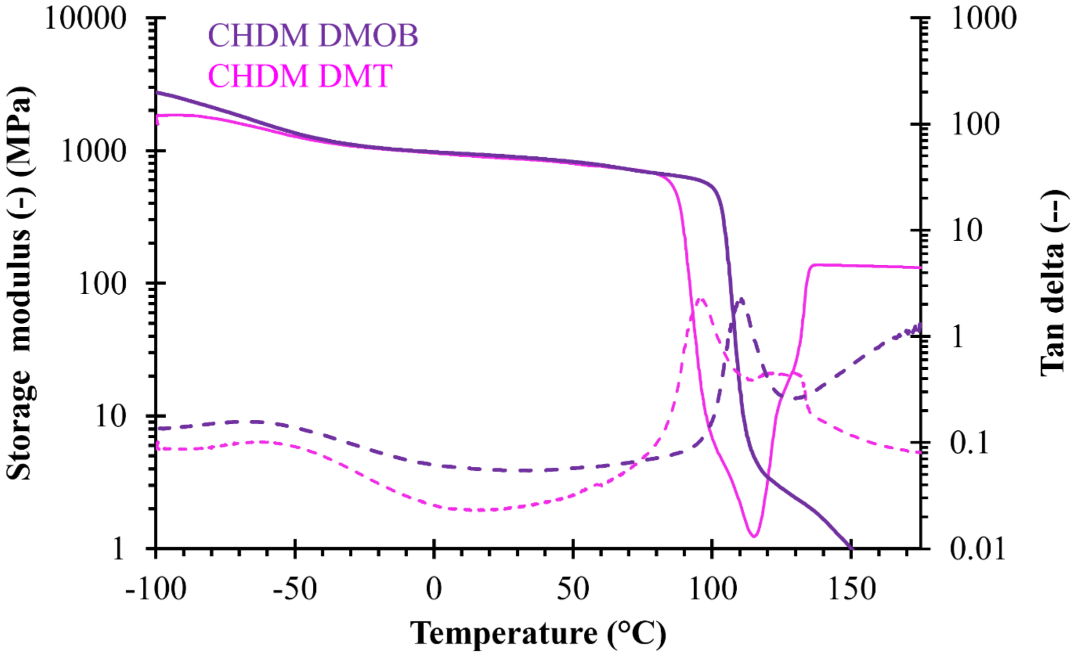

Figure 3.5. Dynamic mechanical analysis confirms the presence of sub T_g relaxations in both CHDM DMT and CHMD DMOB

3.4 Conclusion

Melt transesterification polycondensation of 4,4’ dimethyloxybisbenzoate with cyclohexanedimethanol and varied amounts of dimethyl terephthalate yielded a series of novel polyesters and copolyesters. Melt processing and subsequent quenching in ice water provided creasable polymer films for all polymers, which suggested high molecular weights were achieved. Solubility in either THF or $CHCl_3$ varied depending on polymer composition. Size exclusion chromatography of soluble polymer samples confirmed molecular weights to be on the order of 20,000 g/mol, which is a typical molecular weight achieved from this polymerization strategy. Thermal gravimetric analysis revealed each polymer to display a $T_{d5\%}$ of 395 °C, and DMOB incorporation increased the char yield of polymers with larger DMOB incorporation. DMOB incorporation increased the T_g of CHDM polyesters to 104 °C, and the Fox equation accurately predicted copolymer T_g. Furthermore, the kinked DMOB structure prevented crystallization at 50 wt.% incorporation and higher. Finally, the sub T_g relaxation associated with CHDM ring flipping remained present in DMOB polymers as demonstrated by DMA. This demonstrates DMOB as an attractive monomer for fully amorphous high T_g polyesters.

3.5 References

1. Chen, T. T. D.; Carrodeguas, L. P.; Sulley, G. S.; Gregory, G. L.; Williams, C. K. Bio-Based and Degradable Block Polyester Pressure-Sensitive Adhesives. *Angewandte Chemie* **2020**, *132* (52), 23656–23661. https://doi.org/10.1002/ANGE.202006807.

2. Kausar, A. High Performance Epoxy/Polyester-Based Nanocomposite Coatings for Multipurpose Applications: A Review. *Journal of Plastic Film & Sheeting* **2020**, *36* (4), 391–408. https://doi.org/10.1177/8756087920910481.

3. Snyder, R. L.; Lidston, C. A. L.; De Hoe, G. X.; Parvulescu, M. J. S.; Hillmyer, M. A.; Coates, G. W. Mechanically Robust and Reprocessable Imine Exchange Networks from Modular Polyester Pre-Polymers. *Polym Chem* **2020**, *11* (33), 5346–5355. https://doi.org/10.1039/C9PY01957J.

4. Self, J. L.; Sample, C. S.; Levi, A. E.; Li, K.; Xie, R.; De Alaniz, J. R.; Bates, C. M. Dynamic Bottlebrush Polymer Networks: Self-Healing in Super-Soft Materials. *J Am Chem Soc* **2020**, *142* (16), 7567–7573. https://doi.org/10.1021/JACS.0C01467/ASSET/IMAGES/LARGE/JA0C01467_0005.JPEG.

5. Bartoli, M.; Frediani, M.; Dehcheshmeh, I. M.; Poursattar Marjani, A.; Moghadam, P. N. Historical Aspects of Polyesters. *Applications of Unsaturated Polyester Resins* **2023**, 1–16. https://doi.org/10.1016/B978-0-323-99466-8.00004-6.

6. Allen, R. D.; James, M. I. Chemical Recycling of PET. *ACS Symposium Series* **2021**, *1391*, 61–80. https://doi.org/10.1021/BK-2021-1391.CH004/ASSET/IMAGES/LARGE/BK-2021-00150M_G010.JPEG.

7. Zhang, S.; Hu, Q.; Zhang, Y.-X.; Guo, H.; Wu, Y.; Sun, M.; Zhu, X.; Zhang, J.; Gong, S.; Liu, P.; Niu, Z. Depolymerization of Polyesters by a Binuclear Catalyst for Plastic Recycling. *Nature Sustainability 2023* **2023**, 1–9. https://doi.org/10.1038/s41893-023-01118-4.

8. Arrington, A. S.; Brown, J. R.; Win, M. S.; Winey, K. I.; Long, T. E. Melt Polycondensation of Carboxytelechelic Polyethylene for the Design of Degradable Segmented Copolyester Polyolefins †. **2022**. https://doi.org/10.1039/d2py00394e.

9. Ojha, U. P.; Kumar, A. Design, Synthesis, and Characterization of Main-Chain, Aromatic Polyesters Based on 3,4-Ethylenedioxythiophene. *J Polym Sci A Polym Chem* **2006**, *44* (11), 3479–3486. https://doi.org/10.1002/POLA.21414.

10. Chang, S.; Han, C. D. Effect of Flexible Spacer Length on the Phase Transitions and Mesophase Structures of Main-Chain Thermotropic Liquid-Crystalline Polyesters Having Bulky Pendent Side Groups. *Macromolecules* **1997**, *30* (6), 1670–1684. https://doi.org/10.1021/MA961730N/ASSET/IMAGES/LARGE/MA961730NFB15B.JPEG.

11. Mondschein, R. J.; Dennis, J. M.; Liu, H.; Ramakrishnan, R. K.; Sirrine, J. M.; Weiseman, T.; Colby, R. H.; Nazarenko, S.; Turner, S. R.; Long, T. E. Influence of Bibenzoate Regioisomers on Cyclohexanedimethanol-Based (Co)Polyester Structure-Property Relationships. *Macromolecules* **2019**, *52* (3), 835–843. https://doi.org/10.1021/ACS.MACROMOL.8B02411/SUPPL_FILE/MA8B02411_SI_002.PDF.

12. Light, R. R.; Seymour, R. W. Effect of Sub-Tg Relaxations on the Gas Transport Properties of Polyesters. *Polym Eng Sci* **1982**, *22* (14), 857–864. https://doi.org/10.1002/PEN.760221402.

13. Bhowmik, P. K.; Molla, A. H.; Han, H.; Gangoda, M. E.; Bose, R. N. Lyotropic Liquid Crystalline Main-Chain Viologen Polymers: Homopolymer of 4,4′-Bipyridyl with the Ditosylate of Trans-1,4-Cyclohexanedimethanol and Its Copolymers with the Ditosylate of 1,8-Octanediol. *Macromolecules* **1998**, *31* (3), 621–630. https://doi.org/10.1021/MA971115Z/ASSET/IMAGES/LARGE/MA971115ZF00012.JPEG.

14. Eliot Edling, H.; Mondschein, R. J.; Davis, M. K.; Long, T. E.; Richard Turner, S. Amorphous Copolyesters Based on Bibenzoic Acids and Neopentyl Glycol. *J Polym Sci A Polym Chem* **2019**, *57* (5), 579–587. https://doi.org/10.1002/POLA.29296.

15. Wang, G.; Liang, Y.; Jiang, M.; Zhang, Q.; Wang, R.; Wang, H.; Zhou, G. High Tg and Tough Poly(Butylene 2,5-Thiophenedicarboxylate-Co-1,4-Cyclohexanedimethylene 2,5-Thiophenedicarboxylate)s: Synthesis and Characterization. *J Appl Polym Sci* **2020**, *137* (18), 48634. https://doi.org/10.1002/APP.48634.

16. Porter, R. S.; Jonza, J. M.; Kimura, M.; Desper, C. R.; George, E. R. Polyesters II: A Review of Phase Behavior in Binary Blends: Amorphous, Crystalline, Liquid Crystalline, and on Transreaction. *Polym Eng Sci* **1989**, *29* (1), 55–62. https://doi.org/10.1002/PEN.760290110.

17. Pan, P.; Inoue, Y. Polymorphism and Isomorphism in Biodegradable Polyesters. *Prog Polym Sci* **2009**, *34* (7), 605–640. https://doi.org/10.1016/J.PROGPOLYMSCI.2009.01.003.

18. Akhmetshina, A. I.; Ignat'eva, E. K.; Deberdeev, T. R.; Karimova, L. K.; Yuminova, Y. N.; Berlin, A. A.; Deberdeev, R. Y. Thermotropic Liquid Crystalline Polyesters with Mesogenic Fragments Based on the P-Oxybenzoate Unit. *Polymer Science – Series D* **2019**, *12* (4), 427–434. https://doi.org/10.1134/S1995421219040026/TABLES/1.

19. G., F. T. Influence of Diluent and of Copolymer Composition on the Glass Temperature of a Polymer System. *Bull. Am. Phs. Soc.* **1952**, *1*, 123-.

20. Hamza, A. A.; Sokkar, T. Z. N.; El-Bakary, M. A. Interferometric Determination of the Birefringence of Thermo-Tropic Polyester Fibers and Its Copolymers of Structure

(PCPT-Co-CPO). *J Appl Polym Sci* **2012**, *125* (3), 1814–1821. https://doi.org/10.1002/APP.36267.

21. McIntyre, J. E.; Maj, P. E. P.; Tomka, J. G. Thermotropic Polyesters: Synthesis and Properties of Poly(Chloro-1,4-Phenylene Terephthalate-Co-4,4′-Hexamethylenedioxy-Bisbenzoate)s. *Polymer (Guildf)* **1989**, *30* (4), 732–738. https://doi.org/10.1016/0032-3861(89)90164-X.

22. Heifferon, K. V.; Spiering, G. A.; Talley, S. J.; Hegde, M.; Moore, R. B.; Turner, S. R.; Long, T. E. Synthesis and Characterization of a Nematic Fully Aromatic Polyester Based on Biphenyl 3,4′-Dicarboxylic Acid. *Polym Chem* **2019**, *10* (31), 4287–4296. https://doi.org/10.1039/C9PY00683D.

23. Collins, S.; Peace, S. K.; Richards, R. W.; Macdonald, W. A.; Mills, P.; King, S. M. Transesterification in Poly(Ethylene Terephthalate). Molecular Weight and End Group Effects. **2000**. https://doi.org/10.1021/MA991637.

24. George Socrates. *Infrared and Raman Characteristic Group Frequencies: Tables and Charts*; John Wiley & sons, 2004.

25. Mondschein, R. J.; Hostetler, J.; Arrington, C. B.; Long, T. E. Hydroxyethylresorcinol- and Hydroxyethylhydroquinone-Containing Poly(Ethylene Terephthalate) Copolymers. *Polymer (Guildf)* **2021**, *228*, 123890. https://doi.org/10.1016/J.POLYMER.2021.123890.

26. Shukla, S.; Lochab, B. Role of Higher Aromatic Content in Modulating Properties of Cardanol Based Benzoxazines. *Polymer (Guildf)* **2016**, *99*, 684–694. https://doi.org/10.1016/J.POLYMER.2016.07.074.

27. Sarasua, J.-R.; Zuza, E.; Imaz, N.; Meaurio, E. Crystallinity and Crystalline Confinement of the Amorphous Phase in Polylactides. https://doi.org/10.1002/masy.200851211.

CHAPTER 4

CHARACTERIZATION METHODS TO PREDICT EXTRUSION PERFORMANCE IN THERMOPLASTIC POLYURETHANE BATCHES

4.1 Introduction

Thermoplastic polyurethanes (TPU) are randomly coupled, multiblock copolymers with alternating hard and soft segments.[1] For thermosetting polyurethanes (PU), a polyol and a diisocyanate are subjected to step growth polymerization, and depending on the functionality of the polyol, crosslinks can form resulting in a non-thermoreversible product.[2] Because polyols tend to have relatively high molecular weights, the reactivity and cure progress of polyurethanes is largely driven by the choice of diisocyanate.[3] In this regard, two main factors affect the reactivity of a diisocyanate. First, if the diisocyanate is aromatic, the electron withdrawing effects stabilize transition states during polymerization, which generally increases reactivity compared to aliphatic varieties.[4] Second, if the diisocyanate contains symmetric isocyanate (NCO) groups, polymerization tends to occur in one distinct stage, whereas asymmetric NCO groups cause a distinct two-stage buildup of molecular weight.[5] Reactants such as toluene diisocyanate (aromatic and asymmetric) will therefore react relatively quickly in two stages, whereas hexamethylene diisocyanate (aliphatic and symmetric) will react slower and in one stage.[5] Thus, the choice of diisocyanate, as well the ratio of hydroxyl (OH) groups to NCO groups, will significantly impact the number of hard and soft segments present within the final product.[6]

The hard segments of PU are comprised of diisocyanates and short-chain diols (chain extenders), which are responsible for strength and overall mechanical properties;

conversely, soft segments (polyethers or polyesters) allow for chain mobility and flexibility.[1,7] For linear polyurethanes, the lack of a crosslinked network enables thermoplasticity.[8] This behavior facilitates melt-flow deposition of TPU via fused filament fabrication, selective laser sintering, injection molding, and large scale twin-screw extrusion processes.[9-12] Unfortunately, processing of TPU is a challenging task due to its thermal degradation at elevated temperatures.[13] To complicate matters further, the temperature of thermal degradation of TPUs is relatively close to processing temperatures for extrusion.[13]

The proximity of the degradation and processing temperatures has been observed to lead to an unwanted buildup of solid-like, white particulate material during the extrusion process, illustrated in **Figure 4.1**. This process takes time to occur, such that extrusion operates normally initially, but at some timepoint, particulate defects begin to be observed in the extrudate and the issue worsens to the point that a total blockage occurs inside the extruder. In this respect, chemorheology – whereby viscoelastic properties are tracked for relevant time periods on a torsional rheometer – becomes a vital tool for probing time-dependent changes in physical properties of a material.[14] This protocol has shown promise for tracking both chemical curing kinetics, as well as physical crosslinking processes over extended time periods ranging from hours to days.[5,15,16]

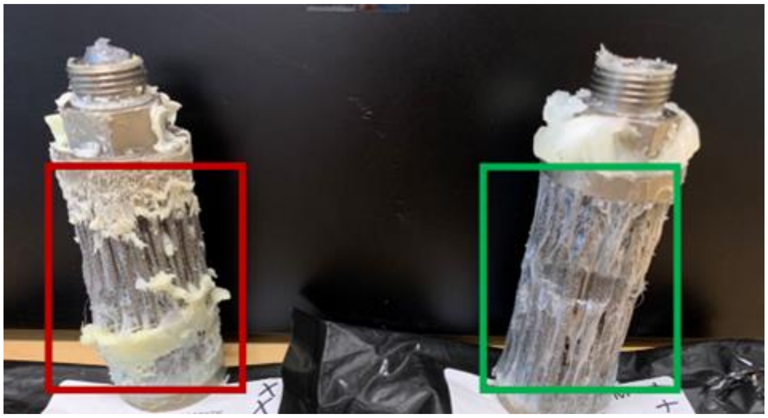

Figure 4.1. (Left) Example of solid white material building up on candle filters during extrusion and (Right) a clean candle filter without any extrudate buildup.

Because chemorheological results only represent the mechanical/viscoelastic behavior of a material over time, morphological and chemical studies are complimentary to determine whether chemical or physical crosslinking is causing solidification. Although the intended product in the reaction between diisocyanates and polyols is a linear polyurethane with only urethane linkages throughout the polymer chain, it is well known that many side reactions can occur both in dry conditions and in the presence of water.[17-19] In this work, a series of poly(tetramethylene oxide)-butane diol-methylene diphenyl diisocyanate (PTMO-BDO-MDI) TPU samples from different manufacturers are investigated. **Scheme 4.1** highlights the specific products from these side reactions during (PTMO-BDO-MDI) polyurethane synthesis.

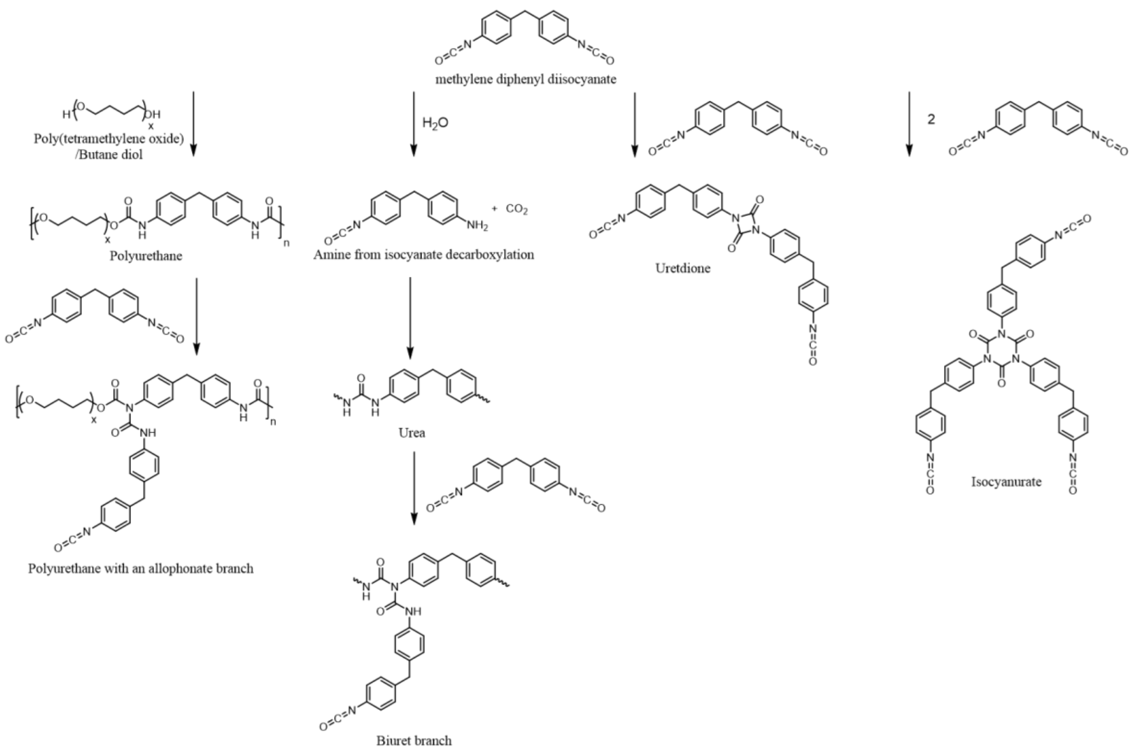

Scheme 4.1: Potential side reactions in PTMO BDO MDI polymerizations

When the nucleophilic nitrogen in the polyurethane backbone reacts with an isocyanate group, an allophanate bond is formed, which introduces a branching point on the polyurethane backbone. Depending on reaction conditions, upwards of 10% of nitrogens react to form these branching points.[20] Additionally, in the presence of water, the isocyanate group decarboxylates forming an amine and carbon dioxide through a carbamic acid intermediate.[21] This amine product reacts with additional isocyanates yielding a urea bond, and the presence of these urea bonds increases upon increased moisture incorporation.[22] The nucleophilic nitrogens in the urea bond also add to present isocyanates forming a biuret branch along the polymer chain.[23] Finally, isocyanates react with one another to form either uretdione or isocyanurate groups, which occur less prevalently than allophanate and biuret formation, and their formation is typically catalyst dependent.[24]

Therefore, it is evident that small changes in reaction conditions such as temperature, ambient humidity, catalyst choice/amount, and reaction time can potentially have profound implications on the ultimate polymer architecture through the introduction of branching points and possibly covalent crosslinks.

This manuscript seeks to elucidate the chemical and/or morphological rearrangement of TPU during a typical extrusion process, which results in undesired solidification within the extruder. Specifically, we explore the buildup of solid-like particulates at extrusion-relevant temperatures using a combination of solubility, spectroscopic, light scattering, and calorimetric techniques. A discussion of the bulk physical (as opposed to chemical) rearrangement of hard and soft segments is provided, which is probed using chemorheological techniques, and then supported through thermal, spectroscopic, and dissolution studies. Several separate lots of TPU from three different companies (A, B, and C) are analyzed, each of which presents varying degrees of extrusion success. Based on the findings in this study, we develop a holistic approach to determine the factors most likely causing an unwanted accumulation of solid matter during melt extrusion of TPU and provide a rapid screening protocol that can be employed by manufacturers to predict extrudability of the TPU lots.

4.2 Materials

Multiple lots of TPU from three separate manufacturers were studied. The variations in the extrusion performance of the samples is more important than the specific details regarding their formulation. Differences in molecular structure, chain branching and architecture are responsible for the characteristics exhibited by the polymers examined in this study. However, it is worth mentioning that the trends in the properties and their relation to extrudability should remain consistent across different grades of TPU.

Because the TPU samples vary in extrusion capability lot-by-lot, each sample is designated here by its respective manufacturer name first, and then the lot number. For example, sample B2 refers to manufacturer B, lot 2. Manufacturer A provided three lots of material. Sample A1 performed well during extrusion, although A2 had inferior/worse extrusion performance, and A3 performed the worst. As a whole, however, TPU from manufacturer A extruded "acceptably" and generally did not experience any signs of solidification. Manufacturer B provided two lots of TPU. The extrusion performance of TPU from manufacturer B was described as "intermediate," and frequently experienced solid particulate formation during extrusion. B1 performed the best, and B2 performed worse. Manufacturer C also provided three lots of samples, and these all portrayed "bad" extrusion capabilities with significant solid-like buildup. Of these, C1 had the best extrusion performance, C2 was worse, and C3 had very poor extrusion outcomes. A summary of these materials is provided in **Table 4.1**.

Table 4.1. Summary of TPU extrusion performance for each manufacturer and lot number.

Manufacturer	Relative Lot Extrusion Performance			Manufacturer Extrusion Performance
	1	2	3	
A	Best	Intermediate	Worst	Acceptable
B	Best	Worst	-------	Intermediate
C	Best	Intermediate	Worst	Bad

For chemical/solubility analyses, all solvents were purchased from Fisher Scientific and used as received. Lithium bromide (LiBr) was purchased from Sigma Aldrich and dried at 120 °C prior to use.

4.3 Experimental

Differential scanning calorimetry (DSC) investigated thermal transitions present in the polyurethane lots. 7 mg of each TPU sample as received from the manufacturer was placed in an aluminum T-Zero pan with a hermetically sealed lid. DSC tests were conducted on a TA Instruments DSC 2500 running under a constant nitrogen flow (50ml/min). The reference pan was an empty aluminum T-Zero pan with a hermetically sealed lid. All DSC experiments were conducted at a heating/cooling rate of 10 °C/min and the data was plotted with endothermic events in the positive direction. Second heat experiments were stopped at 220 °C due to the instability of the urethane bond at these elevated temperatures.

Prior to solution-based characterizations such as dynamic light scattering (DLS) or size exclusion chromatography (SEC), a simple solubility study probed the intermolecular forces which held the TPU samples together. The pellets were all soluble in DMSO for ^{1}H NMR tests, but due to equipment limitations, SEC in DMSO was not possible. The TPU pellets were tested both as received from the manufacturers and after melt pressing at 205 °C for 5 min at 5000 PSI. Approximately 15 mg of TPU was submerged in 3 mL of either tetrahydrofuran (THF), dimethyl formamide (DMF), or a 0.05 $\underline{M}$ LiBr solution in DMF (DMF+LiBr). After overnight solvent submersion, both visual inspection and DLS confirmed or disproved solubility.

4.4 Results

Differential Scanning Calorimetry

Investigation began with differential scanning calorimetry (DSC) analysis of four lots: A1, B1, B2, and C3. These lots were specifically chosen to capture a full range of extrusion capabilities. A1 provides a benchmark for “good” TPU pellets for extrusion and processing, B1 and B2 correspond to “intermediate” extrusion performance, and C3 represents “bad” extrusion lots. DSC of the different lots provides insight into the thermal transitions of the materials. Heat-isotherm-cool-heat DSC experiments of TPU pellets provide information on their thermal history before and after high temperature treatments. The first heat shown in **Figure 4.2a** demonstrates a difference in thermal transitions between lots. Lots B2 and C3 display endothermic peaks from 170-180 °C which are not present in samples A1 and B1. These endotherms are consistent with previously reported DSC data of PTMO-BDO-MDI polyurethanes, which are attributed to agglomeration of MDI-BDO-MDI sequences.[28] Thus, the endotherms in **Figure 4.2a** suggest that C3 contains more of these agglomerates as received from the manufacturer. Furthermore, this endotherm suggests some stable phase exists to a greater degree in B2 and C3 lots as received from the manufacturer. The cooling data in **Figure 4.2b** does not provide any definitive differences between lots, but the second heat (**Figure 4.2c**) displays two larger endothermic events in all samples, which are summarized in **Table 4.2**. The first peak beginning at 170 °C and ending at 207 °C did not display a trend relating to extrusion performance, but confirmed the presence of MDI-BDO-MDI agglomerates in all samples.[28] Furthermore, DSC revealed a second endothermic event beginning at 208 °C and continuing to the experiment end at 220 °C. The enthalpies of this second peak were significantly greater in bad extrusion lots B2 and C3, which suggests these samples contain larger concentrations of phases with thermal transitions in this temperature window. This larger enthalpy directly relates to poor extrusion performance.

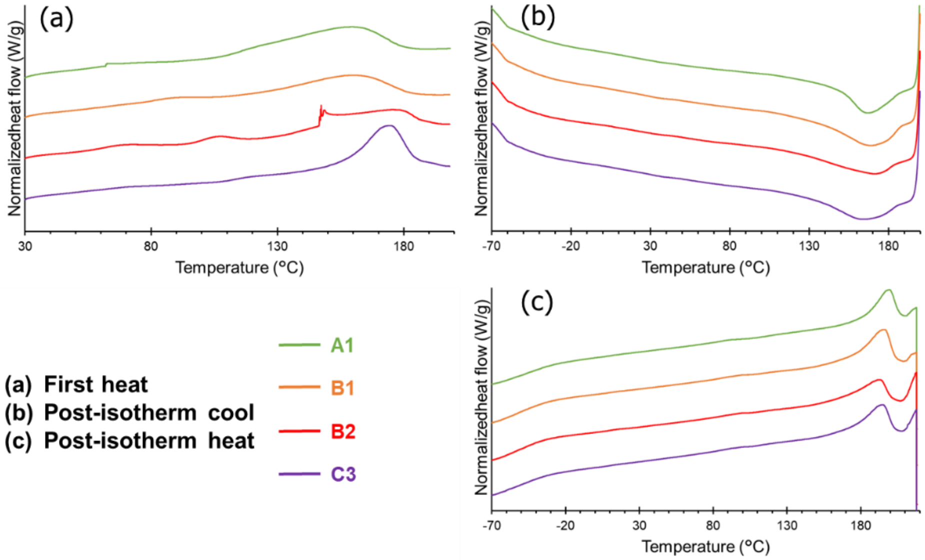

Figure 4.2.DSC thermograms (endo up) for the (a) first heat, (b) cool, and (c) second heat of TPU pellets as received from the manufacturers.

Table 4.2. Summary of enthalpic peak 1 and peak 2 enthalpic events in post-isotherm DSC traces.

Sample	**Peak 1 enthalpy (j/g)**	**Peak 2 enthalpy (j/g)**
A1	9.4	0.6
B1	14.2	0.7
B2	11.2	2.4
C3	12.0	1.7

Spectroscopy

FT-IR and ^{1}H NMR, presented in **Figure 4.3**, do not reveal significant quantifiable differences between the lots. ^{1}H NMR confirmed the general structure of all TPU's as PTMO-BD-MDI polyurethanes consistent with prior literature, a labeled ^{1}H NMR spectrum is provided in **Figure S2**.[29] The ratio of the chemical shift peaks at 1.70 and 1.47 ppm indicated 20% hard segment and 80% soft segment respectively. However, spectroscopy alone did not provide a means to discern differences across lots.

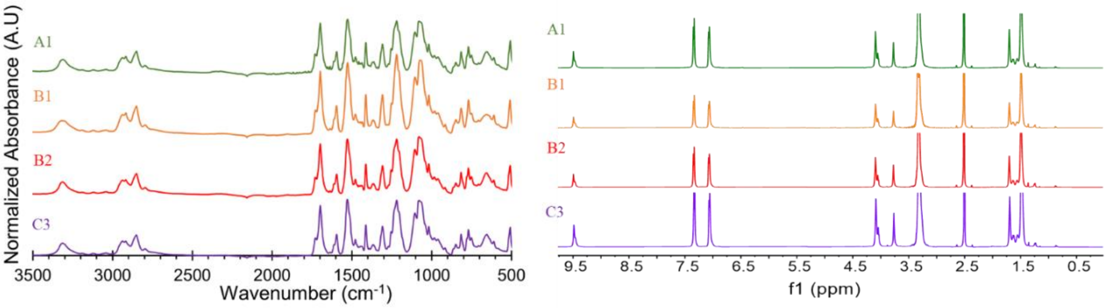

Figure 4.3. FT-IR (left) and ^{1}H NMR (right) did not provide a significant means to observe chemical differences between lots.

Solubility

A series of solubility tests were performed to probe for the presence of chemical and physical crosslinking. Both THF and DMF failed to dissolve the TPU pellets as received, which suggests that either chemical or physical crosslinking prevented dissolution. Although no pellets dissolved in DMF prior to melt pressing, pellets of A1, B1, and B2 were soluble in DMF after melt pressing. However, the C3 lot still failed to dissolve in DMF after melt pressing. **Figure 4.4** visualizes these solubility findings.

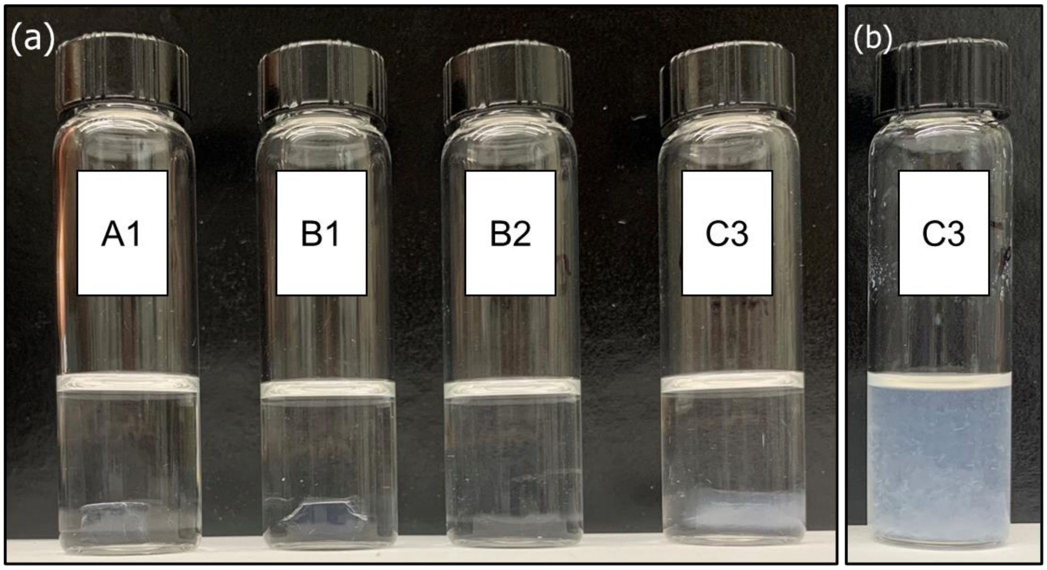

Figure 4.4. (a) All TPU pellets indicating insolubility in DMF and (b) only the C3 lot remaining insoluble after melt pressing.

Furthermore, the addition of LiBr to the DMF solution facilitated dissolution of all four lots – as received and after melt pressing. The LiBr in the DMF solution effectively screened strong intermolecular interactions within the polyurethane which enabled dissolution. Solubility in DMF+LiBr confirmed that pellets were not covalently crosslinked prior to melt pressing.[30] Additionally, the insolubility of the melt pressed C3 lot in DMF without LiBr suggests that stable intermolecularly associated phases exist within the C3 lot after melt pressing. **Table 4.3** summarizes the results of all 24 solubility tests. These solubility studies confirm that physical crosslinking through intermolecular associations between multiple chains in TPU samples presented solubility in low polarity solvents, but covalent crosslinking did not occur to an extent which prevented dissolution in high polarity solvents.

Table 4.3. Solubility of TPU lots before and after melt pressing.

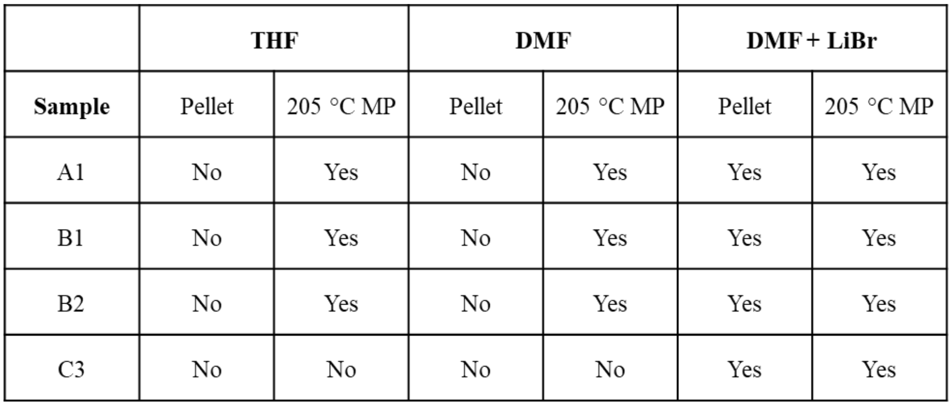

	THF		**DMF**		**DMF + LiBr**	
Sample	Pellet	205 °C MP	Pellet	205 °C MP	Pellet	205 °C MP
A1	No	Yes	No	Yes	Yes	Yes
B1	No	Yes	No	Yes	Yes	Yes
B2	No	Yes	No	Yes	Yes	Yes
C3	No	No	No	No	Yes	Yes

Dynamic Light Scattering

Because DMF+LiBr was the only solvent that successfully dissolved all four TPU lots before and after melt pressing, it was selected for subsequent DLS experiments. DLS samples were prepared in the same fashion as the solubility study. As observed in **Figure 4.5**, DLS probed the size of dissolved TPU chains in solution, and **Table 4.4** summarizes the results. After melt pressing, all four lots displayed similar sizes in solution with a large peak at 6 nm and a smaller peak at approximately 3 nm. However, A1 lot and B1 lots were significantly larger than B2 and C3 prior to melt pressing. This finding suggests that pellets with larger hydrodynamic radii in solution correlate to better processability. This phenomenon is likely explained by differences in polymer architecture between as received lots. It is well documented that branched polymers display smaller hydrodynamic radii in solution.[31] Thus, it is plausible that the synthesis of lots B2 and C3 introduced more branching through side reactions. These side reactions predispose the lots to poor processability. Furthermore, the DLS results confirm polymer architecture changes during melt processing at 205 °C as all samples' hydrodynamic radii decrease to 6 nm. This agrees with the dynamic nature of the urethane, allophanate, and biuret linkages at these temperatures.[22] During this chemical rearrangement, lots B2 and C3 established stable intermolecular interactions in the polyurethane causing poor processability. The exact mechanism of this phenomenon serves as a potential research topic in future work.

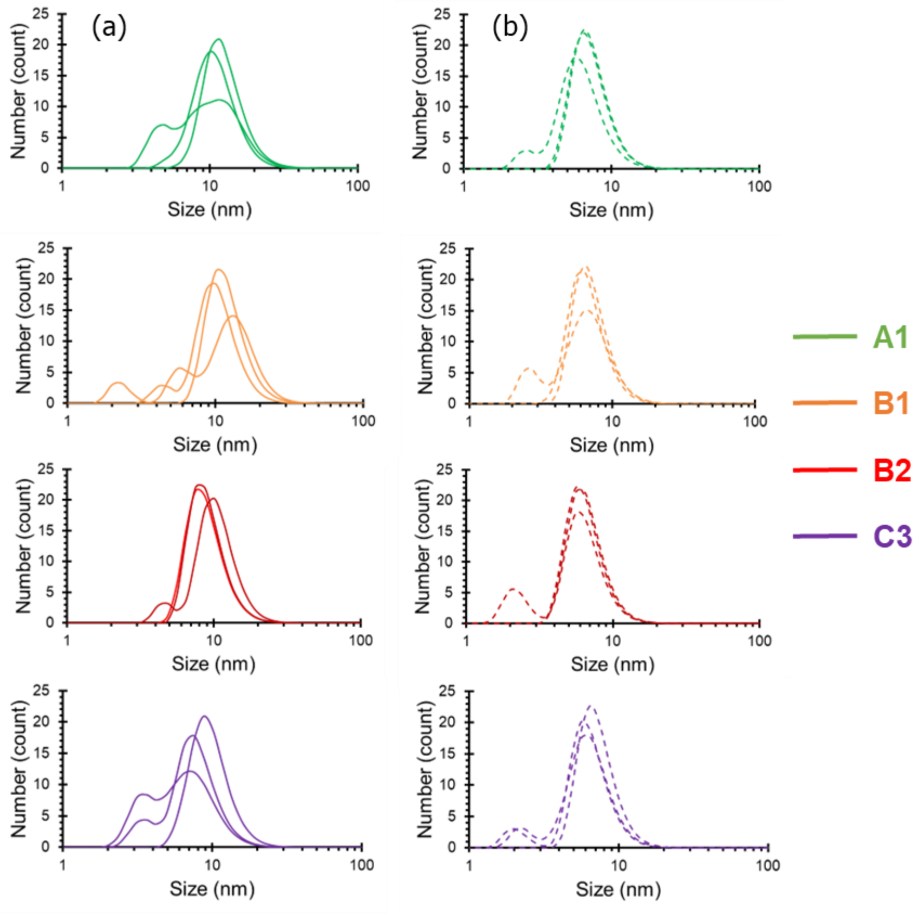

Figure 4.5. Dynamic light scattering results before (a) and after (b) melt-pressing.

Table 4.4. Summary of TPU DLS in DMF + LiBr before and after melt-pressing.

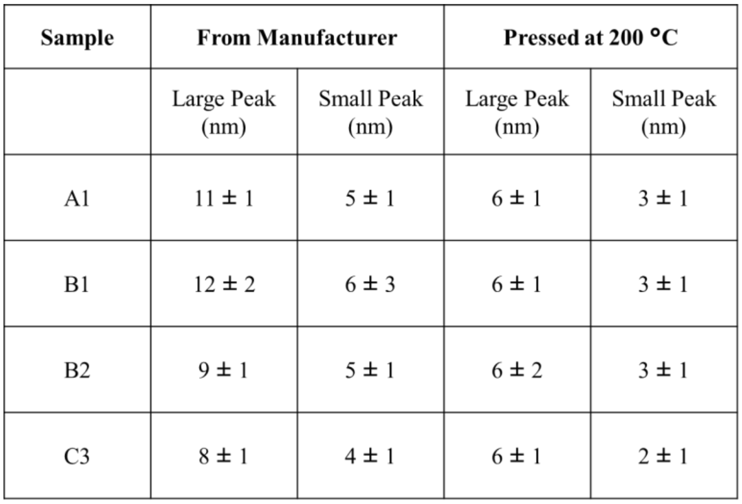

Sample	From Manufacturer		Pressed at 200 °C	
	Large Peak (nm)	Small Peak (nm)	Large Peak (nm)	Small Peak (nm)
A1	11 ± 1	5 ± 1	6 ± 1	3 ± 1
B1	12 ± 2	6 ± 3	6 ± 1	3 ± 1
B2	9 ± 1	5 ± 1	6 ± 2	3 ± 1
C3	8 ± 1	4 ± 1	6 ± 1	2 ± 1

4.5 Conclusions

Elevated temperatures during the extrusion of TPU can lead to unwanted side products which contribute to undesirable solidification of the polymer over time. Depending on the manufacturer and the specific lot of material, the presence of these side products can vary widely. Rheological analysis indicated that manufacturer A possessed almost no time-dependent changes in viscoelastic properties at process-relevant temperatures, suggesting no problems during extrusion. Conversely, manufacturers B and C possessed time-dependent changes in complex viscosity and tan(δ), which provided evidence of solidification. The timescale for solidification was quicker for manufacturer C than manufacturer B, which aligned with the manufacturer extrusion performance. During subsequent spectroscopic analysis, all four tested lots looked nearly identical with FT-IR and ^{1}H NMR. DSC revealed an endothermic transition ranging from 170-180 °C in two of the worst performing lots received from the manufacturers (B2 and C3). However, samples from manufacturer C stood out during solubility tests; TPU from manufacturers A and B were soluble in DMF and THF after melt pressing at 200 °C, but TPU from manufacturer

C was not soluble. Furthermore, DMF + LiBr successfully dissolved all samples before and after melt pressing indicating that intermolecular interactions prevented dissolution. DLS revealed that TPU from manufacturers B and C (“intermediate” and “bad” samples) were smaller in solution prior to melt pressing compared to manufacturer A. This finding suggests that for TPU B and C, larger degrees of branching were incorporated during initial manufacturing. Therefore, when selecting TPU for melt extrusion processing, the choice of manufacturer, and the specific lot of material from the manufacturer, can heavily influence extrusion-related performance. The analyses provided in this manuscript therefore offer potential strategies to screen for solid-like buildup due to branching prior to extrusion, which can save significant amounts of time and money by avoiding solidification within the extruder.

4.6 References

1. D. Nichetti, S. Cossar, N. Grizzuti, Effects of molecular weight and chemical structure on phase transition of thermoplastic polyurethanes, J. Rheol. 49(6) (2005) 1361-1376. https://doi.org/10.1122/1.2071987.

2. A. Kumar, R.K. Gupta, Fundamentals of Polymers, McGraw-Hill 1998.

3. J. Guo, T. Chai, Y. Liu, J. Cui, H. Ma, S. Jing, L. Zhong, S. Qin, G. Wang, X. Ren, Kinetic research on the curing reaction of hydroxyl-terminated polybutadiene based polyurethane binder system via FT-IR measurements, Coatings 8(5) (2018) 175. https://doi.org/10.3390/coatings8050175.

4. C. Korah Bina, K. Kannan, K. Ninan, DSC study on the effect of isocyanates and catalysts on the HTPB cure reaction, J. Therm. Anal. Calorim. 78(3) (2004) 753-760. https://doi.org/10.1007/s10973-005-0442-0.

5. V. Sekkar, S. Venkatachalam, K.N. Ninan, Rheokinetic studies on the formation of urethane networks based on hydroxyl terminated polybutadiene, Eur. Polym. J. 38(1) (2002) 169-178. https://doi.org/10.1016/S0014-3057(01)00106-9.

6. M.A. Pérez-Limiñana, F. Arán-Aís, A.M. Torró-Palau, C. Orgilés-Barcel, J.M. Martín-Martínez, Influence of the hard-to-soft segment ratio on the adhesion of water-borne polyurethane adhesive, J. Adhes. Sci. Technol. 21(8) (2007) 755-773. https://doi.org/10.1163/156856107781362635.

7. J. Silva, D. Meltzer, J. Liu, M. Cox, J. Maia, The influence of thermo-mechanical history on structure development of elastomeric and amorphous glass thermoplastic polyurethanes, Polymer Engineering & Science 54(6) (2014) 1383-1393. https://doi.org/10.1002/pen.23673.

8. A. Frick, A. Rochman, Characterization of TPU-elastomers by thermal analysis (DSC), Polym. Test. 23(4) (2004) 413-417. https://doi.org/10.1016/j.polymertesting.2003.09.013.

9. G. Kim, E. Barocio, R.B. Pipes, R. Sterkenburg, 3D printed thermoplastic polyurethane bladder for manufacturing of fiber reinforced composites, Addit. Manuf. 29 (2019) 100809. https://doi.org/10.1016/j.addma.2019.100809.

10. T. Xu, W. Shen, X. Lin, Y.M. Xie, Mechanical properties of additively manufactured thermoplastic polyurethane (TPU) material affected by various processing parameters,

11. Polymers 12(12) (2020) 3010. https://doi.org/10.3390/polym12123010.[11] X. Lin, P. Coates, M. Hebda, R. Wang, Y. Lu, L. Zhang, Experimental analysis of the tensile property of FFF-printed elastomers, Polym. Test. 90 (2020) 106687. https://doi.org/10.1016/j.polymertesting.2020.106687.

12. H.Y. Mi, X. Jing, M.R. Salick, W.C. Crone, X.F. Peng, L.S. Turng, Approach to fabricating thermoplastic polyurethane blends and foams with tunable properties by twin-screw extrusion and microcellular injection molding, Adv. Polym. Tech. 33(1) (2014). https://doi.org/10.1002/adv.21380.

13. G. Lu, D.M. Kalyon, I. Yilgör, E. Yilgör, Rheology and extrusion of medical-grade thermoplastic polyurethane, Polymer Engineering & Science 43(12) (2003) 1863-1877. https://doi.org/10.1002/pen.10158.

14. M.J. Bortner, V. Bhanu, J.E. McGrath, D.G. Baird, Shear rheological properties of acrylic copolymers and terpolymers suitable for potentially melt processable carbon fiber precursors, J. Appl. Polym. Sci. 93(6) (2004) 2856-2865. https://doi.org/10.1002/app.20833.

15. B. Lucio, J.L. de la Fuente, Kinetic and chemorheological modelling of the polymerization of 2, 4-Toluenediisocyanate and ferrocene-functionalized hydroxyl-terminated polybutadiene, Polymer 140 (2018) 290-303. https://doi.org/10.1016/j.polymer.2018.02.058.

16. G. Santhosh, S. Reshmi, C.R. Nair, Rheokinetic characterization of polyurethane formation in a highly filled composite solid propellant, J. Therm. Anal. Calorim. 140(1) (2020) 213-223. https://doi.org/10.1007/s10973-019-08793-6.

17. M. Špírková, M. Kubin, K. Dušek, Side reactions in the formation of polyurethanes: Stability of reaction products of phenyl isocyanate, Journal of Macromolecular Science-Chemistry 27(4) (1990) 509-522. https://doi.org/10.1080/00222339009349572.

18. M. Špírková, M. Kubin, K. Dušek, Side reactions in the formation of polyurethanes: Model reactions between phenylisocyanate and 1-butanol, Journal of Macromolecular Science—Chemistry 24(10) (1987) 1151-1166. https://doi.org/10.1080/00222338708076935.

19. E. Sacher, A re-examination of the polyurethane reaction, Journal of Macromolecular Science, Part B: Physics 16(4) (1979) 525-538. https://doi.org/doi.org/10.1080/00222347908215180.

20. A.M. Heintz, D.J. Duffy, S.L. Hsu, W. Suen, W. Chu, C.W. Paul, Effects of reaction temperature on the formation of polyurethane prepolymer structures, Macromolecules 36(8) (2003) 2695-2704. https://doi.org/10.1021/MA021559H.

21. Y. Suryawanshi, P. Sanap, V. Wani, Advances in the synthesis of non-isocyanate polyurethanes, Polym. Bull. 76 (2019) 3233-3246. https://doi.org/doi.org/10.1007/S00289-018-2531-7.

22. E. Delebecq, J.-P. Pascault, B. Boutevin, F. Ganachaud, On the versatility of urethane/urea bonds: reversibility, blocked isocyanate, and non-isocyanate polyurethane, Chem. Rev. 113(1) (2013) 80-118. https://doi.org/10.1021/cr300195n.

23. K. Dušek, Theory of network formation by additional crosslinking of polyurethanes due to biuret and allophanate formation, Polym. Bull. 17 (1987) 481-488. https://doi.org/10.1007/BF00255622.

24. J.N. Gibb, J.M. Goodman, The formation of high-purity isocyanurate through proazaphosphatrane-catalysed isocyanate cyclo-trimerisation: computational insights, Organic & Biomolecular Chemistry 11(1) (2013) 90-97. https://doi.org/10.1039/C2OB26547H.

25. M.G. McKee, S. Unal, G.L. Wilkes, T.E. Long, Branched polyesters: recent advances in synthesis and performance, Prog. Polym. Sci. 30(5) (2005) 507-539. https://doi.org/10.1016/j.progpolymsci.2005.01.009.

26. J.M. Dennis, R.J. Mondschein, J.D. Wolfgang, M. Hegde, R. Odle, T.E. Long, Synthesis and characterization of long-chain branched poly (ether imide) s with A3 comonomers, ACS Applied Polymer Materials 2(2) (2020) 958-965. https://doi.org/10.1021/acsapm.9b01148.

27. J.D. Wolfgang, K.J. Reynolds, C.B. Arrington, R.R. Odle, S.I. Nazarenko, T.E. Long, Influence of dianhydride regiochemistry on thermomechanical and rheological properties of 3, 3′-and 4, 4′-polyetherimides, Polymer 212 (2021) 123277. https://doi.org/10.1016/j.polymer.2020.123277.

28. D.J. Martin, G.F. Meijs, P.A. Gunatillake, S.P. Yozghatlian, G.M. Renwick, The influence of composition ratio on the morphology of biomedical polyurethanes, J. Appl. Polym. Sci. 71(6) (1999) 937-952. https://doi.org/10.1002/(sici)1097-4628(19990207)71:6<937::aid-app9>3.0.co;2-0.

29. Q. Tang, K. Gao, Structure analysis of polyether-based thermoplastic polyurethane elastomers by FTIR, 1H NMR and 13C NMR, Int. J. Polym. Anal. Charact. 22(7) (2017) 569-574. https://doi.org/10.1080/1023666X.2017.1312754.

30. L. Zeng, X. Lin, P. Li, F.-Q. Liu, H. Guo, W.-H. Li, Recent advances of organogels: From fabrications and functions to applications, Prog. Org. Coat. 159 (2021) 106417. https://doi.org/10.1016/J.PORGCOAT.2021.106417.

31. J.F. Douglas, J. Roovers, K.F. Freed, Characterization of branching architecture through" universal" ratios of polymer solution properties, Macromolecules 23(18) (1990) 4168-4180. https://doi.org/10.1021/ma00220a022.

CHAPTER 5

PH-CLEAVABLE HYDROGELS VIA FACILE UV-INITIATED THIOL-ENE CROSSLINKING OF ACETAL FUNCTIONAL PEGS

5.1 Introduction

PEG-based hydrogels are frequently used for controlled release applications of bioactive molecules or cells in tissue engineering or for targeted drug delivery.[1-2] PEG is biocompatible, hydrophilic, possesses low immunogenicity and provides anti-fouling properties, which prevents undesired cell-adhesion and non-specific protein adsorption.[3] Despite these benefits, the polyether backbone lacks biodegradability which hinders hydrogel degradation and raises concern about the fate of remaining PEG in the human body.[4] While PEG with a molecular weight below 30 kDa is excreted through the kidneys,[5] the concern of PEG accumulation in human tissue motivated researchers to investigate various methods which facilitate hydrogel degradation,[1] e.g. utilizing degradable crosslinking agents,[6-9] biodegradable block copolymers[10] or incorporating cleavable units to the polyether backbone.[11-13] Stimulus triggered degradation of hydrogels is most attractive because it also allows for on-demand release of encapsulated active molecules or cells. Several body sites possess slightly acidic pH, such as the gastrointestinal tract, the vagina, and tumor or inflamed tissue.[14-15] These local differences in pH are useful to trigger hydrogel degradation, release of an encapsulated cargo and subsequent clearance of the polymer fragments by the human kidney.

Acetals groups are highly promising moieties to enable polymer degradation at slightly acidic pH because they hydrolyze in a mild acidic environment to form alcohols and aldehydes.[16] In contrast to the hydrolysis of biodegradable polyesters, acetals do not form acidic byproducts when hydrolyzed, which reduces the risk of inflammation.[17] Various strategies have been reported to introduce acetal groups into the polyether backbone to yield pH-degradable PEGs for controlled release and drug delivery applications.[18-20] For example, Tomlinson *et al.* used acid-catalyzed step-growth polymerization of triethylene glycol divinyl ether (TEGDV) and a PEG diol to yield acid degradable multi-acetal PEGs as potential polymer therapeutics.[21] Recently, Koberstein and co-workers reinvestigated the step-growth polymerization of divinyl ethers and diols to design pH-degradable polymers with a lower critical solution temperature (LCST) behavior in aqueous solution[17] and demonstrated their potential use as drug delivery vehicles.[22]

While the previous works explored polyacetals as polymer-drug conjugates for drug delivery applications, it inspired us to exploit acetal-functional PEGs as suitable precursors for the design of pH-labile hydrogels. In particular, hydrogels possess the advantage to enable biomolecules and cell encapsulation simultaneously and they allow for tailored release profiles. Step-growth polymerization of PEG-diols with TEGDV yielded polyethers with pH-sensitive acetal-groups along the polyether backbone and vinyl ether end groups (**Scheme 5.1**). Subsequently, UV-induced thiol-ene reactions using a three-arm PEG-based trithiol (THIOCURE® ETTMP 1300) and the PEG precursors in aqueous solution afforded the degradable PEG hydrogels. Varying the number of pH-cleavable moieties allowed for tuning the degradation rate and hydrogel dissolution.

5.2 Discussion

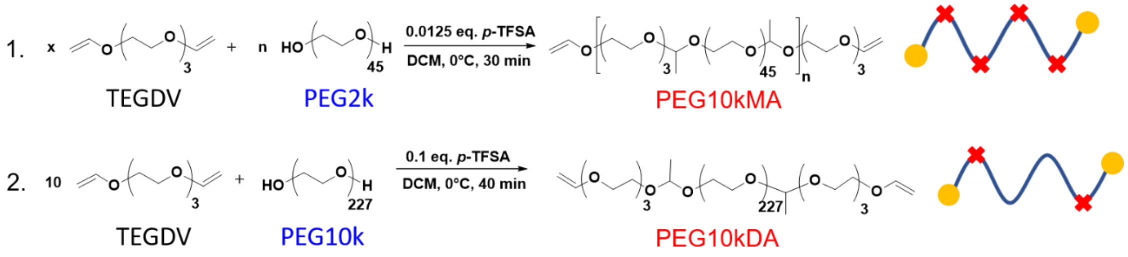

Scheme 5.1. Acid-catalyzed acetal-formation yielded multi-acetal PEGs (PEG10kMA) and diacetal PEGs (PEG10kDA) with vinyl ether end groups.

The acid-catalyzed reaction of TEGDV with PEG-diols of different molecular weight (M_n= 2k and 10k) yielded acetal-functional PEG precursors for the design of pH-labile hydrogels. In particular, step-growth polymerization of PEG2k and TEGDV afforded linear PEG10kMA, possessing multiple acetal moieties distributed along the polyether backbone (**Scheme 5.1**, reaction 1). An excess of TEGDV determined the number average molecular weight (M_n) to 10 kg·mol^{-1} and yielded PEG10kMA with vinyl ether end groups. ^{1}H NMR spectroscopy confirmed the disappearance of PEG's hydroxyl end groups at 4.57 ppm and the appearance of distinct vinyl ether groups at 6.50 ppm (CH_2CHO-) and at 4.18 ppm and 3.96 ppm for CH_2CHO-, respectively (**Figure 5.11**). The latter are important to enable hydrogel formation *via* thiol-ene reactions. In addition, acid-labile acetal moieties were clearly visible at 4.69 ppm (quartet, -C*H*CH$_3$, 1H) and 1.19 ppm (doublet, -CHC*H*$_3$, 3H). ^{13}C NMR spectroscopy further confirmed acetal-formation and defined vinyl ether end groups (**Figure S5.1**).

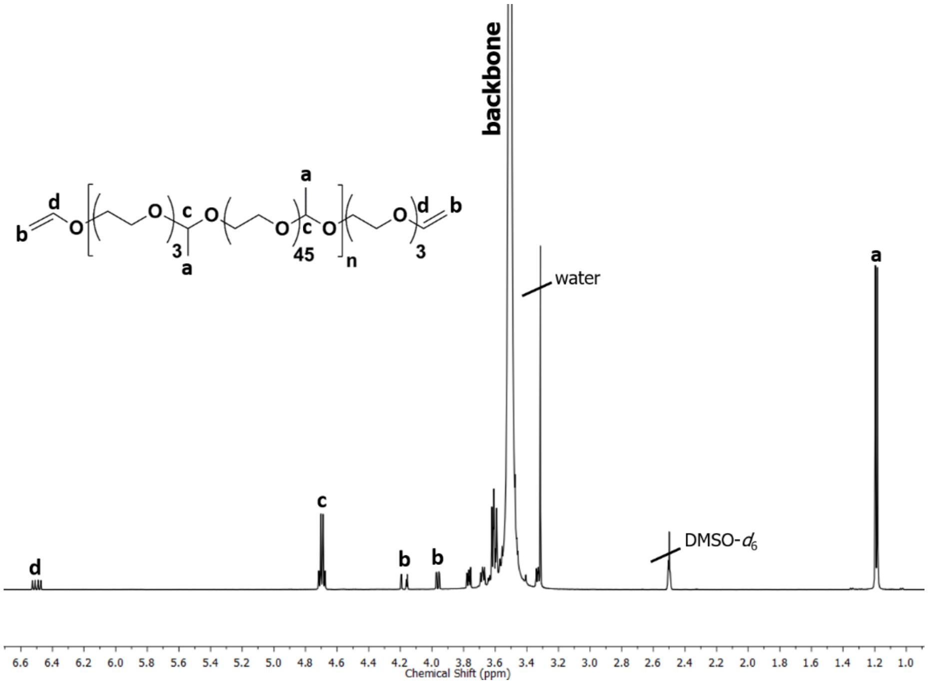

Figure 5.1. ^{1}H NMR spectrum (DMSO-d_6, 400 MHz) of PEG10kMA synthesized *via* step-growth polymerization using PEG2k and TEGDV.

In contrast, the synthesis of PEG10kDA relied on end group modification of a commercial PEG10k with a ten-fold excess of TEGDV (**Scheme 5.1**, reaction 2). This afforded a precursor polymer with only one cleavable moiety at each chain end, which serves as a control with fewer degradation points in the PEG hydrogel. The molecular weight of the precursor polymer is important because it will determine the molecular weight between crosslinks in the network and influence the storage modulus and swelling ratio of the resulting hydrogels, respectively. Both precursor polymers (PEG10kMA and PEG10kDA) showed monomodal distributions in the SEC chromatograms with comparable molecular weights (M_n ~ 10k g·mol^{-1}) (**Figure S5.4-S5.5**).

Despite the similar molecular weight, the thermal bulk properties of the precursor polymers confirmed their slight differences in chemical structure. The incorporated acetal-groups along the polyether backbone impacted the packing ability of the PEG chains, decreasing the melting temperature I and the melting enthalpy (ΔH) of PEG. Differential scanning calorimetry (DSC) measurements revealed a T_m of 41 °C for the PEG10kMA compared to a T_m of 62 °C for neat PEG10k and a decrease in ΔH of 87 $J \cdot g^{-1}$. In contrast, the modified end groups in PEG10kDA decreased the T_m of PEG to only 55 °C and the melting enthalpy decreased by 30 $J \cdot g^{-1}$ (**Table S5.1**).

Because of PEGs hydrophilicity, PEG10kMA and PEG10kDA dissolved rapidly in PBS buffer, which enabled hydrogel preparation in aqueous solution. Crosslinking and hydrogel formation occurred *via* UV-induced "thiol-ene" click reactions between the acetal-functional PEGs bearing vinyl ether end groups and THIOCURE® ETTMP 1300 (Thiocure) (**Scheme 5.2**). Thiocure is a water-soluble three-arm PEG star with a molecular weight of 1300 $g \cdot mol^{-1}$. It bears a thiol group at each chain and has been utilized in literature for the design of injectable hydrogels crosslinked *via* Michael-addition, which suggested a sufficient biocompatibility of Thiocure.[23-25] In contrast to such Michael-systems, UV-initiated "thiol-ene" crosslinking enables spatially and temporally controlled gel formation, which could facilitate potential *in vivo* applications. To enable UV-induced "thiol-ene" crosslinking, a suitable, water-soluble photoinitiator is inevitable. Here, lithium acylphosphinate salt (LAP) served as a type I photoinitiator because of its good water solubility ($\leq$ 8.5 wt%) compared to the commercially available 2-hydroxy-1-[4-(2-hydroxyethoxy)phenyl]-2-methyl-1-propanone (I2959) (< 2 wt%).[26] LAP also possesses strong UV-absorption at 365 nm and good cytocompatibility.[26] Anseth and co-workers utilized 2.2 mM LAP to initiate PEG diacrylate crosslinking for cell encapsulation and reported 96% cell survival after a 1 min exposure to UV-light (365 nm).[26] While the LAP concentration used in this study is slightly higher (c = 3.6 mM), initiator concentrations are adjustable for future potential *in vivo* applications. In general, a photoinitiator possessing sufficient UV-absorption at rather long wavelength (≥ 365 nm) is crucial to enable potential biomedical applications, reducing phototoxicity and tissue damage because shorter UVA light (< 360 nm) is more likely to cause oxidative DNA modifications and the generation of pyrimidine dimers, which alter the DNA.[27-28]

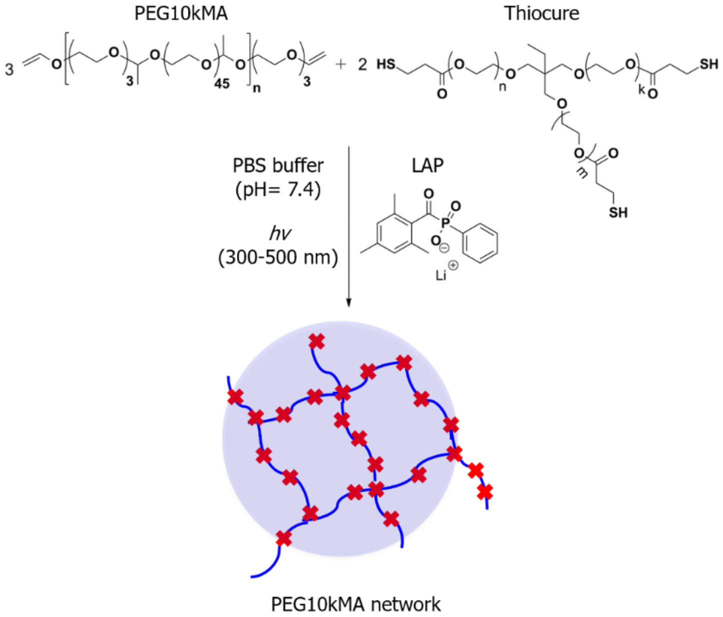

Scheme 5.2. Crosslinking and hydrogel formation *via* UV-initiated “thiol-ene” click reactions using PEG10kMA, Thiocure and LAP as photoinitiator.

We investigated three different hydrogel compositions to study the influence of number of acetal groups in the PEG precursor on hydrogel dissolution times. The first hydrogel utilized PEG10kMA solely, the second consisted of a mixture of 50 mol% PEG10kMA and 50 mol% PEG10kDA and the last utilized PEG10kDA. All hydrogels have been prepared using a 1:1 mole stoichiometry of vinyl ether to thiol (Thiocure) at 20 wt% solids and 0.5 wt% LAP, calculated on the wt% of polymer solids. Photorheological measurements revealed short gel times (≤ 3 s) for all hydrogel compositions and they reached full gelation in less than 13 s. This is significantly faster than gels prepared using Michael addition, which often required several minutes for full gelation.[9, 23-24, 29] The gel state moduli (G_0^N) ranged from 6 to 10 kPa for networks with a water content of 80 wt%. The difference in G_0^N might arise from slight variations in molecular weight of the PEG precursors (PEG10kMA and PEG10kDA). For an ideal network, the molecular weight between crosslinks ($\overline{M}_c$) is defined as $\overline{M}_c = 2\left(\frac{MW_{ene}}{f_{ene}} + \frac{MW_{thiol}}{f_{thiol}}\right)$.[9] In the case where the acetal-functional PEGs with a $\overline{M}_n$ of about 10 kg·mol^{-1} and a functionality of 2 reacted with Thiocure ($\overline{M}_n$=1300 g·mol^{-1}, f = 3), a $\overline{M}_c$ of ~11k g·mol^{-1} resulted. Consequently, the rather broad dispersity of the synthesized PEG10kMA precursors (*Đ* = 2) would directly affect the $\overline{M}_c$ of the network and ultimately alter the G_0^N value.

Crosslinking conversion will influence the measured elastic modulus of the formed networks as well. Thiol-ene photopolymerizations follow step-growth behavior, which should result in high crosslinking conversion. Dialysis of the crosslinked films in methanol and subsequent drying determined the gel fractions and the crosslinking yield of each hydrogel type. A gel fraction of 99.5 ± 0.5% for the PEG10kDA networks indicated quantitative crosslinking. The networks prepared from PEG10kMA and PEG10kMA/DA showed a gel fraction of 87.7± 0.8% and 88.0 ± 1.1%, respectively. This slightly higher soluble fraction directly lowered the elastic modulus for the PEG10kMA and

PEG10kMA/DA gels compared to the PEG10kDA. However, gel fractions close to 90% are promising to avoid unfavorable leaching of unreacted polymer into the human body, which potentially causes inflammatory response in future biomedical applications.

Another factor influencing the elastic modulus of the gel is the vinyl ether “ene” to thiol ratio. Slight imbalance altered the gel state modulus noticeably. For example, **Figure S5.6** shows the storage modulus versus irradiation time of varied thiol to vinyl ether ratios for PEG10kDA and Thiocure at 20 wt% solids. A ratio close to 1:1 is crucial to afford gels with a high crosslinking density. Stochiometric imbalance led to defects in the polymer network which lowers the number of elastically active chains per crosslink and consequently lowers the mechanical strength. However, a slight excess of thiol groups would render free thiols in the hydrogel, which are attractive for future attachment of drug molecules, peptides or fluorescence labels. Alternatively, the facile hydrogel formation shows promise to attach thiol-functional active molecules during crosslinking.

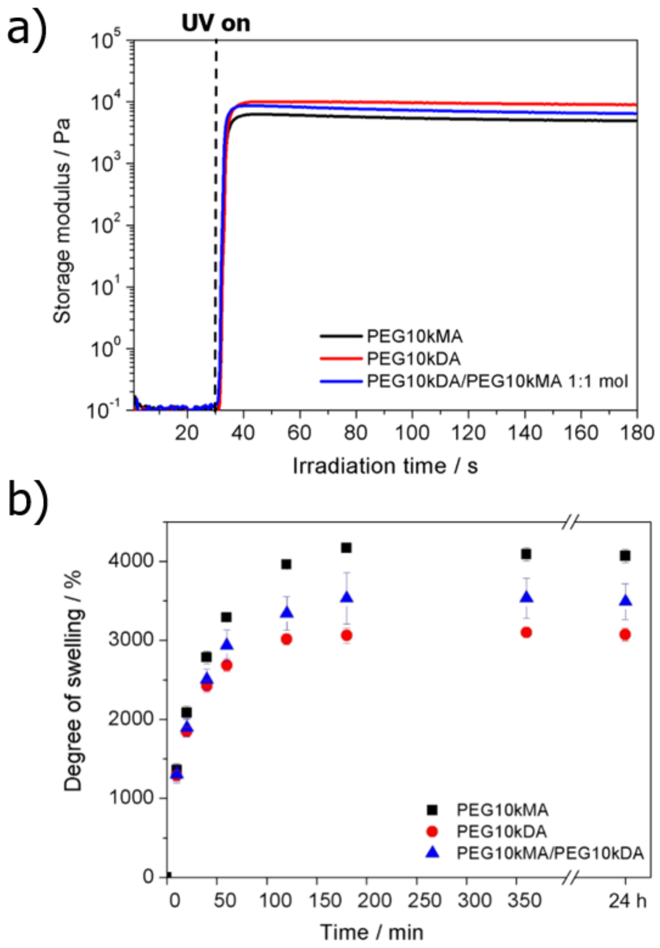

Figure 5.2. a) Storage modulus (Pa) versus irradiation time (s) from photorheology data for the different hydrogel compositions with a thiol to ene ratio of 1:1. Irradiation starts at 30 s. b) Degree of swelling (%) of the different hydrogels versus time (min).

Swelling studies in PBS buffer further confirmed slight difference in molecular weight between crosslinks. **Figure 5. b** illustrates the water uptake of the three hydrogels after freeze-drying. The water uptake of PEG10kMA hydrogel reached ~4000% while PEG10kDA showed swelling of ~3000% after 24 h. However, the degree of swelling collaborated with the storage modulus measured *via* photorheology, whereas the PEG10kMA network possessed the lowest G_0^N and showed the highest degree of swelling.

In addition to the differences in molecular weight, multi-acetal functional PEGs are known to degrade slowly at pH 7.4[17, 21] which might further contribute to a higher water uptake due to hydrolysis and the formation of defects.

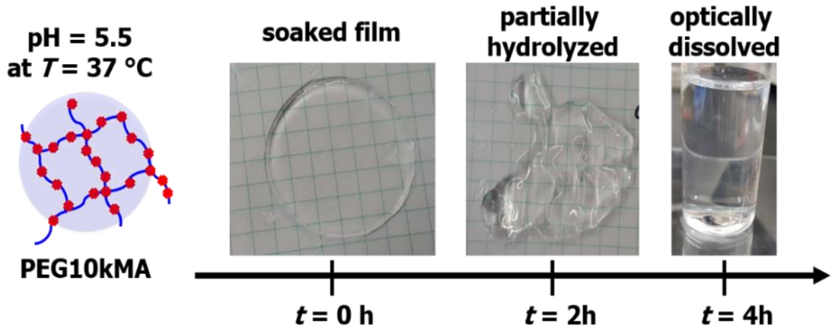

Figure 5.3. Images of the hydrogel film (PEG10kMA) directly after soaking in PBS buffer (*t* = 0), after 2 h in citrate buffer (pH = 5.5) at 37 °C and after 4h. After 2 h, the hydrogel is extremely soft and expanded, indicating partial hydrolysis. The film is optically dissolved after 4 h.

Hydrogel degradation and dissolution were studied in four different buffer solutions. Citrate-phosphate buffer with a pH of 5.5 and 6.5 enabled to monitor acetal hydrolysis and hydrogel degradation at a pH, which is observed extracellularly in tumor tissue or chronic wounds. Studies in PBS buffer (pH = 7.4) enabled to evaluate hydrogel performance under physiological pH. A phosphate-carbonate buffer with a pH of 8 enabled to study cleavage of the ester groups and subsequent hydrogel dissolution. All studies occurred at 37 °C to mimic body temperature, relevant for potential biomedical applications and were conducted in triplicates. Degradation was tracked by visual evaluation of the hydrogel as shown in **Figure 5.**. In a slightly acid environment, the acetal-moieties reacted and formed alcohols and acetaldehyde, which caused hydrogel dissolution (**Scheme S5.2**). The hydrogel possessing the highest number of acetal groups (PEG10kMA) was already extremely soft and expanded in size after only 2 h at pH = 5.5, indicating partial hydrolysis (**Figure 5.**). After another 2 h (*t* = 4h), the PEG10kMA hydrogel was optically dissolved.

Decreasing the number of acetals groups in the hydrogel slowed down hydrolysis and the PEG10kMA/DA gels required 8 h for full dissolution at pH 5.5. The hydrogels consisting of PEG10kDA were optically vanished within 24 h. This demonstrated that the number of acetal groups affected degradation and hydrogel dissolution. However, it is important to note that hydrogel dissolution does not require all acetal-groups to be cleaved. The hydrolysis of a few acetal-groups generated water-soluble polyether structures, which might still comprise of unreacted acetal-groups but cause hydrogel dissolution. This is important because hydrogel dissolution times are shorter than reported degradation times for the respective non-crosslinked polymer chains. For example, Tomlinson *et al.* reported the degradation of 50% of a multi-acetal PEG (M_n = 26700 g·mol^{-1}) after 50 h at pH 5.5.[21] Increasing the pH from 5.5 to 6.5 impacted the dissolution of the hydrogels significantly. In particular, the hydrogels based on PEG10kMA required 29 h for dissolution, while degradation of PEG10kMA/DA and PEG10kDA required 3 d and 6 d, respectively. Acetal moieties are rather stable at physiological pH (7.4), which was also reflected by their degradation time in PBS buffer. PEG10kMA hydrogels were optically dissolved after 3.5 d, while the PEG10kMA/DA and PEG10kDA hydrogels were hydrolyzed after 4.5 d and 6 d, respectively. In comparison, Tomlinson *et al.* reported a 25% weight loss for the multi-acetal PEG (M_n = 26700 g·mol^{-1}) after about 10 d at a pH of 7.4.

The ester groups of the crosslinking agent in close proximity to the formed thioether groups are also prone to hydrolysis.[9] While Langer and co-workers reported rather slow degradation times of PEG hydrogels prepared from PEG diacrylates and Thiocure via Michael-addition (2 wt% a week over 9 weeks) under physiological pH,[23] Bowman and co-workers demonstrated that slightly basic conditions accelerated ester cleavage umificantly.[7, 30] This motivated degradation studies of the acetal-PEG/Thiocure hydrogels at pH 8 using a sodium phosphate buffer. All three different hydrogel types hydrolyzed within 2.5 d, which clearly indicated the influence of the ester groups because acetal groups are stable under basic conditions. Degradation in a slightly alkaline environment is also attractive because it enables hydrogel hydrolysis over a large pH spectrum (acidic or basic), while the gels are rather stable under physiological pH. If no degradation at alkaline pH is desired, a crosslinking agent without ester groups can easily be chosen.

The potential application of acetal-functional PEG hydrogels for biomedical applications requires low cytotoxicity. Tomlinson *et al.* reported multi-acetal PEGs formed from TEGDV and PEG2k and their respective degradation products as non-cytotoxic toward B16F10 cells with concentrations up to 5 mg·mL^{-1}.[21] The authors further report that both, the polyacetals and their degradation products were nonhemolytic over 24 h. In addition, Koberstein and co-workers exposed fibroblasts to a polyacetal generated from TEGDV and triethylene glycol. The polyacetal with a molecular weight of 14.7 kg·moL^{-1} and vinyl ether end groups showed no impact on the cells up to a concentration of 10 mg·mL^{-1}. Also, while acetaldehyde is considered cytotoxic, aldehyde dehydrogenase enzymes in the human body readily oxidize acetaldehyde to acetic acid, which is metabolized by muscle tissue.[17, 31-32] **Figure 5.** shows cell viability studies of the acetal functional hydrogels and PEG10k as a control. While PEG10k with a concentration of 25 µg·mL^{-1} showed no impact on the viability of MDA-MB-231 human breast cancer cells, the hydrogels placed onto the cells reduced their viability slightly. PEG10kMA and PEG10kMA/DA showed a cell viability near 80%, which is the threshold value for being considered cell viable (**Figure 5.**). The hydrogel prepared from PEG10kDA showed a reduced cell viability of ~70%. This is surprising because PEG10kDA is chemically most similar to neat PEG. However, the hydrogels were placed on top of the cells for all cell viability tests. This was likely to reduce the diffusion of oxygen, which negatively impacted cell viability.[33] Similar observations have been reported for sugar-derived poly(β-thioester) films[34] and also correlated with PEG10kDA gels possessing the lowest degree of swelling and the highest G_N^0. For future studies, alternative cell cytotoxicity tests will be conducted.

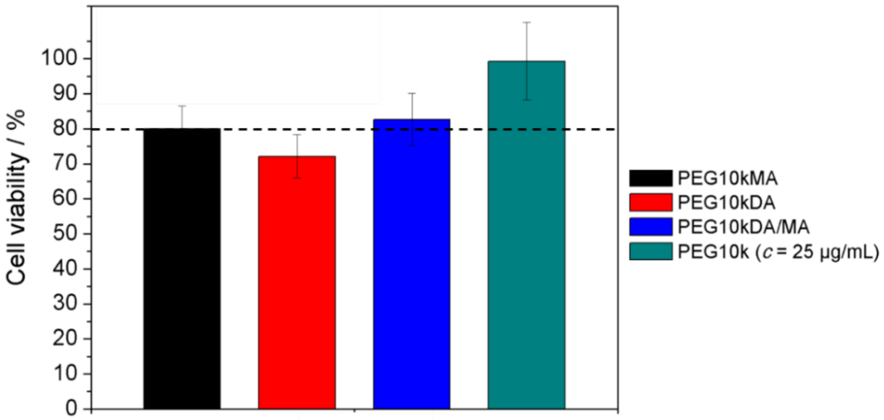

Figure 5.4. Cell cytotoxicity assay of MDA-MB-231 human breast cancer cells incubated with three different hydrogel types (PEG10kMA, PEG10kDA and PEG10kMA/DA) and PEG10k ($c = 25 \mu g \cdot mL^{-1}$) as control.

5.3 Conclusions

In summary, we presented the synthesis of acid-labile PEG precursors to yield pH-sensitive PEG hydrogels. The choice of PEG-diols (2k and 10k) and their ratio to TEGDV determined the number of acetal groups along the polyether backbone and enabled the synthesis of multi-acetal (PEG10kMA) and diacetal functional PEGs (PEG10kDA) with a number average molecular weight of 10 kg·mol^{-1} and defined vinyl ether end groups. The vinyl ether end groups allowed for UV-initiated “thiol-ene” reaction using THIOCURE® ETTMP 1300 in PBS buffer and a water-soluble photoinitiator (LAP). Photorheology revealed short gel times (< 3s) and the formation of hydrogels with gel state moduli ranging from 6-10 kPa at 20 wt% solids. The choice of precursor polymer enabled to tune the degradation times of the hydrogels from 4 h to 21 h at pH 5.5. The use of Thiocure further enabled network degradation at slightly alkaline pH. Cell cytotoxicity studies showed marginal impact of the hydrogel on the cell viability. The slightly reduced cell viability was most likely caused by reduced oxygen diffusion through the hydrogel. Overall, we demonstrated the potential of acetal functional PEGs for the design of pH-degradable hydrogels for biomedical applications.

5.4 Acknowledgements

The authors would like to formally acknowledge the National Science Foundation Research Experiences for Undergraduates Program (Award Number: CHE-1560240). The authors thank Dr. John Matson for the possibility to use the THF SEC and Kyle and Clay Arrington for their technical assistance. Furthermore, the authors acknowledge Bruno Bock Thiochemicals for their kind donation of the THIOCURE® ETTMP 1300.

5.5 References

1. Lin, C. C.; Anseth, K. S., PEG hydrogels for the controlled release of biomolecules in regenerative medicine. *Pharm Res* **2009,** *26* (3), 631-43.

2. Peppas, N. A.; Hilt, J. Z.; Khademhosseini, A.; Langer, R., Hydrogels in Biology and Medicine: From Molecular Principles to Bionanotechnology. *Advanced Materials* **2006,** *18* (11), 1345-1360.

3. Herzberger, J.; Niederer, K.; Pohlit, H.; Seiwert, J.; Worm, M.; Wurm, F. R.; Frey, H., Polymerization of Ethylene Oxide, Propylene Oxide, and Other Alkylene Oxides: Synthesis, Novel Polymer Architectures, and Bioconjugation. *Chem Rev* **2016,** *116* (4), 2170-243.

4. Palombo, M.; Deshmukh, M.; Myers, D.; Gao, J.; Szekely, Z.; Sinko, P. J., Pharmaceutical and toxicological properties of engineered nanomaterials for drug delivery. *Annu Rev Pharmacol Toxicol* **2014,** *54*, 581-98.

5. Caliceti, P., Pharmacokinetic and biodistribution properties of poly(ethylene glycol)–protein conjugates. *Advanced Drug Delivery Reviews* **2003,** *55* (10), 1261-1277.

6. Zustiak, S. P.; Leach, J. B., Hydrolytically degradable poly(ethylene glycol) hydrogel scaffolds with tunable degradation and mechanical properties. *Biomacromolecules* **2010,** *11* (5), 1348-57.

7. Rydholm, A. E.; Anseth, K. S.; Bowman, C. N., Effects of neighboring sulfides and pH on ester hydrolysis in thiol-acrylate photopolymers. *Acta Biomater* **2007,** *3* (4), 449-55.

8. Rizzi, S. C.; Ehrbar, M.; Halstenberg, S.; Raeber, G. P.; Schmoekel, H. G.; Hagenmuller, H.; Muller, R.; Weber, F. E.; Hubbell, J. A., Recombinant protein-co-PEG networks as cell-adhesive and proteolytically degradable hydrogel matrixes. Part II: biofunctional characteristics. *Biomacromolecules* **2006,** *7* (11), 3019-29.

9. Metters, A.; Hubbell, J., Network formation and degradation behavior of hydrogels formed by Michael-type addition reactions. *Biomacromolecules* **2005,** *6* (1), 290-301.

10. Mason, M. N.; Metters, A. T.; Bowman, C. N.; Anseth, K. S., Predicting Controlled-Release Behavior of Degradable PLA-b-PEG-b-PLA Hydrogels. *Macromolecules* **2001,** *34* (13), 4630-4635.

11. Worm, M.; Leibig, D.; Dingels, C.; Frey, H., Cleavable Polyethylene Glycol: 3,4-Epoxy-1-butene as a Comonomer to Establish Degradability at Physiologically Relevant pH. *ACS Macro Letters* **2016,** *5* (12), 1357-1363.

12. Dingels, C.; Frey, H., From Biocompatible to Biodegradable: Poly(Ethylene Glycol)s with Predetermined Breaking Points. In *Hierarchical Macromolecular Structures: 60 Years after the Staudinger Nobel Prize II*, 2013; pp 167-190.

13. Lundberg, P.; Lee, B. F.; van den Berg, S. A.; Pressly, E. D.; Lee, A.; Hawker, C. J.; Lynd, N. A., Poly[(ethylene oxide)-co-(methylene ethylene oxide)]: A hydrolytically-degradable poly(ethylene oxide) platform. *ACS Macro Lett* **2012,** *1* (11), 1240-1243.

14. Schmaljohann, D., Thermo- and pH-responsive polymers in drug delivery. *Adv Drug Deliv Rev* **2006,** *58* (15), 1655-70.

15. Gupta, P.; Vermani, K.; Garg, S., Hydrogels: from controlled release to pH-responsive drug delivery. *Drug Discovery Today* **2002,** *7* (10), 569-579.

16. Brocchini, S. C. S., Polyacetals. *Natural and Synthetic Biomedical Polymers* **2014**, 219-233.

17. Samanta, S.; Bogdanowicz, D. R.; Lu, H. H.; Koberstein, J. T., Polyacetals: Water-Soluble, pH-Degradable Polymers with Extraordinary Temperature Response. *Macromolecules* **2016,** *49* (5), 1858-1864.

18. Pohlit, H.; Bellinghausen, I.; Schomer, M.; Heydenreich, B.; Saloga, J.; Frey, H., Biodegradable pH-Sensitive Poly(ethylene glycol) Nanocarriers for Allergen Encapsulation and Controlled Release. *Biomacromolecules* **2015,** *16* (10), 3103-11.

19. Wang, Y.; Morinaga, H.; Sudo, A.; Endo, T., Synthesis of amphiphilic polyacetal by polycondensation of aldehyde and polyethylene glycol as an acid-labile polymer for controlled release of aldehyde. *Journal of Polymer Science Part A: Polymer Chemistry* **2011,** *49* (3), 596-602.

20. Plyduang, T.; Arminan, A.; Movellan, J.; England, R. M.; Wiwattanapatapee, R.; Vicent, M. J., Polyacetal-Based Combination Therapy for the Treatment of Prostate Cancer. *Macromol Rapid Commun* **2018**, e1800265.

21. Tomlinson, R.; Klee, M.; Garrett, S.; Heller, J.; Duncan, R.; Brocchini, S., Pendent Chain Functionalized Polyacetals That Display pH-Dependent Degradation: A Platform for the Development of Novel Polymer Therapeutics. *Macromolecules* **2002,** *35* (2), 473-480.

22. Samanta, S.; De Silva, C. C.; Leophairatana, P.; Koberstein, J. T., Main-chain polyacetal conjugates with HIF-1 inhibitors: temperature-responsive, pH-degradable drug delivery vehicles. *Journal of Materials Chemistry B* **2018,** *6* (4), 666-674.

23. Pritchard, C. D.; O'Shea, T. M.; Siegwart, D. J.; Calo, E.; Anderson, D. G.; Reynolds, F. M.; Thomas, J. A.; Slotkin, J. R.; Woodard, E. J.; Langer, R., An injectable thiol-acrylate poly(ethylene glycol) hydrogel for sustained release of methylprednisolone sodium succinate. *Biomaterials* **2011,** *32* (2), 587-97.

24. Moon, N. G.; Pekkanen, A. M.; Long, T. E.; Showalter, T. N.; Libby, B., Thiol-Michael 'click' hydrogels as an imageable packing material for cancer therapy. *Polymer* **2017,** *125*, 66-75.

25. Peach, M. S.; Moore, J.; Long, T. E.; Moon, N.; Showalter, T.; Libby, B., Preclinical Testing of a Novel Biodegradable Hydrogel Based Intravaginal Spacer for HDR Gynecologic Brachytherapy. *Brachytherapy* **2018,** *17* (4), S15-S16.

26. Fairbanks, B. D.; Schwartz, M. P.; Bowman, C. N.; Anseth, K. S., Photoinitiated polymerization of PEG-diacrylate with lithium phenyl-2,4,6-trimethylbenzoylphosphinate: polymerization rate and cytocompatibility. *Biomaterials* **2009,** *30* (35), 6702-7.

27. Christopher Kielbassa, L. R., Bernd Epe, Wavelength dependence of oxyidative DNA damage induced by UV and visible light. *Carcinogenesis* **1997,** *18* (4), 811-816.

28. Kielbassa, C.; Epe, B., [39] DNA damage induced by ultraviolet and visible light and its wavelength dependence. In *Singlet Oxygen, UV-A, and Ozone*, 2000; pp 436-445.

29. O'Shea, T. M.; Aimetti, A. A.; Kim, E.; Yesilyurt, V.; Langer, R., Synthesis and characterization of a library of in-situ curing, nonswelling ethoxylated polyol thiol-ene hydrogels for tailorable macromolecule delivery. *Adv Mater* **2015,** *27* (1), 65-72.

30. Rydholm, A. E.; Reddy, S. K.; Anseth, K. S.; Bowman, C. N., Development and Characterization of Degradable Thiol-Allyl Ether Photopolymers. *Polymer (Guildf)* **2007,** *48* (15), 4589-4600.

31. Marchitti, S. A.; Brocker, C.; Stagos, D.; Vasiliou, V., Non-P450 aldehyde oxidizing enzymes: the aldehyde dehydrogenase superfamily. *Expert Opin Drug Metab Toxicol* **2008,** *4* (6), 697-720.

32. Crabb, D. W.; Matsumoto, M.; Chang, D.; You, M., Overview of the role of alcohol dehydrogenase and aldehyde dehydrogenase and their variants in the genesis of alcohol-related pathology. *Proceedings of the Nutrition Society* **2007,** *63* (01), 49-63.

33. Drury, J. L.; Mooney, D. J., Hydrogels for tissue engineering: scaffold design variables and applications. *Biomaterials* **2003,** *24* (24), 4337-4351.

34. Moon, N. G.; Mazzini, F.; Pekkanen, A. M.; Wilts, E. M.; Long, T. E., Sugar-Derived Poly(β-thioester)s as a Biomedical Scaffold. *Macromolecular Chemistry and Physics* **2018**.

5.6 Supplemental information

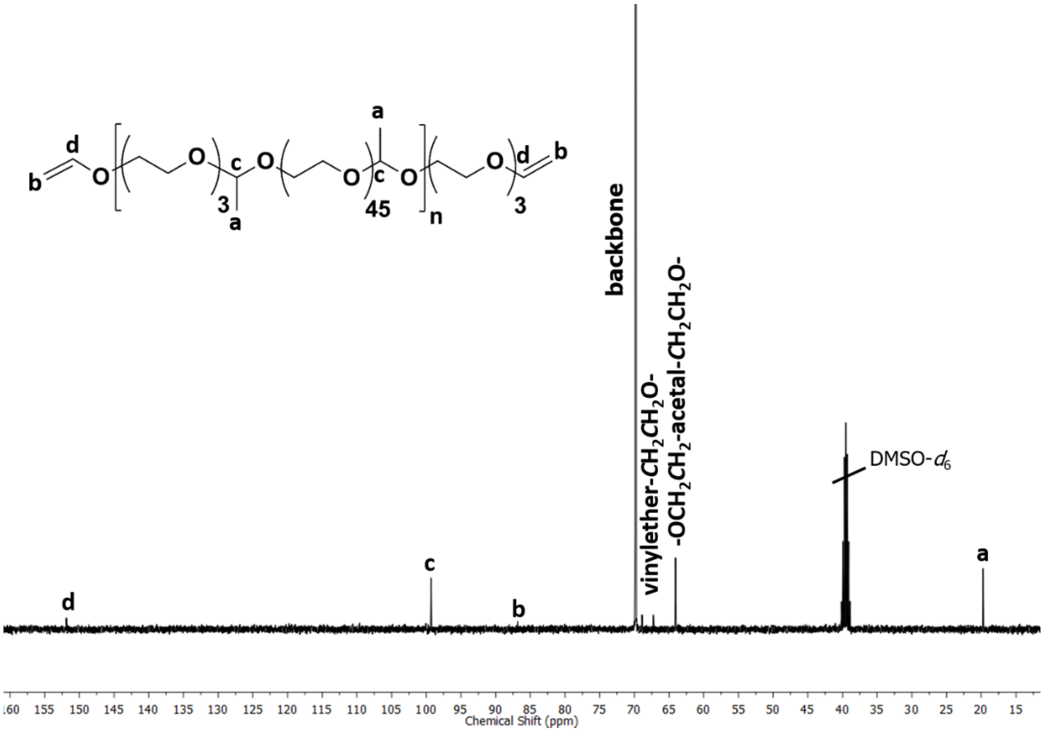

Figure S5.2. ^{13}C NMR spectrum (DMSO-d_6, 400 MHz) of PEG10kMA.

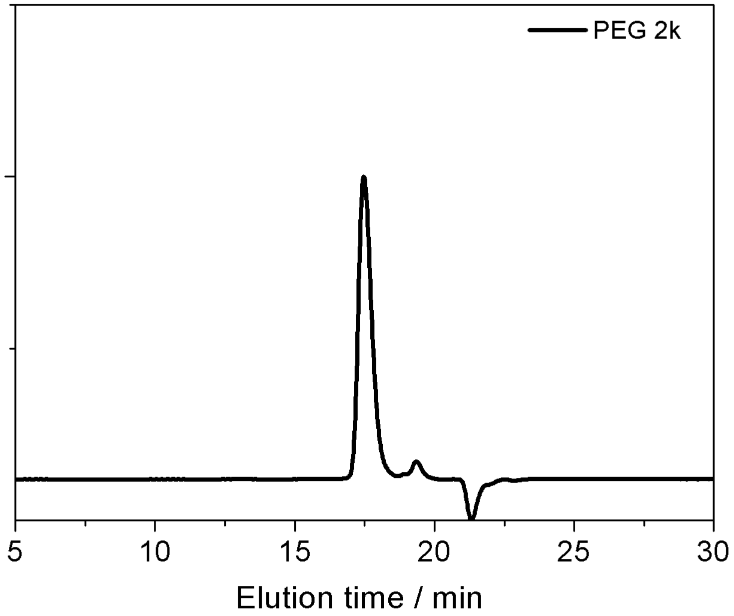

Figure S5.3. SEC trace of PEG2k (THF, RI signal).

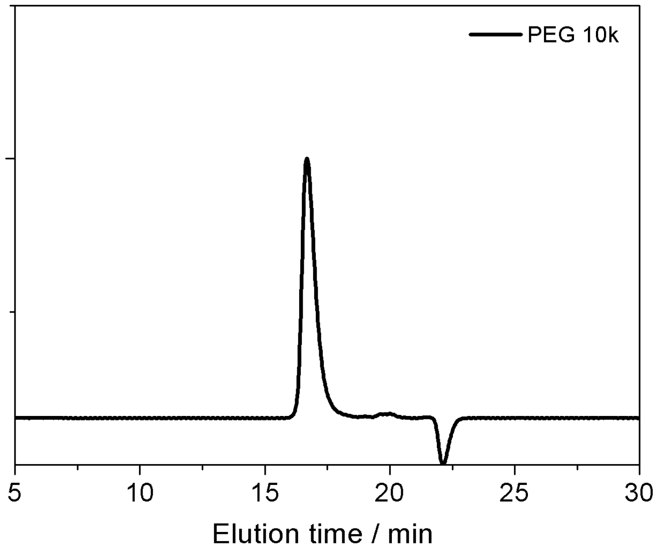

Figure S5.4. SEC trace of PEG10k (THF, RI signal).

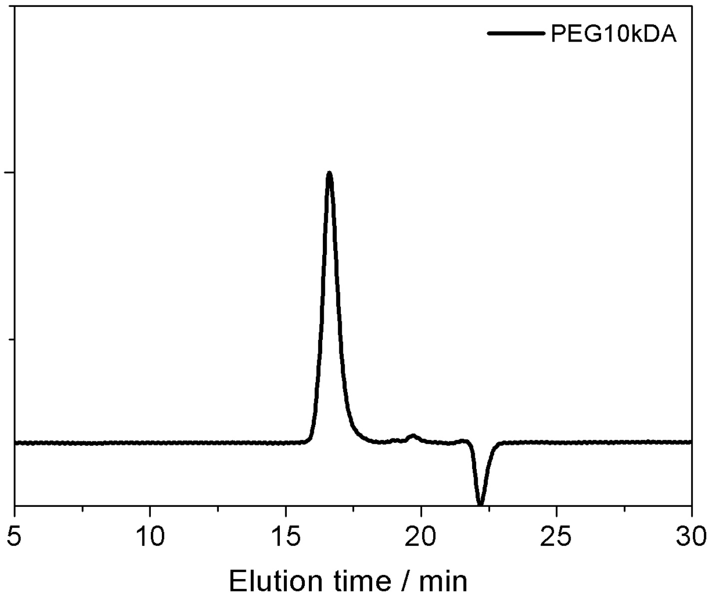

Figure S5.5. SEC trace of PEG10kDA (THF, RI signal).

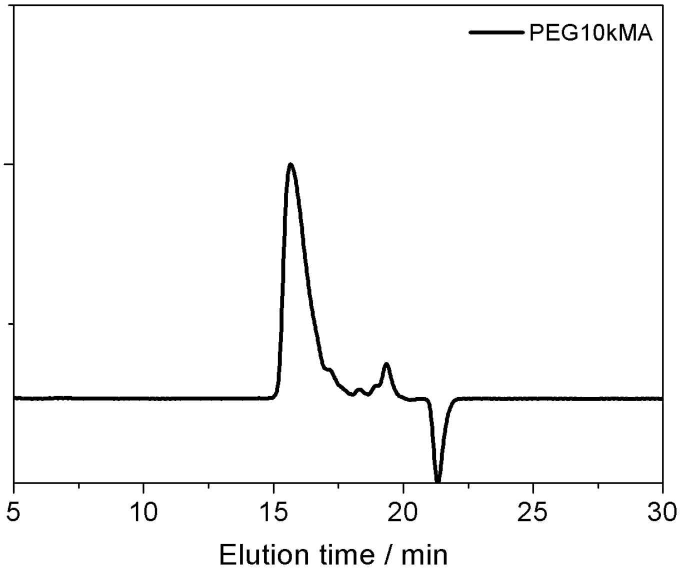

Figure S6.5. SEC trace of PEG10kMA (THF, RI signal).

Table S5.1. DSC data of PEG (starting material) and acetal-functional PEG precursors.

Sample	***T*$_g$ / °C**	***T*$_m$ / °C**	**Δ*H* / J·g^{-1}**
PEG2k	N/A	53	153
PEG10k	N/A	62	163
PEG10kDA	-62	55	135
PEG10kMA	-54	41	76

T_g: Glass transition temperature
T_m: Melting temperature
Δ*H*: Melting enthalpy

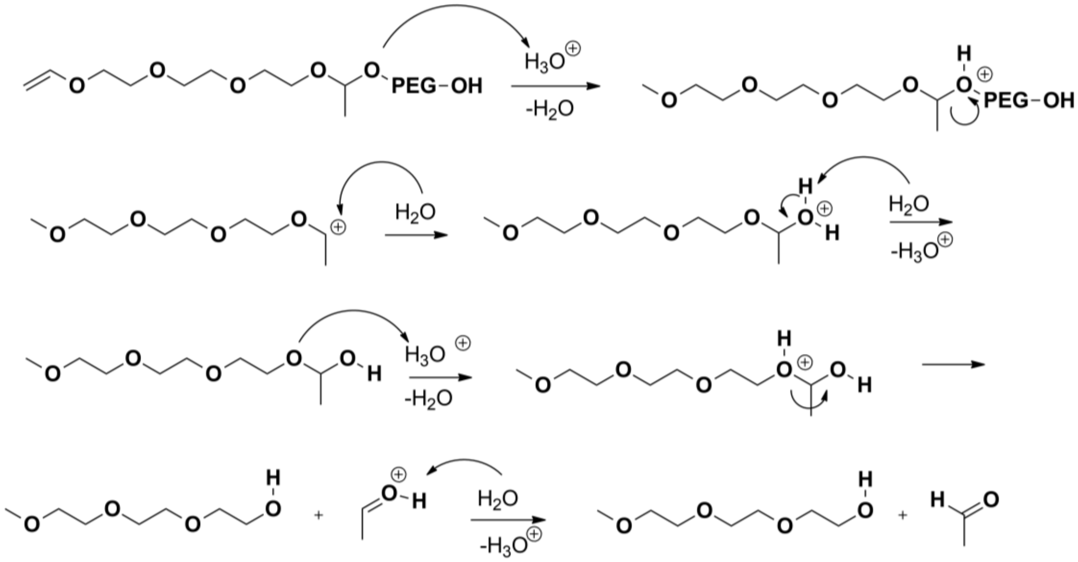

Scheme S5.1. Acid-catalyzed cleavage of multiacetal functional PEGs.

CHAPTER 6

BINARY THIOL-ACRYLATE PHOTOPOLYMERIZATION FOR THE DESIGN OF DEGRADABLE ACETAL-FUNCTIONALIZED HYDROGELS

ABSTRACT: Degradable poly(ethylene glycol) (PEG) hydrogels provide a versatile platform for drug delivery and tissue engineering, and acetal functionalization now enables photo-processible PEG oligomers with selective and facile degradation in acidic environments. Tailored morphologies within novel acetal-functionalized hydrogels provided fundamental understanding of multiphase network degradation. End group modification of poly(ethylene glycol) (M_n = 2,000 g/mol) with 2-(vinyloxy)ethyl acrylate yielded polyether precursors with both pH-sensitive acetals and photo-curable acrylate end groups. UV-initiated binary thiol-acrylate crosslinking of the acetal-functionalized PEG diacrylate with varied amounts of a thiol-functionalized three-armed PEG provided pH-degradable networks. Controlled stoichiometric imbalance of thiol and acrylate functionalities ensured predictable plateau storage moduli from 2×10^5 to 8×10^5 Pa. Small angle X-ray scattering (SAXS) and dynamic mechanical analysis (DMA) confirmed that the thiol:acrylate molar ratio provided hydrogels with varying network architectures and crosslink densities. Spectroscopic monitoring of an imbedded mobile dye (Direct Red-81) quantified hydrogel degradation rates. Degradable hydrogels exhibited bulk degradation in acidic solution. Gels with the lowest crosslink density fully degraded in aqueous solutions at pH 3.4 within 60 h while the highly crosslinked gels fully degraded over 3 weeks. All hydrogels displayed long term stability in phosphate buffered saline (pH 7.4) beyond 3 mo, suggesting stable hydrogels for selective degradation and cargo release in low pH environments.

6.1 Introduction

Selectively degradable polymeric materials address critical challenges in many fields including additive manufacturing, sustainability, and biomedical engineering.[1-4] Light-assisted additive manufacturing techniques such as vat photopolymerization (VP) and UV-assisted direct ink write (UV-DIW) conventionally utilize photopolymerizable monomers and crosslinkers to produce solid structures from liquid precursors.[5] These approaches have enabled 3-dimensional (3D) printing of elastomers, high performance polymers, and biocompatible materials for tissue engineering. [5-7] These covalently crosslinked networks present issues such as embrittlement, insolubility, lack of reprocessability, and *in vivo* complications. To address these issues, researchers developed new photopolymerizable monomers and crosslinkers specifically designed for degradation.[8] As more polymeric materials are designed for triggerable degradation, it is paramount to fundamentally understand the predictive structure-property-processing relationships that enable triggered degradation in chemically crosslinked networks.

The acetal functionality degrades in mildly acidic environments but remains stable at neutral pH, and as a result, the acetal functionality has served as a common protecting group in synthetic organic chemistry.[9] Acetals degrade at acidic pH below 6.5 forming alcohols and an aldehyde as hydrolysis byproducts; as expected, lower pH accelerates degradation rates.[10] Mild and selective hydrolysis render the acetal as an attractive functionality for predictive network degradation. Recently, our research group replaced poly(ethylene glycol) (PEG) diacrylate crosslinkers with acetal-functionalized diacrylate analogues as scaffolds for 3D printing elastomers after selective degradation and removal of the crosslinked scaffold.[11] Our prior work warranted further investigation of acetal- and acrylate-containing networks for potential delivery vehicles with tunable release rates.

Photo-processible hydrogels provide a desirable platform for rapidly emerging applications in tissue engineering and targeted drug delivery.[12-15] 3D printed hydrogels have previously received intense attention for critical brain injuries, intervaginal packing for cancer brachytherapy, and immunologically inert encapsulants that protect cargo from the immune system.[13, 16] However, covalent crosslinks that are present in most hydrogels lack desirable *in vivo* degradation rates. Previous strategies for degradable hydrogels employed biodegradable polyester crosslinking agents and or degradable block copolymers.[17-19] The acetal functionality presents another common functionality in degradable hydrogels, and the degradation liberates hydroxyls and a carbonyl, often acetaldehyde. Despite acetaldehyde cytotoxicity, aldehyde dehydrogenase enzymes in the human body readily oxidize acetaldehyde to acetic acid, and muscle tissue subsequently metabolizes acetic acid.[20-22] The relatively benign *in vivo* degradation of acetals suggests their suitability for biological applications.

Light-assisted additive manufacturing techniques provide 3D structures upon rapid photopolymerization of multifunctional monomers and crosslinkers. Photo-initiated free radical polymerization of activated alkenes such as acrylates, methacrylates, fumarates, and vinylpyrrolidones remains the most prolific approach for these manufacturing techniques.[23-25] In addition, radical thiol-ene polymerization with both activated and deactivated alkenes received significant earlier attention.[26, 27] In particular, Bowman *et. al* pioneered binary thiol-ene and acrylate polymerizations to generate complex network architectures with a stoichiometric imbalance of thiols and acrylates.[28] The thiol-ene reaction dominated network formation until complete consumption of available thiols, and after all thiols reacted with available acrylates, acrylate homopolymerization continued to further develop the network (**Scheme 6.1**).[29] This thiol-acrylate polymerization process generated networks with complex morphologies, which provided precise control of mechanical properties and performance. Prior work investigated binary thiol-acrylate hydrogel degradation.[28] However, different hydrolysis kinetics between alkyl esters in the acrylate phase and beta thioether esters in the thiol-ene phase complicated these studies.[30,31] Coupling selective and relatively fast acetal degradation with tailored network architectures from binary thiol-ene and acrylate polymerizations will afford a direct means to study degradation in hydrogels with precisely controlled networks.

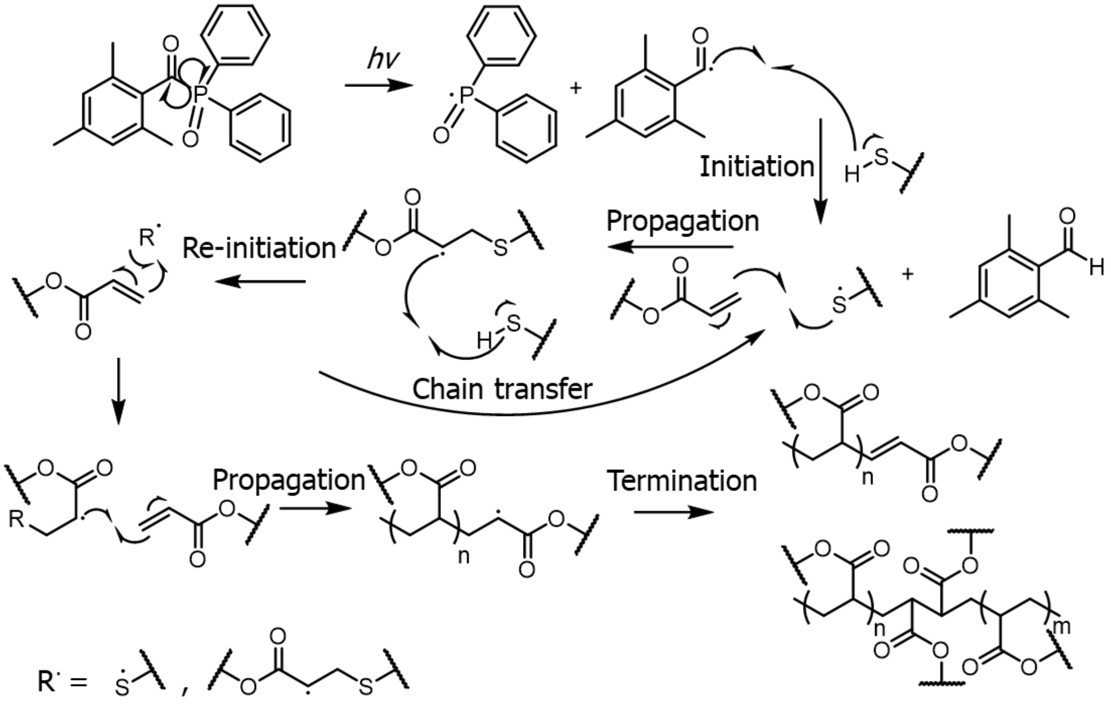

Scheme 6.1. Acrylate functionality participates in thiol-ene addition and homopolymerization

This manuscript provides fundamental insight into the degradation of acetal-functionalized hydrogels prepared from binary thiol-acrylate polymerizations. The acetal functionality provided selective degradation in low pH environments, and thiol-acrylate polymerizations tailored the network architecture during photopolymerization. Stoichiometric imbalance of functional groups provided diverse network architectures to elucidate the role of network architecture on release kinetics. The network architecture as defined using x-ray scattering and mechanical property measurements significantly impacted hydrogel durability and crosslink degradation rates.

6.2 Experimental Details

6.2.1 Materials.

PEG2k, PEG10k, *para*-toluenesulfonic acid monohydrate 98.5% (*p*-TSA), calcium hydride (CaH_2), ethylene glycol mono-vinyl ether, acryloyl chloride, triethyl amine ($N(Et)_3$), Diphenyl(2,4,6-trimethylbenzoyl)phosphine oxide (TPO), and Direct Red-81 were purchased from Sigma Aldrich. Thiocure ETTMP 1300 was kindly donated by Bruno Bock Thiochemicals. Deuterated solvents were received from Cambridge isotope. Dichloromethane (CH_2Cl_2) over molecular sieve was purchased from Acros Organics, all other solvents were received from Fisher scientific and used as received. Phosphate-buffered saline (PBS-buffer) tablets (pH = 7.4) were purchased from VWR. All citrate-phosphate buffer were prepared with citric acid and trisodium citrate purchased from Sigma Aldrich, and the pH was confirmed using a pH-electrode.

6.2.2 Instrumentation.

^{1}H NMR (400 MHz) and ^{13}C NMR (100 MHz) spectra were recorded using an Agilent U4-DD2 spectrometer equipped with a 96-sample robot. All spectra were referenced internally to residual proton signals of the deuterated solvent, e.g., DMSO-d_6. Photo-rheology was conducted using a TA Instruments DHR-2 rheometer equipped with an Omnicure S2000 photo-accessory (high-pressure mercury light source with 320-500 nm filter), Smart Swap^{TM} UV geometry, 20 mm quartz lower parallel plate, and 20 mm aluminum upper parallel plate. The samples were measured at 0.3 % oscillatory strain, a frequency of 1 Hz and the gap distance was set to 500 µm. All samples were equilibrated for 60 s, with the axial force set to 0 N. All measurements were conducted under air. The crossover times were determined from the intersection of the loss and storage moduli. The plateau storage modulus was calculated by averaging the values over the last 60 s (values from 120 s-180 s). All measurements were performed in triplicate and data denote the mean.

6.2.3 Synthesis of 2-(vinyloxy)ethyl acrylate.

2-(vinyloxy)ethyl acrylate was synthesized following the procedure first described by Jiang *et. al*.[32] Ethylene glycol monovinyl ether (10 g, 1 eq) and triethylamine (46 g, 4 eq) were dissolved in 50 mL of dichloromethane within a 250-mL round-bottomed flask equipped with an addition funnel. Acryloyl chloride (21 g, 2 eq) was diluted with 20 mL dichloromethane and charged to the addition funnel. The reaction vessel was cooled to 0 °C and was stirred with a magnetic stir bar. The acryloyl chloride solution was added dropwise over 2 h. The precipitated triethylammonium salts were filtered off before the addition of 50 mL of saturated $NaHCO_3$ solution. Following the $NaHCO_3$ extraction, the organic layer was washed twice with 100 mL of brine. The organic solution was dried over magnesium sulfate, filtered, and the solvent was removed under vacuum to yield a brown oil. Column chromatography with dichloromethane as an eluent produced a pale-yellow oil. 63 % yield. ^{1}H NMR ($CDCl_3$, δ, **Figure S6.1**, Supplemental Information) 6.46–6.51 (dd, 1H, 3), 6.42–6.47 (dd, 1H, 8), 6.12-6.19 (dd, 1H, 6), 5.84-5.87 (dd, 1H, 7) 4.39-4.41 (m, 2H, 5), 4.19-4.23 (dd, 1H, 2), 4.04-4.06 (dd, 1H, 1), 3.92-3.94 (m, 1H, 4); ^{13}C NMR: ($CDCl_3$, *δ,* **Figure S6.2**, Supplemental Information) 166.00, 151.39, 131.28, 128.03, 87.07, 65.70, 62.70.

6.2.3 Synthesis of PEG 2k diacetal diacrylate (PEG2kdAdAc).

PEG2k with acetals adjacent to acrylate end groups (PEG2kdAdAc) exemplifies a typical synthetic procedure. PEG2k (10 g) was dissolved in 100 mL dichloromethane and stirred over molecular sieves with g 2-(vinyloxy)ethyl acrylate (1.6 g, 2.2 eq). The solution was chilled to 0 °C before 0.108 g *p*-TSA (0.125 eq) dissolved in 1 mL THF was added. The reaction was stirred for 50 min before quenching with 10 mL saturated $NaHCO_3$ solution. The collected aqueous solution was washed with DCM and the combined organic layers were dried over $MgSO_4$, filtered, and precipitated into ice cold diethyl ether. The collected polymer was dried at room temperature under vacuum. 92% yield, white solid. ^{1}H NMR ($CDCl_3$, δ, **Figure S3**, Supplemental Information) 6.34–6.39 (dd, 2H, 1), 6.05–6.12 (dd, 2H, 3), 5.76-5.80 (dd, 2H, 2), 4.74-4.78 (q, 2H, 6, 4.23-4.26 (m, 4H, 4) 3.40-3.80 (m, 340H, 5,8), 1.26-1.28 (d, 6H, 7)

6.2.4 Hydrogel preparation.

Hydrogels were prepared from PEG2kDADAc and varied mol % of the trithiol crosslinker THIOCURE® ETTMP 1300 (0, 50, 100 mol % thiol to acrylate). Hydrogel precursor solutions were prepared with 50 wt. % reactants in a 50/50 wt. % ethanol/PBS solution prepared with 5 wt. % TPO. This yielded a final photo-curable solution with 50 wt. % reactants and 2.5 wt. % TPO. All hydrogels were produced using a TA Instruments DHR-2 rheometer equipped with an Omnicure S2000 photo-accessory. The intensity of the photo-source was set to 10 mW/cm^2. UV irradiation started at 30 s and samples were exposed to UV-light for 150 s. Acetal free analogues, PEG2k diacrylate (PEG2kDAc) hydrogels, were prepared in an equivalent manner.

6.2.5 PEG2kdAdAc hydrogel degradation study.

Sections of the prepared PEG2kDADAc and PEG2kDAc hydrogels were extracted in methanol for 24 h, and then dried under reduced pressure. The dried covalent networks were weighed, and then soaked in a 0.005 M solution of Direct-Red 81 prepared with PBS for 24 h. The swollen hydrogels were patted dry and the mass was recorded before the films were placed in either 15 mL of PBS buffer or 15 mL of citric acid buffer (CAB) pH (3.4). Every 3 h, a 0.10 mL aliquot was taken from each sample and diluted to a final volume of 1 mL for UV-Vis measurements. UV-vis spectroscopic measurements were performed on an Agilent 8543 spectrometer in a PMMA cell with pathlength= 1 cm. Absorbance values at the Direct Red-81 λ_{max}= 500 nm were obtained in triplicate for each aliquot. The mass of solution absorbed by the gel revealed the possible maximum concentration of Direct Red-81 after full hydrogel degradation. The absorption of each aliquot calculated the Direct

Red-81 concentration and thus afforded normalized degradation at each time step. The full process was repeated in triplicate for each PEG2kdAdAc hybrid formulation.

6.2.6 Small angle x-ray scattering (SAXS) of PEG2kdAdAc based hydrogels.

SAXS experiments were performed using a Rigaku S-Max 3000 3 pinhole system, equipped with a rotating anode emitting X-ray with a wavelength of 0.154 nm (Cu Kα). The sample-to-detector distance was 1600 mm, and the q-range was calibrated using a silver behenate standard. Two-dimensional SAXS patterns were obtained using a 2D multiwire, proportional counting, gas-filled detector, with an exposure time of 2 h. The data were corrected for sample thickness and transmission and were placed on an absolute scale by correction using a glassy carbon standard from the Advanced Photon Source (APS). All the data were analyzed using the SAXSGUI software package to obtain radially integrated intensity versus scattering vector q, where $q = (4\pi/\lambda)\sin(\theta)$, θ is one half of the scattering angle and λ is the X-ray wavelength.

6.3 Results and Discussion

End group modification of PEG2k with 2-(vinyloxy)ethyl acrylate yielded PEG with both degradable acetals and polymerizable acrylates at the chain ends (PEG2kdAdAc) (**Scheme 6.2**). The acrylate served as both a step-growth thiol-ene acceptor and chain growth acrylate homopolymerization crosslinker. UV-initiated photopolymerization of the PEG crosslinkers with varied amounts of THIOCURE® ETTMP 1300, a trithiol crosslinking agent, resulted in hydrogels with tunable crosslink densities (**Scheme 6.3**). Crosslinking neat PEG2kdAdAc in the absence of trithiol yielded hydrogels with high crosslink densities, and in contrast, a stoichiometric balance of thiols and acrylates produced hydrogels with lower crosslink densities. Finally, an intermediate composition with 50 mol % thiol developed a network with highly crosslinked polyacrylate phases surrounded by a crosslinked thiol acrylate network with a lower crosslink density. As expected, varying the crosslink density predicted mechanical properties, swelling behavior, degradation rates, and hydrogel dissolution times, which are commonly observed trends.[33-35]

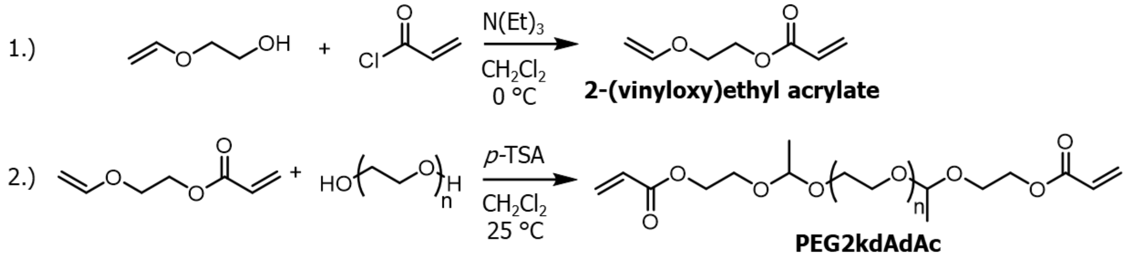

Scheme 6.2. Facile two-step synthesis of telechelic acrylate-functionalized PEG with adjacent acetals (PEG2kdAdAc).

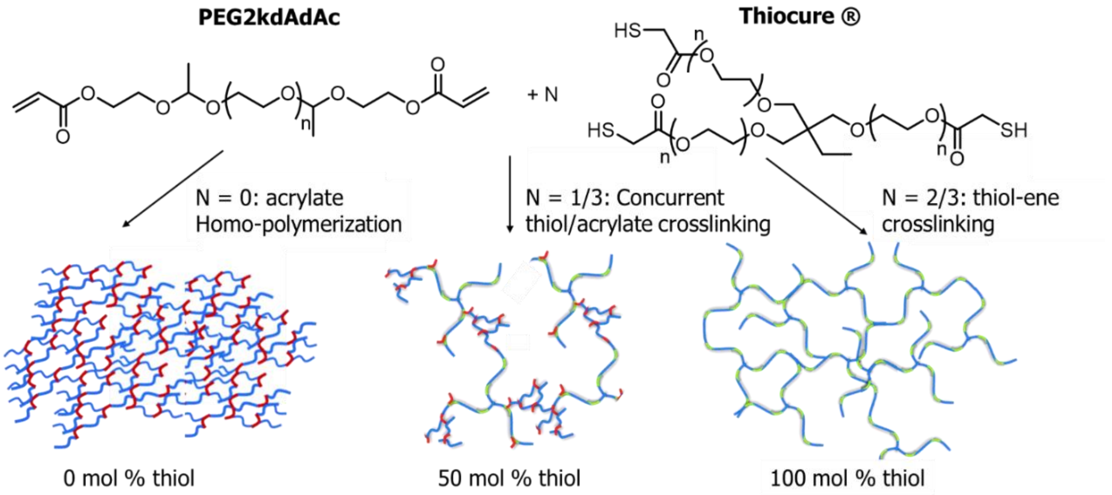

Scheme 6.3. Illustrations of various formulations with Thiocure ® to establish networks from high to low crosslink densities.

The mol % of thiols relative to acrylates varied from 0 to 100%, which tailored the mechanical properties of the resulting hydrogels. Photo-rheological measurements revealed thiol-acrylate polymerization with 100 mol % thiols provided hydrogels with a lower plateau storage modulus compared to formulations with an excess of acrylates (**Figure 6.1)**. PEG2kdAdAc continued to crosslink after complete thiol consumption and resulted in hydrogels with higher crosslink densities. These binary reaction kinetics, first described by Bowman *et. al*, predicted a decrease in plateau storage modulus as the mol % thiol increased.[29] The mol % of incorporated thiol tuned hydrogel plateau storage moduli from 2 x 10^5 to 8 x 10^5 Pa, nearly an order-of-magnitude. Furthermore, the acetal functionalization did not significantly affect photo-crosslinking rates as compared to poly(ethylene glycol) diacrylate (PEGdAc) controls. Additionally, these rheological investigations informed VP additive manufacturing parameters. An ETEC Envision One VP platform generated a 3D part with complex geometries (**Figure S6.4**). **Figure 6.2** summarizes swelling studies in PBS, which further highlighted the effects of varied thiol incorporation. Thiol-acrylate crosslinking afforded hydrogel networks with less crosslinks, which as expected resulted in greater swelling.[36]

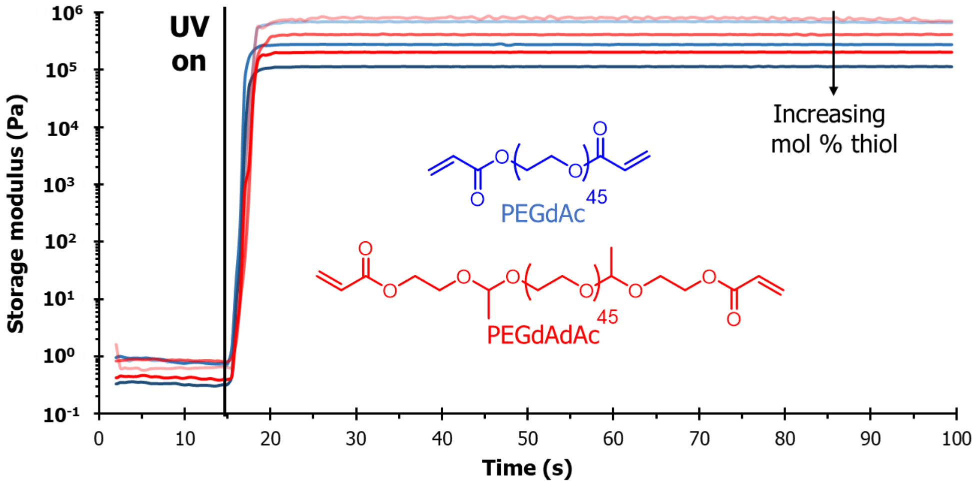

Figure 6.1. Acetal-functionalized PED2kdAdAc displays crossover times comparable to traditional acrylate functionalized PEGdAc. Λ = 300-450 nm, 10 mW/cm^2, irradiation starts at 15 s.

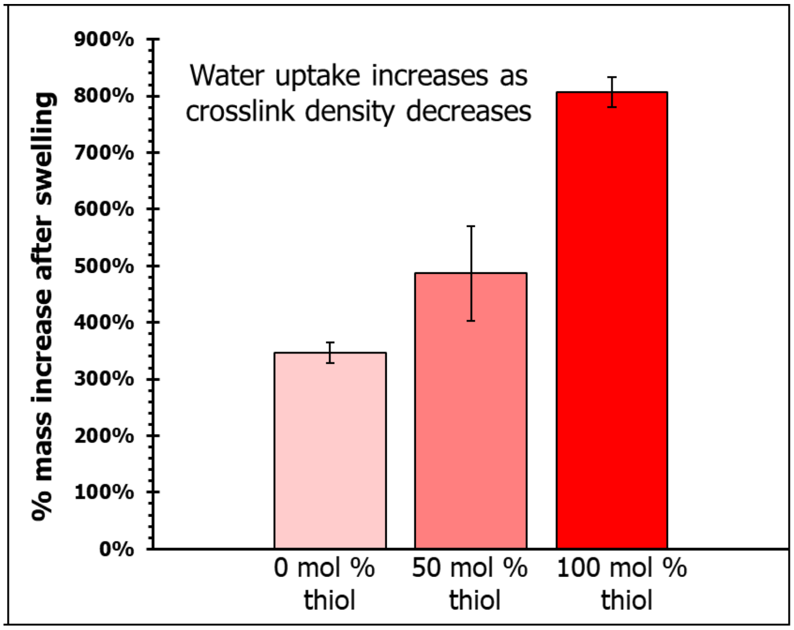

Figure 6.2. Water uptake in PBS increases as mol % thiol increases. Mass increase determined after swelling in PBS for 24 h.

DMA of the extracted and dried films provided further evidence that higher thiol mol % compositions decreased hydrogel crosslink density (**Figure 6.3**). Dried hydrogels prevented slippage and artifacts from drying during the DMA experiment. Samples were tested from room temperature as the plateau tensile modulus (E') after the PEG melting point I was of most interest. DMA highlighted semicrystallinity in each sample. And the measured T_ms were consistent with the T_m of PEG.[37] As the mol % thiol increased, E' also decreased. E' inversely relates to the molecular weight between crosslinks.[38] Films with larger mol % thiol exhibited a lower crosslink density, which ultimately increased the average molecular weight between crosslinks and thus decreased E'.

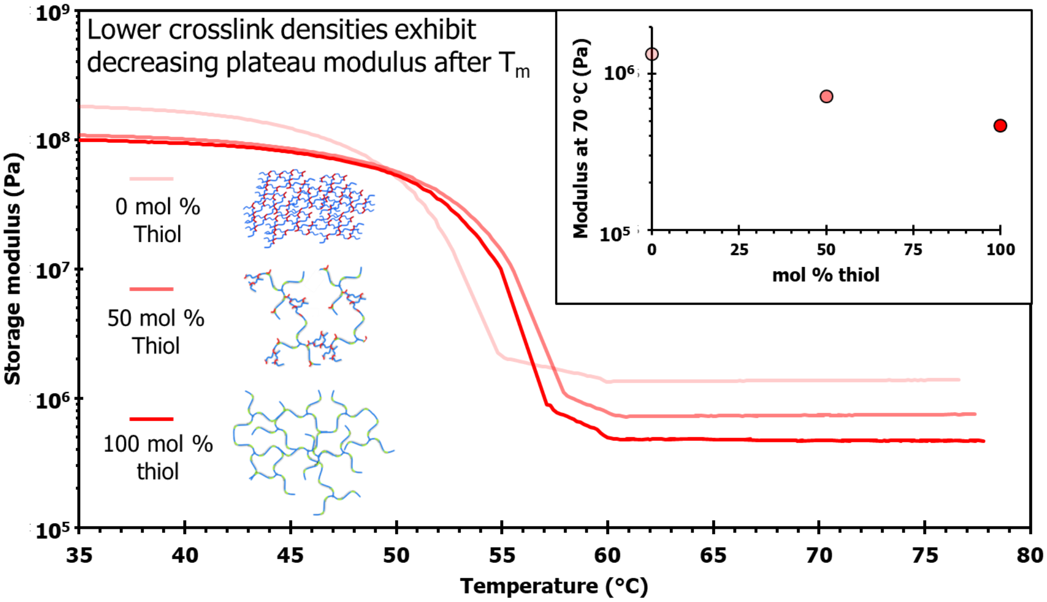

Figure 6.3. DMA revealed lower plateau moduli at 70 °C as the crosslink density decreased through the incorporation of the trifunctional crosslinker. 0.1 % strain, 1 Hz, 3 °C/min.

Differences in hydrogel compositions affected the covalent network architecture of the crosslinked hydrogels. Hydrogels with more acrylate homopolymerization contained higher crosslink densities and thus shorter distances between crosslinks as compared to the hydrogels, which were dominated by thiol-ene addition. SAXS measurements of the swollen hydrogels revealed a decreased intensity of the scattering peak (q) associated with the network spacing between highly crosslinked domains formed through the acrylate homopolymerization.[39] The prominence of the 6.16 nm spacing present in the fully acrylate homopolymerized (0 mol % thiol) sample decreased as the networks moved to a fully thiol-ene architecture (100 mol % thiol) whose domain spacing was outside of the SAXS detectable range seen in **Figure 6.4**. These highly crosslinked domains required more than one acetal hydrolysis event to disconnect an elastically active chain from the hydrogel network. Thus, it is expected that the high crosslink density domains provided a means to slow network degradation.

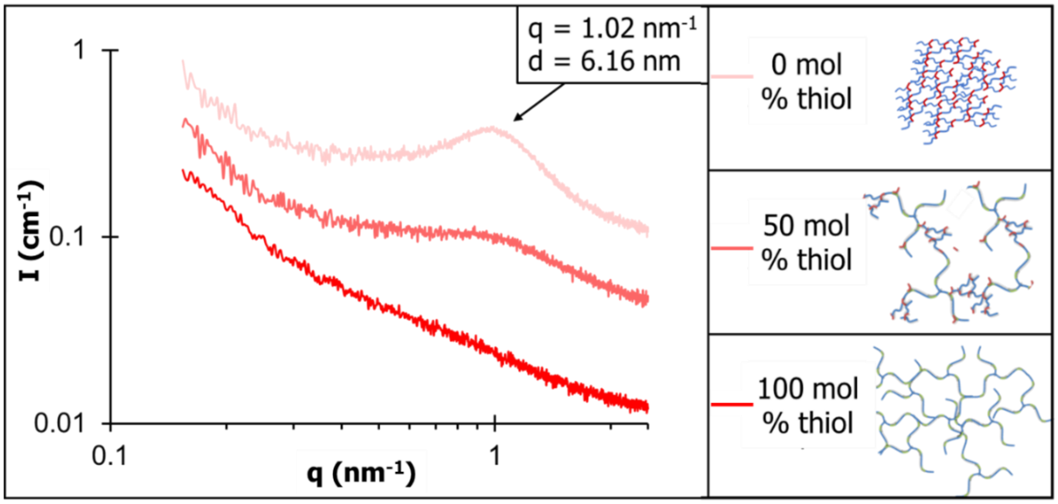

Figure 6.4. SAXS monitored the disappearance of the 6.16 nm interdomain spacing associated with the acrylate homopolymerized domains in swollen hydrogels. SAXS profiles vertically shifted for clarity.

Hydrogel samples were swollen with 0.005M Direct Red-81 solution to explore degradation rates as a function of thiol incorporation. This dye provided an opportunity to track degradation with a UV-Vis assay. Prior to quantitatively investigating the change in degradation rates as a function of thiol incorporation, two qualitative control experiments, which are shown in (**Figure S6.5**), probed degradation selectivity. First, the acetal-free PEGdAc control in citric acid buffer released a relatively low level of dye compared to the acetal-containing PEGdAdAc test groups in the first 48 h of submersion. This highlighted relatively fast acetal hydrolysis rates compared to ester hydrolysis. Furthermore, PEGdAdAc samples submerged in phosphate buffered saline (pH 7.4) showed dye release in agreement with the acetal-free control group. This dye release eventually reached equilibrium, and the gels remained intact for at least 3 mo (**Figure S6.6**). This result informs the long term stability of acetal-containing networks in neutral environments and selective hydrolysis in acidic environments. In contrast to the two controls, the PEGdAdAc samples submerged in citric acid buffer (pH 3.4) released a clearly distinguishable amount of Direct Red-81 dye. This experiment validated the dye release assay to track hydrogel degradation on these time scales.

Acetals degraded in an acidic environment which enabled hydrogel dissolution. UV-vis monitoring of released dye (λ = 500 nm) from degrading PEG2kdAdAc hydrogels submerged in a citric acid buffer established degradation profiles for the three different formulations plotted in **Figure 6.5**. All hydrogels displayed degradation profiles consistent with bulk degradation, and hydrogels without thiol-ene crosslinking displayed greater stability in the citric acid buffer.[40] The fully acrylate system established highly crosslinked domains due to the higher acrylate functionality when homopolymerized. In a thiol-ene system, the diacrylate is difunctional as an unsaturated site only reacted with a single thiol without further propagation. However, in the absence of thiols, a propagating acrylate radical formed, which initiated free radical polymerization where remaining diacrylates had a crosslinking functionality of four. This higher functionality provided high crosslink density areas within the covalent network. These highly crosslinked domains demand more network degradation, which allowed for controlled hydrogel degradation rates. Thus, tailored network architecture dictated degradation profiles in a manner consistent with the crosslinking mechanism, and the kinetics that drove network formation.[16, 19, 27, 40]

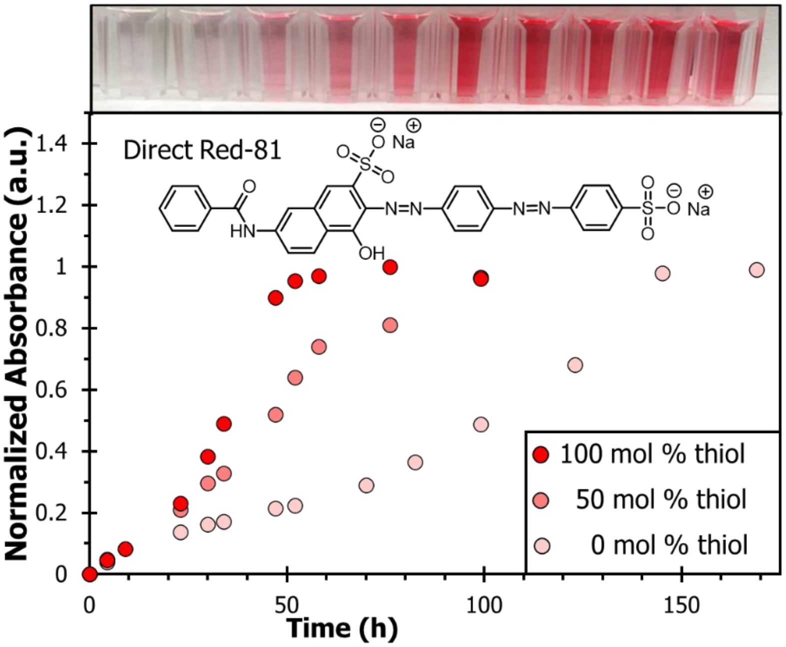

Figure 6.5. Normalized absorbance of Direct Red-81 dye released in citric acid buffer (pH=3.4, 25 °C) confirmed that the hydrogels with a low crosslink density degraded more rapidly than those with high crosslink densities.

6.4 Conclusions

A facile two-step synthesis yielded an acid-labile and photopolymerizable crosslinker. Binary thiol-acrylate photopolymerization of PEG2kdAdAc and Thiocure ® yielded a series of pH-sensitive hydrogels with varied crosslink densities. Stoichiometric offset of thiols and acrylates afforded a means to predict hydrogel crosslink densities and network morphologies. The acetal functionality enabled a direct means to explore network architecture effects on degradation in binary thiol-acrylate hydrogels. SAXS confirmed these network architecture variations and revealed an excess of acrylate formed a tightly crosslinked domain with a characteristic 6.16 nm domain spacing. This application of binary thiol-acrylate photopolymerization generated hydrogel networks with understood morphologies. Leveraging these two fundamental understandings informed novel material design with degradable functionality. These morphological differences affected hydrogel swelling, mechanical properties, and most importantly the hydrogel degradation profiles. Controlled degradation experiments revealed hydrogel degradation to be tunable from three days to two weeks while maintaining long term stability in neutral pH. This degradation was predictable from the chemical structure of the monomers and their unique reaction kinetics during photo-processing. Binary thiol acrylate photopolymerization of acetal-acrylate functionalized PEGs developed hydrogels with selective and tunable degradation.

6.5 Acknowledgements

The authors would like to thank both Arizona State University and Virginia Tech for their efforts to support collaboration of this work. We would also like to thank the Biodesign Institute for their continuous support of research within our group. We would also like to thank Garvit Nayyar for his contribution to the additive manufacturing presented in this work. This material is based in-part upon work supported by the National Science Foundation under Grant No. DMR-1809291. Any opinions, findings, and conclusions or recommendations expressed in this material are those of the author(s) and do not necessarily reflect the views of the National Science Foundation.

6.6 References

1. Jothimani, B.; Venkatachalapathy, B.; Karthikeyan, N.; Ravichandran, C., A review on versatile applications of degradable polymers. *Green Biopolymers and their Nanocomposites* **2019**, 403-422.

2. Binauld, S.; Stenzel, M. H., Acid-degradable polymers for drug delivery: a decade of innovation. *Chemical communications* **2013,** *49* (21), 2082-2102.

3. Mohanty, S.; Larsen, L. B.; Trifol, J.; Szabo, P.; Burri, H. V. R.; Canali, C.; Dufva, M.; Emnéus, J.; Wolff, A., Fabrication of scalable and structured tissue engineering scaffolds using water dissolvable sacrificial 3D printed moulds. *Materials science and engineering: C* **2015,** *55*, 569-578.

4. Tetsuka, H.; Shin, S. R., Materials and technical innovations in 3D printing in biomedical applications. *Journal of materials chemistry B* **2020,** *8* (15), 2930-2950.

5. Herzberger, J.; Sirrine, J. M.; Williams, C. B.; Long, T. E., Polymer Design for 3D Printing Elastomers: Recent Advances in Structure, Properties, and Printing. *Progress in Polymer Science* **2019,** *97*, 101144.

6. Weyhrich, C. W.; Long, T. E., Additive manufacturing of high-performance engineering polymers: present and future. *Polymer International* **2022,** *71* (5), 532-536.

7. Mondschein, R. J.; Kanitkar, A.; Williams, C. B.; Verbridge, S. S.; Long, T. E., Polymer structure-property requirements for stereolithographic 3D printing of soft tissue engineering scaffolds. *Biomaterials* **2017,** *140*, 170-188.

8. Cucciniello, R.; Anastas, P. T., Design for degradation or recycling for reuse? *Current Opinion in Green and Sustainable Chemistry* **2021,** *31*, 100528.

9. Schelhaas, M.; Waldmann, H., Protecting group strategies in organic synthesis. *Angewandte Chemie International Edition in English* **1996,** *35* (18), 2056-2083.

10. Brocchini, S. C. S., Polyacetals. *Natural and Synthetic Biomedical Polymers* **2014**, 219-233.

11. Kasprzak, C.; Brown, J. R.; Feller, K.; Scott, P. J.; Meenakshisundaram, V.; Williams, C.; Long, T., Vat Photopolymerization of Reinforced Styrene–Butadiene Elastomers: A Degradable Scaffold Approach. *ACS Applied Materials & Interfaces* **2022,** *14* (16), 18965-18973.

12. Lin, C. C.; Anseth, K. S., PEG hydrogels for the controlled release of biomolecules in regenerative medicine. *Pharm Res* **2009,** *26* (3), 631-43.

13. Peppas, N. A.; Hilt, J. Z.; Khademhosseini, A.; Langer, R., Hydrogels in biology and medicine: from molecular principles to bionanotechnology. *Advanced materials* **2006,** *18* (11), 1345-1360.

14. Pritchard, C. D.; O'Shea, T. M.; Siegwart, D. J.; Calo, E.; Anderson, D. G.; Reynolds, F. M.; Thomas, J. A.; Slotkin, J. R.; Woodard, E. J.; Langer, R., An injectable thiol-acrylate poly (ethylene glycol) hydrogel for sustained release of methylprednisolone sodium succinate. *Biomaterials* **2011,** *32* (2), 587-597.

15. Lin, C.-C.; Anseth, K. S., PEG hydrogels for the controlled release of biomolecules in regenerative medicine. *Pharmaceutical research* **2009,** *26* (3), 631-643.

16. Moon, N. G.; Pekkanen, A. M.; Long, T. E.; Showalter, T. N.; Libby, B., Thiol-Michael 'click'hydrogels as an imageable packing material for cancer therapy. *Polymer* **2017,** *125*, 66-75.

17. Mason, M. N.; Metters, A. T.; Bowman, C. N.; Anseth, K. S., Predicting controlled-release behavior of degradable PLA-b-PEG-b-PLA hydrogels. *Macromolecules* **2001,** *34* (13), 4630-4635.

18. Metters, A.; Hubbell, J., Network formation and degradation behavior of hydrogels formed by Michael-type addition reactions. *Biomacromolecules* **2005,** *6* (1), 290-301.

19. Worm, M.; Leibig, D.; Dingels, C.; Frey, H., Cleavable polyethylene glycol: 3, 4-epoxy-1-butene as a comonomer to establish degradability at physiologically relevant pH. *ACS Macro Letters* **2016,** *5* (12), 1357-1363.

20. Samanta, S.; Bogdanowicz, D. R.; Lu, H. H.; Koberstein, J. T., Polyacetals: Water-Soluble, pH-Degradable Polymers with Extraordinary Temperature Response. *Macromolecules* **2016,** *49* (5), 1858-1864.

21. Marchitti, S. A.; Brocker, C.; Stagos, D.; Vasiliou, V., Non-P450 aldehyde oxidizing enzymes: the aldehyde dehydrogenase superfamily. *Expert Opin Drug Metab Toxicol* **2008,** *4* (6), 697-720.

22. Crabb, D. W.; Matsumoto, M.; Chang, D.; You, M., Overview of the role of alcohol dehydrogenase and aldehyde dehydrogenase and their variants in the genesis of alcohol-related pathology. *Proceedings of the Nutrition Society* **2007,** *63* (01), 49-63.

23. Cai, Z.; Wan, Y.; Becker, M. L.; Long, Y.-Z.; Dean, D., Poly (propylene fumarate)-based materials: Synthesis, functionalization, properties, device fabrication and biomedical applications. *Biomaterials* **2019,** *208*, 45-71.

24. Zhang, J.; Xiao, P., 3D printing of photopolymers. *Polymer Chemistry* **2018,** *9* (13), 1530-1540.

25. Scott, P. J.; Meenakshisundaram, V.; Hegde, M.; Kasprzak, C. R.; Winkler, C. R.; Feller, K. D.; Williams, C. B.; Long, T. E., 3D printing latex: a route to complex geometries of high molecular weight polymers. *ACS applied materials & interfaces* **2020,** *12* (9), 10918-10928.

26. Leonards, H.; Engelhardt, S.; Hoffmann, A.; Pongratz, L.; Schriever, S.; Bläsius, J.; Wehner, M. M.; Gillner, A. In *Advantages and drawbacks of Thiol-ene based resins for 3D-printing*, Laser 3D Manufacturing II, SPIE: 2015; pp 52-58.

27. Cook, C. C.; Fong, E. J.; Schwartz, J. J.; Porcincula, D. H.; Kaczmarek, A. C.; Oakdale, J. S.; Moran, B. D.; Champley, K. M.; Rackson, C. M.; Muralidharan, A., Highly tunable thiol-ene photoresins for volumetric additive manufacturing. *Advanced Materials* **2020,** *32* (47), 2003376.

28. Rydholm, A. E.; Reddy, S. K.; Anseth, K. S.; Bowman, C. N., Controlling network structure in degradable thiol− acrylate biomaterials to tune mass loss behavior. *Biomacromolecules* **2006,** *7* (10), 2827-2836.

29. Hoyle, C. E.; Bowman, C. N., Thiol–ene click chemistry. *Angewandte Chemie International Edition* **2010,** *49* (9), 1540-1573.

30. Rydholm, A. E.; Anseth, K. S.; Bowman, C. N., Effects of neighboring sulfides and pH on ester hydrolysis in thiol-acrylate photopolymers. *Acta Biomater* **2007,** *3* (4), 449-55.

31. Rydholm, A. E.; Reddy, S. K.; Anseth, K. S.; Bowman, C. N., Development and Characterization of Degradable Thiol-Allyl Ether Photopolymers. *Polymer (Guildf)* **2007,** *48* (15), 4589-4600.

32. Jiang, T.; He, Y.; Jian, Y.; Nie, J., Exploration for decreasing the volume shrinkage for photopolymerization. *Progress in Organic Coatings* **2012,** *75* (4), 398-403.

33. Tierney, C. M.; Haugh, M. G.; Liedl, J.; Mulcahy, F.; Hayes, B.; O'Brien, F. J., The effects of collagen concentration and crosslink density on the biological, structural and mechanical properties of collagen-GAG scaffolds for bone tissue engineering. *Journal of the mechanical behavior of biomedical materials* **2009,** *2* (2), 202-209.

34. Krongauz, V. V., Crosslink density dependence of polymer degradation kinetics: photocrosslinked acrylates. *Thermochimica Acta* **2010,** *503*, 70-84.

35. Khalfa, A. L.; Becker, M. L.; Dove, A. P., Stereochemistry-controlled mechanical properties and degradation in 3D-printable photosets. *Journal of the American Chemical Society* **2021,** *143* (42), 17510-17516.

36. Hoti, G.; Caldera, F.; Cecone, C.; Rubin Pedrazzo, A.; Anceschi, A.; Appleton, S. L.; Khazaei Monfared, Y.; Trotta, F., Effect of the cross-linking density on the swelling and rheological behavior of Ester-bridged β-cyclodextrin nanosponges. *Materials* **2021,** *14* (3), 478.

37. D'souza, A. A.; Shegokar, R., Polyethylene glycol (PEG): a versatile polymer for pharmaceutical applications. *Expert opinion on drug delivery* **2016,** *13* (9), 1257-1275.

38. Sirrine, J. M.; Meenakshisundaram, V.; Moon, N. G.; Scott, P. J.; Mondschein, R. J.; Weiseman, T. F.; Williams, C. B.; Long, T. E., Functional siloxanes with photo-activated, simultaneous chain extension and crosslinking for lithography-based 3D printing. *Polymer* **2018,** *152*, 25-34.

39. Jones, B. H.; Alam, T. M.; Lee, S.; Celina, M. C.; Allers, J. P.; Park, S.; Chen, L.; Martinez, E. J.; Unangst, J. L., Curing behavior, chain dynamics, and microstructure of high Tg thiol-acrylate networks with systematically varied network heterogeneity. *Polymer* **2020,** *205*, 122783.

40. Martens, P.; Metters, A. T.; Anseth, K. S.; Bowman, C. N., A Generalized Bulk-Degradation Model for Hydrogel Networks Formed from Multivinyl Cross-linking Molecules. *The Journal of Physical Chemistry B* **2001,** *105* (22), 5131-5138.

6.7 Supplemental Information

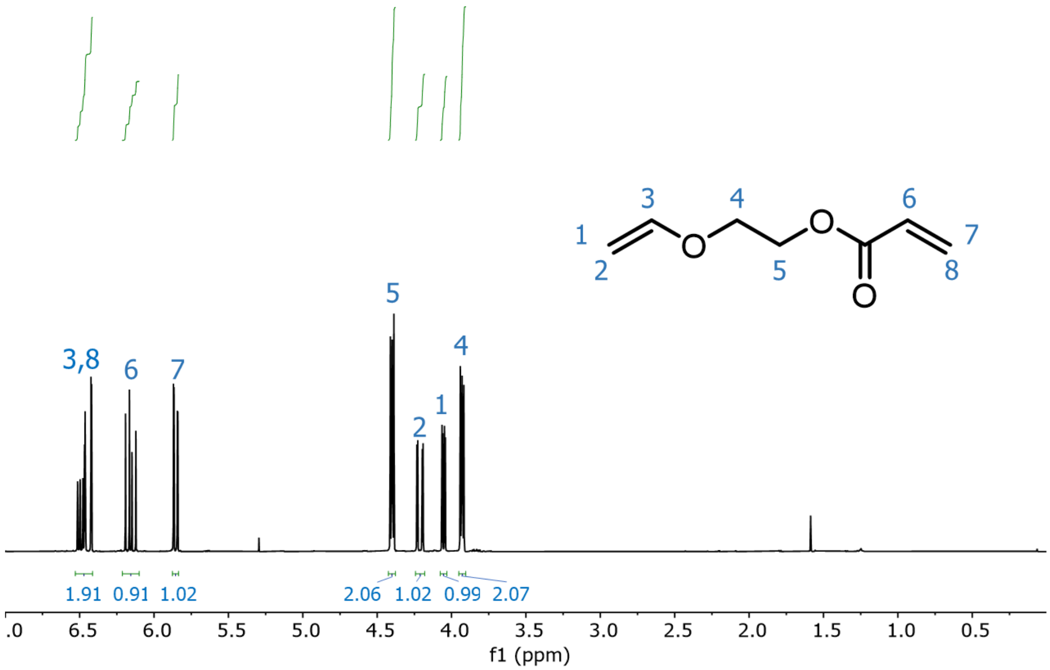

Figure S6.1. ^{1}H NMR of 2-(vinyloxy)ethyl acrylate

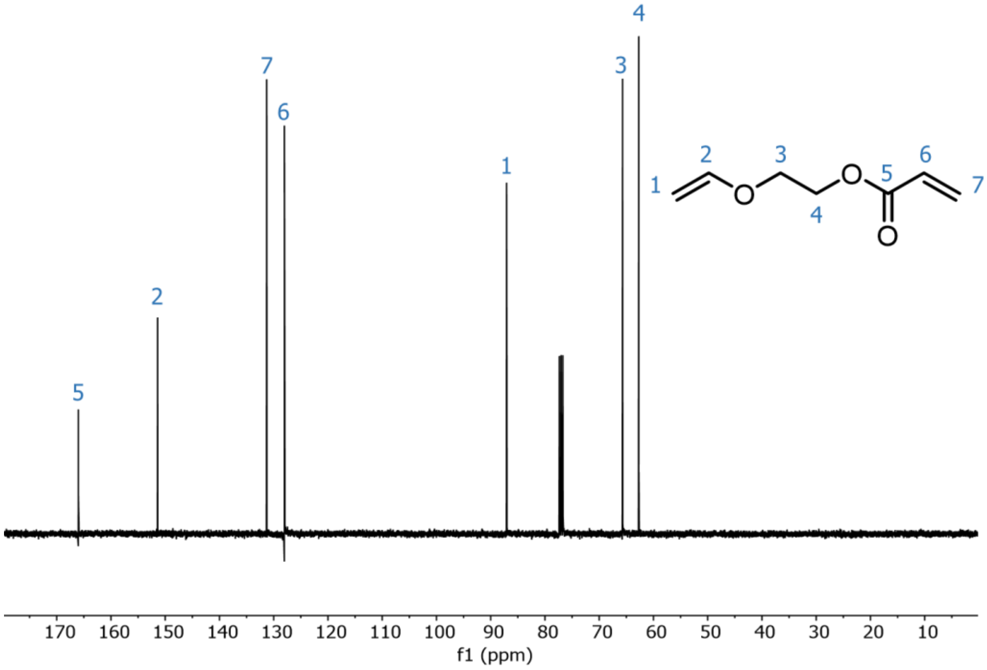

Figure S6.2. ^{13}C NMR of 2-(vinyloxy)ethyl acrylate

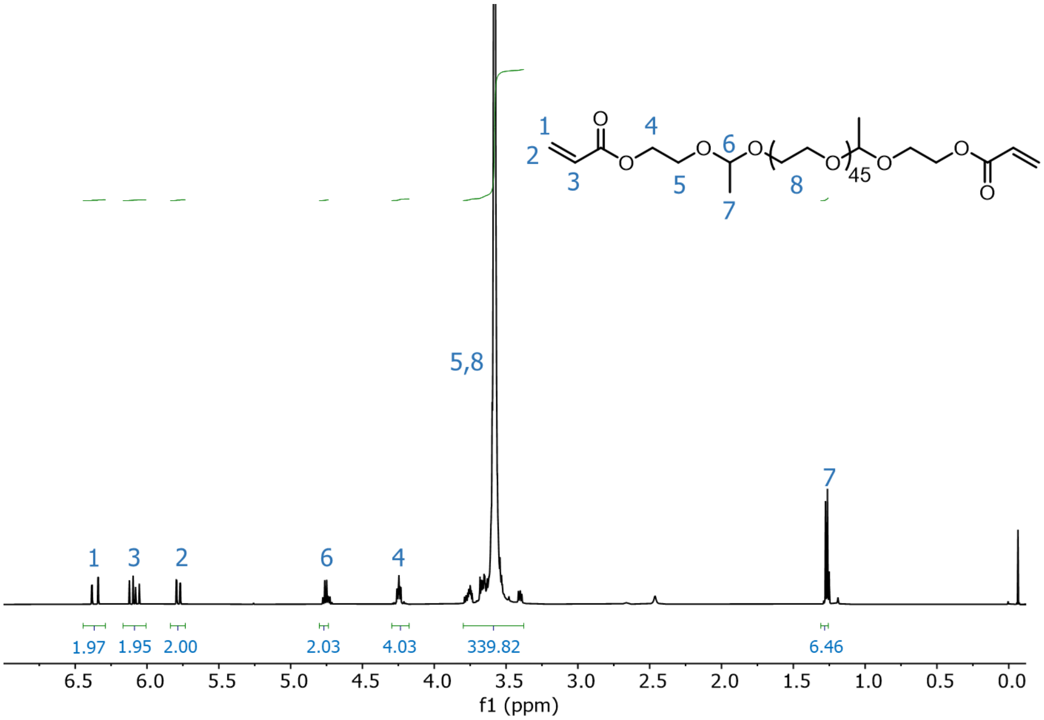

Figure S6.3. ^{1}H NMR of PEG 2k diacetal diacrylate (PEG2kdAdAc)

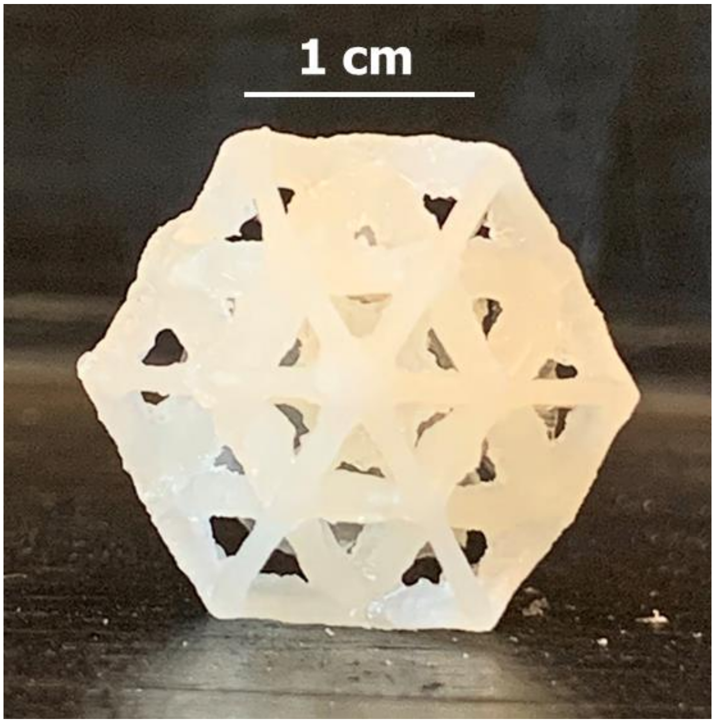

Figure S6.4. 3D part with complex geometries printed with PEG2kdAdAc crosslinker.

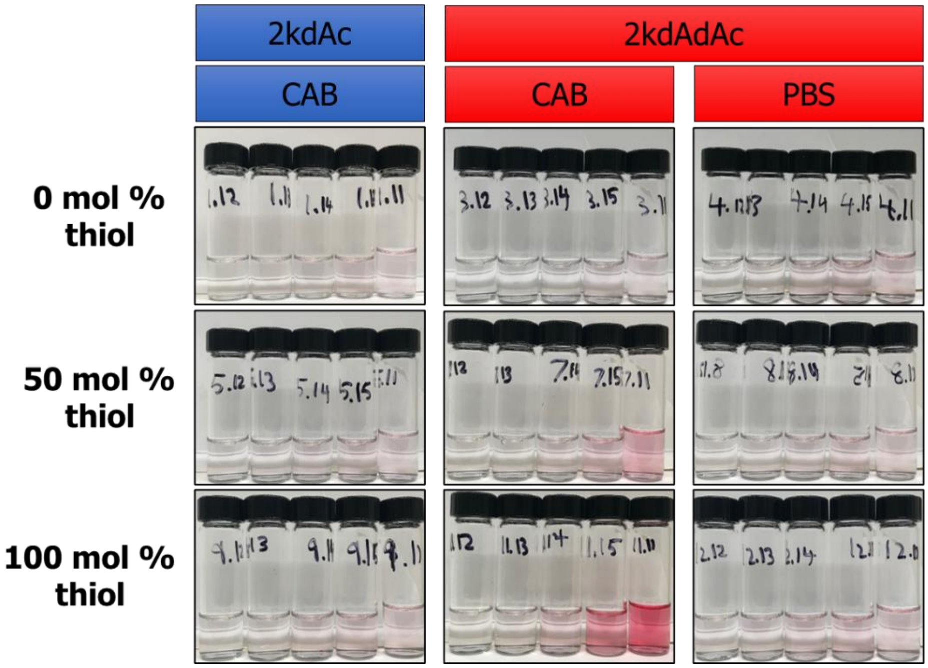

Figure S6.5. Degradation control experiments highlight the necessity of the acetal functionality for acidic degradation in citric acid buffer and reveal relatively small amounts of dye release from diffusion out of the hydrogel in phosphate buffered saline.

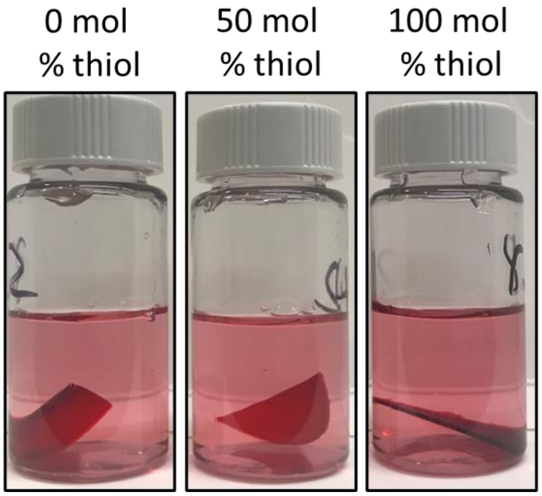

Figure S6.6. Hydrogel samples remained intact after 3 mo of submersion in phosphate buffered saline.

CHAPTER 7

PHOTO-ACID GENERATORS FOR PHOTOCURABLE DEGRADABLE ACETAL NETWORKS

7.1 Introduction

Recyclable networks provide an opportunity for closed loop processing infrastructures. Materials designed for depolymerization and subsequent reprocessing provide critical platforms for a sustainable materials economy. The photoresist industry presents an opportunity to expand upon existing technologies to establish more sustainable manufacturing processes based on closed loop circular economies. This field has intentionally designed materials for depolymerization in negative photoresist technologies for many years, but little work has focused on leveraging this depolymerized material for reprocessing.[1] An upcyclable material composition will extend material lifetime to multiple reprocessing steps, which will reduce waste .

Lithography is a widely used technique in the semiconductor industry for patterning features on the surface of materials.[2] This technique involves using a lithographic mask to selectively expose a photosensitive precursor to transfer a pattern onto a substrate. The photoreactive precursor, also known as a photoresist, undergoes a chemical reaction upon exposure to light. There are two main types of photoresists in lithographic applications, either a positive resist or negative resist, which differ in their response to exposure. In positive photoresists, exposure to light causes depolymerization in the photoresist which results in a positive image of the pattern on the substrate.[2,3] In contrast, exposure to light in negative photoresists causes the photoresist to polymerize or covalently crosslink, which results in a negative image of the pattern on the substrate. Positive photoresists provide an opportunity for recovery of depolymerized material and subsequent reuse.

Acetal functionalization demonstrates a common protecting group strategy in synthetic organic chemistry owing to its facile and selective degradation, and its return to hydroxyl starting functionality.[4,5] Thus, it is an attractive functionality for circular processes as its degradation products remain viable for reuse. The acetal is hydrolytically stable at pH greater than 6.5. However, it is readily hydrolysable at lower pHs in the presence of water. Polyacetals are commonly synthesized via the nucleophilic addition of a hydroxyl group to a resonance stabilized protonated vinyl ether.[6,7] Depolymerization of acetals synthesized in this manner return to hydroxyl monomers and crosslinkers with minimal mass loss through the loss of volatile acetaldehyde. These hydroxyl monomers and crosslinkers can easily be recovered as the biproduct of degradation leaves as a gas. Subsequently, additional vinyl ether monomers can be added and the material can be recycled. However, as this material undergoes recycling in this manner, the average crosslinker functionality decreases which will cause a decrease in mechanical properties during each recycling.

Vinyl ether monomers and crosslinkers undergo cationic polymerization in the presence of an acid catalyst as shown in **Scheme 7.1**.[8] Additionally, when a hydroxyl group is present, the resonance stabilized carbocation intermediate serves as an electrophile. The nucleophilic addition of the hydroxyl group yields a readily hydrolysable acetal linkage. However, the product of vinyl ether homopolymerization is a stable carbon-carbon bond. During photoacid catalysis of systems with both vinyl ether and hydroxyl functional groups, both competing reactions occur.[9,10] However, the kinetics of these competing reactions remain unexplored. Changes in the stoichiometric ratio between hydroxyl and vinyl ether functional groups thus change the total hydrolysability of the entire covalent network. Excess vinyl ethers will form non-hydrolysable domains within the network. After hydrolysis of the acetals within the network, these stable domains provide hydroxyl crosslinkers with high functionalities. These degradation products will provide networks with higher crosslink densities after recharging with additional divinyl ether monomers.

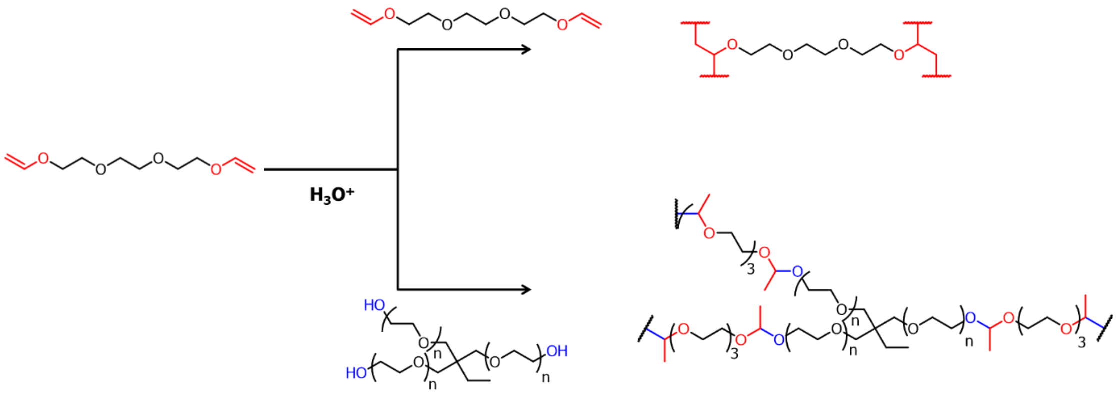

Scheme 7.1. Vinyl ethers react through both cationic homopolymerization with other vinyl ether monomers (top) and nucleophilic attack from hydroxyl functionalities (bottom), which provides control over the crosslink density of organogels.

This work explores the fundamental reactivity and mechanical properties of a series of acetal functionalized organogels developed from photo-acid generator (PAG) catalyzed acetal formation. The effects of PAG loading on crossover times and network mechanical properties are explored. Additionally, stoichiometric excess of vinyl ethers in precursor formulations leveraged cationic vinyl ether homopolymerization to increase the storage modulus and decrease the degradability of the hydrogel. Time-resolved spectroscopy identified reaction kinetics in these competing reaction pathways during photopolymerization. Stabilization strategies addressed the inherent instability of acid-sensitive networks developed through acid catalysis. The results are discussed in the context of identifying critical fundamental aspects of acetal functionalized photoresists developed via photo acid generation.

7.2 Materials and methods

7.2.1 Materials

Triarylsulfonium hexafluorphosphate, triethylene glycol divinyl ether (TEGDVE), trimethylol propane ethoxylate M_n= 450 g/mol (TMPE), cyclohexanedimethanol divinyl ether (CHDMDVE), butane diol divinyl ether (BDDVE), and triethylamine were purchased from Sigma Aldrich and used as received. Optima grade HPLC water was purchased from Fischer Scientific and used without further purification.

7.2.2 Photorheological analysis

Photorheology experiments were conducted on a TA Instruments DHR-2 rheometer equipped with a UV-curing accessory. Oscillatory time sweep experiments were conducted with a 20 mm parallel plate geometry and sample at 0.1% strain and a frequency of 1 1/s. UV light was delivered from an Omnicure S2000 lamp attached to the UV-curing accessory through a liquid light guide. UV intensity was calibrated with a Silverline UV radiometer prior to experimentation.

7.2.3 Basic hydrogel stabilization and gel fraction characterization

Following select photorheology experiments, crosslinked gels were immediately removed from the rheometer geometry and submerged in a 5 wt.% aqueous solution of triethylamine for 1 h. Following stabilization, gels were dried at room temperature in a vacuum oven under a reduced pressure of 30 mmHg for 24 h. Dried gels were weighed on an analytical balance prior to Soxhlet extraction in methanol. Following three Soxhlet extraction cycles, the hydrogels were again weighed, and gel fractions were determined by dividing the final mass by the initial mass.

7.2.4 Time resolved UV FT-IR spectroscopy

Time resolved UV FT-IR spectroscopy was conducted on a Thermofisher Nicolet iS50 FT-IR spectrometer equipped with a Pike ATR stage, which afforded UV irradiation from beneath the ATR stage. A single drop of photopolymerizable solution was placed on the stage and irradiated throughout the course of the experiment. Data was recorded with a time resolution of 1 s.

7.3 Results and discussion

Triarylsulfonium hexafluorophosphate PAG afforded photo-crosslinkable solutions when combined with TMPE and TEGDVE. Primary photorheology experiments explored the effects of UV exposure and PAG wt % loading while keeping the hydroxyl to vinyl ether molar ratio constant at 1:1. These experiments, summarized in **Figure 7.1**, established a working curve which predicted crossover times as a function of relative acid generation (RAG). The arithmetic product of wt.% PAG loading, UV intensity measured in mW/cm^2, and the UV exposure time calculated RAG values as shown in **Equation 7.1**. In summary, these experiments revealed a minimum achievable crossover time of 15s when the hydroxyl to vinyl ether molar ratio was 1:1. This crossover time was consistent after RAG values equal to 5000. When the molar ratio is 1:1, step growth kinetics dominate the reactions leading to network formation. As a result, the network molecular weight remains small at lower conversions before reaching sufficient conversions to establish a crosslinked gel. Thus, the gel forming reaction becomes diffusion limited at high catalyst loadings or high UV exposures and crossover times can not be lowered beneath 15 s. Furthermore, it is important to note that dark polymerization occurs in PAG systems as the catalytic species remains stable under the photorheology experimental conditions.[11]

Equation 7.1

$$\boldsymbol{R.A.G. = wt.\%\ PAG\ x\ UV\ Intensity\ \left(\frac{mW}{cm^2}\right) x\ Exposure\ time\ (s)}$$

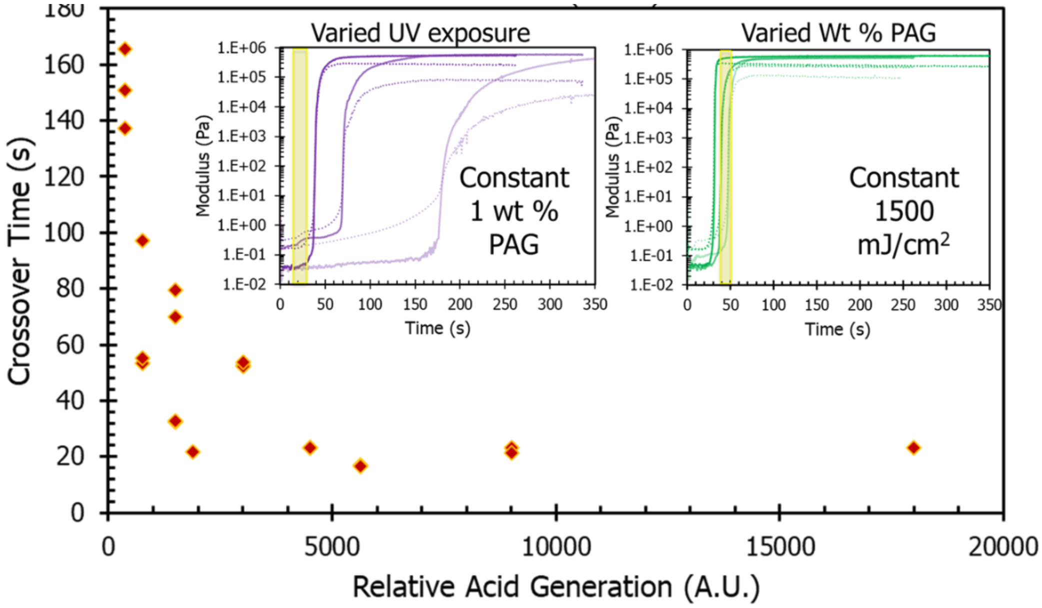

Figure 7.1. photoacid generator amount and UV exposure effects on crossover time

Furthermore, these initial tests revealed material property trends as a function of differing crossover times. The plateau storage modulus remained constant regardless of crossover times as shown in **Figure 7.2**. However, the plateau loss modulus decreased in samples with longer crossover times. A higher loss modulus indicates the presence of more dangling chain ends and elastically inactive chains which act as network defects.[12] On the other hand, a lower loss modulus suggests more elastically active chains incorporated in the covalent network, and a more homogenous network with less defects. This is consistent with other step growth gelation processes with fast crossover times.[13] Thus, when considering processing applications, achieving a minimum crossover time must also be balanced with producing a satisfactorily homogenous network if loss modulus effects are critical to the application. These experiments informed subsequent photoreactive monomer mixtures to be prepared with 1 wt % PAG, 100 mW/cm^2 UV intensity, and a 15 s exposure time.

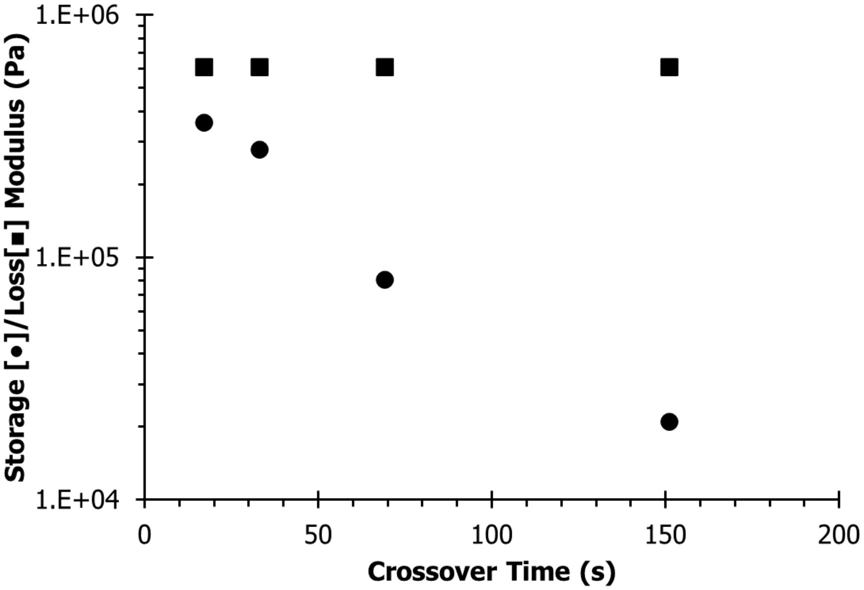

Figure 7.2. loss modulus vs crossover time for PAG catalyzed acetal networks developed from triethylene glycol divinyl ether and TMPE.

Variations in vinyl ether to hydroxyl molar ratio provided a means to predict the plateau storage modulus. Excess vinyl ether monomers undergo cationic homopolymerization forming carbon-carbon bonds within the crosslinked network. Additionally, when TEGDVE monomer reacts in this manner, the crosslinking functionality increased to 4 as opposed to 2 in the acetal forming reaction with TMPE. As a result, this reaction pathway provided a more tightly crosslinked network, which ultimately resulted in higher plateau storage moduli shown in **Figure 7.3**. This is consistent with other crosslinking systems containing both step growth and chain growth gelation mechanisms.[6] Across the tested range of stoichiometric ratios from 1:1 to 4:1 vinyl ether:hydroxyl, the plateau storage modulus increased from 4 x 10^5 Pa to 4 x 10^6 Pa. This provided a means to tune material hardness across an order of magnitude.

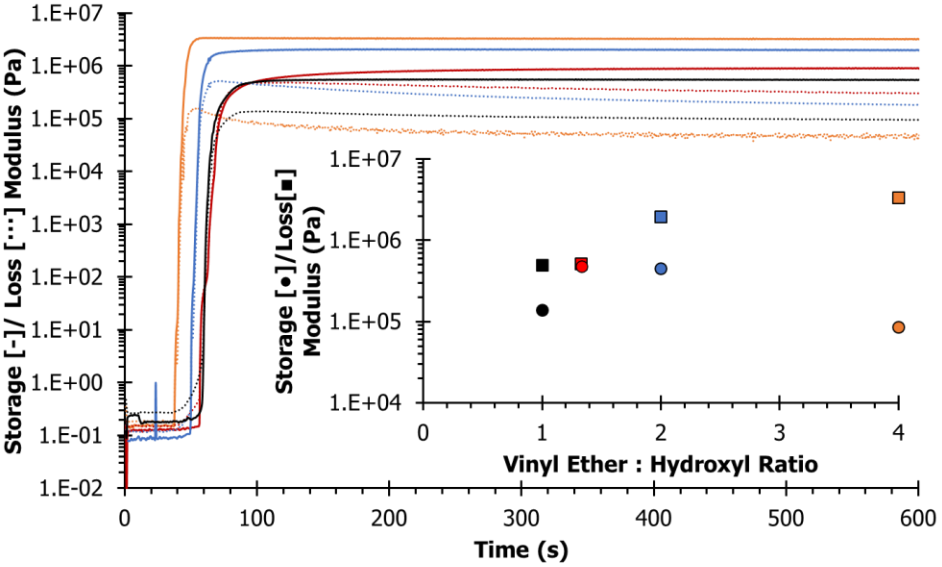

Figure 7.3. Photorheology with different amounts of TEGDVE

During crosslinking in the presence of additional vinyl ether monomers, both cationic photopolymerization of vinyl ethers and hydroxyl addition to vinyl ethers occurred. However, it remained unknown if these reactions occurred concurrently, or in a subsequent fashion. Time resolved FT-IR spectroscopy, shown in **Figure 7.4**, monitored C=C stretch at associated with the vinyl ether functionality at 1620 cm^{-1} and the O-H stretch associated with the hydroxyl functionality at 3470 cm^{-1}.[14] Samples were illuminated with UV irradiation from the bottom of the ATR stage as shown in **Figure S7.1**. These experiments revealed the rate of vinyl ether and hydroxyl conversion to be equivalent across all stoichiometric ratios of vinyl ether and hydroxyl functionalities. This demonstrated both vinyl ether homopolymerization and hydroxyl addition to the vinyl ether group to occur concurrently during gel formation.

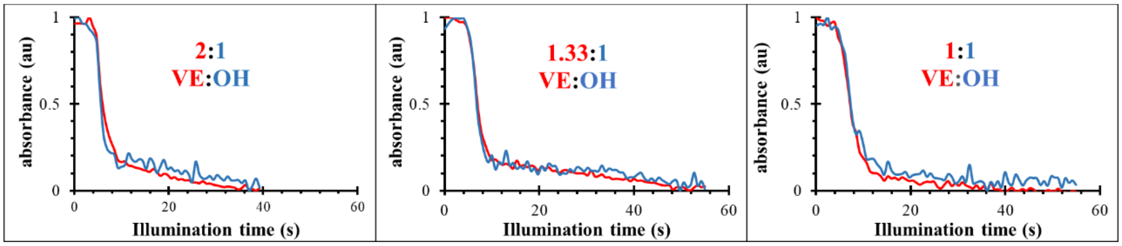

Figure 7.4. photo FTIR of vinyl ether hydroxyl crosslinking with varied stoichiometry

Crosslinked acetal networks demonstrated significant instability following photopolymerization. Residual acid from the PAG catalyzed network formation catalyzed hydrolysis of acetal linkages which lead to full film degradation in only 12 h in ambient humidity. This degradation caused crosslinked films to degrade into liquid monomers following acetal hydrolysis, as shown in **Figure 7.5**. A simple neutralization in 5 wt.% aqueous triethylamine rendered stable hydrogels that no longer demonstrated depolymerization on the bench top. This highlights acetal functional group stability at neutral or slightly basic conditions. Further investigations will optimize this neutralization step to prevent film warpage, swelling, and cracking, which was occasionally observed during the neutralization step.

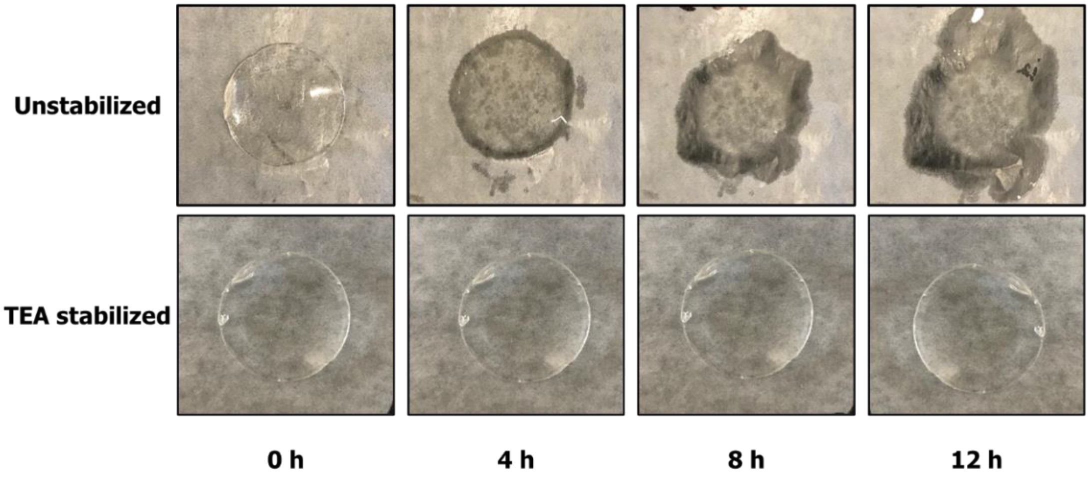

Figure 7.5. Time lapse pictures of crosslinked TEGDVE TMPE gels with (bottom) and without (top) TEA stabilization highlight degradation caused by residual PAG.

Following triethylamine stabilization, the hydrogels remained stable affording subsequent characterizations such as gel fraction determination. The gel fraction is the ratio of retained mass after extraction to the initial hydrogel mass prior to extraction. This measurement informs the amount of material covalently bound within the crosslinked networks. **Figure 7.6** highlights that all TMPE TEGDVE hydrogels displayed gel fractions on the order of 90 % across different vinyl ether: hydroxyl ratios. Differences in average gel fractions across this series fell within the standard deviation between samples. Thus, there is no significant change in gel fraction as additional TEGDVE is incorporated in hydrogel formulation.

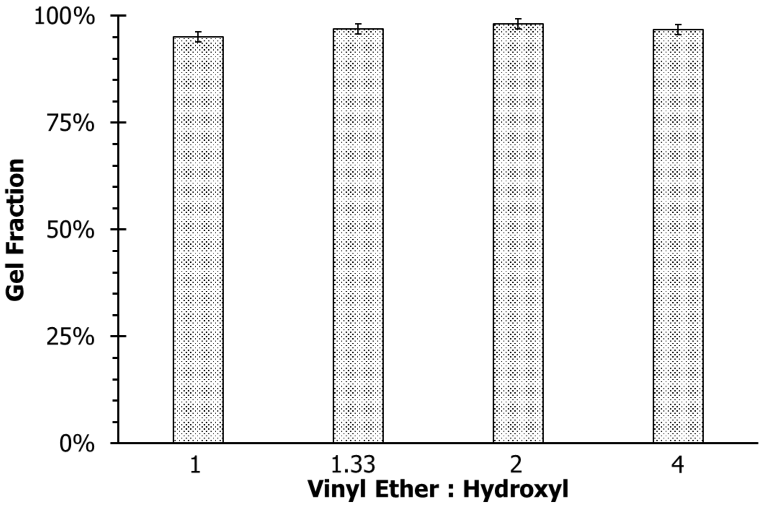

Figure 7.6. Gels display large gel fractions after stabilization in TEA with across vinyl ether incorporation.

In addition to TMPE TEGDVE based hydrogels, photorheology experiments assessed PAG catalyzed photo-processability with two other divinyl ether monomers. Hydroxyl:vinyl ether ratios were maintained at 1:1 when assessing these monomers photoprocessability. **Figure 7.7** demonstrates divinyl monomer effects plateau storage modulus, plateau loss modulus, and crossover times. All divinyl monomers demonstrated similar crossover times, which indicated consistent reactivity between different monomers. However, butane diol divinyl ether (BDDVE) achieved a slightly higher plateau storage modulus than TEGDVE whereas cyclohexane dimethanol divinyl ether (CHDMDVE) reached a significantly lower plateau modulus below 10^4 pa. This decreased performance renders CHDMVE unsuitable for lithographic applications, which require plateau moduli exceeding number. The cause of this significant modulus decrease remains the interest of future work to fully understand structure property relationships in PAG catalyzed hydroxyl:vinyl ether crosslinking systems.

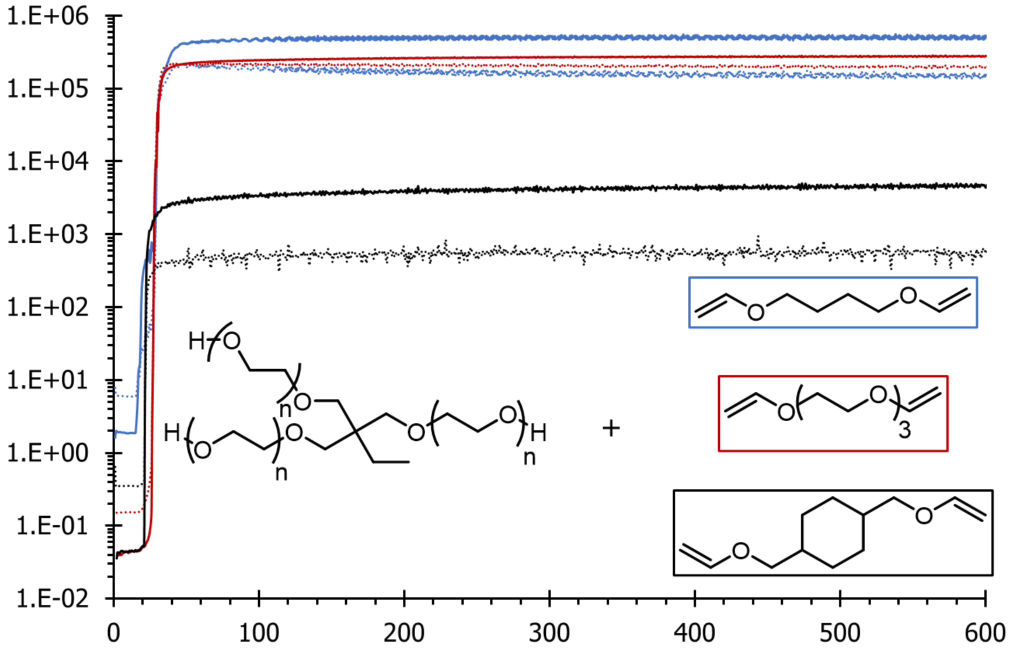

Figure 7.7. different vinyl ether monomers also provide covalently crosslinked gels in the presence of triarylsulfonium PAG.

7.4 Conclusion

Triarylsulfonium hexafluorophosphate proved to be a viable photoacid generator to catalyze the acetal forming hydroxyl addition to vinyl ether monomers. This developed covalently crosslinked thermosets with degradable acetal functionality installed at the crosslinking sites. Increased catalyst loading decreased the crossover time of this poho-initiated reaction, but these faster crossover times also decreased the storage modulus, which highlights the presence of elastically inactive polymer chains in the network. Additionally, this PAG also catalyzed cationic vinyl ether homopolymerization, which provided a means to increase the cured storage modulus of thermosets when the molar equivalents of vinyl ether functional groups were greater than the molar equivalents of hydroxyl functional groups. Time-resolved FT-IR experiments revealed the hydroxyl addition to the vinyl ether and the cationic polymerization of the vinyl ether to occur simultaneously and not in a stepwise fashion. Acetal crosslinked gels remained unstable due to the remaining PAG after crosslinking. However, neutralization in aqueous TEA provided gels with high gel fractions. Future work will explore the recyclability of these covalent networks for closed loop manufacturing processes.

7.5 References

1. Manouras, T.; Argitis, P. High Sensitivity Resists for EUV Lithography: A Review of Material Design Strategies and Performance Results. *Nanomaterials 2020, Vol. 10, Page 1593* **2020**, *10* (8), 1593. https://doi.org/10.3390/NANO10081593.

2. Bratton, D.; Yang, D.; Dai, J.; Ober, C. K. Recent Progress in High Resolution Lithography. *Polym Adv Technol* **2006**, *17* (2), 94–103. https://doi.org/10.1002/PAT.662.

3. Luo, C.; Xu, C.; Lv, L.; Li, H.; Huang, X.; Liu, W. Review of Recent Advances in Inorganic Photoresists. *RSC Adv* **2020**, *10* (14), 8385–8395. https://doi.org/10.1039/C9RA08977B.

4. Baek, J.; Kim, M.; Park, Y.; Kim, B. S. Acetal-Based Functional Epoxide Monomers: Polymerizations and Applications. *Macromol Biosci* **2021**, *21* (11), 2100251. https://doi.org/10.1002/MABI.202100251.

5. Kisla, M. M.; Hassan, M. A.-K.; Osman, H. M.; Aydin, A. S.; Sen, H. T.; Khazei, S.; Kul, P.; Kuş, C. Incorporation of Protecting Groups in Organic Chemistry: A Mini-Review. *Curr Org Synth* **2022**, *20* (5), 491–503. https://doi.org/10.2174/1570179419666220820152723.

6. Brown, J. R.; Herzberger, J.; Spiering, G. A.; Wilts, E.; Moore, R. B.; Long, T. E. Binary Thiol-Acrylate Photopolymerization for the Design of Degradable Acetal-Functionalized Hydrogels. *ACS Appl Polym Mater* **2022**, *5*, 1030–1036. https://doi.org/10.1021/ACSAPM.2C01978/ASSET/IMAGES/LARGE/AP2C01978_0006.JPEG.

7. Dingels, C.; Müller, S. S.; Steinbach, T.; Tonhauser, C.; Frey, H. Universal Concept for the Implementation of a Single Cleavable Unit at Tunable Position in Functional Poly(Ethylene Glycol)s. *Biomacromolecules* **2013**, *14* (2), 448–459. https://doi.org/10.1021/BM3016797/SUPPL_FILE/BM3016797_SI_001.PDF.

8. Kottisch, V.; Michaudel, Q.; Fors, B. P. Cationic Polymerization of Vinyl Ethers Controlled by Visible Light. *J Am Chem Soc* **2016**, *138* (48), 15535–15538. https://doi.org/10.1021/JACS.6B10150/ASSET/IMAGES/LARGE/JA-2016-10150B_0004.JPEG.

9. Decker, C.; Bianchi, C.; Decker, D.; Morel, F. Photoinitiated Polymerization of Vinyl Ether-Based Systems. *Prog Org Coat* **2001**, *42* (3–4), 253–266. https://doi.org/10.1016/S0300-9440(01)00203-X.

10. K Rajaraman, S. S.; Mowers, W. A.; Crivello, J. V. Interaction of Epoxy and Vinyl Ethers During Photoinitiated Cationic Polymerization. *J Polym Sci A: Polym Chem* **1999**, *37*, 4007–4018. https://doi.org/10.1002/(SICI)1099-0518(19991101)37:21.

11. Michaudel, Q.; Kottisch, V.; Fors, B. P. Cationic Polymerization: From Photoinitiation to Photocontrol. *Angewandte Chemie International Edition* **2017**, *56* (33), 9670–9679. https://doi.org/10.1002/ANIE.201701425.

12. Shen, J.; Lin, X.; Liu, J.; Li, X. Effects of Cross-Link Density and Distribution on Static and Dynamic Properties of Chemically Cross-Linked Polymers. *Macromolecules* **2019**, *52* (1), 121–134. https://doi.org/10.1021/ACS.MACROMOL.8B01389/ASSET/IMAGES/LARGE/MA-2018-01389Y_0010.JPEG.

13. Shih, H.; Lin, C. C. Cross-Linking and Degradation of Step-Growth Hydrogels Formed by Thiol-Ene Photoclick Chemistry. *Biomacromolecules* **2012**, *13* (7), 2003–2012. https://doi.org/10.1021/BM300752J/ASSET/IMAGES/LARGE/BM-2012-00752J_0011.JPEG.

14. George Socrates. *Infrared and Raman Characteristic Group Frequencies: Tables and Charts*; John Wiley & sons, 2004.

7.6 Supplemental information

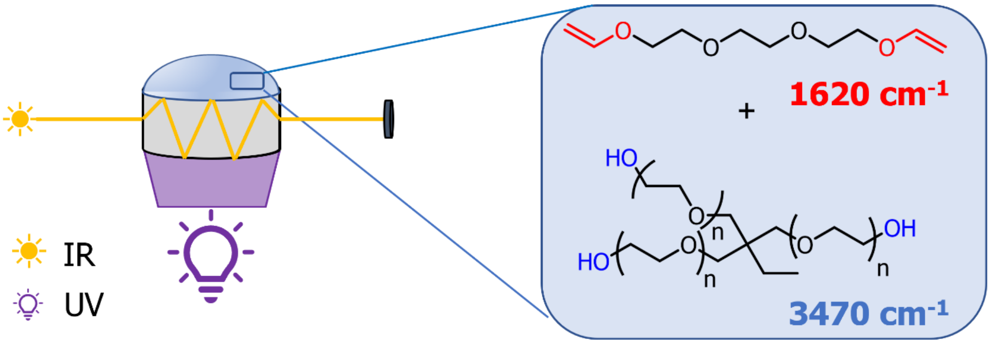

Figure S7.1. Schematic of time resolved UV-FTIR instrumental setup

CHAPTER 8

IDENTIFYING BARRIERS TO PHOTO-BASE GENERATOR CATALYZED CARBON MICHAEL ADDITIONS

8.1 Introduction

Additive manufacturing presents an attractive process for rapid prototyping, complex geometries, dematerialization, and lightweighting applications compared to traditional subtractive manufacturing processes.[1,2] Photo-assisted additive manufacturing techniques such as vat photopolymerization and UV-assisted direct ink writing leverage reactive monomers or oligomers and a photoactivated catalyst or initiator to selectively polymerize irradiated areas.[3] These processes generate three dimensional geometries in a layer by layer fashion. Currently, free radical polymerizations remain the most used polymerization strategy in the design of materials for these manufacturing techniques. However, recent research has demonstrated successful additive manufacturing with both photoacid generators and photobase generators through cationic polymerization or ring opening of lactones or epoxides.[4–6] This emerging research space presents opportunities for novel material design which take advantage of PAGs and PBGs since these platforms require monomers other than free radical polymerization monomers.

Photobase generators describe a family of photocatalysts which generate a base catalyst upon UV-irradiation. Common families of PBGs include photosensitized carboxylate and carbamate salts, which generate carbon dioxide and a base upon UV irradiation, and tetraphenylborate cages like those shown in **Scheme 8.1**.[7] The latter remains a more attractive PBG species as it does not generate a gas upon irradiation which may lead to bubbles and irregularities in printed parts. Upon irradiation, the PBG undergoes a triplet state rearrangement and subsequent decomposition into radical species and a deprotonated base. However, tetraphenylborate cage PBGs require low wavelength UV light to access this triplet state. Previous research increased their effectiveness through the covalent attachment of a thioxanthone photosensitizer.[8] **Scheme 8.1** presents the two PBG structures explored in this work where one contains a thioxanthone photosensitizer (TX-DBU BPh_h) and the other does not (DBU BPh_4).

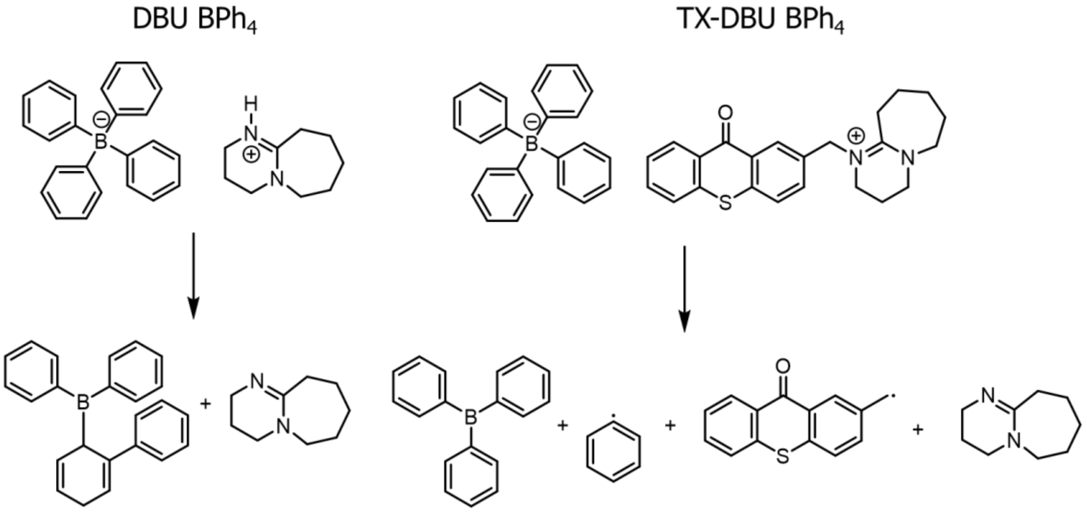

Scheme 8.1. PBG decompositions to active base and radical species.

While previous research leveraged PBGs in additive manufacturing, these approaches were limited to ring-opening polymerizations of lactones and epoxides. The carbon-Michael reaction is an attractive reaction platform for the design of new photopolymerizable precursors for UV-assisted additive manufacturing processes.[9] This base catalyzed reaction utilizes a base catalyst to deprotonate a carbon Michael donor such as acetoacetate. Following deprotonation, a readily nucleophilic carbanion is formed, which then reacts with a Michael acceptor such as an acrylate functionality.[10] This step growth process is well known to form robust gels through base catalysis and provides a starting platform to expand the library of monomers and oligomers suitable for PBG catalyzed network formation.

Currently, only one other research paper investigated PBG catalyzed Michael reactions with acrylates as the Michael accepting species.[11] Bowman et. al demonstrated successful PBG catalyzed thiol-Michael polymerization by overcoming inherent issues in the reaction system. Notably, PBGs generate radical species upon decomposition, which serve as free radical initiators for acrylate homopolymerization. The addition of TEMPO as a radical chain transfer agent prevented this side reaction and afforded crosslinked gels from PBG catalyzed thiol-Michael reactions.[11] However, a radical thiol-ene reaction and a base catalyzed thiol-Michael reaction yield the same anti-Markovnikov product and it remains uncertain if this reaction truly proceeded through a base catalyzed path or simply the rapid radical thiol-ene addition.[12]

This work seeks to develop suitable oligomeric crosslinkers for PBG catalyzed carbon-Michael reactions, the acetoacetate functionality will not generate a reactive radical species, and thus if crosslinking occurs the only two possible reaction pathways are the base catalyzed carbon-Michael reaction or the free radical acrylate homopolymerization. In this work, no evidence of PBG catalyzed carbon-Michael reaction was observed, but we report several instances of unintended free radical polymerization, which was not overcome with the addition of TEMPO or other radical inhibitors such as BHT or TEMPO. Model compound studies and isolated monomer investigations determined the acrylate Michael acceptor to be unviable with current PBG technologies.

8.2 Materials and methods

8.2.1 Materials

Trimethylol propane ethoxylate M_n =450 g/mol (TMPE), trimethylol propane ethoxylate triacrylate M_n= 664 g/mol (TMPE TA), tertbutyl acetoacetate, hexyl acrylate, Amberlyst 15 resin, 1,8-Diazabicyclo[5.4.0]undec-7-ene (DBU), 2,2,6,6-Tetramethyl-1-piperidinyloxy (TEMPO), 3,5-Di-tert-butyl-4-hydroxytoluene (BHT), hydroquinone, and methanol were purchased from Sigma Aldrich and used as received. The photobase generators DBU BPh_4 and TX-DBU BPh_4 were synthesized and purified by Xabier Lopez in the Haritz Sardon group according to previous literature within their research group.[8,13]

8.2.2 Instrumentation

^1H NMR and spectra were recorded using a Bruker Avance NEO 500 MHz NMR equipped with a 5mm iProbe. Photorheology experiments were conducted on a TA Instruments DHR-2 rheometer equipped with a UV-curing accessory. Oscillatory time sweep experiments were conducted with a 20 mm parallel plate geometry and sample at 0.1% strain and a frequency of 1 1/s. UV light was delivered from an Omnicure S2000 lamp attached to the UV-curing accessory through a liquid light guide. UV intensity was calibrated with a Silverline UV radiometer prior to experimentation. In-*situ* FT-IR spectroscopy with a Mettler Toledo ReactIR15 equipped with a SiComp probe collected time resolved FT-IR spectrum with a time resolution of 15 s. HPLC measurements were performed on a Shimadzu LCMS-2020 equipped with a Kromasil EternityXT-2.5-C18 column at a flow rate: 1.5 mL/min following a 4 minute gradient elution from 10-100% acrylonitrile in water. Chromatograms were generated by an electron spray single quadrupole mass spectrometer and photodiode array detector.

8.2.3 Synthesis of trimethylolpropane ethoxylate triacetoacetate (TMPE TAcAc)

TMPE TAcAc was synthesized in a similar fashion to previous acetoacetate functionalization reported from our research group.[9] TMPE (25 g, 1 eq) and tert-butyl acetoacetate (52.73 g, 6 eq) in addition to Amberlyst 15 (1 g) were charged to a 100 mL round-bottomed flask equipped with a magnetic stir rod, dean stark trap, and condenser. The reaction was heated to 80 °C in an oil bath and the dean stark trap was drained as needed. After 3 h, the round bottom was removed from the oil bath, and the pale yellow product was decanted from the Amberlyst catalyst into another 100 mL round bottomed flask. Residual tert-butyl acetoacetate was removed under reduced pressure. The product was used in subsequent reactions without further purification.

8.2.4 DBU catalyzed gel formation

TMPE TAcAc (0.50 g) and TMPE TA (0.5 g) were combined in a 4 dram scintillation vial and mixed until a homogenous solution formed. DBU (0.01 g) was added to scintillation and quickly vortex mixed at 3000 rpm before the reactive mixture was poured into a Teflon dish. The reaction mixture solidified after 5 minutes to yield a transparent yellow film. The gel was left for 2 h prior to Soxhlet extraction in methanol.

8.2.5 Photorheology and gel fractions of PBG catalyzed crosslinking

Like the DBU catalyzed control TMPE TAcAc (0.50 g) and TMPE TA (0.50 g) were combined in a 4 dram scintillation vial along with either DBU BPh_4 or ITX- DBU BPh_4 (0.01 g). Select samples also included 0.01 g of either TEMPO, BHT, or hydroquinone. 0.20 mL of the reactive mixture was placed on the quartz lower geometry of the rheometer and the gap was set to 500 μm. After 30 s of initial viscoelastic sampling, the samples were exposed to 125 mW/cm^2 broadband UV light for 570 s. The crosslinked gels were then extracted via Soxhlet extraction in methanol. Gel fractions were calculated by dividing the mass after extraction by the mass prior to extraction.

8.2.6 HPLC analysis of PBG decomposition with additives

To determine if the antioxidant and radical inhibiting additives affected PBG decomposition, ITX-DBU BPh_4 (0.01 g) either TEMPO or BHT (0.01 g) were dissolved in 1 mL of acetonitrile inside a 4 dram scintillation vial. Samples were exposed to UV irradiation from an Omnicure S2000 lamp through the top of the open vial for 15 min. prior to elution through the HPLC system.

8.2.7 ^{1}H NMR analysis of tert-butyl acetoacetate upon irradiation

To test the stability of the acetoacetate functionality under UV-irradiation, tert-butyl acetoacetate was exposed to UV-irradiation from an Omnicure S2000 lamp through the top on an open 4 dram vial prior to preparation of an ^{1}H NMR samples in $CDCl_3$.

8.2.8 Model compound in-*situ* FT-IR experiments

A stock solution of tert-butyl acetoacetate (10.0 g, 1 eq) and hexyl acrylate (9.9 g, 1 eq) was prepared to ensure consistent stoichiometry across all model compound studies. 1 g aliquots were taken from this stock solution and combined with either DBU BPh_4 or ITX- DBU BPh_4 (0.01 g). Select samples also included 0.01 g of either TEMPO, BHT, or hydroquinone. The SiComp probe was submerged in the reactive mixture and the flask was left open to the atmosphere. UV irradiation was delivered from an Omnicure S2000 lamp and directed through the side of the vial at an intensity of 125 mW/cm^2. Data presented in this manuscript report trends associated with the C=C bending vibrational mode at 810 cm^{-1}

8.3 Results and Discussion

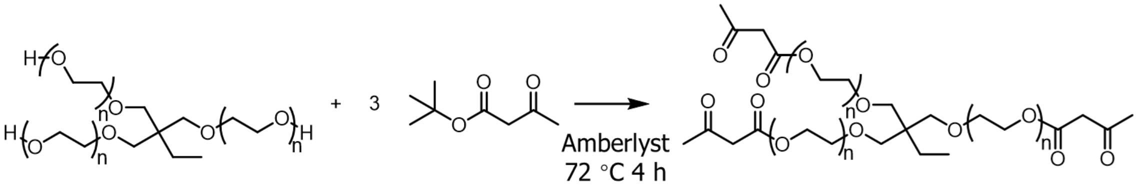

Scheme 8.2. Synthesis of TMPE TAcAc through acid catalyzed transesterification.

To investigate PBG catalyzed carbon-Michael additions a suitable Michael donor functionalized crosslinker was synthesized. Prior research highlighted efficient DBU catalyzed carbon-Michael crosslinking with acetoacetate functionalized macromonomers. Thus, acid catalyzed transesterification afforded a trifunctional acetoacetate crosslinker as shown in **Scheme 8.2.** Prior to photorheological experiments with the PBGs of interest, a control crosslinking experiment with DBU as a base catalyst validated the synthesized crosslinker as a suitable trifunctional carbon donor for base catalyzed carbon-Michael additions. **Figure 8.1** demonstrates the formation of a robust organogel formed from the base catalyzed carbon-Michael crosslinking between TMPE TAcAc and TMPE Ta. This experiment confirmed this monomer combination's potential for base-catalyzed gelation.

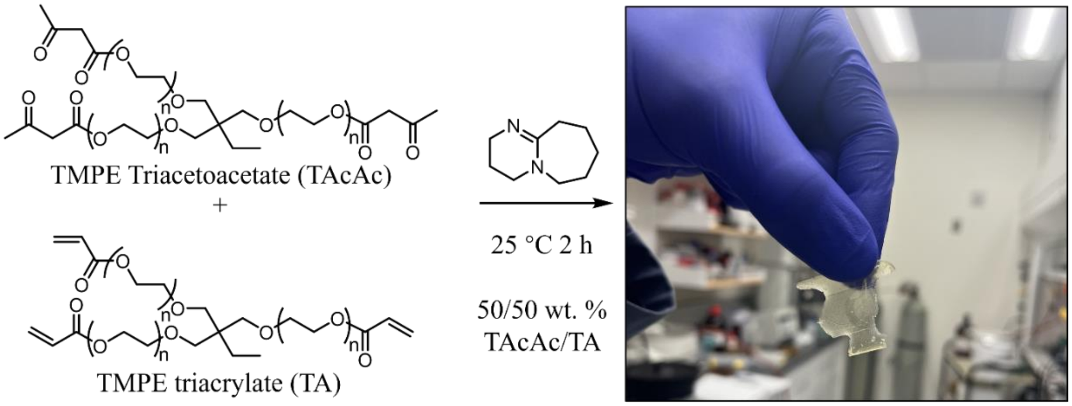

Figure 8.1. TMPE TAcAc and TMPE TA readily form crosslinked gels through base catalyzed carbon Michael addition.

Photorheology experiments with the previously discussed monomer combination and 1 wt.% of either DBU BPh_4 or TX-DBU BPH_4, shown in **Figure 8.2**, demonstrated that each PBG effectively decomposed and generated reactive species which caused solidification following either carbon-Michael addition or acrylate homopolymerization. Additionally, the photosensitized PBG TX-DBU BPh_4 lead to more rapid crossover times than the non-photosensitized analogue, which highlighted the benefit of the covalently attached thioxanthone functionality. Furthermore, the addition of BHT did not impact the crossover times or plateau storage moduli. However, the Addition of TEMPO prevented any crosslinking reactions from occurring. The plateau storage moduli and loss moduli all reached similar values of 2 x 10^6 Pa.

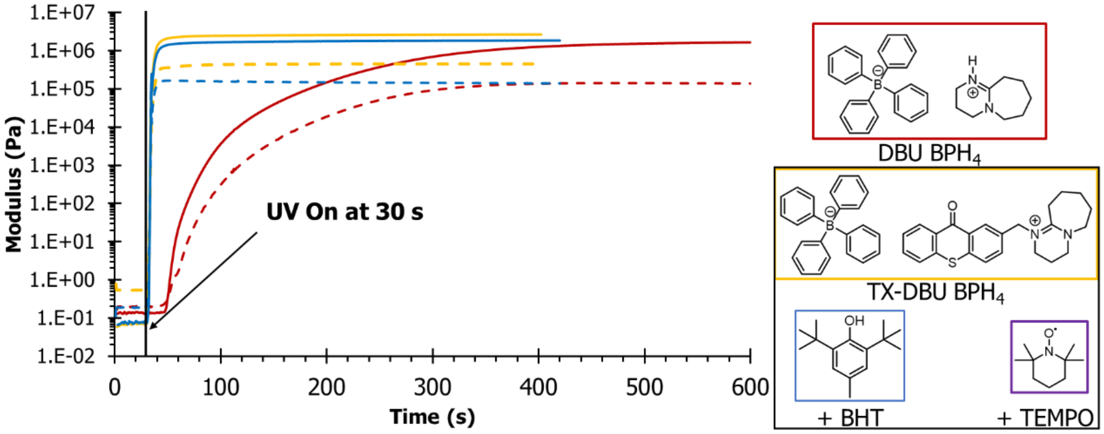

Figure 8.2. Photorheology summary of TMPE TAcAc TMPE crosslinking with photobase generators and additives.

Gel fraction measurements after Soxhlet extraction, shown in **Figure 8.3**, in methanol determined gel contents for the three photo-crosslinked gels in addition to the control gel formed with only DBU. TEMPO is plotted as 0 % gel fraction as the reactive mixture remained fully soluble after exposure to UV light. Notably, the gel fraction of the DBU control was on average 90 %, whereas each of the PBG catalyzed reactions demonstrated gel fractions below 50 %. The reactive mixture was a 50:50 wt.% combination of both TMPE TAcAc and TMPE Ta, and therefore this data suggested that the primary crosslinking reaction that occurred was acrylate homopolymerization. This inspired model compound studies between small molecule monomers to better understand the fundamental reactivity that exists within this system.

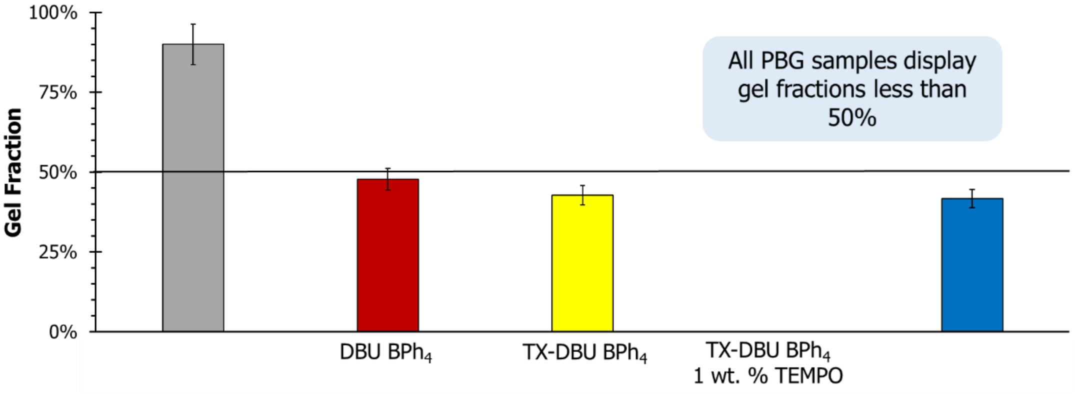

Figure 8.3. Gel fraction measurements reveal PBG catalyzed samples have less than 50 wt.% gel content.

A model compound in-*situ* FT-IR study explored the reaction between tert-butyl acetoacetate and hexyl acrylate with 1 wt.% addition of basic catalysts. The acrylate functionality participates in both carbon-Michael additions as a Michael acceptor and as a monomer for free radical polymerizations, and thus the acrylate peak at 810 cm^{-1} monitored the rate of reaction.[14] **Figure 8.4** demonstrates vast differences in reactivity between basic

DBU catalyzed carbon-Michael addition and free radical initiated acrylate polymerization. In the DBU catalyzed reaction, full acrylate conversion occurred after 230 min, which informed the previous gel fraction measurements for the DBU control system. At 120 min, the reaction only reached 80 % conversion which explains the 90 % gel fraction. In comparison, the photoinitiated free radical control with TPO reached full conversion in only 15 min. Finally, the TX-DBU BPh_4 initiated reaction reached full conversion in 70 min. It should also be noted that the DBU catalyzed reaction did not significantly increase in viscosity, but the TPO and TX-DBU BPh_4 reactions demonstrated large increase in viscosity, which further confirmed homopolymerization of hexyl acrylate.[15]

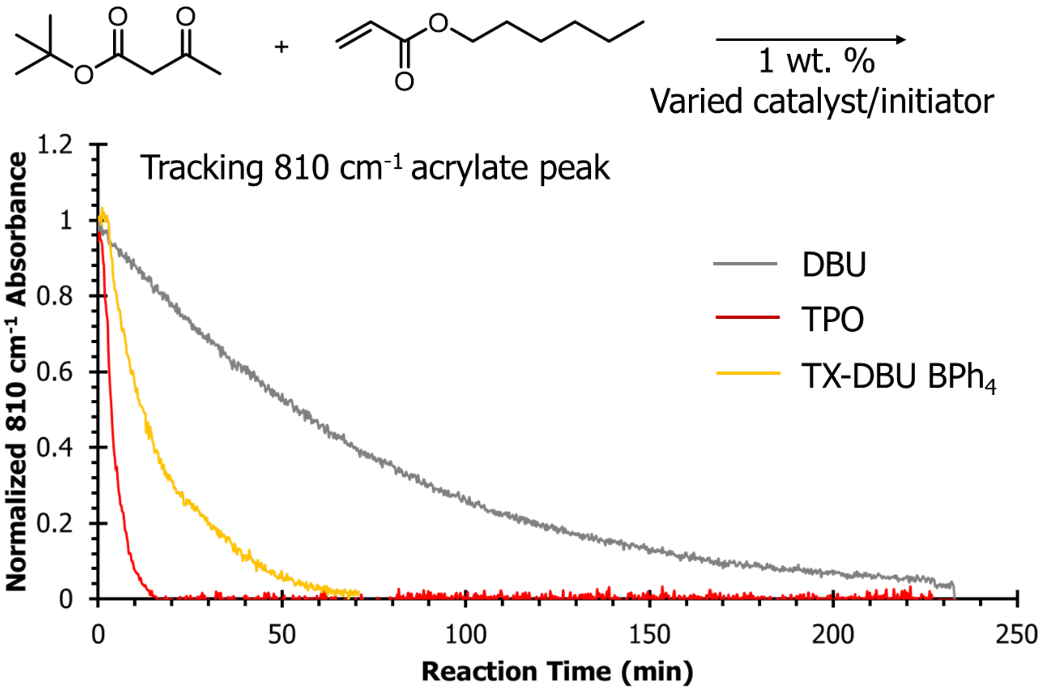

Figure 8.4. model compound in-*situ* FTIR experiment monitors acrylate conversion with both radical and bass catalysts.

Similar in-*situ* FT-IR experiments with the addition of either TEMPO, hydroquinone, or BHT, shown in **Figure 8.5**, provided further understanding of this reaction. Addition of antioxidants hydroquinone and BHT significantly slowed the reaction, but the product remained a viscous liquid, which confirmed acrylate homopolymerization remained the dominant reaction pathway. However, when UV exposure stopped, as demonstrated in the BHT experiment, acrylate consumption stopped. This data suggested that the antioxidant additive interfered with PBG decomposition as the carbon-Michael addition should have occurred if a base was present. The TEMPO containing experiments also suggested some interference between the additive and the PBG since acrylate concentration remained constant throughout the experiment.

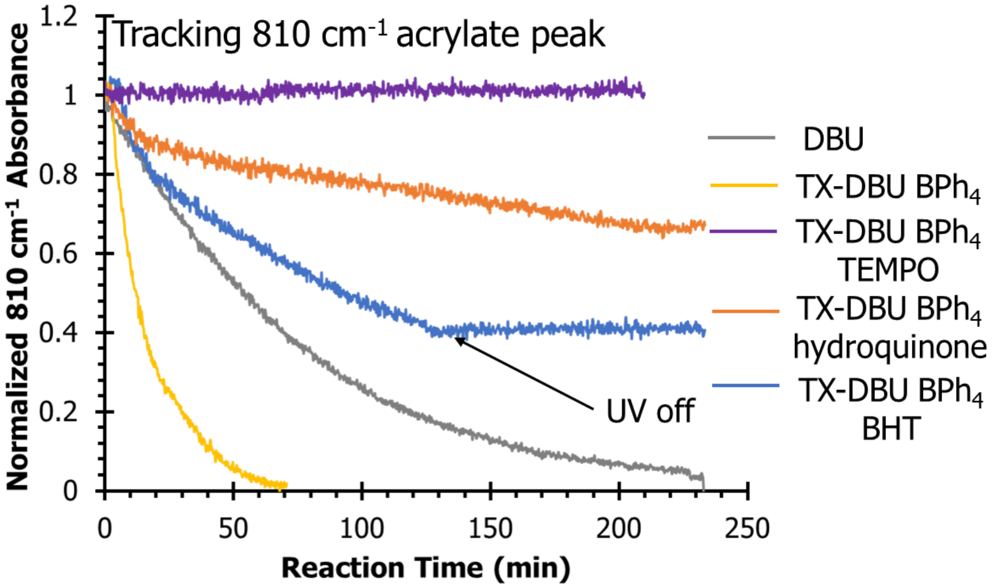

Figure 8.5. Further model compound in-*situ* FTIR experiments show acrylate conversion continues with both hydroquinone and BHT.

To test the previous hypotheses, the PBG species was isolated and exposed to UV irradiation in the presence of either TEMPO or BHT. Following irradiation, HPLC analyzed the fragmented sample as seen in **Figure 8.6.** These experiments revealed no distinguishable differences between the control PBG after irradiation and upon the addition of TEMPO. This data shows that TEMPO addition did not cause a measurable difference in DBU generation upon UV irradiation. Similarly, BHT did not cause any changes in PBG decomposition. These results indicated that the PBG itself remained agnostic to these additive additions. Thus, it was hypothesized that the additives affected the acetoacetate nucleophilicity through a side reaction.

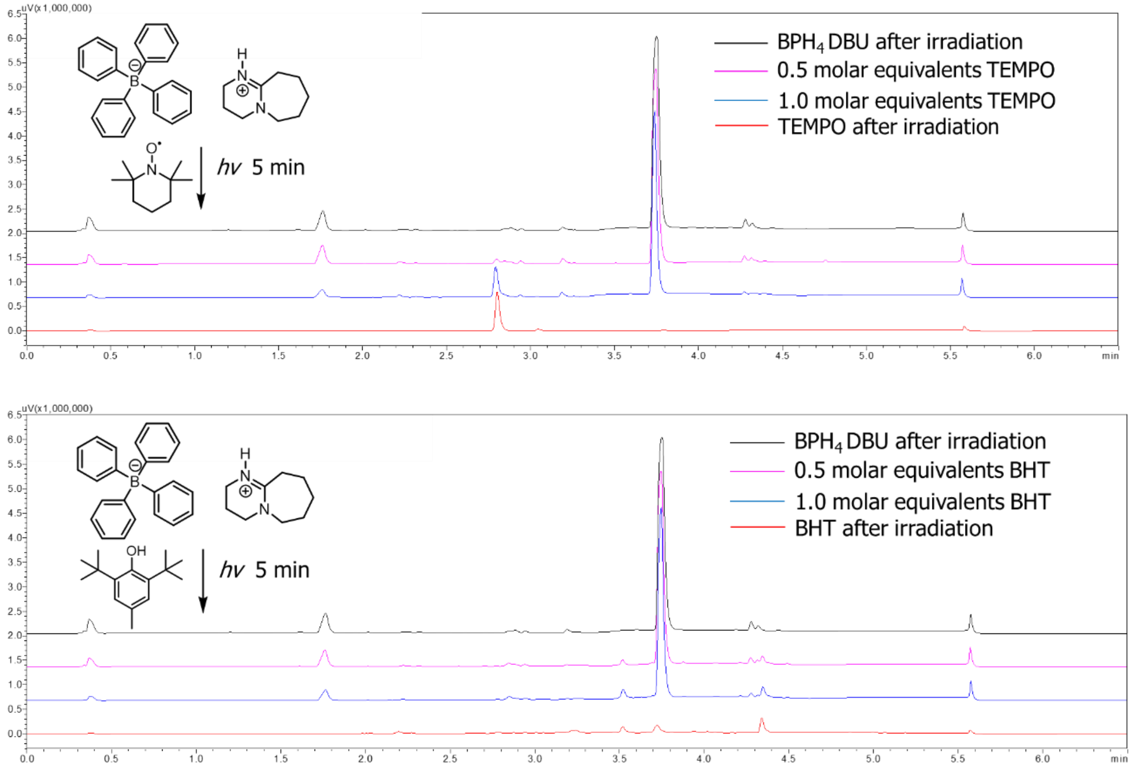

Figure 8.6. HPLC reveals TEMPO (top) and BHT (bottom) do not affect PBG decomposition fragments.

^{1}H NMR of tert-butyl acetoacetate before and after irradiation, shown in **Figure 8.7.** Confirmed that the acetoacetate remained after UV exposure and no side products were produced. Additionally, similar NMR experiments did not reveal any effect upon addition of BHT or TEMPO. These spectra remain identical to those presented in **Figure 8.7.** The HPLC and ^{1}H NMR investigations of the PBG catalyst and the acetoacetate Michael donor demonstrated that both functionalities were not perturbed by UV-irradiation or the addition of TEMPO or BHT. Thus, the problem remains localized to the unintended and relatively fast free radical polymerization of the acrylate Michael acceptor. Future work should explore varied levels of TEMPO addition as it remains the only additive which provided evidence for PBG catalyzed thiol-Michael additions.[11] However, a PBG that liberates a basic species through a non-radical generating process presents more promising solution to this problem. Unfortunately, no such PBG has been synthesized to date.

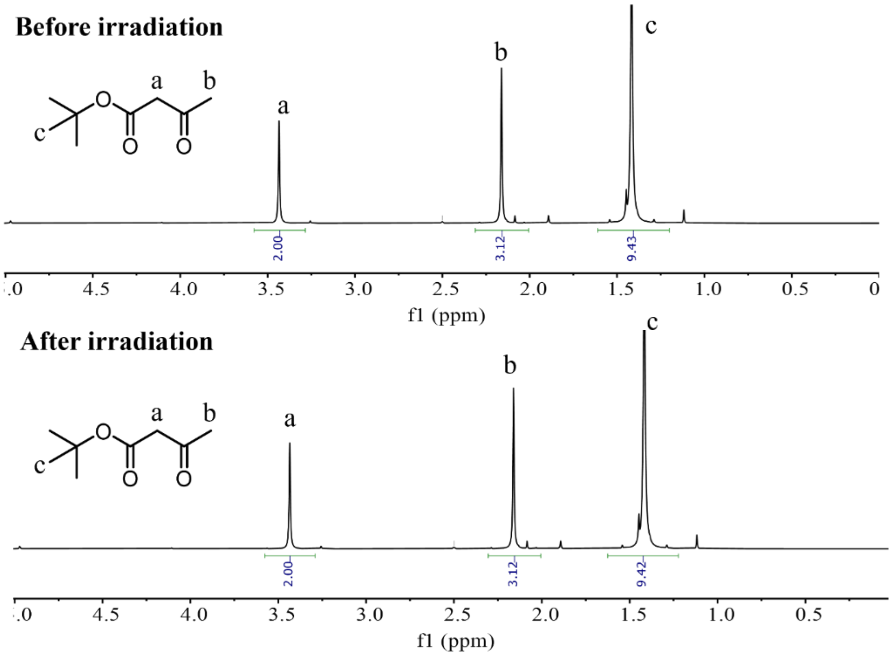

Figure 8.7. ^{1}H NMR of tert-butyl acetoacetate before (top) and after (bottom) irradiation reveals no significant change in the chemical structure.

8.4 Conclusions

Acid catalyzed transesterification yielded a triacetate functionalized trimethylolpropane ethoxylate triacetoacetate. This crosslinker proved suitable as a trifunctional Michael donor for base catalyzed carbon-Michael reaction in the presence of a trifunctional Michael acceptor. This control liberated gels with high gel contents (90 %). However, when a PBG was used instead of DBU, these gel fractions decreased to less than 50 % which suggested acrylate homopolymerization was the dominant reaction pathway. Addition of TEMPO, BHT, and hydroquinone did not overcome this unintended side reaction. Model compound studies with tert-butyl acetoacetate and hexyl acrylate further confirmed this side reaction through the formation of a viscous product from acrylate homopolymerization. HPLC and ^{1}H NMR confirmed stability of the PBG and acetoacetate under the reaction conditions and thus it is concluded that PBG catalyzed carbon-Michael additions are wholly prevented by the much faster radically initiated acrylate polymerization. Currently, this reaction demands a PBG that does not generate a radical species upon irradiation.

8.5 Acknowledgements

The authors would like to thank Xabier Lopez for providing both PBGs tested in this work in addition to Arizona State University and POLYMAT for supporting this international collaborative effort.

8.6 References

1. Rau, D. A.; Herzberger, J.; Long, T. E.; Williams, C. B. Ultraviolet-Assisted Direct Ink Write to Additively Manufacture All-Aromatic Polyimides. *ACS Appl Mater Interfaces* **2018**, *10* (41), 34828–34833. https://doi.org/10.1021/ACSAMI.8B14584/ASSET/IMAGES/LARGE/AM-2018-145849_0003.JPEG.

2. Beaman, J. J.; Bourell, D. L.; Seepersad, C. C.; Kovar, D. Additive Manufacturing Review: Early Past to Current Practice. *Journal of Manufacturing Science and Engineering, Transactions of the ASME* **2020**, *142* (11). https://doi.org/10.1115/1.4048193/1086507.

3. Behera, D.; Cullinan, M. Current Challenges and Potential Directions towards Precision Microscale Additive Manufacturing – Part I: Direct Ink Writing/Jetting Processes. *Precis Eng* **2021**, *68*, 326–337. https://doi.org/10.1016/J.PRECISIONENG.2020.12.009.

4. Manuel De Lardizabal, P. Development of Polythiourethane Based Resins for 3D Printing Applications Using Photobase Generators. **2022**.

5. Zivic, N.; Kuroishi, P. K.; Dumur, F.; Gigmes, D.; Dove, A. P.; Sardon, H. Recent Advances and Challenges in the Design of Organic Photoacid and Photobase Generators for Polymerizations. *Angewandte Chemie International Edition* **2019**, *58* (31), 10410–10422. https://doi.org/10.1002/ANIE.201810118.

6. Lopez De Pariza, X.; Cordero Jara, E.; Zivic, N.; Ruipérez, F.; Long, T. E.; Sardon, H. Novel Imino- and Aryl-Sulfonate Based Photoacid Generators for the Cationic Ring-Opening Polymerization of ε-Caprolactone. *Polym Chem* **2021**, *12* (28), 4035–4042. https://doi.org/10.1039/D1PY00734C.

7. Sun, X.; Gao, J. P.; Wang, Z. Y. Bicyclic Guanidinium Tetraphenylborate: A Photobase Generator and a Photocatalyst for Living Anionic Ring-Opening Polymerization and Cross-Linking of Polymeric Materials Containing Ester and Hydroxy Groups. *J Am Chem Soc* **2008**, *130* (26), 8130–8131. https://doi.org/10.1021/JA802816G/SUPPL_FILE/JA802816G-FILE001.PDF.

8. Zivic, N.; Sadaba, N.; Almandoz, N.; Ruipérez, F.; Mecerreyes, D.; Sardon, H. Thioxanthone-Based Photobase Generators for the Synthesis of Polyurethanes via the Photopolymerization of Polyols and Polyisocyanates. *Macromolecules* **2020**, *53* (6), 2069–2076. https://doi.org/10.1021/ACS.MACROMOL.9B02648/ASSET/IMAGES/LARGE/MA9B02648_0004.JPEG.

9. Williams, S. R.; Miller, K. M.; Long, T. E. Michael Addition Reaction Kinetics of Acetoacetates and Acrylates for the Formation of Polymeric Networks. *Progress in*

Reaction Kinetics and Mechanism **2007**, *32* (4). https://doi.org/10.3184/146867807X247730.

10. Mather, B. D.; Viswanathan, K.; Miller, K. M.; Long, T. E. Michael Addition Reactions in Macromolecular Design for Emerging Technologies. *Prog Polym Sci* **2006**, *31* (5), 487–531. https://doi.org/10.1016/J.PROGPOLYMSCI.2006.03.001.

11. Chatani, S.; Gong, T.; Earle, B. A.; Podgorski, M.; Bowman, C. N. Visible-Light Initiated Thiol-Michael Addition Photopolymerization Reactions. *ACS Macro Lett* **2014**, *3* (4), 315–318. https://doi.org/10.1021/MZ500132J/SUPPL_FILE/MZ500132J_SI_001.PDF.

12. Hoyle, C. E.; Bowman, C. N. Thiol-Ene Click Chemistry. *Angewandte Chemie - International Edition*. 2010. https://doi.org/10.1002/anie.200903924.

13. Wutzel, H.; Jarvid, M.; Bjuggren, J. M.; Johansson, A.; Englund, V.; Gubanski, S.; Andersson, M. R. Thioxanthone Derivatives as Stabilizers against Electrical Breakdown in Cross-Linked Polyethylene for High Voltage Cable Applications. *Polym Degrad Stab* **2015**, *112*, 63–69. https://doi.org/10.1016/J.POLYMDEGRADSTAB.2014.12.002.

14. George Socrates. *Infrared and Raman Characteristic Group Frequencies: Tables and Charts*; John Wiley & sons, 2004.

15. Nunes, R. W.; Martin, J. R.; Johnson, J. F. Influence of Molecular Weight and Molecular Weight Distribution on Mechanical Properties of Polymers. *Polym Eng Sci* **1982**, *22* (4), 205–228. https://doi.org/10.1002/PEN.760220402.

CHAPTER 9

REVEALING FOAM STABILITY FOR CATIONIC AND ZWITTERIONIC TRIETHYLSILYL-CONTAINING SURFACTANTS

Abstract

Fundamental understanding of surfactant structure-property-performance relationships will inform the design of next-generation alternatives to perfluoroalkyl substances (PFAS) in aqueous film forming foams (AFFF). This manuscript describes the synthesis, solution properties, and foam stability of novel triethylsilyl-containing surfactants, which elucidated the influence of the hydrophilic head group on critical micelle concentration (CMC), surface tension, and foam stability. Photocatalyzed hydrosilylation of triethylsilane and N,N-dimethyl allylamine yielded N,N-dimethyl-3-(triethylsilyl)propane-1-amine. Subsequent functionalization with either propane sultone or bromoethane afforded zwitterionic sulfobetaine surfactant, 3-(dimethyl(3-(triethylsilyl)propyl)ammonio)propane-1-sulfonate (TESDMAPS) and cationic quaternary ammonium surfactant, N-ethyl-N,N-dimethyl-3-(triethylsilyl)propane-1-ammonium bromide (TESDMABr), respectively. Dynamic light scattering (DLS) and cryo-transmission electron microscopy (TEM) characterized micelle size and shape in solutions above the CMC. Surface tensiometer analysis determined minimum TESDMAPS and TESDMABr solution surface tensions of 37.7 and 35.9 mN/m respectively. Molecular dynamics simulations related this decrease in surface tension to a larger average interfacial area of 88 Å^2 per TESDMABr molecule compared to 66 Å^2 per TESDMAPS molecule. Steady-shear rheological measurements showed consistent exponential viscosity scaling relationships between TESDMAPS and TESDMABr solutions $\leq$ 30 wt.%. Above this

concentration, TESDMAPS displayed solution viscosities greater than TESDMABr and a mixture of surfactants provided an intermediate concentration dependent viscosity scaling. Dynamic foam analysis (DFA) revealed TESDMABr foams displayed longer 25% foam drainage times than TESDMAPS. Oscillatory rheology of TESDMABr solutions demonstrated solid-like solution behavior at low shear rates. Finally, polarized light imaging rheology highlighted the formation of birefringent structures in TESDMABr solutions under shear. For the first time, this work relates solution viscoelasticity from shear-induced surfactant assembly to foam stability with implications on fluorine-free, next-generation, fire-fighting foams.

9.1. Introduction

Fluorinated surfactants provide advantageous properties in many fields including cleaning agents, industrial lubricants, and as critical components in fire-fighting foam formulations.[1,2] Most notably, aqueous film forming foams (AFFF) contain significant amounts of fluorinated surfactants.[3] These formulations historically contained PFAS prepared from the acid fluoride forms of perfluorooctanoic acid (PFOA) and perfluorooctanesulfonic acid (PFOS).[4] Subsequently, hydrolysis of these surfactants in the environment yield PFOA or PFOS contaminants.[5] The chemical stability of these fluorinated surfactants causes bioaccumulation in aqueous and terrestrial environment, and furthermore, these surfactants display significant toxicity to organisms in these ecosystems.[6,7] Thus, there is intense interest to understand the structure-property-performance relationships of surfactants more fully in AFFF to remove PFAS in next-generation AFFF formulations. Moreover, it is necessary to develop more facile synthetic strategies that efficiently deliver a versatile molecular toolbox for future surfactant designs.

AFFF is primarily used to extinguish flammable liquid fires, and the critical feature of AFFF is the formation of a stable aqueous film on the surface of the flammable liquid.[8] This unique feature of AFFF provides a liquid barrier, which protects the underlying fuel from ignition. Previous research identified the spreading coefficient as a determinant for the ability for foam formulation to form an aqueous film.[8,9] The relative surface tensions between fuel and air (γ_f), surfactant solution and air (γ_s), and surfactant solution and fuel (γ_{fs}), determine the spreading coefficient S shown in **Equation 9.1**. A surfactant solution with a positive spreading coefficient will form an aqueous film over the fuel, whereas a surfactant solution with a negative spreading coefficient will drain beneath the fuel layer. PFAS provides significantly lower surface tensions to aqueous solutions with a minimum surface tension of 15-20 mN/m compared to hydrocarbon surfactant surface tensions of 30-40 mN/m.[10,11] This plays a critical role in achieving a positive spreading coefficient and thus aqueous film formation. In recent years, researchers identified siloxane-containing surfactants as leading competitors to fluorinated surfactants in firefighting applications and lowering solution surface tensions to 20 mN/m was achievable.[12,13] However, other silicon-based tails remain unexplored in surfactant applications and thus present an opportunity to discover novel surfactant systems together with facile synthetic methods.

(Equation 9.1)

$$\boldsymbol{S = \gamma_f - \gamma_s - \gamma_{sf}}$$

While a positive spreading coefficient is a key parameter that determines AFFF performance, the roles of surfactant self-assembly and foam microstructure on firefighting performance remains unknown. These self-assembled structures arise at concentrations above the CMC, which is the concentration where surfactant molecules completely saturate the interface of the solution and the solubility limit of free surfactant in solution is reached.[14] Above the CMC, additional surfactant molecules in solution form micelle structures to reduce hydrophobic interactions and reduce the free energy of the system. The hydrophobic tail, hydrophilic head, temperature, ionic strength, and pH collectively influence the CMC. Above the CMC, dissolved surfactant molecules self-assemble to reduce hydrophobic repulsive interactions between the hydrophobic surfactant tail and the aqueous solution.[15,16] These self-assembled structures span spherical micelles, wormlike micelles, vesicles, and bilayer sheets, and as expected, differences in self-assembled structures in solution greatly impact solution properties.[17] For example, spherical micelles do not significantly impact solution viscosity, whereas wormlike micelles drastically increase solution viscosity and behave akin to polymer chains in solution. [18,19] For example, a common cause of flame reignition in firefighting is fuel diffusion through the foam, and the rate of diffusion is proportional to solution viscosity.[20,21]Thus, it is proposed that wormlike micelles in solution will presumably display improved fuel vapor suppression and ultimately improved performance compared to spherical micelles, although this presumption remains unverified.

The molecular structure of the surfactant directly informs the shape of self-assembled nanostructures in solution above the CMC. The geometric packing parameter (*P*), as shown in **Equation 9.2,** mathematically describes the ratio of the hydrophobic volume (*V*) of a single surfactant, hydrophobic length (*l*), and the polar/non-polar interfacial area (*a*). Linear, single tail, hydrocarbon surfactants, such as sodium dodecyl sulfate (SDS), display packing parameters ranging from 0 to 1/3, which describes a molecule that adopts a cone shape during self-assembly of spherical micelles. Gemini surfactants, which contain two hydrophobic tails and two covalently connected hydrophilic heads, display packing parameters ranging from ½ to 1.[22] This packing parameter describes surfactants that appear as truncated cones and thus form wormlike micelle self-assemblies.[23,24] Some surfactants, such as phospholipids have packing parameters very close to 1 and form very large planar bilayers and vesicles, as shown in **Figure 9.1**.[25] This structural guidance informs the molecular design of next generation wormlike micelle-forming surfactants for fire-fighting foams with potentially improved fuel vapor suppression.

(Equation 2)

$$\boldsymbol{P = \frac{V}{l * a}}$$

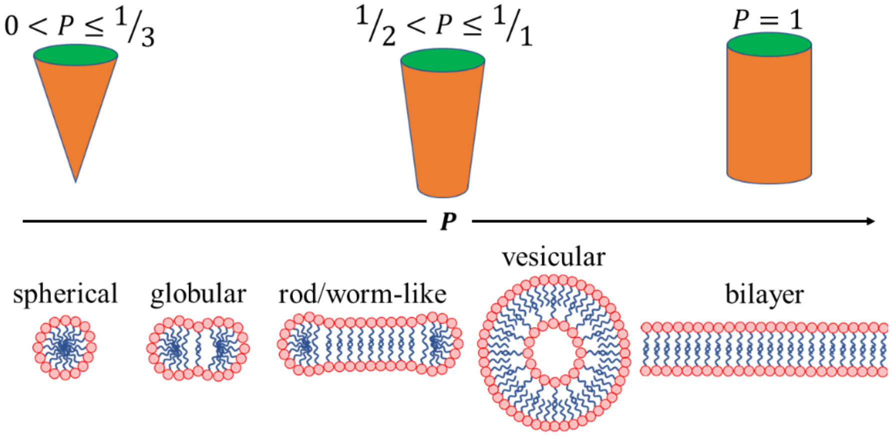

Figure 9.1. Surfactant shape and theoretical geometric packing parameter inform self-assembled structure in solution.

The hydrophilic head of a surfactant enables solubility by overcoming the hydrophobic repulsive forces between the aqueous solution and the hydrophobic surfactant tail. Hydrophilic heads are commonly ionic functionality such as anionic carboxylates, sulfates, and sulfonates, or cationic ammoniums, and phosphoniums with either cationic or anionic counterions, respectively.[26] When ionic surfactants disperse in aqueous solution, the counterion fully dissociates from the surfactant molecule leaving a single positive or negative charge covalently bound to the hydrophobic tail. Electrostatic repulsive forces between these similarly charged head groups act as an energetic barrier to surfactant self-assembly, which in turn increases the CMC and the polar/non-polar interfacial area term within the packing parameter.[27] Zwitterionic hydrophilic heads such as carboxybetaines and sulfobetaines contain both positive and negative charges covalently bound to the hydrophobic tails. These afford a net neutral ionic charge to the hydrophilic head group, which decreases both the CMC and the polar/non-polar interfacial area term within the packing parameter.[27,28]

This manuscript reports triethylsilyl-containing surfactants and explores surfactant structure-property-performance relationships with self-assembled structure, rheological behavior, surface properties, and foam stability. Tetraalkylsilane-containing surfactant tails explore the role of the silicon atom in surfactant hydrophobic tails in the absence of previously reported Si-O-Si bonds. Triethylsilyl-containing tails provide truncated cone hydrophobic tails, which predict self-assembled worm-like micelles in solution. The exploration of both zwitterionic or cationic head groups reveals differences in head group interactions, which impact both the CMC and self-assembled structural interactions. The conclusions are discussed in the context of fluorine-free surfactants for fire-fighting applications.

9.2. Experimental Details

9.2.1 Materials

All reagents and solvents were purchased from Sigma-Aldrich and used without further purification. Triethylsilane was stored under dry nitrogen in Acro sealed containers. Dimethyl allylamine was synthesized from allyl chloride and dimethylamine and purified following a procedure adapted from Yu *et. al*.[29]

9.2.2 Instrumentation

^{1}H NMR and ^{13}C NMR spectra were recorded using a Bruker Avance NEO 500 MHz NMR equipped with a 5mm iProbe. NMR solutions were prepared in D_2O. All other surfactant solutions were prepared with HPLC grade deionized water. DLS data was collected on a Malvern Zetasizer set to 23 °C. Steady shear surfactant solution viscosities and oscillatory rheology data were measured on a TA Instruments DHR-3 rheometer equipped with 40 mm 2° cone and plate geometry with an 80 μm truncation gap. Experiments were conducted at 23 °C, and the temperature was controlled with a Peltier plate. Stress sweep oscillatory experiments were conducted at 10 rad/s. Polarized light imaging rheology was performed on an Anton Parr rheometer equipped with the Anton Parr polarized light imaging accessory and a polished 20 mm parallel plate. Solution surface tensions were measured with a Kruss Force Tensiometer K100 and tests were conducted using the Wilhelmy Plate Method at room temperature. Foam collapse time results from DFA were measured with a Kruss Dynamic Foam Analyzer. 30 mL aqueous solution was placed into the DFA glass cylinder with an inner diameter of 40 mm. Air flow through a porous glass disk (25 µm to 50 µm pore size) at the bottom of the cylinder at a flow rate of 0.2 L/min for 20 s generated foam. After foam generation, the liquids drainage with time was measured directly by ADVANCE software. Cryo-transmission electron microscopy images were collected on a Titan Krios with a 30 keV accelerating voltage.

9.2.3 Simulation Details

Molecular dynamics simulations of surfactant-laden water-vapor interfaces were performed with GROMACS 2020.3-modified software package.[30] The system consisted of three components: a substrate, a water layer, and a surfactant monolayer. The substrate is fixed to keep the water and the surfactant monolayer from moving in the z−direction. Surfactants were placed at the water-vapor interface in such a way that its hydrophilic heads faced the water phase, while its hydrophobic tails faced the vapor phase. The dimensions of the simulation system were 4.9, 4.9, and 20 nm in the x, y, and z directions, respectively. Periodic boundary conditions were applied in all directions. The number of water molecules is 3800 in all simulations, which leads to a water layer of ∼5 nm thick to simulate bulk-like solution behavior. The substrate was modeled as a silicon slab built using the Inorganic Builder Plugin (Version 0.1) in VMD.[31] The spc/e model simulated water molecules, and the surfactant molecules were modeled using the OPLS force fields parameters generated by a web-based service LigParGen.[32,33] Counter-ions were modeled as charged Lennard-Jones (LJ) spheres with parameters developed by Joung et al.[34]

Packmol code was used to develop the simulation.[35] After initial configuration an energy minimization run using the steepest descent algorithm was performed until maximal force was less than 100 kJ mol^{-1} nm^{-1}. Then, a 50 ns simulation in the canonical (NVT) ensemble was performed at 300 K to ensure equilibration. The velocity-rescaling thermostat with a relaxation time of 0.1 ps kept solution temperature at 300 K. A cutoff of 1.4 nm computed LJ potentials. The particle mesh Ewald (PME) method with an FFT spacing of 0.12 nm and a tolerance of 10−5 computed electrostatic interactions.

9.2.4 Area-per-molecule estimation

The number of surfactant molecules at the water-vapor interface varied to estimate the saturated surfactant density at the interface. Assuming 50 ns provides sufficient time for the surfactant monolayer to reach equilibrium, final configurations and their trajectories were inspected to observe any detached surfactants from its monolayer which are dissolved in water. **Table S9.1** summarizes case studies which determined saturated surfactant densities at water-vapor interface. In simulations with relatively high surfactant density, some surfactants deviated from the monolayer. Simulations with lower surfactant density were performed until none of the surfactants deviated during 50ns.

9.2.5 Synthesis of N,N-dimethyl-3-(triethylsilyl)propane-1-amine

Photocatalyzed hydrosilylation yielded triethylsilyl dimethylamine. In an example reaction, N,N,dimethyl allyl amine (4.92 g, 0.0578 mol, 1.00 eq) and triethylsilane (7.00 g, 0.0602 mol, 1.04 eq) were added to a 20-mL scintillation vial under a nitrogen atmosphere equipped with a magnetic sir bar. Platinum(II) bis(acetylacetonate) dissolved in toluene (0.01 M, 3 mL, 250 ppm) was added prior to irradiation with an Omnicure S2000 broadband UV-photosource (λ= 275-575 nm). The reaction proceeded until FT-IR spectroscopy confirmed complete conversion of the allylic functionality (k= 900 cm^{-1}). The light brown product was used in subsequent reaction steps without further purification.

9.2.6 Synthesis of 3-(dimethyl(3-(triethylsilyl)propyl)ammonio)propane-1-sulfonate (TESDMAPS)

Ring-opening of a cyclic sultone yielded the zwitterionic TESDMAPS. Propane sultone (7.41 g, 0.0607 mol, 1.00 eq) was dissolved in anhydrous tetrahydrofuran (75 mL) in a 250-mL round-bottomed flask equipped with a magnetic stir bar. The reaction flask was kept under a nitrogen atmosphere. Triethylsilyl dimethyl amine (11.6 g, 0.0578 mol, 0.952 eq) was added to the reaction flask and the reaction proceeded for 18 h. The white solid product was collected via vacuum filtration and washed with additional tetrahydrofuran. ^{1}H NMR (D_2O, δ, **Figure S9.1**, Supplemental Information) 3.55-3.46 (m, 2H, a), 3.38-3.30 (m, 2H, b), 3.20-3.10 (s, 6 H, c), 3.01-2.96 (t, 2H, d), 2.29-2.21(m, 2H, e), 1.83-174 (m, 2H, f), 1.04-0.98 (t, 9H, g), 0.67-0.60 (q, 6H, h), 0.60-0.57 (d, 2H, h'); ^{13}C NMR: (D_2O, δ, **Figure S9.2**, Supplemental Information) 64.02, 58.90, 48.33, 44.61, 15.85, 14.27, 4.31, 4.11, 0.03. ^{29}Si NMR: (D_2O, δ, **Figure S9.3**, Supplemental Information) 7.15.

9.2.7 Synthesis of N-ethyl-N,N-dimethyl-3-(triethylsilyl)propane-1-ammonium bromide (TESDMABr)

Nucleophilic substitution of bromoethane yielded the cationic surfactant triethylsilyl dimethyl ammonium bromide. Bromoethane (6.61 g, 0.0607 mol, 1.00 eq) was dissolved with anhydrous tetrahydrofuran (75 mL) in a 250-mL round-bottomed flask equipped with a magnetic stir bar. The solution was heated to 60 °C under a nitrogen atmosphere.

Triethylsilyl dimethyl amine (11.6 g, 0.0578 mol, 0.952 eq) was added to the reaction flask and the reaction proceeded for 18 h. The white solid product was collected upon vacuum filtration and washed with additional tetrahydrofuran. ^{1}H NMR (D_2O, δ, **Figure S9.4**, Supplemental Information) 3.42-3.34 (m, 2H, a), 3.30-3.23 (m, 2H, b), 3.07-3.00 (s, 6H, c), 1.80-1.70 (m, 2H, d), 1.39-1.31 (t, 3H, e) 1.00-0.91 (t, 9H, f) 0.63-0.56 (q, 6H, g), 0.56-0.54 (d, 2H, g'); ^{13}C NMR: (D_2O, δ, **Figure S9.5**, Supplemental Information) 63.69, 57.21, 47.46, 13.91, 5.01, 4.71, 4.52, 0.01. ^{29}Si NMR: (D_2O, δ, **Figure S9.6**, Supplemental Information) 7.15.

9.3 Results and Discussion

Photocatalyzed hydrosilylation provided hydrophobic N,N-dimethyl-3-(triethylsilyl)propan-1-amine. Subsequent reaction with either 1,3-propane sultone or bromoethane as depicted in **Scheme 9.1**, provided two surfactants with the same hydrophobic tail but differing hydrophilic heads. Ring-opening of 1,3-propane sultone provided a zwitterionic surfactant with both positive and negative charges covalently bound to the triethylsilyl hydrophobic tail (TESDMAPS). In contrast, the S_N2 reaction with bromoethane provided a cationic surfactant wherein only the positive charge was covalently bound to the hydrophobic tail and the bromide counteranion was not covalently bound to the hydrophobic tail (TESDMABr). These surfactants provided an opportunity to explore head group effects on the CMC, surface tension, foam stability, and viscoelastic behavior of a new family of silicon-containing surfactants.

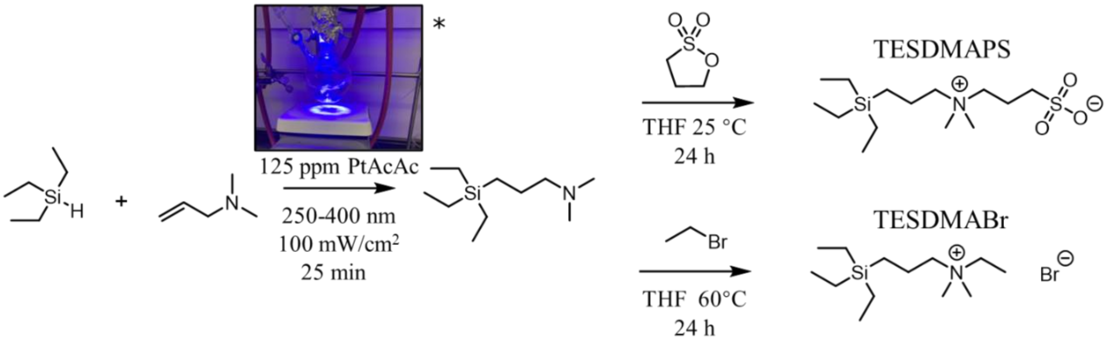

Scheme 9.1. Two-step synthesis of zwitterionic TESDMAPS (top) and cationic TESDMABr (bottom) triethylsilyl-containing surfactants.

DLS, as shown in **Figure 9.2,** revealed both CMC and size of surfactant self-assemblies in solution above the CMC. Exemplary DLS data is provided in **Figure S9.7**. Surfactant solutions ranging from 0.1 wt.% to 25 wt.% surfactant in water provided size *versus* concentration data for triethylsilyl-containing surfactants. The concentration when particle size increased from the baseline 0.7 nm particles to larger particles indicated the CMC. These data revealed zwitterionic TESDMAPS to self-assemble in solution at 1 wt.%. In comparison, cationic TESDMABr surfactant formed self-assemblies at 3 wt.%. Greater electrostatic repulsive forces between cationic heads imparted an additional energy barrier to micelle formation, which required a greater hydrophobic force and ultimately a higher concentration to self-assemble.[27] Additionally, a 50:50 wt.% mixture of TESMAPs and TESDMABr formed self-assemblies in solution at 2 wt.%, which suggests an averaging effect when zwitterionic and cationic surfactants with the same tails are mixed. These results are consistent with many previous studies exploring head effects on CMC.[28] Surface tension measurements across surfactant concentration, shown in **Figure S9.8**, confirmed these trends. Furthermore, DLS experiments showed TESDMAPS self-assembled structure increased in size above the CMC whereas the cationic surfactant remained consistent at 2 nm above the CMC.

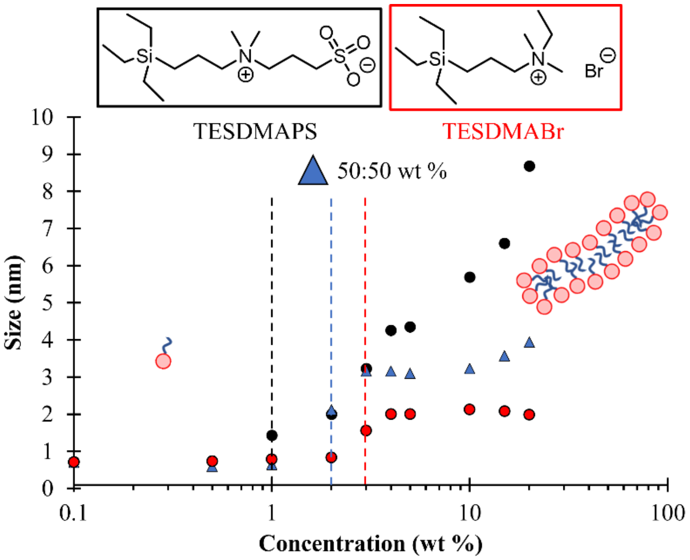

Figure 9.2. Size vs. concentration data from DLS revealed TESDMAPS and TESDMABr CMC and self-assembled size above the CMC.

TESDMAPS displayed a continual size increase above the CMC, which suggested either micelle to micelle aggregation in the zwitterionic surfactant, or the development of larger micelles in solution at these concentrations.[36] Cryo-transmission electron microscopy, as shown in **Figure 9.3**, revealed the nanoscale structure of TESDMAPS self-assembly in solution. TESDMAPS self-assembled structures appeared similar to previously reported short rod/wormlike micelles.[18,22,37] Furthermore, large irregularly shaped aggregates were observed within the TEM grid, which presumably accounted for increased sizes above the CMC as observed with DLS. Association between zwitterionic head groups enabled micelle to micelle aggregation at these concentrations and resulted in the presence of larger particles.

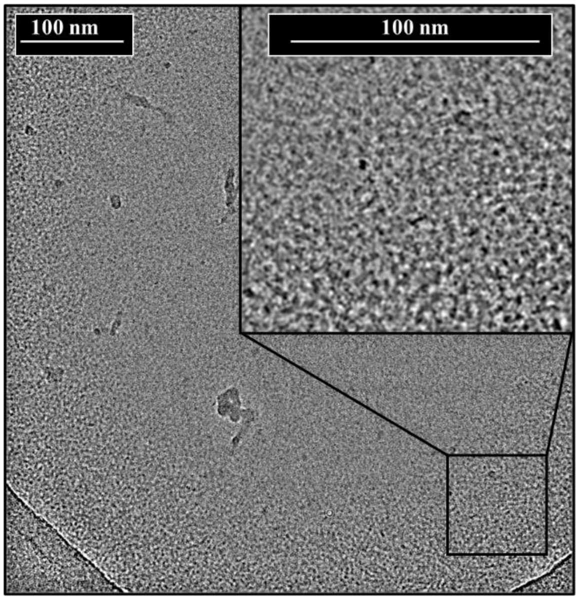

Figure 9.3. TEM micrograph of 5 wt.% TESDMAPS reveals formation of short/branched rod/wormlike micelles in addition to larger assemblies.

It is well known that surfactant solution surface tension plays a critical role in AFFF formulation. PFAS surfactant solutions with surface tensions of approximately 17 mN/m afforded a positive spreading coefficient, which enabled aqueous film formation on top of the fuel layer. This mechanism is known to afford improved fire-fighting performance. Previous work showed siloxane surfactants provided minimum surface tensions on the order of 20 mN/m, which enabled aqueous film formation and improved fire suppression.[38] This improved surface activity was often attributed to Si-O-Si bond flexibility, which results in improved surface activity.[39–41] However, other silicon-based surfactants have not been investigated to confirm this hypothesis. Triethylsilyl-containing surfactants provided a platform to isolate silicon effects within the hydrophobic tail without Si-O-Si bonds. Surface tension measurements at concentrations above the CMC, as summarized in **Table 9.1**, revealed both TESDMAPs and TESDMABr surfactants only lowered surface tension to 38.2 and 35.9 mN/m, respectively. This confirmed the desirability of Si-O-Si bonds in silicon-containing surfactant tails to sufficiently lower surface tension for AFFF applications.

Table 9.1. Summary of surface tension data for TESDMAPS, TESDMABr, and the 50:50 wt. % mixture.

Sample	**γ_{CMC} (mN/m)**	**γ_{3xCMC} (mN/m)**
TESDMAPS	37.7	38.2
50:50 wt.%	37.4	36.2
TESDMABr	37.8	35.9

Although triethylsilyl-containing surfactants did not sufficiently lower aqueous solution surface tension for AFFF applications, TESDMAPS and TESDMABr enabled fundamental understanding of hydrophilic head effects in the surface activity of surfactants. Cationic TESDMABr solutions at concentrations above the CMC demonstrated lower surface tensions than the zwitterionic TESDMAPS analogue. In addition, the 50:50 wt.% mixture of TESDMAPS and TESDMABr achieved an intermediate surface tension and synergistic head type effects were not observed. Molecular dynamics simulations at the air-water interface, as depicted in **Figure 9.4**, predicted molecular interfacial areas of individual surfactant molecules. TESDMABr occupied 88 Å^2 per molecule whereas TESDMAPS occupied only 66 Å^2 per molecule. This was consistent with head group repulsive forces that were present in cationic surfactants at the interface, which spaced surfactant molecules further from each other, thus decreasing surface tension.

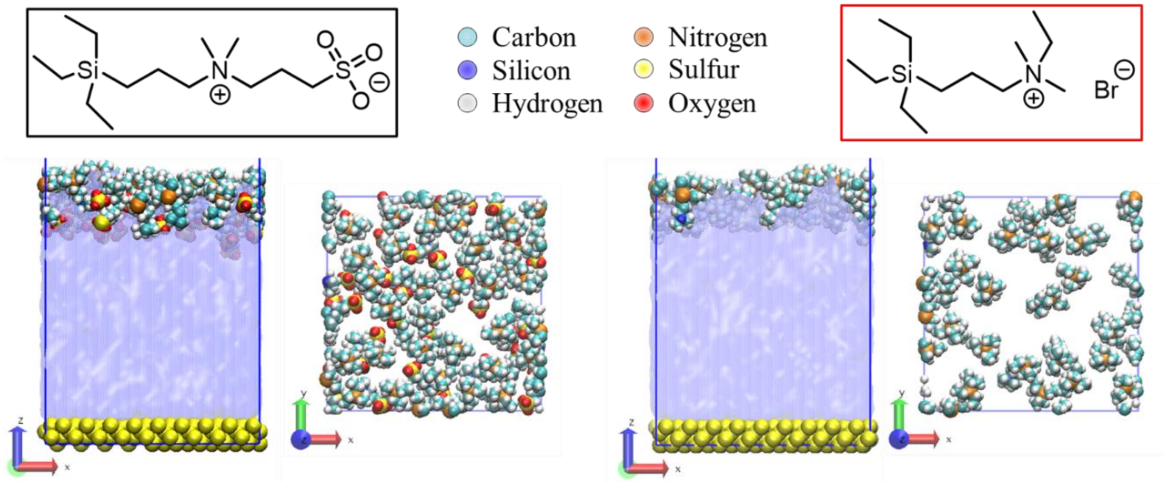

Figure 9.4. Zwitterion and cation molecular dynamics simulations highlight larger repulsive forces present in TESDMABr, which result in further distances between surfactant molecules at the air-water interface.

The flow behavior of solution self-assemblies has been shown to influence foam properties such as drainage time and expansion ratio.[38,42] During extrusion from a high shear rate nozzle during fire-fighting, solutions experience shear rates on the order of 10^3-10^4 1/s.[43] Thus, initial rheological experiments probed solution viscosities at shear rates equal to 10^3 1/s as shown in **Figure 9.5**. Steady-shear solution viscosity measurements revealed consistent exponential viscosity scaling trends between TESDMAPS, TESDMABr, and a 50:50 wt.% mixture of each surfactant from 5 wt.% to 30 wt.%. Differences in self-assembled structures in solution are known to impart large differences in viscosity.[44] Thus, consistent rheological behavior between surfactants indicated TESDMABr formed similar short/branched worm-like micelles in solution at these concentrations. However, at concentrations greater than 30 wt.%, the zwitterionic TESDMAPS surfactant displayed increased exponential viscosity scaling compared to cationic TESDMABr. In addition, the 50: 50 wt.% mixture of TESDMAPS and TESDMABr displayed an intermediate scaling relationship. The exponential scaling differed from many concentration dependent viscosity scaling relationships for macromolecules, which typically demonstrate power law scaling.[17,22,45,46] These high concentration solution rheology data demonstrated that stronger intermolecular interactions between zwitterionic self-assemblies resulted in greater solution viscosities under shear at these concentrations.

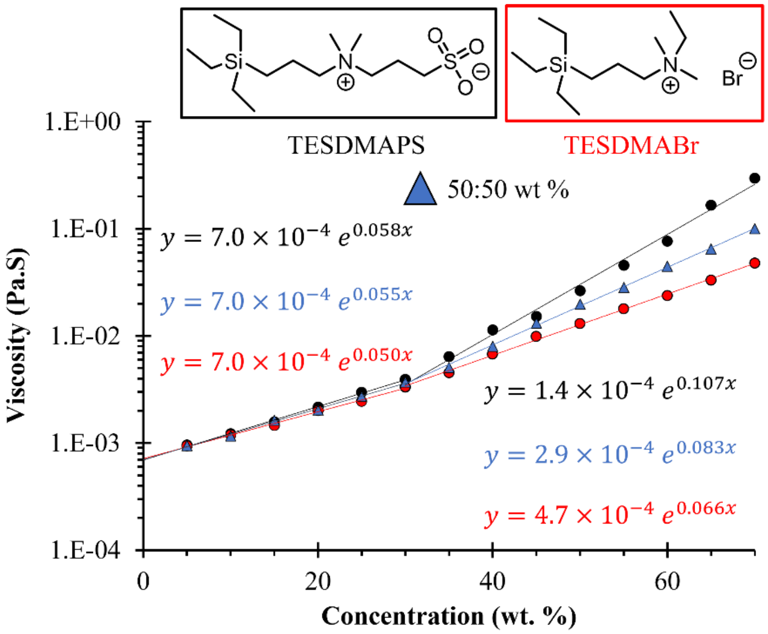

Figure 9.5. Triethylsilyl-containing surfactants display exponential concentration dependent viscosity scaling, and blends result in intermediate values. Data is fit to an exponential equation from 5 to 30 wt.% and from 30 to 70 wt.%.

DFA of 5 wt.% surfactant solutions, as shown in **Figure 9.6**, monitored foam height as a function of time following a 20 s air sparge. Cationic TESDMABr displayed the longest total drainage time, which exceeded the time scale of data collection. Time to 25% foam drainage from maximum foam height is typically reported when considering foams for fire-fighting applications.[47,48] TESDMABr drained 25% maximum foam height in 140 s whereas both TESDMAPS and the 50:50 wt.% mixture drained 25% maximum foam height in only 25 s. For reference, under identical experimental conditions, a 5 wt.% solution of sodium dodecyl sulfate (SDS) drained 25% maximum foam height in 94 s. TESDMAPS, TESDMABr, and the 50:50 wt.% mixture solutions displayed similar steady shear viscosities in the previously discussed rheological experiments and thus foam drainage was not directly linked to steady shear solution viscosity. Furthermore, the 50:50 wt.% mixed surfactant solutions did not display intermediate drainage time, which suggested net surface charge at the foam interface did not directly impact foam drainage times.

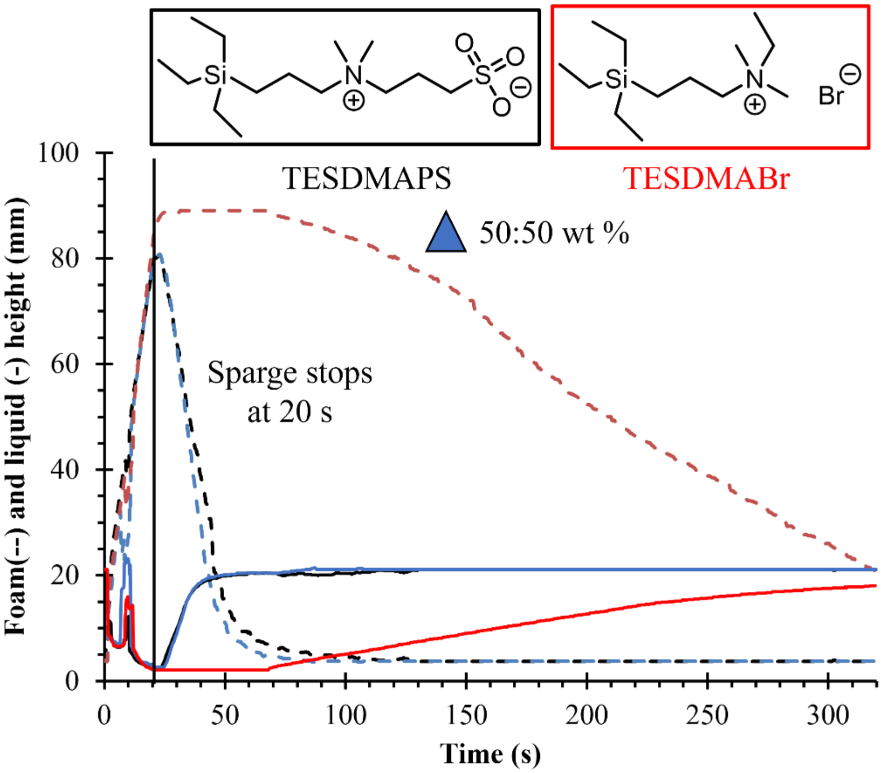

Figure 9.6. DFA results reveal TESDMABr solutions produce more stable foams following air sparge, and the 50:50 wt.% mixture displayed drainage times consistent with TESDMAPS.

Drainage time results from DFA experiments initially appeared counterintuitive with viscosity trends observed at high shear rates. However, foam drainage occurs at much lower shear rates driven by weak stresses generated from gas in the foam microstructure.[49,50] Previous work correlated low shear rate steady-shear viscosities of concentrated surfactant solutions to foam drainage, but the viscoelastic behavior of these solutions was not investigated.[38,47,48] For these reasons, oscillatory rheological measurements probed viscoelastic properties of concentrated surfactant solutions to elucidate foam solution properties at low shear rates, which were deemed to be more representative of foam drainage. Preliminary oscillatory rheological experiments demonstrated pre-shear effects on TESDMABr solution viscoelasticity (shown in **Figure S9.7)**. In the absence of pre-shear, the loss modulus of the solution remained greater than the storage modulus across all % strains. However, in experiments with a pre-shear step, the loss modulus of the material was less than the storage modulus at low shear rates, which revealed TESDMABr solutions displayed more solid-like viscoelasticity with the imposition of shear. A 60 s 10 1/s pre-shear produced the most consistent results across replicate experiments, and thus this pre-shear method was chosen for comparisons between TESDMAPs, the 50:50 wt.% mixture, and TESDMABr solutions. These rheological investigations, exemplified in **Figure 9.7**, revealed only TESDMABr solutions formed solid-like gels after shear, which correlated to significantly longer foam drainage times observed in DFA experiments.

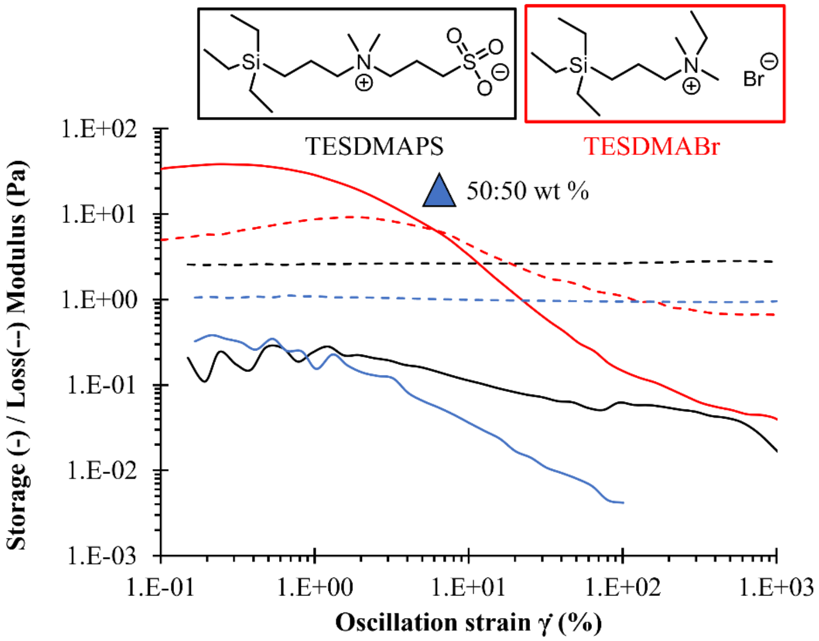

Figure 9.7. Oscillatory rheology showed concentrated (70 wt.%) cationic TESDMABr solution to display solid-like properties at low strain rates after a 60 s 10/1s pre-shear, whereas both TESDMAPS and the 50:50 wt.% mixture remained liquid-like at the same concentration.

These rheological experiments suggested TESDMABr surfactants formed stable structures under shear, which provided solid-like mechanical properties to the solution. Other worm-like micelles have been observed to form birefringent structures during shear, which prompted polarized light imaging rheological investigations.[51] **Figure 9.8** depicts concentrated TESDMABr solutions aligning in the shear direction, which formed anisotropic assemblies perpendicular to the rheometer plate radius over time. Differences in the refractive index of these anisotropic structures resulted in birefringence when viewed between cross polarizers.[52] In contrast, TESDMAPS did not display birefringence, and thus TESDMAPS did not form stable anisotropic structures under shear. The 50:50 wt.% mixture did not immediately display birefringence, but after 15 min of steady shear, birefringent structures appeared. However, birefringent structures initially formed at the plate edge where shear rates are the highest and additional aligned structures continued to form with time. Additional rheological investigations will be pursued in the future to better understand concentration, temperature, gap height, shear rate, and kinetic effects on triethylsilyl-containing surfactant assembly under shear.

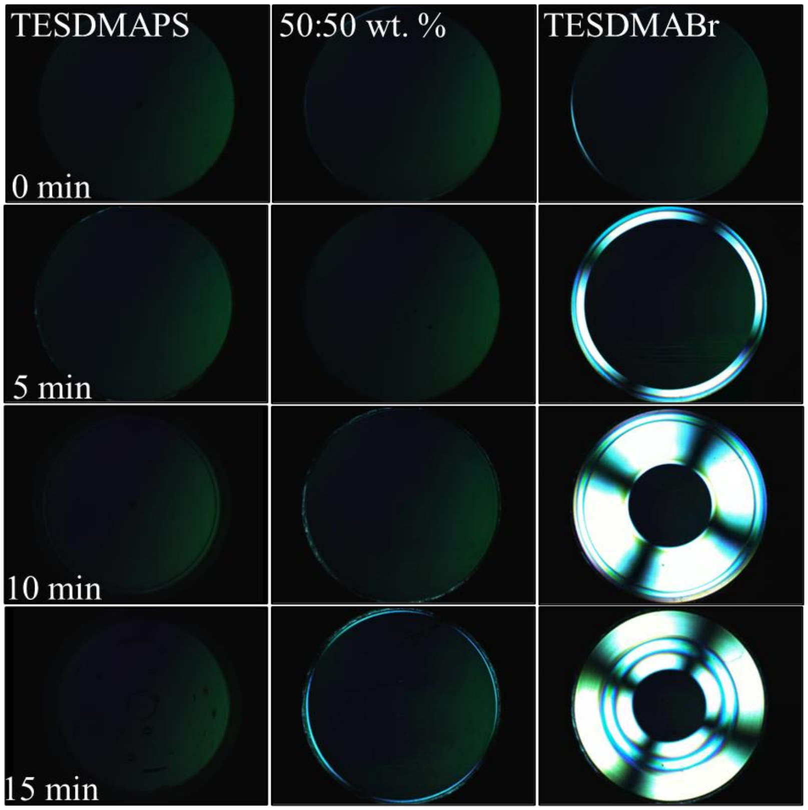

Figure 9.8. Polarized light rheology highlights surfactant alignment over time at 1000 1/s shear rate. Plate diameter is 25 mm.

9.4 Conclusion

Triethylsilyl-containing surfactants provided a platform to further understand hydrophilic head group effects on surfactant performance. Zwitterionic sulfobetaine TESDMAPS and cationic quaternary ammonium TESDMABr confirmed CMC trends where zwitterionic heads lowered the CMC. In addition, the cationic head group in TESDMABr provided lower minimum surface tensions than the zwitterionic analogue. Each surfactant displayed similar exponential concentration dependent viscosity scaling at concentrations below 30 wt.%, but TESDMAPS increased viscosity more effectively past this concentration. A 50:50 wt.% mixture of TESDMAPS and TESDMABr increased viscosity at an intermediate rate at these concentrations, which demonstrated the effect of zwitterionic association on solution viscosity. TESDMABr solutions significantly extended foam drainage times compared to TESDMAPS and the 50:50 wt.% mixture. Oscillatory rheological experiments revealed TESDMABr solution viscoelasticity, which afforded more solid-like mechanical properties at low shear rates representative of foam drainage. This solid-like behavior was not observed in either TESDMAPS solutions or the 50:50 wt.% mixture. Polarized light imaging rheology corroborated this phenomenon and monitored the formation of anisotropic birefringent structures under shear. The formation of stable anisotropic structures during high-shear foam generation improved low-shear foam drainage times. This understanding informed advantageous structure-property-performance relationships for future surfactant design to replace PFAS in AFFF.

9.5 Acknowledgements

The authors would like to thank the Department of Defense Strategic Environmental Research and Development Program (DOD SERDP) award number WP20-3048 for sponsoring this work. Any opinions, findings, and conclusions or recommendations expressed in this publication are those of the author(s) and do not necessarily reflect the views of DOD SERDP. The authors also thank Dr. Dewight Williams for his assistance with cryo-TEM imaging.

9.6 References

1. Lehmler, H. J. Synthesis of Environmentally Relevant Fluorinated Surfactants—a Review. *Chemosphere* **2005**, *58* (11), 1471–1496. https://doi.org/10.1016/J.CHEMOSPHERE.2004.11.078.

2. Hussain, S. M. S.; Adewunmi, A. A.; Mahboob, A.; Murtaza, M.; Zhou, X.; Kamal, M. S. Fluorinated Surfactants: A Review on Recent Progress on Synthesis and Oilfield Applications. *Adv Colloid Interface Sci* **2022**, *303*, 102634. https://doi.org/10.1016/J.CIS.2022.102634.

3. Filipovic, M.; Woldegiorgis, A.; Norström, K.; Bibi, M.; Lindberg, M.; Österås, A. H. Historical Usage of Aqueous Film Forming Foam: A Case Study of the Widespread Distribution of Perfluoroalkyl Acids from a Military Airport to Groundwater, Lakes, Soils and Fish. *Chemosphere* **2015**, *129*, 39–45. https://doi.org/10.1016/J.CHEMOSPHERE.2014.09.005.

4. Place, B. J.; Field, J. A. Identification of Novel Fluorochemicals in Aqueous Film-Forming Foams Used by the US Military. *Environ Sci Technol* **2012**, *46* (13), 7120–7127. https://doi.org/10.1021/ES301465N/SUPPL_FILE/ES301465N_SI_001.PDF.

5. Guenthner, F. A.; Vietor, M. L. SURFACE ACTIVE MATERIALS FROM PERFLUOROCARBOXYLIC AND PERFLUOROSULFONIC ACIDS.

6. Gao, S.; Cao, Z.; Niu, Q.; Zong, W.; Liu, R. Probing the Toxicity of Long-Chain Fluorinated Surfactants: Interaction Mechanism between Perfluorodecanoic Acid and Lysozyme. *J Mol Liq* **2019**, *285*, 607–615. https://doi.org/10.1016/J.MOLLIQ.2019.04.134.

7. Moody, C. A.; Field, J. A. Perfluorinated Surfactants and the Environmental Implications of Their Use in Fire-Fighting Foams. *Environ Sci Technol* **2000**, *34* (18), 3864–3870. https://doi.org/10.1021/ES991359U/ASSET/IMAGES/LARGE/ES991359UF00003.JPEG.

8. Hinnant, K. M.; Giles, S. L.; Smith, E. P.; Snow, A. W.; Ananth, R. Characterizing the Role of Fluorocarbon and Hydrocarbon Surfactants in Firefighting-Foam Formulations for Fire-Suppression. *Fire Technol* **2020**, *56*, 1413–1441. https://doi.org/10.1007/s10694-019-00932-7.

9. Sheng, Y.; Jiang, N.; Lu, S.; Li, C. Fluorinated and Fluorine-Free Firefighting Foams Spread on Heptane Surface. *Colloids Surf A Physicochem Eng Asp* **2018**, *552*, 1–8. https://doi.org/10.1016/J.COLSURFA.2018.05.004.

10. Kovalchuk, N. M.; Trybala, A.; Starov, V.; Matar, O.; Ivanova, N. Fluoro- vs Hydrocarbon Surfactants: Why Do They Differ in Wetting Performance? *Adv Colloid Interface Sci* **2014**, *210*, 65–71. https://doi.org/10.1016/J.CIS.2014.04.003.

11. Kunieda, H.; Shinoda, K. Solubilizing Power of Aqueous Solutions of Fluorinated Surfactants.

12. Hetzer, R. H.; Kümmerlen, F.; Wirz, K.; Blunk, D. Fire Testing a New Fluorine-Free AFFF Based on a Novel Class of Environmentally Sound High Performance Siloxane Surfactants. **2014**. https://doi.org/10.3801/IAFSS.FSS.11-1261.

13. Ananth, R.; Snow, A. W.; Hinnant, K. M.; Giles, S. L.; Farley, J. P. Synergisms between Siloxane-Polyoxyethylene and Alkyl Polyglycoside Surfactants in Foam Stability and Pool Fire Extinction. *Colloids Surf A Physicochem Eng Asp* **2019**, *579*. https://doi.org/10.1016/j.colsurfa.2019.123686.

14. Moradighadi, N.; Lewis, S.; Dominguez Olivo, J.; Young, D.; Brown, B.; Neši´c, S. N. Determining Critical Micelle Concentration of Organic Corrosion Inhibitors and Its Effectiveness in Corrosion Mitigation. **2021**. https://doi.org/10.5006/3679.

15. Meyer, E. E.; Rosenberg, K. J.; Israelachvili, J. Recent Progress in Understanding Hydrophobic Interactions. *Proceedings of the National Academy of Sciences* **2006**, *103* (43), 15739–15746. https://doi.org/10.1073/PNAS.0606422103.

16. Romsted, L. S. Introduction to Surfactant Self-Assembly. *Supramol Chem* **2012**. https://doi.org/10.1002/9780470661345.SMC013.

17. Fan, H.; Yan, Y.; Li, Z.; Xu, Y.; Jiang, L.; Xu, L.; Zhang, B.; Huang, J. General Rules for the Scaling Behavior of Linear Wormlike Micelles Formed in Catanionic Surfactant Systems. *J Colloid Interface Sci* **2010**, *348* (2), 491–497. https://doi.org/10.1016/J.JCIS.2010.04.065.

18. Molchanov, V. S.; Kuklin, A. I.; Orekhov, A. S.; Arkharova, N. A.; Philippova, O. E. Temporally Persistent Networks of Long-Lived Mixed Wormlike Micelles of Zwitterionic and Anionic Surfactants. *J Mol Liq* **2021**, *342*, 116955. https://doi.org/10.1016/J.MOLLIQ.2021.116955.

19. Hemp, S. T.; Hudson, A. G.; Allen, M. H.; Pole, S. S.; Moore, R. B.; Long, T. E. Solution Properties and Electrospinning of Phosphonium Gemini Surfactants. *Soft Matter* **2014**, *10* (22), 3970–3977. https://doi.org/10.1039/C4SM00271G.

20. Weissman, S.; Mason, E. A. Determination of Gaseous-Diffusion Coefficients from Viscosity Measurements. *J Chem Phys* **2004**, *37* (6), 1289. https://doi.org/10.1063/1.1733277.

21. Ronteltap, A. D.; Damsté, B. R.; De Gee, M.; Prins, A. The Role of Surface Viscosity in Gas Diffusion in Aqueous Foams. I. Theoretical. *Colloids and Surfaces* **1990**, *47* I, 269–283. https://doi.org/10.1016/0166-6622(90)80078-I.

22. Cashion, M. P.; Li, X.; Geng, Y.; Hunley, M. T.; Long, T. E. Gemini Surfactant Electrospun Membranes. *Langmuir* **2010**, *26* (2), 678–683. https://doi.org/10.1021/LA902287B/ASSET/IMAGES/LARGE/LA-2009-02287B_0007.JPEG.

23. Svenson, S. Controlling Surfactant Self-Assembly. *Curr Opin Colloid Interface Sci* **2004**, *9* (3–4), 201–212. https://doi.org/10.1016/J.COCIS.2004.06.008.

24. Nagarajan, R. Molecular Packing Parameter and Surfactant Self-Assembly: The Neglected Role of the Surfactant Tail. *Langmuir* **2002**, *18* (1), 31–38. https://doi.org/10.1021/LA010831Y/ASSET/IMAGES/MEDIUM/LA010831YE00021.GIF.

25. McKee, M. G.; Layman, J. M.; Cashion, M. P.; Long, T. E. Phospholipid Nonwoven Electrospun Membranes. *Science (1979)* **2006**, *311* (5759), 353–355. https://doi.org/10.1126/SCIENCE.1119790/SUPPL_FILE/MCKEE.SOM.PDF.

26. Kume, G.; Gallotti, M.; Nunes, G. Review on Anionic/Cationic Surfactant Mixtures. *J Surfactants Deterg* **2008**, *11* (1), 1–11. https://doi.org/10.1007/S11743-007-1047-1/FIGURES/17.

27. Nagarajan, R.; Ruckenstein, E. Theory of Surfactant Self-Assembly: A Predictive Molecular Thermodynamic Approach. *Langmuir* **1991**, *7*, 2934–2969.

28. *Critical Micelle Concentrations of Aqueous Surfactant Systems,*. https://apps.dtic.mil/sti/citations/ADD095344 (accessed 2023-03-16).

29. The Preparation Method and Aldehyde-Free Colour Stabilizer of DMAA. **2017**.

30. Abraham, M. J.; Murtola, T.; Schulz, R.; Páll, S.; Smith, J. C.; Hess, B.; Lindah, E. GROMACS: High Performance Molecular Simulations through Multi-Level Parallelism from Laptops to Supercomputers. *SoftwareX* **2015**, *1–2*, 19–25. https://doi.org/10.1016/J.SOFTX.2015.06.001.

31. Humphrey, W.; Dalke, A.; Schulten, K. VMD: Visual Molecular Dynamics. *J Mol Graph* **1996**, *14* (1), 33–38. https://doi.org/10.1016/0263-7855(96)00018-5.

32. Dodda, L. S.; De Vaca, I. C.; Tirado-Rives, J.; Jorgensen, W. L. LigParGen Web Server: An Automatic OPLS-AA Parameter Generator for Organic Ligands. *Nucleic Acids Res* **2017**, *45* (W1), W331–W336. https://doi.org/10.1093/NAR/GKX312.

33. Mark, P.; Nilsson, L. Structure and Dynamics of the TIP3P, SPC, and SPC/E Water Models at 298 K. *Journal of Physical Chemistry A* **2001**, *105* (43), 9954–9960.

https://doi.org/10.1021/JP003020W/ASSET/IMAGES/LARGE/JP003020WF00004.JPEG.

34. Joung, I. S.; Cheatham, T. E. Determination of Alkali and Halide Monovalent Ion Parameters for Use in Explicitly Solvated Biomolecular Simulations. *Journal of Physical Chemistry B* **2008**, *112* (30), 9020–9041. https://doi.org/10.1021/JP8001614/SUPPL_FILE/JP8001614-FILE003.PDF.

35. Martinez, L.; Andrade, R.; Birgin, E. G.; Martínez, J. M. PACKMOL: A Package for Building Initial Configurations for Molecular Dynamics Simulations. *J Comput Chem* **2009**, *30* (13), 2157–2164. https://doi.org/10.1002/JCC.21224.

36. Pan, Y.; Tong, K.; Lin, M.; Zhuang, W.; Zhu, W.; Chen, X.; Li, Q. Aggregation Behaviours of Sulfobetaine Zwitterionic Surfactants in EAN. *J Mol Liq* **2022**, *368*, 120608. https://doi.org/10.1016/J.MOLLIQ.2022.120608.

37. Liu, Q.; Lv, D.; Zhang, J.; Huang, C.; Yin, B.; Wei, X.; Li, J. Triple-Responsive Wormlike Micelles Based on Cationic Surfactant and Sodium Trans-o-Methoxycinnamic Acid. *J Mol Liq* **2021**, *324*, 114680. https://doi.org/10.1016/J.MOLLIQ.2020.114680.

38. Hinnant, K. M.; Ananth, R.; Farley, J. P.; Whitehurst, C. L.; Giles, S. L.; Maza, W. A.; Snow, A. W.; Karwosky, S.; Hughes Jensen. *Extinction Performance Summary of Commercial Fluorine-Free Firefighting Foams over a 28 Ft2 Pool Fire Detailed by MIL-PRF-24385*; 2019. https://apps.dtic.mil/sti/citations/AD1100426 (accessed 2023-03-13).

39. Snow, S. A.; Fenton, W. N.; Owen, M. J. Synthesis and Characterization of Zwitterionic Silicone Sulfobetaine Surfactants. *Langmuir* **1990**, *6*, 385–391.

40. Hill, R. M. Silicone Surfactants—New Developments. *Curr Opin Colloid Interface Sci* **2002**, *7* (5–6), 255–261. https://doi.org/10.1016/S1359-0294(02)00068-7.

41. Ananth. Zwitterionic and Glucoside Surfactant Formulations for Fire-Fighting Foam Applications. **2022**, *444*.

42. Yu, X.; Li, F.; Fang, H.; Miao, X.; Wang, J.; Zong, R.; Lu, S. Foaming Behavior of Fluorocarbon Surfactant Used in Fire-Fighting: The Importance of Viscosity and Self-Assembly Structure. *J Mol Liq* **2021**, *327*, 114811. https://doi.org/10.1016/J.MOLLIQ.2020.114811.

43. Carnicer, V.; Alcázar, C.; Orts, M. J.; Sánchez, E.; Moreno, R. Microfluidic Rheology: A New Approach to Measure Viscosity of Ceramic Suspensions at Extremely High Shear Rates. *Open Ceramics* **2021**, *5*, 100052. https://doi.org/10.1016/J.OCERAM.2020.100052.

44. Zhou, J.; Ranjith, P. G. Self-Assembly and Viscosity Changes of Binary Surfactant Solutions: A Molecular Dynamics Study. *J Colloid Interface Sci* **2021**, *585*, 250–257. https://doi.org/10.1016/J.JCIS.2020.11.022.

45. Liu, B.; Brown, J. R.; Zeng, C.; Rajput, H.; McDonough, R. K.; Westerhoff, P.; Long, T. E. Spiropyran-Containing Water-Soluble and Photoreversible Copolymers. *Polymer (Guildf)* **2023**, *272*, 125827. https://doi.org/10.1016/J.POLYMER.2023.125827.

46. Lopez, C. G.; Colby, R. H.; Graham, P.; Cabral, J. T. Viscosity and Scaling of Semiflexible Polyelectrolyte NaCMC in Aqueous Salt Solutions. *Macromolecules* **2017**, *50* (1), 332–338. https://doi.org/10.1021/ACS.MACROMOL.6B02261/ASSET/IMAGES/LARGE/MA-2016-022618_0005.JPEG.

47. Magrabi, S. A.; Dlugogorski, B. Z.; Jameson, G. J. A Comparative Study of Drainage Characteristics in AFFF and FFFP Compressed-Air Fire-Fighting Foams. *Fire Saf J* **2002**, *37* (1), 21–52. https://doi.org/10.1016/S0379-7112(01)00024-8.

48. Yekeen, N.; Idris, A. K.; Manan, M. A.; Samin, A. M.; Risal, A. R.; Kun, T. X. Bulk and Bubble-Scale Experimental Studies of Influence of Nanoparticles on Foam Stability. *Chin J Chem Eng* **2017**, *25* (3), 347–357. https://doi.org/10.1016/J.CJCHE.2016.08.012.

49. Dhasindrakrishna, K.; Pasupathy, K.; Ramakrishnan, S.; Sanjayan, J. Effect of Yield Stress Development on the Foam-Stability of Aerated Geopolymer Concrete. *Cem Concr Res* **2020**, *138*, 106233. https://doi.org/10.1016/J.CEMCONRES.2020.106233.

50. Stone, H. A.; Koehler, S. A.; Hilgenfeldt, S.; Durand, M. Perspectives on Foam Drainage and the Influence of Interfacial Rheology. *Journal of Physics: Condensed Matter* **2002**, *15* (1), S283. https://doi.org/10.1088/0953-8984/15/1/338.

51. Mykhaylyk, O. O.; Warren, N. J.; Parnell, A. J.; Pfeifer, G.; Laeuger, J. Applications of Shear-Induced Polarized Light Imaging (SIPLI) Technique for Mechano-Optical Rheology of Polymers and Soft Matter Materials. *J Polym Sci B Polym Phys* **2016**, *54* (21), 2151–2170. https://doi.org/10.1002/POLB.24111.

52. Bragg, W. L.; Pippard, A. B.; IUCr. The Form Birefringence of Macromolecules. *Urn:issn:0365-110X* **1953**, *6* (11–12), 865–867. https://doi.org/10.1107/S0365110X53002519.

9.7 Supplemental Information

Table S9.1. Case studies to determine the saturated surfactant density at water-vapor interface.

The number of surfactant (surfactant type)	The number of surfactants in monolayer	The number of surfactants in water
50 *(zwitterionic)*	44	6
40 *(zwitterionic)*	36	4
36 *(zwitterionic)*	36	0
36 *(cationic)*	30	6
30 *(cationic)*	30	0
27 *(cationic)*	27	0

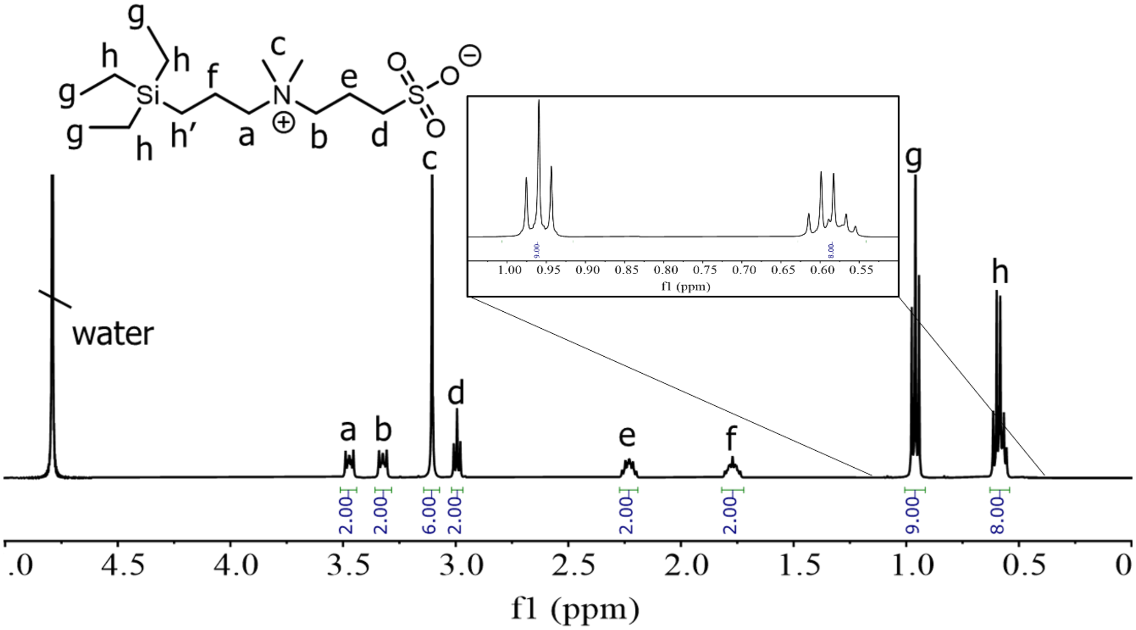

Figure S9.1. ^{1}H NMR spectrum of 3-(dimethyl(3-(triethylsilyl)propyl)ammonio)propane-1-sulfonate.

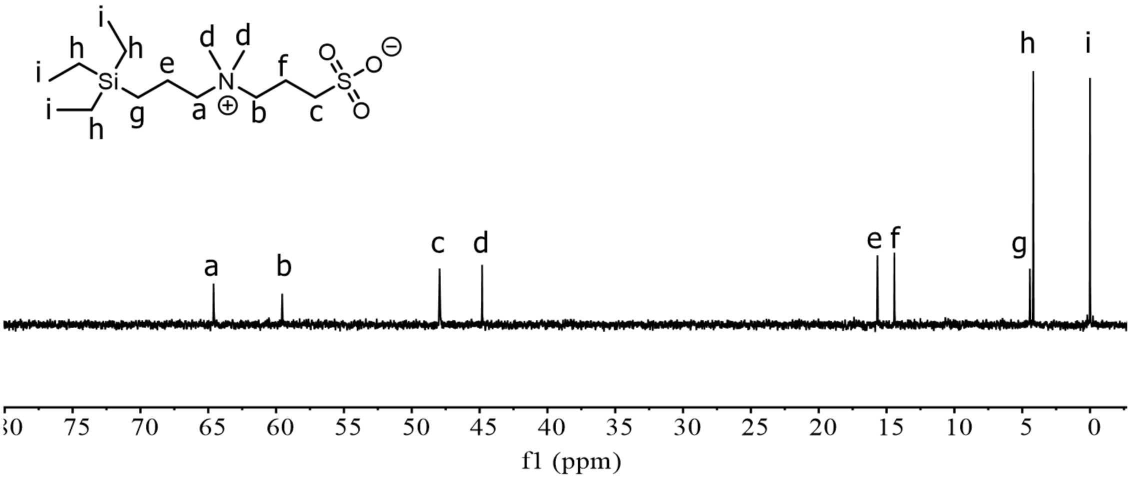

Figure S9.2. ^{13}C NMR spectrum of 3-(dimethyl(3(triethylsilyl)propyl)ammonio)propane-1-sulfonate.

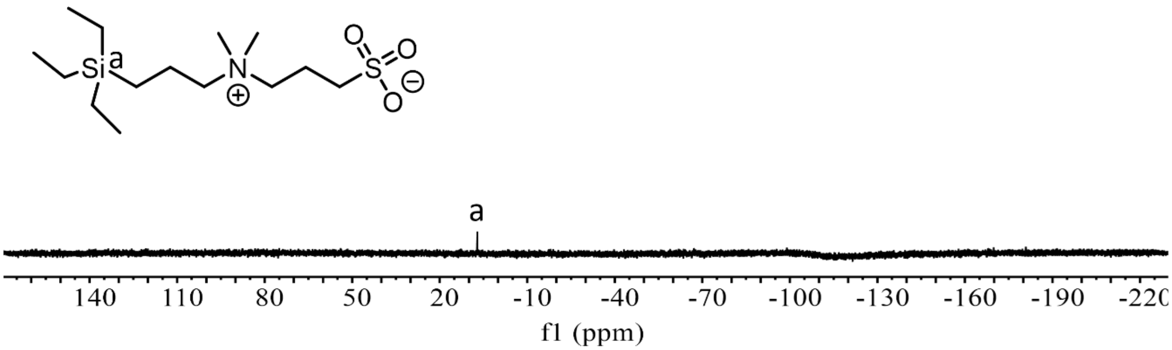

Figure S9.3. ^{29}Si NMR spectrum of 3-(dimethyl(3-(triethylsilyl)propyl)ammonio)propane-1-sulfonate.

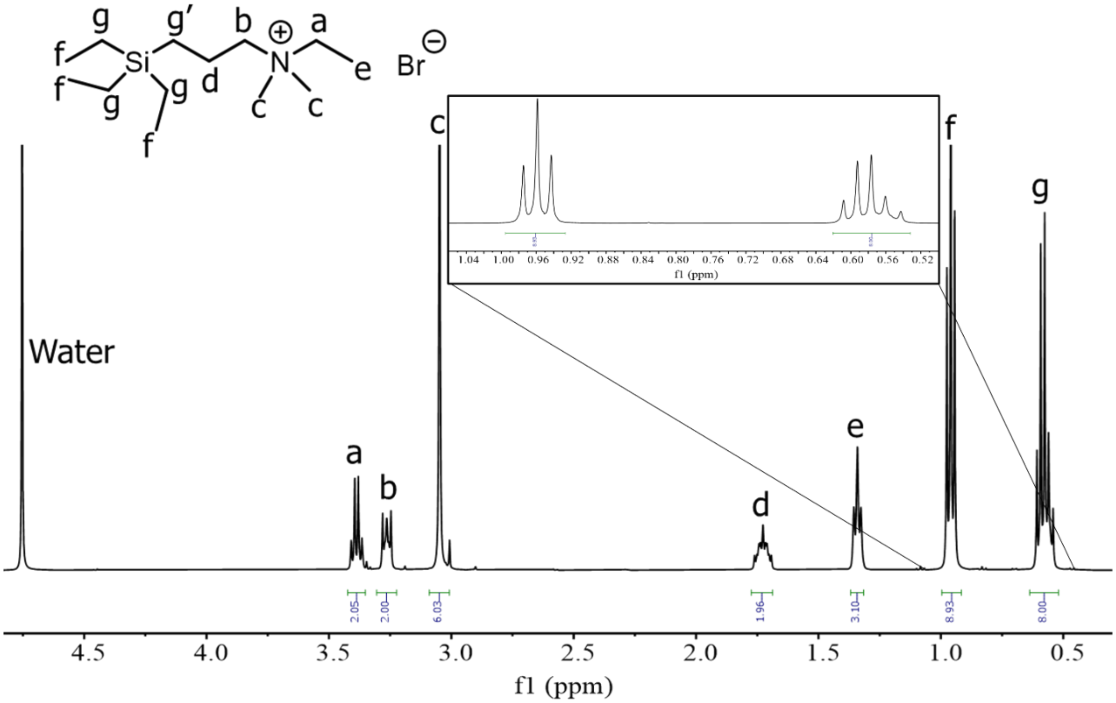

Figure S9.4. ^{1}H NMR spectrum of N-ethyl-N,N-dimethyl-3-(triethylsilyl)propane-1-ammonium bromide.

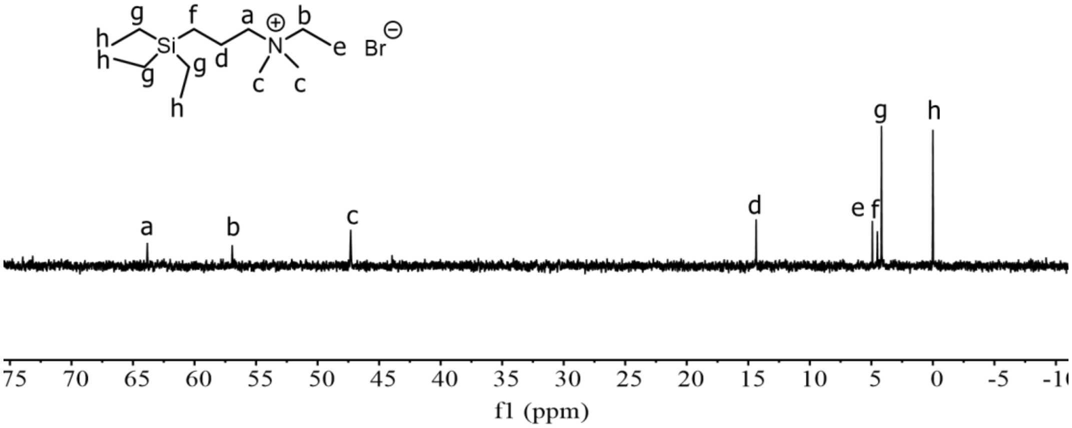

Figure S9.5. ^{13}C NMR spectrum of N-ethyl-N,N-dimethyl-3-(triethylsilyl)propane-1-ammonium bromide.

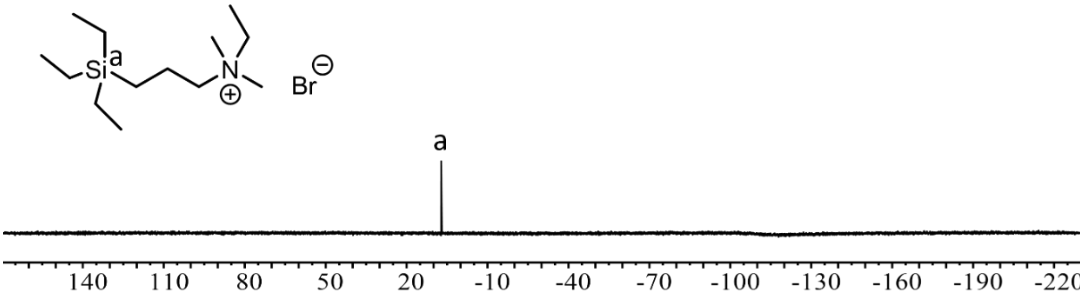

Figure S9.6. ^{29}Si NMR spectrum of N-ethyl-N,N-dimethyl-3-(triethylsilyl)propane-1-ammonium bromide.

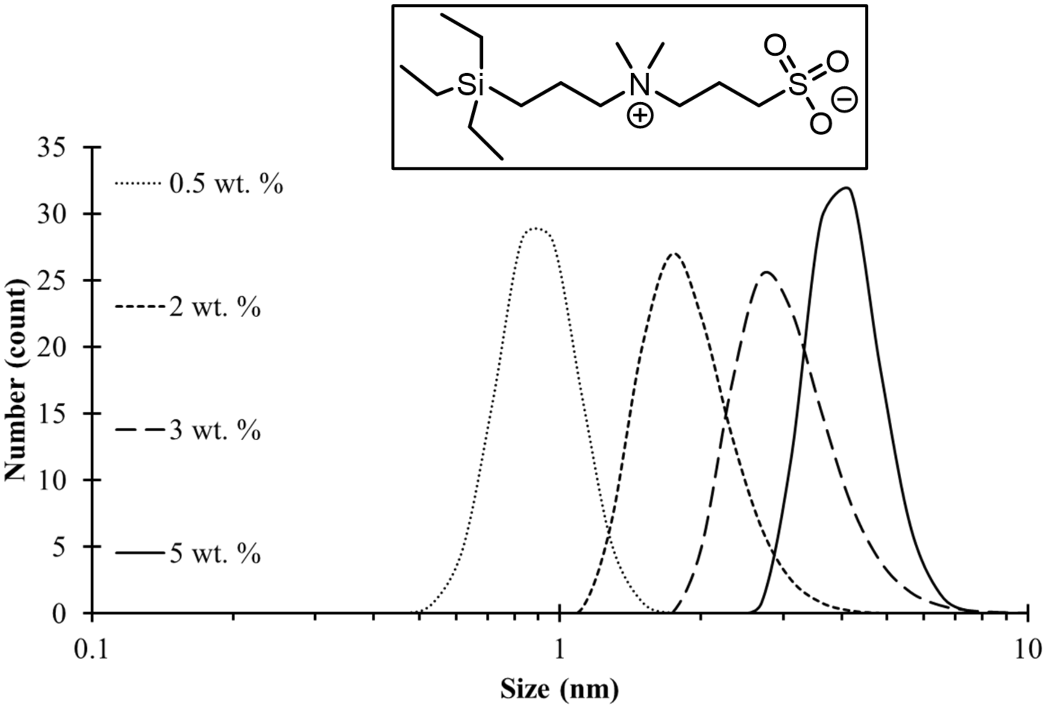

Figure S9.7. Exemplary DLS data used to determine particle size across surfactant concentrations.

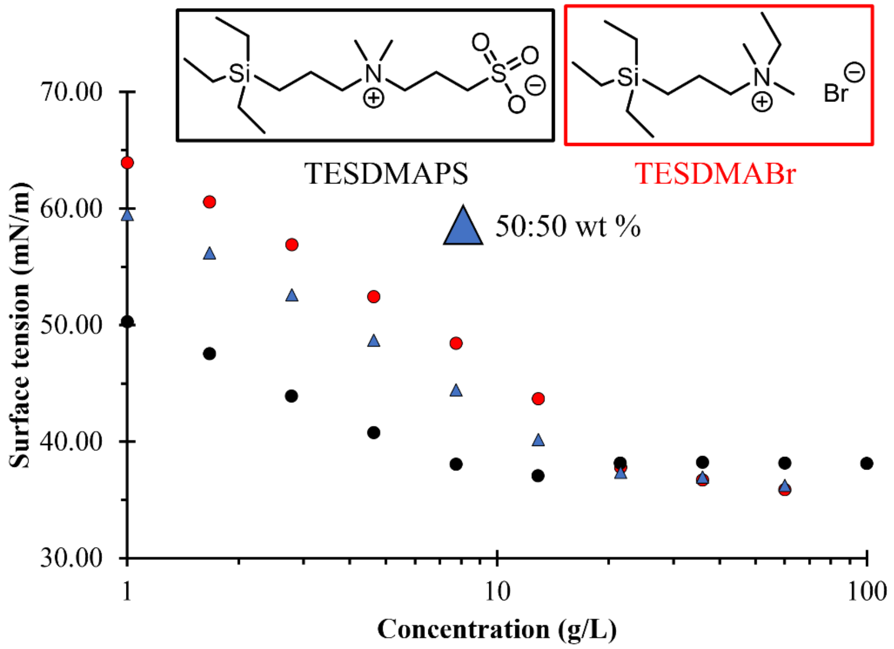

Figure S9.8. Surface tension vs. concentration data used to determine surface tension and confirm CMC trends.

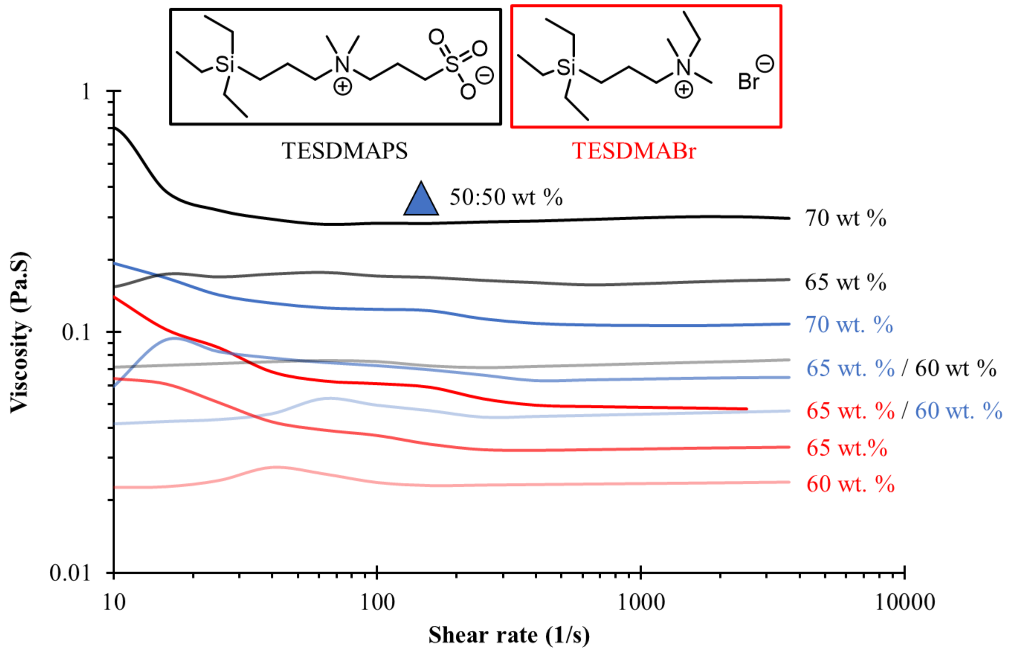

Figure S9.9. Exemplary shear sweep rheological data used to determine viscosity scaling profiles at 1000 1/s

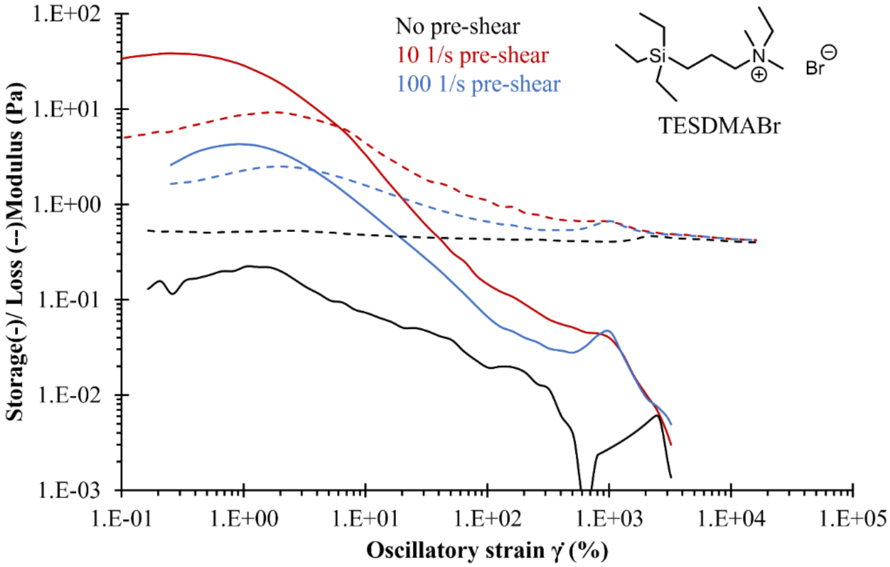

Figure S9.10. TESDMABr oscillatory rheology confirms structure development during shear, which displayed solid-like properties at low oscillatory strain.

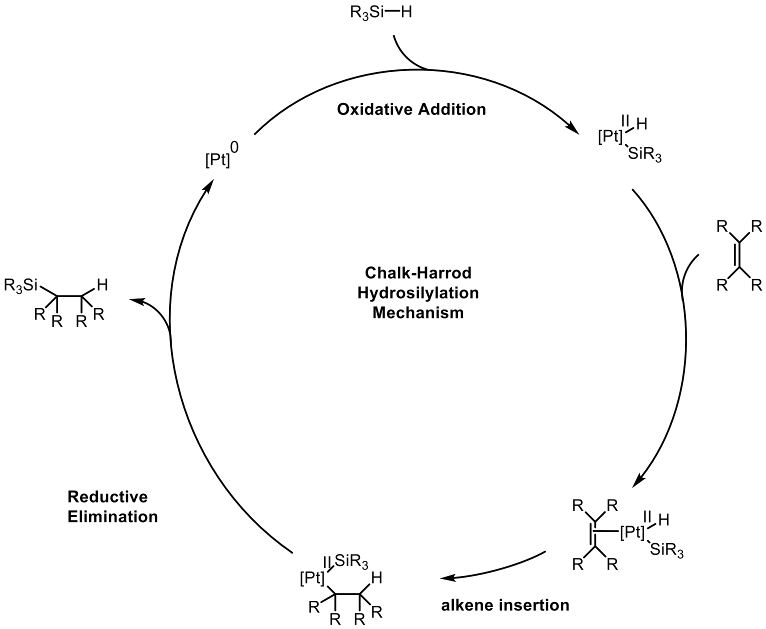

Figure S9.11. Generalized Chalk-Harrod hydrosilylation mechanism.

CHAPTER 10

FUTURE WORKS

10.1 Triethylsilyl and Trisiloxane Gemini Surfactants for Enhanced Foam Stability and Reduced Surface Tension

Work conducted in chapter 9 identified that triethylsilyl surfactants with cationic heads formed self-assembled structures in solution, which formed stable higher order structures under shear. This property of cationic surfactants encouraged investigation into gemini surfactants with two cationic heads covalently bound to one another. Furthermore, chapter 9 demonstrated that triethylsilyl surfactants do not sufficiently lower solution surface tension for AFFF applications.[1,2] This finding emphasized the need for trisiloxane functionality in silicon-containing surfactants for AFFF applications. Thus, both triethylsilyl and trisiloxane gemini surfactants were synthesized in a similar manner to the reactions outlined in chapter 9 (**Scheme 10.1**). These structures will further inform tail effects in surfactant design and will also confirm shear alignment effects from surfactant heads attached to different tails.

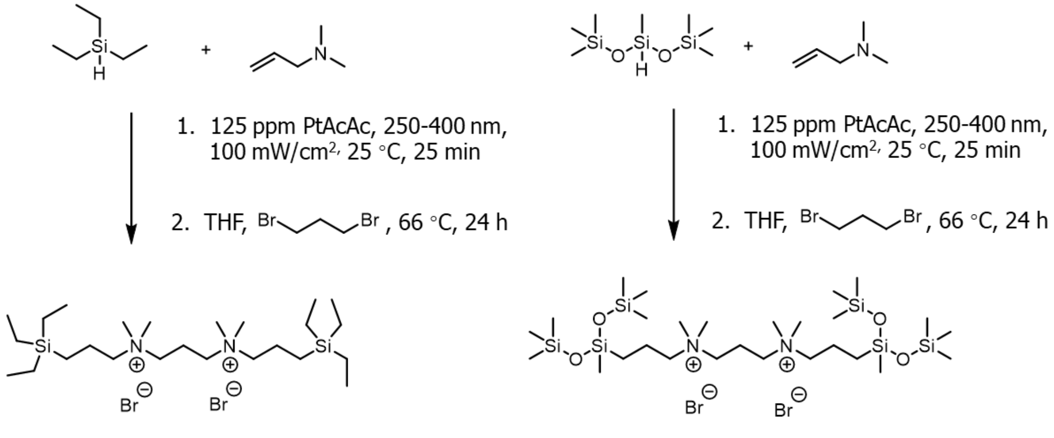

Scheme 10.1. Synthesis of triethylsilyl cationic gemini (left) and trisiloxane gemini cationic surfactant (right) surfactants.

Preliminary analysis of the triethylsilyl gemini surfactant informed gemini head effects on surface tension and foam stability. Surface tensiometry, shown in **Figure 10.1a** elucidated that the gemini head lowered minimum surface tension of triethylsilyl surfactant solutions to 28.2 mN/m. This value is significantly lower than both the zwitterionic and cationic triethylsilyl surfactants, which had minimum surface tensions of 37.7 and 35.9 mN/m respectively. This result further encourages development of novel gemini surfactant structures, as this head type profoundly decreased surface tension compared to cationic and zwitterionic surfactants with similar tail types. If this trend follows in trisiloxane tails, the 25% decrease in surface tension compared to a zwitterionic head will ensure aqueous film formation in fire-fighting applications.[3]

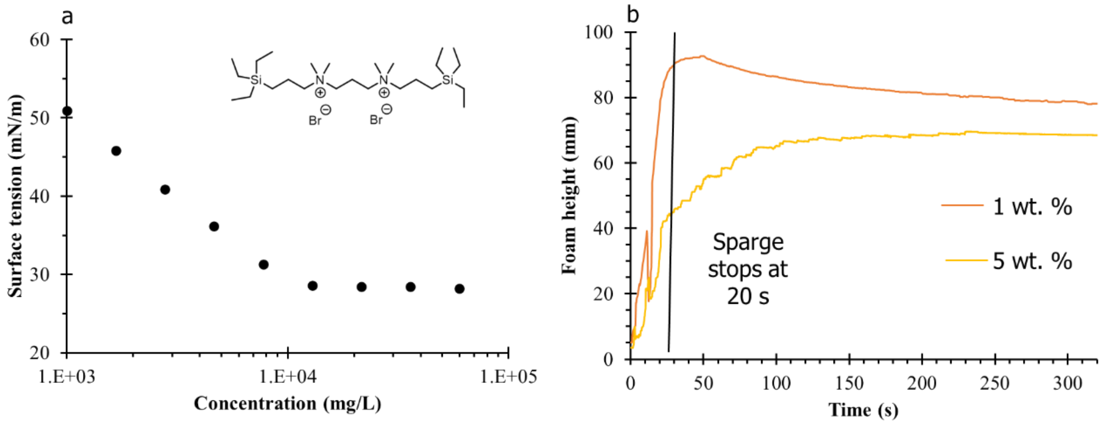

Figure 10.1. (a) surface tensiometry revealed the cationic gemini surfactant to display significantly lower surface tensions compared to triethylsilyl surfactants with different head types.

In addition to surface tensiometry, dynamic foam analysis measured foam height over time shown in **Figure 10.1b.** These experiments demonstrated the gemini surfactant to form very stable foams, which did not drain to 75 % foam height within the timeframe of the experiment. Furthermore, with a 5 wt. % solution, foam height increased after the air sparge, which was unique to this surfactant solution from all other tested samples. The increased foam stability of the cationic triethylsilyl surfactant suggested the surfactant also formed self-assemblies which established stable micelle alignments under shear as seen in the triethylsilyl cationic surfactant in chapter 9. Preliminary rheological experiments shown in **Figure 10.2** tested this hypothesis by measuring viscoelastic properties of concentrated triethylsilyl surfactant solutions before and after shear. As expected, the solution remained liquid like across the oscillatory stress sweep without performing a pre-shear step in the experiment. Additionally, the solution behaved as a viscoelastic solid at low oscillatory stresses following a 60 second pre-shear at 1000 1/s. This validated the previous rheological methodology when applied to another surfactant system and it also suggests the triethylsilyl cationic gemini surfactant self-assemblies formed stable aligned structures under shear, which improved foam stability. Further polarized optical rheology will confirm the formation of these structures under shear as they have for other wormlike micelles.[4]

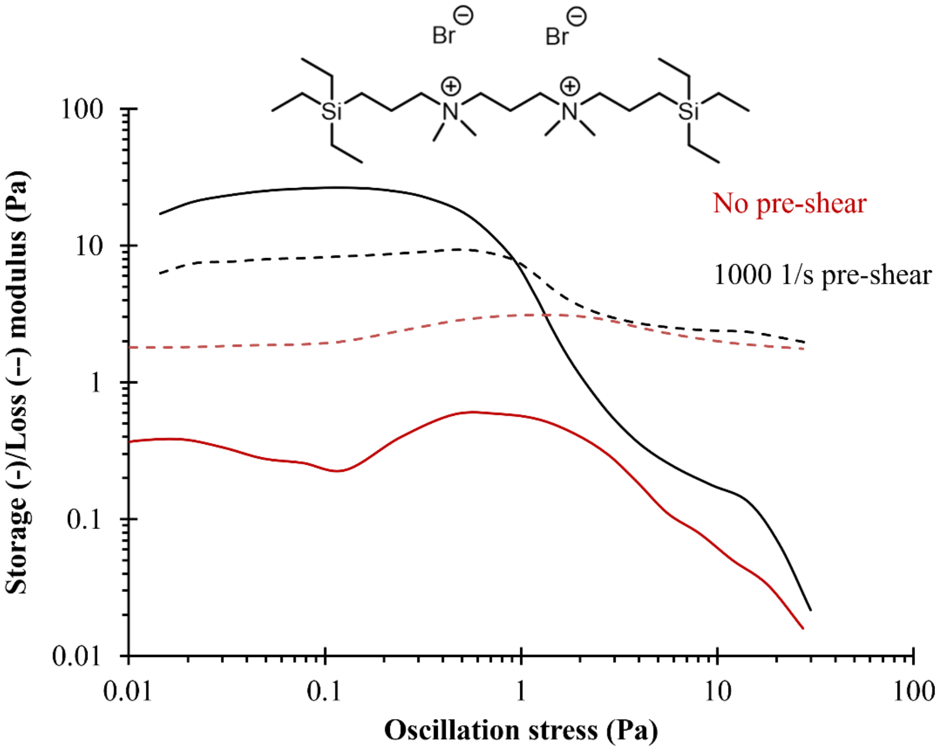

Figure 10.2. Oscillatory rheology revealed 70 wt.% triethylsilyl cationic gemini surfactant solutions to behave as viscoelastic solids following shear-induced micelle alignment.

Preliminary DLS investigations, shown in **Figure 10.3a,** revealed trisiloxane cationic gemini surfactant solutions to contain large self-assemblies greater than 100 nm in aqueous solution at concentrations greater than or equal to 0.0001 wt.%. These large surfactant-self-assemblies are either micelle to micelle aggregates or vesicles surrounding an internal aqueous phase. Zeta potential measurements of 0.01 wt. % solutions of the synthesized trisiloxane cationic gemini surfactant, shown in **Figure 10.3b**, revealed an average zeta potential of 47 mV. This zeta potential is much larger than 30 mV, which is often regarded as a lower limit to prevent aggregation of suspended particles.[5] Thus, it is unlikely that these surfactant self-assemblies aggregate in solution, and it is more likely that these large self-assemblies are vesicles in solution. Further morphological experiments such as small angle neutron scattering and cryo-transmission electron microscopy remain necessary to further validate this hypothesis.

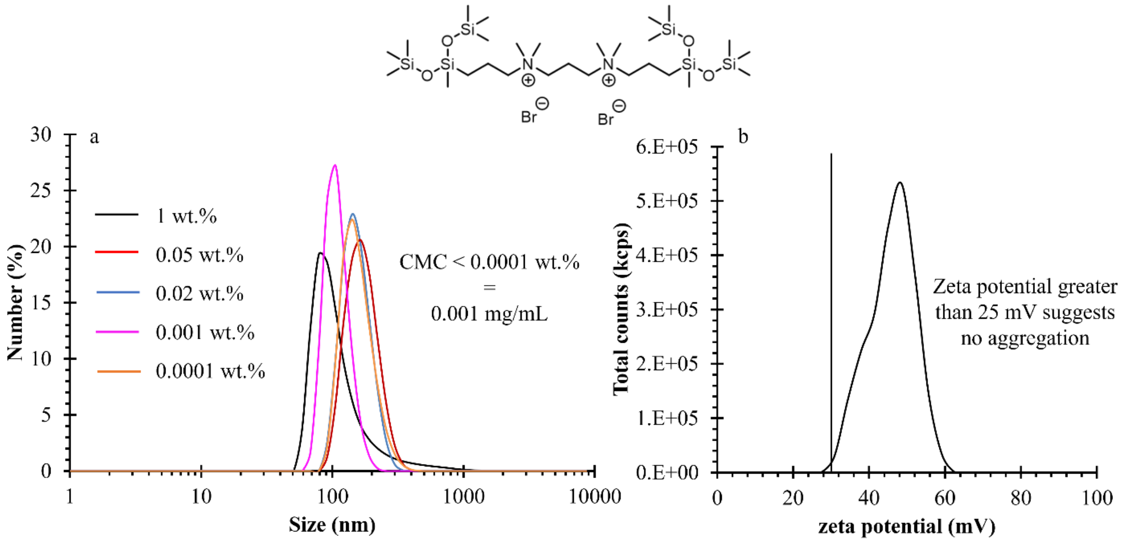

Figure 10.3. a) dynamic light scattering revealed trisiloxane cationic gemini surfactants to form large self-assemblies in solution at low wt.% concentrations. B) zeta potential measurements of 0.01 w.t% solutions of trisiloxane cationic gemini surfactants suggested no micelle to micelle aggregation occurred.

Additionally, solutions of trisiloxane cationic gemini surfactants formed stable foams following gentle shaking agitation as shown in **Figure 10.4**. Furthermore, the amount of foam formed varied as a function of concentration. Foams did not form stable foams at concentrations less than 0.001 wt.%, and solutions with concentrations greater than 0.01 wt. % formed stable foams. This data highlights decreased surface tension in these surfactant solutions, which affords foamability. Dynamic foam analysis will further quantify the expansion ratios and drainage times of these surfactants as a function of concentration. Additionally, surface tensiometry will quantify the minimum surface tension of this surfactant, which will validate the trend towards lower surface tension observed in the triethylsilyl cationic gemini surfactant.

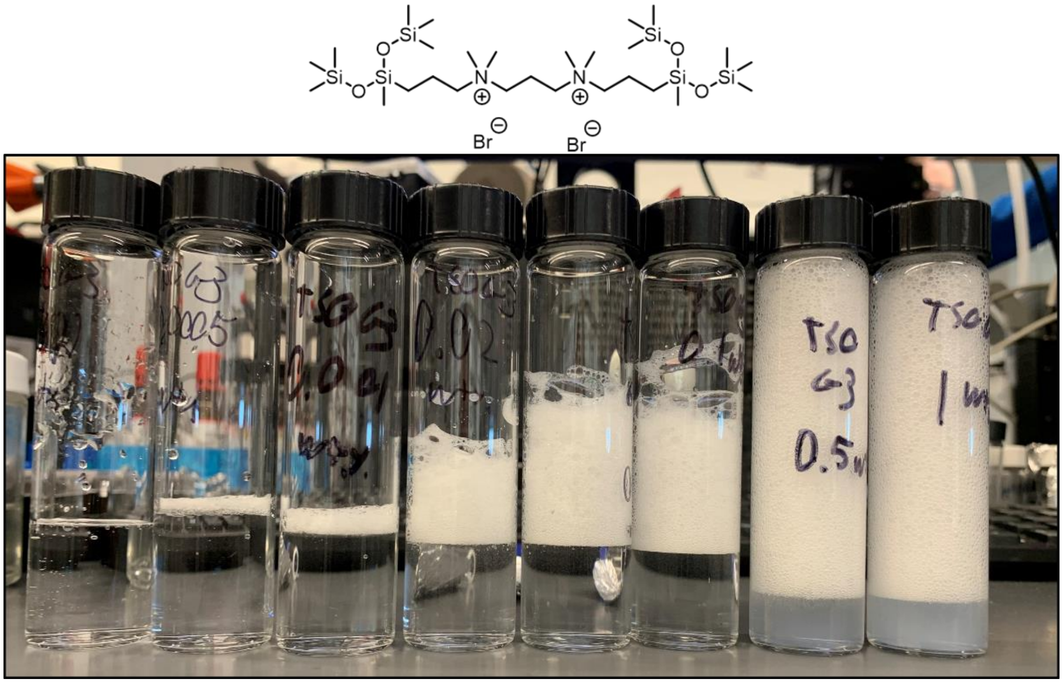

Figure 10.4. Trisiloxane cationic gemini surfactant formed stable foams upon agitation and the expansion ratio varied as a function of surfactant concentration.

Gemini surfactant structures present an additional structure variable in surfactant design, which is the spacer covalently binding hydrophilic head groups together. Prior surfactant research identified spacer length and type effects on critical micelle concentration and the interfacial area term in the packing parameter for hydrocarbon surfactants.[6] This inspires the design of a series of silicon containing cationic gemini surfactants with differed spacer lengths and types. Increased spacer length will increase the interfacial area term of the packing parameter as seen in prior research, and if the interfacial area term is sufficiently increased, the surfactant packing parameter will decrease to values below ½, which will afford wormlike micelles as opposed to the vesicular assemblies formed from the trisiloxane cationic gemini surfactant with a spacer length of three carbons.[7,8]

Historically, gemini silicon-containing surfactants have been limited to either nonionic or cationic gemini head types.[9] Little work has explored zwitterionic silicon-containing gemini surfactants, which limits surfactants to form stable foams. Fire-fighting applications require optimized drainage times to facilitate the efficient spreading of an aqueous film over the fuel, while also maintaining enough foam to suppress reignition.[10] The data presented in chapter 9 highlighted rapid drainage times for zwitterionic surfactants, and thus zwitterionic gemini surfactants remain of interest to further decrease the surface tension of solutions while providing a fast draining foam. The zwitterionic surfactant synthesis requires a tertiary amine in the propane sultone ring-opening step.[11] Thus, it is necessary to synthesize a secondary amine prior to the coupling reaction with a difunctional alkyl bromide. Substitution of allyl chloride with methylamine as opposed to dimethyl amine will afford an alkene functionalized secondary amine suitable for hydrosilylation reactions with various hydrosilanes.[12] **Scheme 10.2** introduces a possible synthetic strategy for these surfactants to test these hypotheses.

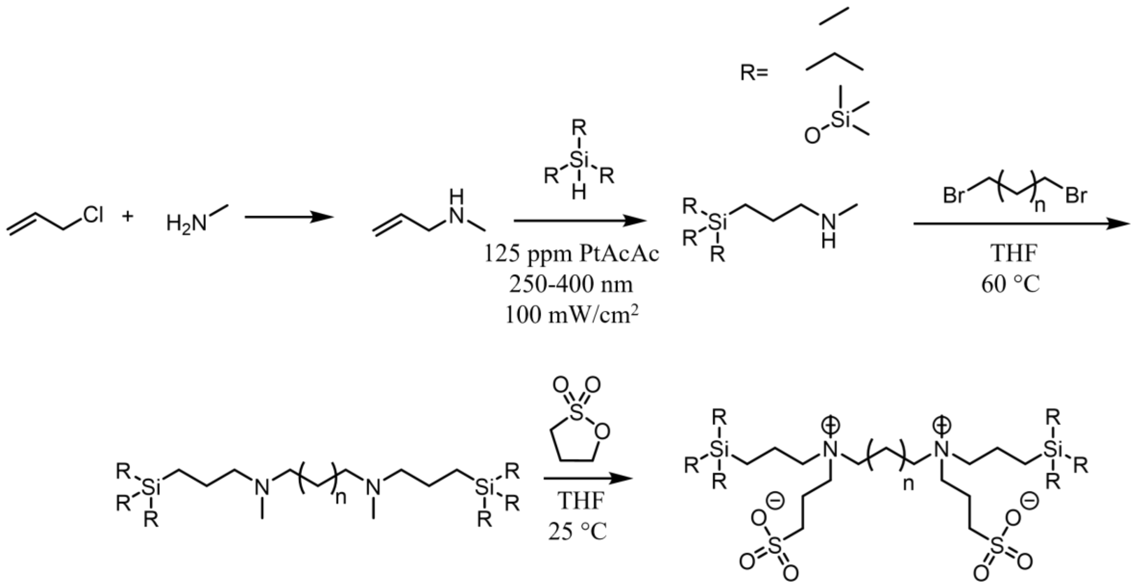

Scheme 10.2. Synthetic strategy to develop a catalogue of silicon-containing zwitterionic gemini surfactants.

10.2 Single tail and Double Tail Silicon-Containing Surfactants: Controlling the Packing Parameter Through Mixtures

Triethylsilyl surfactants presented in chapter 9 present interest for further fundamental investigations on surfactant self-assembly in solution. Single tail triethylsilyl zwitterionic surfactants formed short wormlike micelles in solution, which suggested the packing parameter was on the order of 1/3. Similar reaction strategies presented in chapter 9 yielded a double tail triethylsilyl surfactant from diallyl methylamine (**Scheme 10.3**). Following successful synthesis and purification, the double tail triethylsilyl zwitterionic surfactant did not dissolve in water, which suggests the surfactant packing parameter to be greater than 1. Incorporation of a double tail triethylsilyl zwitterionic surfactant will introduce a platform to tune the average hydrophobic volume of surfactants without introducing additional head-head repulsive forces as shown in **Figure 10.5**. Thus, mixtures of single-tail and double-tail surfactants provide access to a range of packing parameters in solution from approximately 1/3 to values greater than 1.

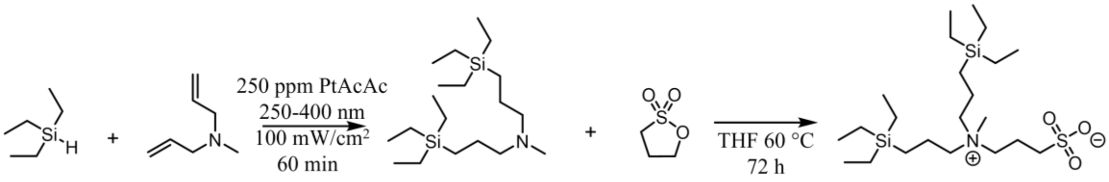

Scheme 10.3. Synthesis of double tail triethylsilyl zwitterionic surfactant from diallylmethlyamine.

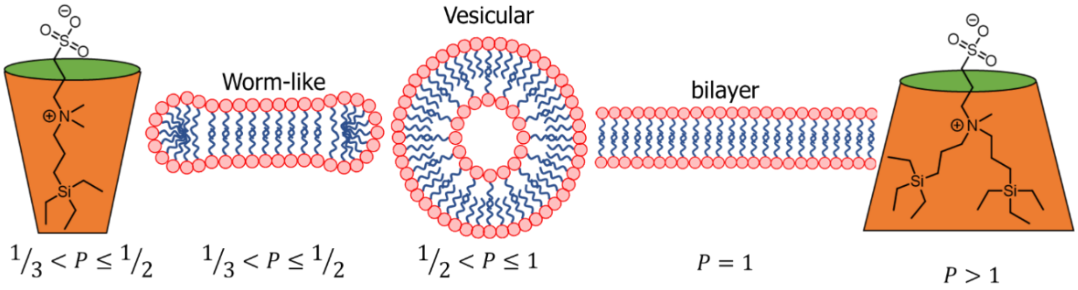

Figure 10.5. Combinations of single tail and double tail triethylsilyl zwitterionic surfactants access average packing parameters from approximately 1/3 to values greater than 1.

Preliminary investigations revealed double tail triethylsilyl zwitterionic surfactants remained insoluble in water. However, DLS data shown in **Figure 10.6**, confirmed that a mixture of single tail and double tail triethylsilyl zwitterionic surfactants provided homogenous solutions up to 20 wt.% double tail surfactant when the total surfactant concentration was 5 wt.%. Furthermore, across this soluble mixing window from 0-20 wt.% double tail, micelle size systematically increased and remained a monomodal distribution, which suggested the surfactants combined to form larger micelles composed of both single tail and double tail surfactants as opposed to forming separate micelles composed of only single tail or only double tail. At concentrations greater than 20 wt.% double tail, the solution phase separated forming an insoluble hydrated surfactant phase. While simply mixing the single tail and double tail surfactants provides control over the hydrophobic volume term in the packing parameter, temperature changes will provide a means to change the interfacial area term as the sum of hydrophobic and electrostatic interactions changes as a function of temperature.[13] This will provide two easily controlled variables to systematically tailor the packing parameter for surfactant applications.

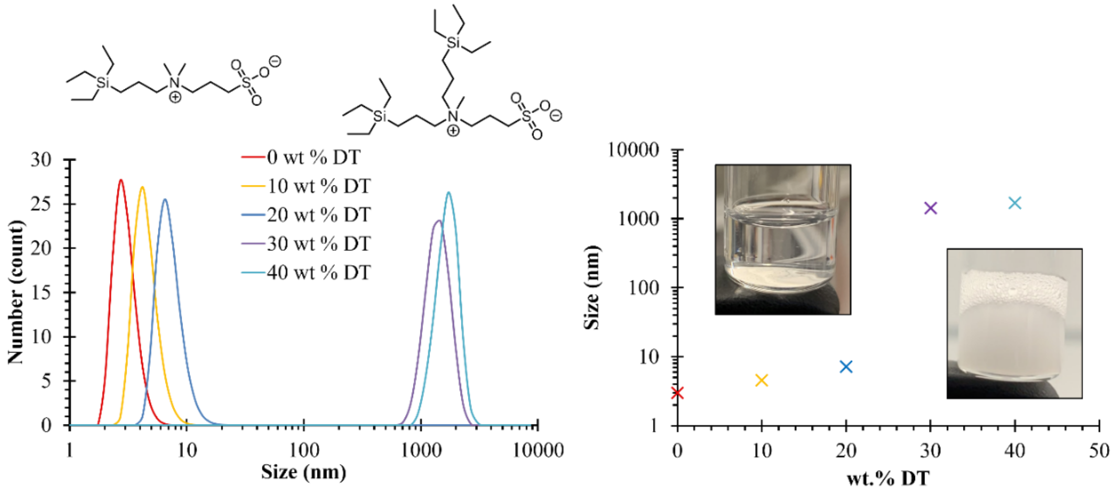

Figure 10.6. Dynamic light scattering of mixed single tail and double tail (DT) surfactants at total concentrations of 5 wt.% in aqueous solution highlights the shift between soluble micelle forming solutions and insoluble suspensions at concentrations below or greater than 25 wt. % respectively.

While this preliminary work highlights mixtures of single tail and double tail zwitterionic triethylsilyl surfactants, the synthetic methodology and hypothesis extends to other surfactant systems. Most notably, this strategy should be expanded to trisiloxane hydrophobic tails and cationic quaternary ammonium hydrophilic heads as shown in **Figure 10.7.** Dynamic light scattering will expose the effect of total hydrophobic volume on the CMC as it approaches insolubility. Furthermore, rheological characterization techniques will also provide deeper understanding of shear-induced surfactant assembly in these mixed surfactant systems as the average packing parameter changes. Ultimately these fundamental solution trends will inform surfactant design and development from a quantifiable structure-property relationship perspective.

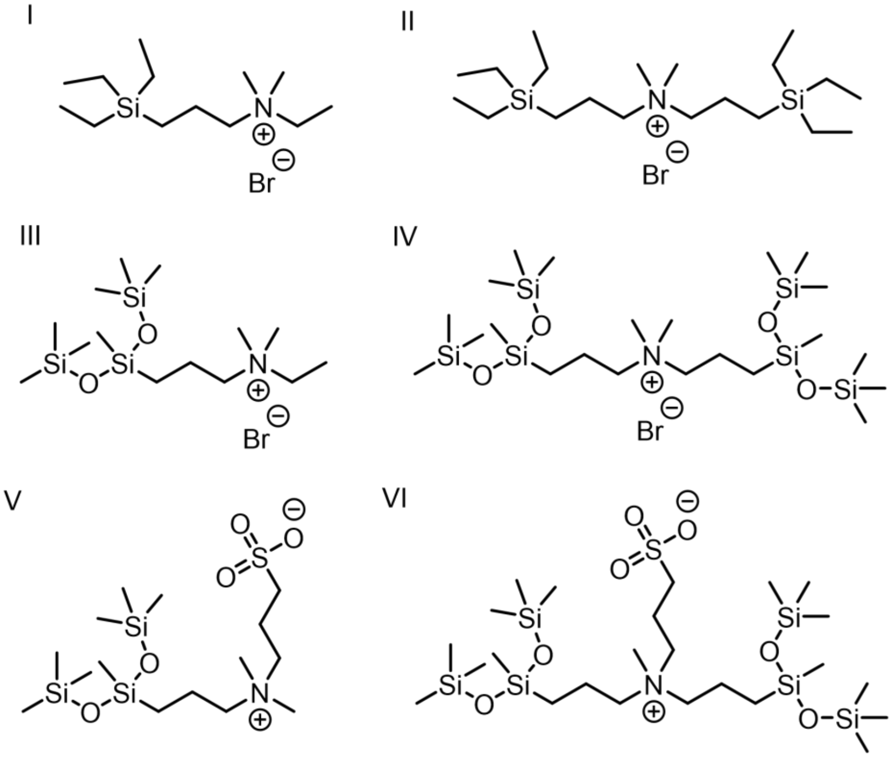

Figure 10.7. Additional silicon-containing surfactants to explore mixtures of single tail and double tail surfactants. (I) Single tail triethylsilyl cation, (II) double tail triethylsilyl cation, (III) single tail trisiloxane cation, (IV) double tail trisiloxane cation, (V) single tail trisiloxane zwitterion, (VI) double tail trisiloxane zwitterion.

10.3 Crystalline Morphology of Double Tail Triethylsilyl Zwitterionic Surfactants

While exploring mixtures of single tail and double tail triethylsilyl zwitterionic surfactants, the double tail surfactant was notably insoluble in water. However, this surfactant was readily soluble in organic solvents such as dimethyl sulfoxide (DMSO). Prior work within our research group explored zwitterionic and gemini surfactants which formed wormlike micelles in organic solution.[14–16] This prompted an exploration into solution casting robust films from these solutions by leveraging wormlike micelles with ionic interactions inside the organophobic phase. However, initial attempts to form these solution cast films yielded unique and unprecedented crystalline structures shown in **Figure 10.8.** These crystals were grown from a 10 wt.% solution of the double tail triethylsilyl zwitterion surfactant, which was heated to 100 °C in a Teflon dish covered with a petri dish and left to evaporate slowly over 7 d. The crystallites were removed from the solution and dried in vacuo for 24 h.

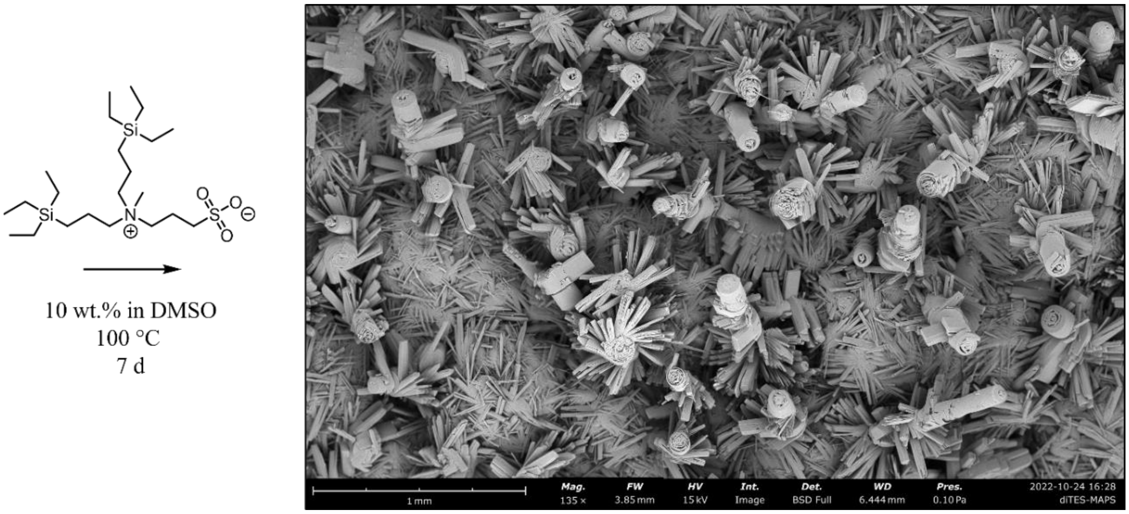

Figure 10.8 Scanning electron microscopy imaging of double tail triethylsilyl surfactants crystallized from DMSO.

Upon initial observation, multiple types of crystal structures present themselves throughout the sample. There appear to be straight lamella like structures present as highlighted in **Figure 10.9** in addition to cochleate crystallites as shown in **Figure 10.10.** These crystal structures remain uncharacterized and present interesting avenues for future morphological analysis such as powder X-ray diffraction and single crystal X-ray diffraction. **Figures 10.9** and **10.10** also include possible crystalline structures for the straight lamella and cochleate crystallites. The electrostatic attraction between the cationic quaternary ammonium and the anionic sulphate most likely templates the crystalline morphology as they precipitate from organic solution.[17] Furthermore, there are three possible hypothetical configurations for these ionic interactions to occur. The first possibility, shown in **Figure 10.9** demonstrates an elongated state of the zwitterionic head where the positive and negative charges are aligned between two surfactants. In a similar fashion, the zwitterionic head may adopt a six-membered ring conformation and similarly form lamella crystallites. However, this is less likely owing to recent investigations into sulfobetaine monomer conformations, which did not observe evidence of six-membered ring conformations.[18] Finally, the zwitterionic head may form a staggered conformation as shown in **Figure 10.10** where the quaternary ammonium and sulphate from a single surfactant is coordinated with adjacent zwitterionic heads in a staggered conformation.

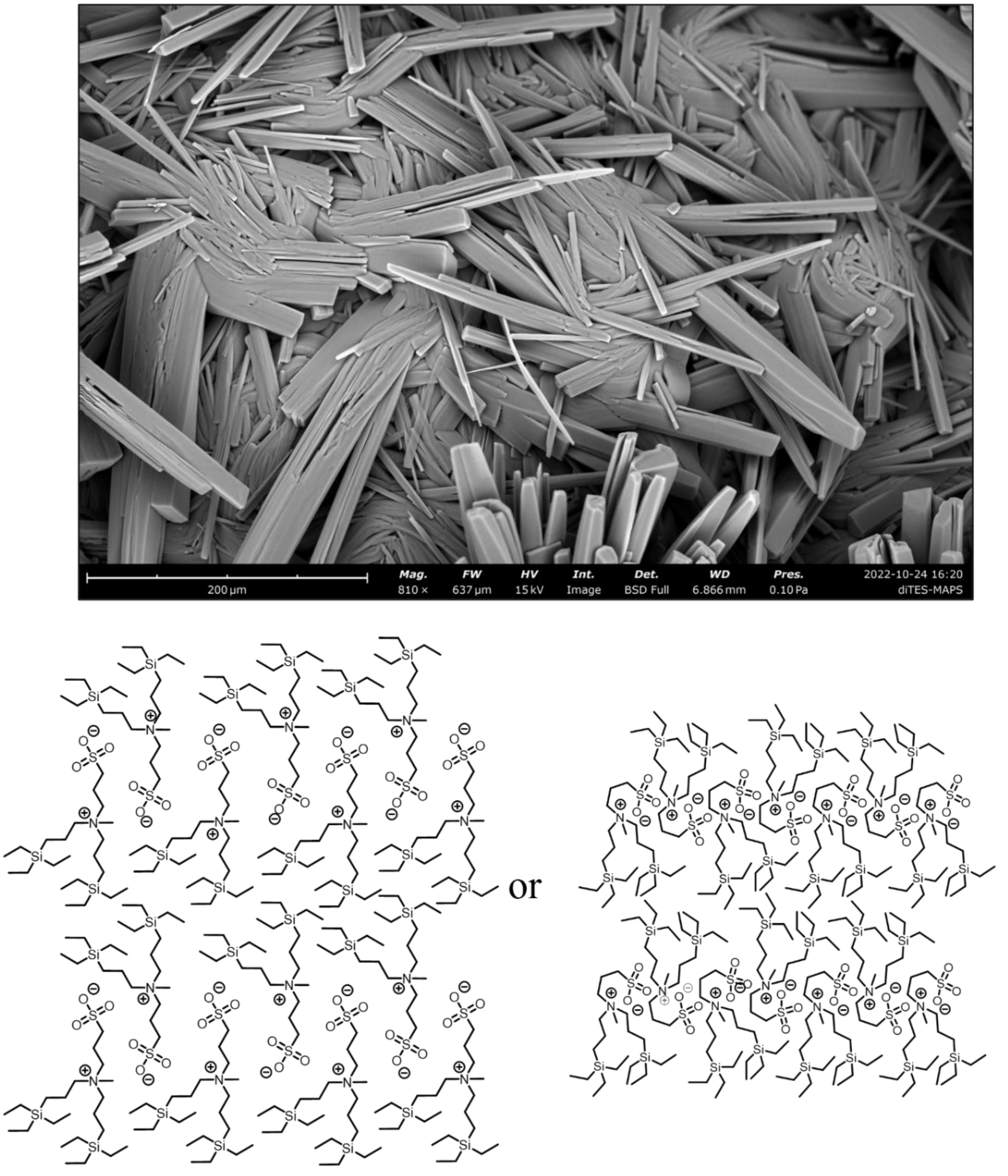

Figure 10.9. Hypothetical crystalline conformations of double tail triethylsilyl zwitterionic surfactants to form lamella crystallites.

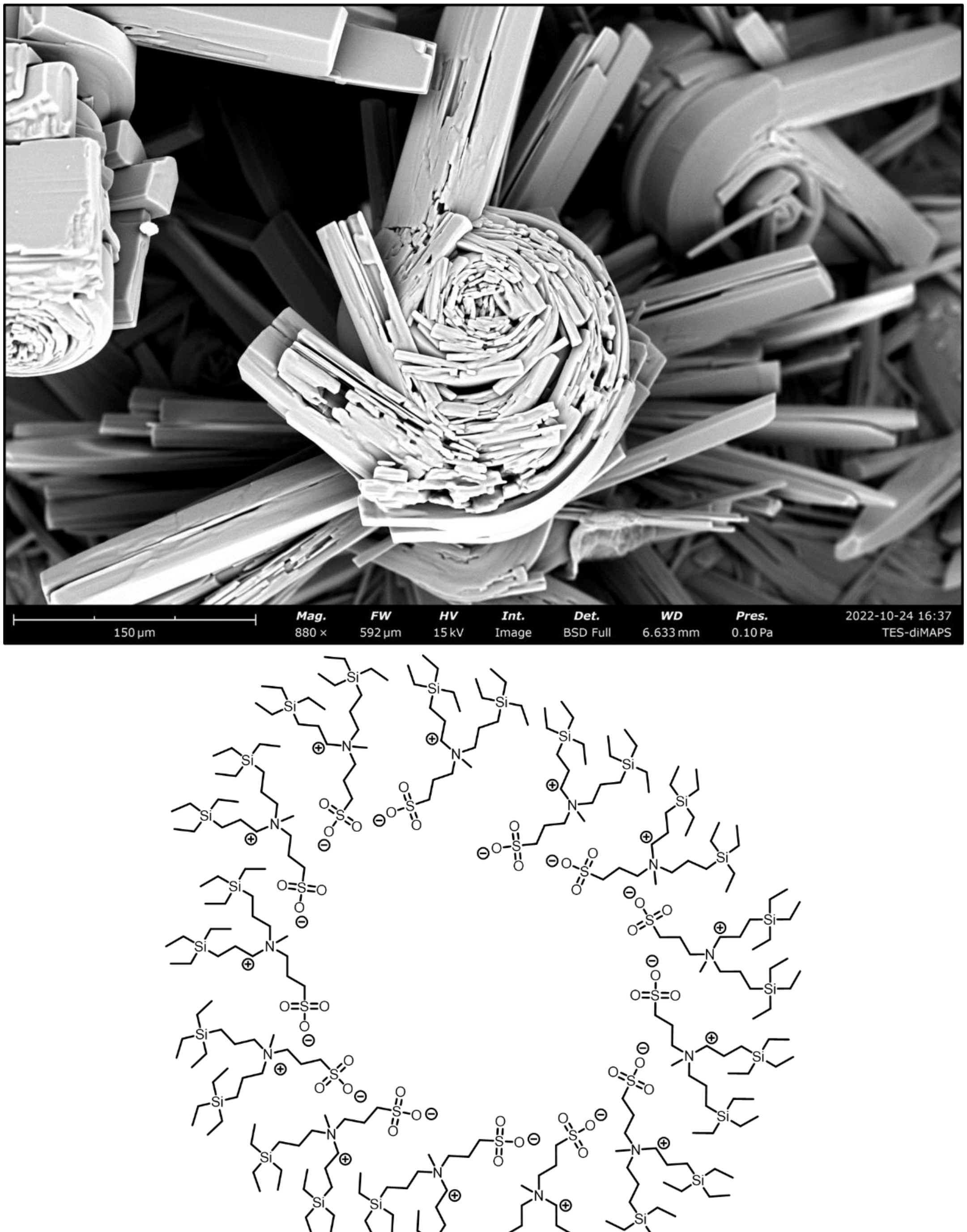

Figure 10.10. Possible orientation of double tail triethylsilyl zwitterionic surfactants to form the cochleate features observed in SEM.

To test these hypothetical crystal structures, single crystal XRD of a single spiraled pillar crystallite attempted to characterize these complex crystal structures. The result of this analysis, shown in **Figure 10.11** demonstrated that the cochleate morphology showed a scattering pattern consistent with a polymorphic sample.[19] Thus, many crystal structures orient themselves in such a way to yield this cochleate crystal. However, the exact structure of these distinct crystallites remains unknown, and future work with powder XRD will reveal possible crystal structures within these samples. Furthermore, variations in crystal growing strategies such as changes in initial concentration, annealing temperature, and solvent will reveal processing conditions in which each of these different crystal structures or favored. Detailed morphological studies of this unique and unprecedented crystal structure will provide valuable insight into the structure-processing relationships dictating the self-assembly of organic matter.

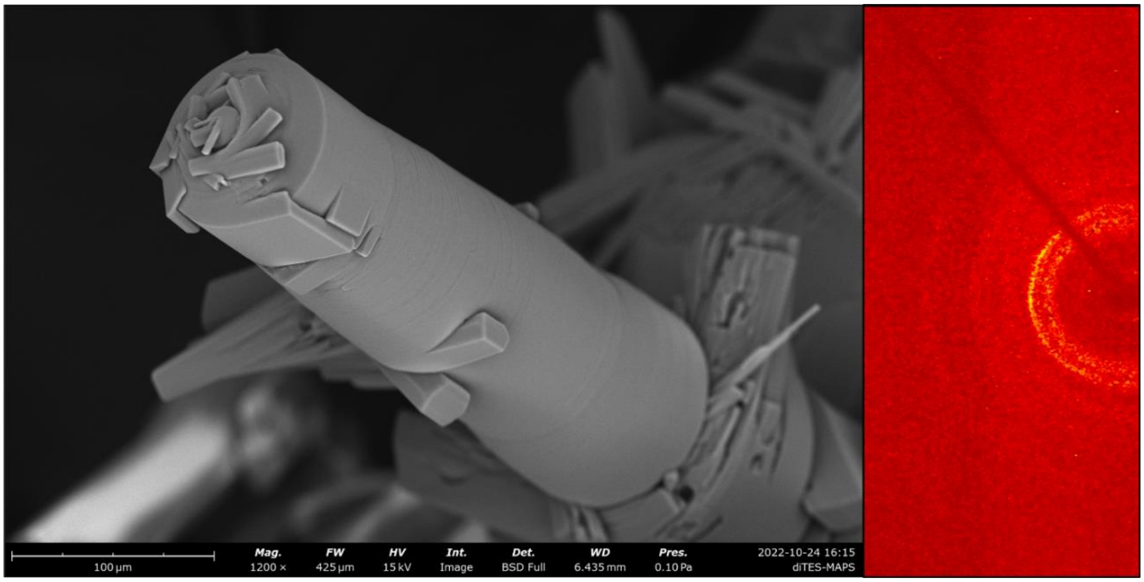

Figure 10.11. Single crystal XRD scattering pattern obtained from a cochleate crystallite of double tail triethylsilyl zwitterionic surfactant.

10.4 Expanding Trisiloxane Surfactant Platforms to Bolaform and Polymeric Trisiloxane Surfactants

Trisiloxane hydrophobic tails remain leading competitors to fluorinated surfactants in fire-fighting foam formulations owing to the flexibility of the Si-O-C bond. Chapter 9 demonstrated that other silicon-containing surfactants do not sufficiently reduce solution surface tension to form aqueous films over the fuel layer. Currently, there is an extensive catalogue of synthesized trisiloxane surfactants, which includes various examples cationic, anionic, nonionic, zwitterionic, and gemini trisiloxane surfactants.[9] However, there are no reported accounts of bolafrom siloxane surfactants or ionene siloxane surfactants deployed in fire-fighting foams. Bolaform surfactants contain two hydrophilic heads but differ from gemini surfactants as the two hydrophilic heads are joined together by the hydrophobic tail. This typically increase the critical micelle concentration of the surfactant.[20] Furthermore, bolaform surfactant self-assemblies differ from other surfactant self-assemblies since they assemble in an elongated form, which leads to self-assemblies with covalent bonds across the width of the self-assemblies. This further stabilizes the micelles, which will likely lead to increased foam stability compared to other surfactant types. **Scheme 10.3** introduces a two step synthetic strategy to develop cationic and zwitterionic bolaform trisiloxane surfactants from 1,1,3,3,5,5, hexamethyl dihydrosiloxane.

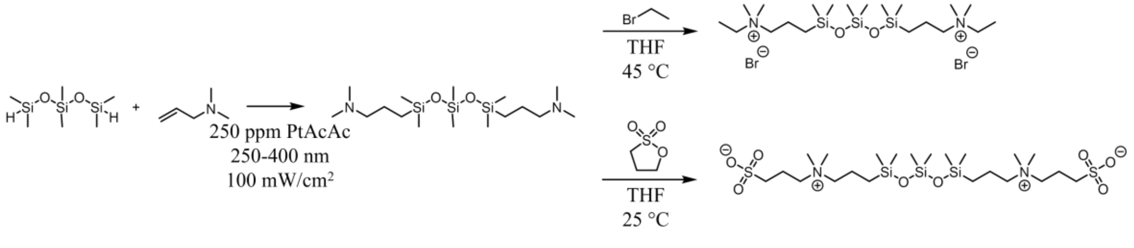

Scheme 10.3. Synthetic strategy for cationic (top) and zwitterionic (bottom) trisiloxane bolaform surfactants.

Initial synthetic efforts successfully synthesized the cationic bolaform trisiloxane surfactant, and ^{1}H NMR, shown in **Figure 10.12**, confirmed the structure after recrystallization from 80:20 vol.% mixture of tetrahydrofuran and isopropanol. Upon agitation a 1 wt.% aqueous solution of this bolaform surfactant formed a stable foam, which did not fully drain over the course of several days. Future work will initially determine the critical micelle concentration and minimum solution surface tension of this novel surfactant structure using dynamic light scattering and surface tensiometry. Dynamic foam analysis will also quantify both solution drainage time and foam drainage time across various surfactant concentrations. Oscillatory stress sweep rheology of concentrated surfactant solutions will probe solution viscoelasticity before and after shear, which will demonstrate shear induced alignment of bolaform surfactants for the first time. The combination of these preliminary experiments will validate this novel surfactant for applications in fire-fighting foams while providing deeper fundamental understanding of bolaform surfactants.

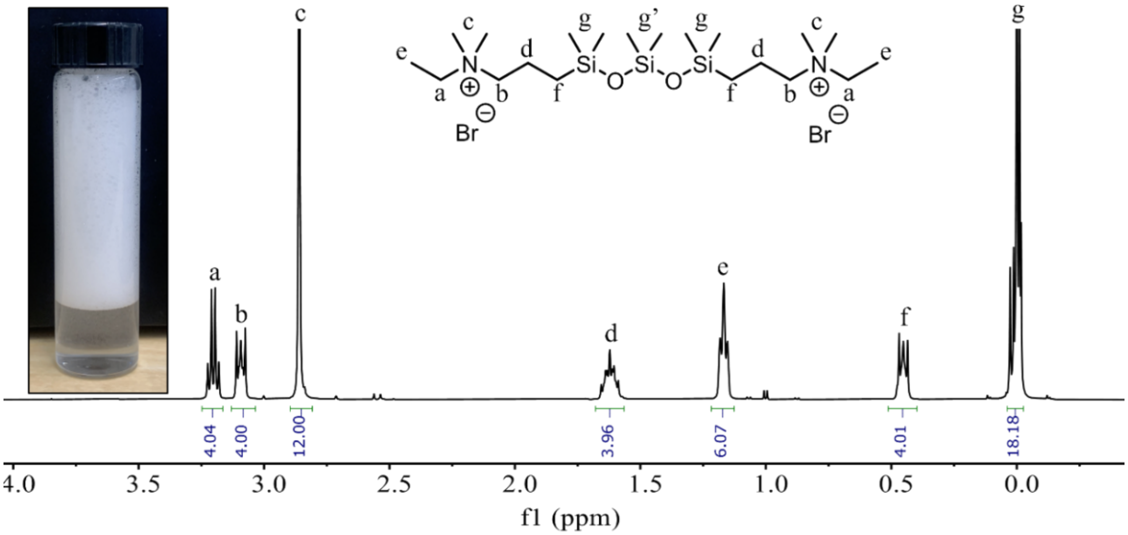

Figure 10.12. ^{1}H NMR spectrum of trisiloxane cationic bolaform surfactant confirmed successful synthesis. (inset) 1 wt.% solution of trisiloxane bolaform surfactant forms stable foam after agitation.

In addition to bolaform trisiloxane surfactants, siloxane ionenes remain unexplored polymer families in fire-fighting applications. Ionenes describes a family of polyelectrolytes where the charge-bearing functionality exists within the main polymer chain.[21] 1,1,3,3,5,5, hexamethyl dihydrotrisiloxane provides a suitable difunctional monomer for step growth hydrosilylation polymerization with diallylmethylamine. This step growth polymerization provides molecular weight control through stoichiometric offset according to the modified Carothers equation. Subsequent functionalization of this poly(trisiloxane N,N,Ndiethylmethylamine) with either bromoethane or propane sultone will yield either a cationic or zwitterionic ionene respectively. This polymeric surfactant platform will introduce additional structure variables such as molecular weight, percent functionalization, and siloxane segment length to further understand fundamental structure property relationships of siloxane containing ionenes in not only within fire-fighting foam formulations, but also within the field of thermoplastic elastomers.

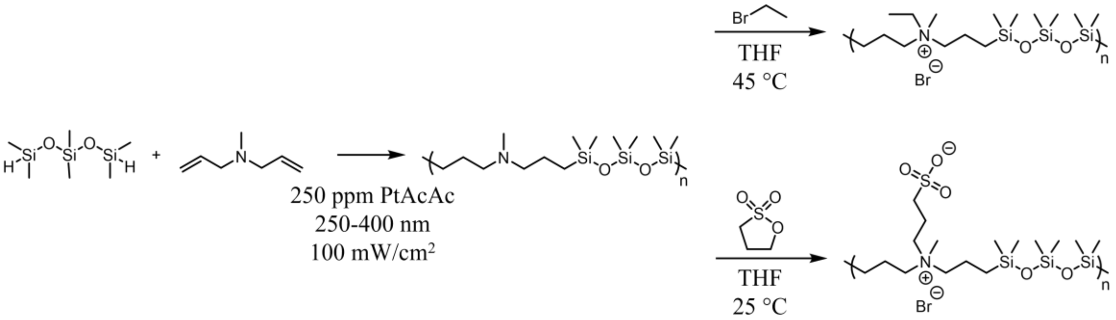

Scheme 10.4. Synthetic strategy for cationic (top) and zwitterionic (bottom) trisiloxane ionene surfactants.

10.5 Templated Photopolymerizable Domains Through Shear-Induced Alignment of Methacrylate Functionalized Surfactants

The work presented in chapter 9 highlighted the shear induced alignment of triethylsilyl cationic wormlike micelles, which had implications for firefighting foam applications. However, this finding and these trends are not limited to producing stable foams but should be expanded to other research areas such as photo-assisted additive manufacturing. This future work section proposes an avenue to template photopolymerizable surfactants through high shear extrusion, such as direct ink-writing, and then subsequently photopolymerizing these templated nanoscale domains to liberate aligned nanoscale fibers from solution. **Figure 10.13** depicts this process schematically for a generalized photopolymerizable surfactant monomer. Schoen et. al amongst others reported polymerizable surfactants in the late 90s, but these processes yielded anisotropic suspensions of polymerized tubules at low concentration.[22,23] These studies leveraged only vesicle forming micelles in which the bilayer polymerized, and upon solidification formed straight rigid tubules. While this work demonstrated exciting preliminary results for the field of photopolymerizable surfactants, little work has pushed this field forward in the last 25 years. Research in this space would provide both novel material design and would catalyze deeper fundamental understanding of self-assembly templated polymerization strategies.

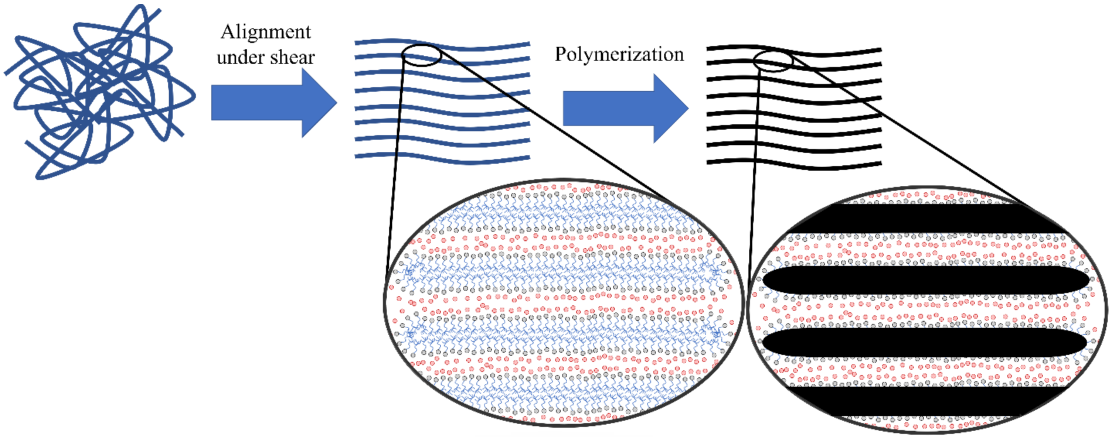

Figure 10.13. Cartoon depiction of shear induced micelle alignment and subsequent polymerization of templated hydrophobic domains.

Dimethylaminoethyl methacrylate (DMAEMA) is a readily available and extensively used photopolymerizable monomer for additive manufacturing processes ranging from vat photopolymerization to UV-assisted direct ink-writing.[24–26] Prior work leveraged the basicity of the tertiary amine to establish supramolecular interactions between carboxylic residues in both polymers and small polymers, but this tertiary amine also demonstrated significant nucleophilicity to form cationic and cationic gemini surfactants. Thus, this monomer presents an opportunistic starting ground for initial efforts in templated photopolymerization. A gemini surfactant will more likely favor wormlike micelle self-assembly relative to a simple quaternary ammonium cationic surfactant based on previous research. Therefore, initial efforts in this research space should explore gemini surfactants. **Scheme 10.6** proposes a facile synthetic path for the synthesis of a cationic gemini surfactant from DMAEMA and 1,3 dibromopropane. If this structure provides insufficient hydrophobicity, longer chain dimethyl amino methacrylates should be synthesized from dimethylamino propane or dimethylaminobutane and methacryloyl chloride. Finally, addition of a hydrophobic dimethacrylate or diacrylate such as butane diacrylate will provide additional crosslinking within the shear-aligned micelles.

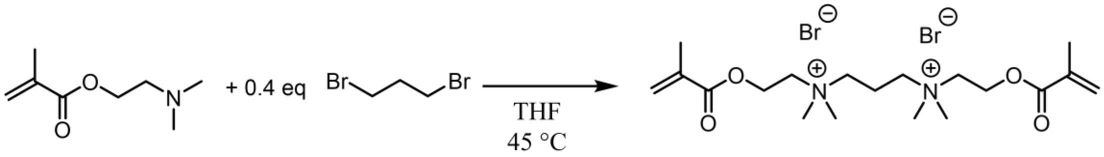

Scheme 10.6. Synthetic strategy to develop photopolymerizable cationic gemini surfactant from DMAEMA and 1,3 dibromopropane.

10.6 References

1. Ananth, R.; Snow, A. W.; Hinnant, K. M.; Giles, S. L.; Farley, J. P. Synergisms between Siloxane-Polyoxyethylene and Alkyl Polyglycoside Surfactants in Foam Stability and Pool Fire Extinction. *Colloids Surf A Physicochem Eng Asp* **2019**, *579*. https://doi.org/10.1016/j.colsurfa.2019.123686.

2. Hetzer, R. H.; Kümmerlen, F.; Wirz, K.; Blunk, D. Fire Testing a New Fluorine-Free AFFF Based on a Novel Class of Environmentally Sound High Performance Siloxane Surfactants. **2014**. https://doi.org/10.3801/IAFSS.FSS.11-1261.

3. Snow, S. A.; Fenton, W. N.; Owen, M. J. Synthesis and Characterization of Zwitterionic Silicone Sulfobetaine Surfactants. *Langmuir* **1990**, *6*, 385–391.

4. Mykhaylyk, O. O.; Warren, N. J.; Parnell, A. J.; Pfeifer, G.; Laeuger, J. Applications of Shear-Induced Polarized Light Imaging (SIPLI) Technique for Mechano-Optical Rheology of Polymers and Soft Matter Materials. *J Polym Sci B Polym Phys* **2016**, *54* (21), 2151–2170. https://doi.org/10.1002/POLB.24110.

5. Lowry, G. V.; Hill, R. J.; Harper, S.; Rawle, A. F.; Hendren, C. O.; Klaessig, F.; Nobbmann, U.; Sayre, P.; Rumble, J. Guidance to Improve the Scientific Value of Zeta-Potential Measurements in NanoEHS. *Environ Sci Nano* **2016**, *3* (5), 953–965. https://doi.org/10.1039/C6EN00136J.

6. Wettig, S. D.; Verrall, R. E. Thermodynamic Studies of Aqueous m–s–m Gemini Surfactant Systems. *J Colloid Interface Sci* **2001**, *235* (2), 310–316. https://doi.org/10.1006/JCIS.2000.7348.

7. Svenson, S. Controlling Surfactant Self-Assembly. *Curr Opin Colloid Interface Sci* **2004**, *9* (3–4), 201–212. https://doi.org/10.1016/J.COCIS.2004.06.008.

8. Nagarajan, R. Molecular Packing Parameter and Surfactant Self-Assembly: The Neglected Role of the Surfactant Tail. *Langmuir* **2002**, *18* (1), 31–38. https://doi.org/10.1021/LA010831Y/ASSET/IMAGES/MEDIUM/LA010831YE00021.GIF.

9. Hill, R. M. Silicone Surfactants—New Developments. *Curr Opin Colloid Interface Sci* **2002**, *7* (5–6), 255–261. https://doi.org/10.1016/S1359-0294(02)00068-7.

10. Rakowska, J. Best Practices for Selection and Application of Firefighting Foam. https://doi.org/10.1051/matecconf/201824700014.

11. Lu, J.; Pu, W.; He, W.; Zou, B.; Li, B.; Liu, R. Progress in Research of Sulfobetaine Surfactants Used in Tertiary Oil Recovery. *J Surfactants Deterg* **2022**. https://doi.org/10.1002/JSDE.12651.

12. Chukhajian, E. O.; Ayrapetyan, L. V.; Mkrtchyan, H. S.; Panosyan, H. A. Synthesis of Mixed Secondary and Tertiary Amines. *Russian Journal of Organic Chemistry* **2020**, *56* (2), 353–355. https://doi.org/10.1134/S1070428020010311/SCHEMES/2.

13. Kunz, W.; Testard, F.; Zemb, T. Correspondence between Curvature, Packing Parameter, and Hydrophilic-Lipophilic Deviation Scales around the Phase-Inversion Temperature. https://doi.org/10.1021/la8028879.

14. McKee, M. G.; Layman, J. M.; Cashion, M. P.; Long, T. E. Phospholipid Nonwoven Electrospun Membranes. *Science (1979)* **2006**, *311* (5759), 353–355. https://doi.org/10.1126/SCIENCE.1119790/SUPPL_FILE/MCKEE.SOM.PDF.

15. Cashion, M. P.; Li, X.; Geng, Y.; Hunley, M. T.; Long, T. E. Gemini Surfactant Electrospun Membranes. *Langmuir* **2010**, *26* (2), 678–683. https://doi.org/10.1021/LA902287B/ASSET/IMAGES/LARGE/LA-2009-02287B_0007.JPEG.

16. Hemp, S. T.; Hudson, A. G.; Allen, M. H.; Pole, S. S.; Moore, R. B.; Long, T. E. Solution Properties and Electrospinning of Phosphonium Gemini Surfactants. *Soft Matter* **2014**, *10* (22), 3970–3977. https://doi.org/10.1039/C4SM00271G.

17. Rudert, R.; Schmaucks, G. Crystal and Molecular Structure of 1-Ethyl-3-[Tris(Trimethylsiloxanyl)Silyl]Pyrrolinium Hydrochloride. *Crystal Research and Technology* **1997**, *32* (2), 347–352. https://doi.org/10.1002/CRAT.2170320219.

18. Laschewsky, A.; Touillaux, R.; Hendlinger, P.; Vierengel, A. Characterization of Sulfobetaine Monomers by Nuclear Magnetic Resonance Spectroscopy: A Note. *Polymer (Guildf)* **1995**, *36* (15), 3045–3049. https://doi.org/10.1016/0032-3861(95)94357-Y.

19. Goubet, N.; Albouy, P. A.; Thompson, A.; Pileni, M. P. Polymorphism in Nanoparticle-Based Crystals Depending upon Their Single or Polycrystalline Character. *CrystEngComm* **2016**, *18* (33), 6166–6175. https://doi.org/10.1039/C6CE01006G.

20. Gonçalves, R. A.; Holmberg, K.; Lindman, B. Cationic Surfactants: A Review. *J Mol Liq* **2023**, *375*, 121335. https://doi.org/10.1016/J.MOLLIQ.2023.121335.

21. Williams, S. R.; Long, T. E. Recent Advances in the Synthesis and Structure–Property Relationships of Ammonium Ionenes. *Prog Polym Sci* **2009**, *34* (8), 762–782. https://doi.org/10.1016/J.PROGPOLYMSCI.2009.04.004.

22. Holmberg, K. Polymerizable Surfactants. *Prog Org Coat* **1992**, *20* (3–4), 325–337. https://doi.org/10.1016/0033-0655(92)80022-O.

23. Yager, P.; Schoen, P. E. Molecular Crystals and Liquid Crystals Formation of Tubules by a Polymerizable Surfactant. https://doi.org/10.1080/00268948408071454.

24. Arrington, C. B.; Rau, D. A.; Vandenbrande, J. A.; Hegde, M.; Williams, C. B.; Long, T. E. 3D Printing Carbonaceous Objects from Polyimide Pyrolysis. *ACS Macro Lett* **2021**, *10* (4), 412–418. https://doi.org/10.1021/ACSMACROLETT.1C00032/ASSET/IMAGES/LARGE/MZ1C00032_0004.JPEG.

25. Rau, D. A.; Herzberger, J.; Long, T. E.; Williams, C. B. Ultraviolet-Assisted Direct Ink Write to Additively Manufacture All-Aromatic Polyimides. *ACS Appl Mater Interfaces* **2018**, *10* (41), 34828–34833. https://doi.org/10.1021/ACSAMI.8B14584/ASSET/IMAGES/LARGE/AM-2018-145849_0003.JPEG.

26. Herzberger, J.; Meenakshisundaram, V.; Williams, C. B.; Long, T. E. 3D Printing All-Aromatic Polyimides Using Stereolithographic 3D Printing of Polyamic Acid Salts. **2018**. https://doi.org/10.1021/acsmacrolett.8b00126.

CHAPTER 11

SUMMARY AND CONCLUSIONS

Fundamental structure-processing-property trends informed material design across a range of material families including thermoplastic polymers, covalently crosslinked polymer networks, and small molecule self-assemblies in solution. These investigations provided new insight to address emerging topics in sustainability such as molecular design for chemical recyclability, material waste reduction, additive manufacturing, and replacements for chemicals with known environmental toxicity. Throughout each chapter, spectroscopic, thermomechanical, rheological, and light scattering analysis provided a holistic understanding of both chemical and physical interactions responsible for ultimate material properties. The consistent analytical strategies revealed fundamental similarities regarding material assembly in solid viscoelastic materials with storage moduli spanning 9 orders of magnitude from 10 to 10^9 Pa. The influence of reactivity, thermodynamic self-assembly, and shear induced alignment informed appropriate design, processing, and analysis of next-generation technologies in the field of sustainability.

The fundamental concept of thermodynamic self-assembly presents itself across numerous industries including packaging, adhesives, high-performance materials, biomedical engineering, additive manufacturing, and fire-fighting technologies. IUPAC defines self-assembly as “spontaneous and reversible organization of molecular entities by noncovalent interactions”. Thus, polymer crystallization, polymer aggregation in solution, and small molecule self-assembly presented three subdivisions of this critical field of chemistry to investigate fundamental trends in solubility and mechanical properties. Chapter 3 presented the incorporation of a kinked aromatic unit in the design of a novel family of linear polyesters with predictable glass transition temperatures and crystallinity. In addition to this molecular level influence on thermomechanical properties, this work demonstrated the effect of polymer semicrystallinity on solubility. Whereas amorphous polymers demonstrated solubility, semicrystalline polymers remained insoluble owing to the strong non-covalent physical interactions present between polymer chains.

This concept was applied to a more complex polyurethane copolymer system, in chapter 4, where side reactions impacted polymer processability. It previously remained uncertain if covalent crosslinking or physical interactions were responsible for differences in extrudability between spectroscopically similar batches. Progressive increases in the polarity of an organic solvent revealed all polyurethane samples to be soluble in sufficiently polar solvents. However, those lots which demonstrated poor extrudability remained insoluble in solvents incapable of disrupting physical interactions between all polymer chains in solution. This simple solubility study suggested physical interactions were largely responsible for poor extrusion performance. Furthermore, differential scanning calorimetry revealed poor extrusion lots demonstrated larger endothermic events at temperatures greater than the extrusion temperature which provided additional evidence of these non-covalent self-assemblies in poor extrusion lots.

While chapter 4 highlighted the deleterious effects of side reactions during polymer synthesis, chapters 5-7 demonstrated control of multiple reaction pathways during photochemical processes to predictably tune mechanical properties and degradation profiles. Chapter 5 introduced radical thiol-ene addition to this body of work in the design of degradable hydrogels for medical applications. This work revealed a need for precise stoichiometric control in simple thiol-ene gelation. Chapter 6 demonstrated intentional incorporation of a known thiol-ene side reaction, acrylate polymerization. This additional reaction pathway afforded hydrogels with increased modulus compared to the previous work and demonstrated the formation of highly crosslinked domains in hydrogel networks with increased acrylate homopolymerization. These highly crosslinked domains controlled bulk degradation rates. However, it remains unknown if these highly crosslinked domains resulted from the kinetics of each reaction or if they were templated by self-assembly in solution prior to polymerization.

Chapter 7 and 8 expanded on this concept in two additional systems with multiple crosslinking reaction pathways. Photoacid generators provided a photoinitiated avenue to establish acetal functionality from vinyl ether and hydroxyl functionalized monomers, which were previously synthesized with a simple *para*-toluene sulfonic acid catalyst. The photoacid generator provided controllable acid generation, which not only catalyzed the acid forming reaction, but also initiated vinyl ether cationic homopolymerization. In a similar fashion to the reactive systems presented in chapter 6, a simple stoichiometric offset of vinyl ether and hydroxyl functionality provided control over crosslink density. This control predicted both mechanical properties and degradation behavior. Chapter 8 expanded this binary photopolymerization strategy to base catalyzed carbon-Michael additions, in which the acrylate functionality participated as both a Michael acceptor and as a free radical monomer. However, as the investigated photobase generators produced both a radical and basic species, the acrylate homopolymerization occurred at a much faster rate, which ultimately prevented any detectable carbon-Michael additions.

Furthermore, the addition of radical scavengers and antioxidants did not ameliorate this kinetic issue.

Finally, the concepts of thermodynamic self-assembly, photoinitiated reactivity, and shear-induced morphological rearrangements provided deeper understanding of structure-processing-property relationships in fire-fighting foams. Photoinitiated hydrosilylation afforded two novel surfactant structures based on triethylsilyl hydrophobic tails. Dynamic light scattering and concentration dependent rheology revealed the zwitterionic surfactant to possess a lower critical micelle concentration than the cationic surfactant. Most notably, cationic surfactants significantly improved foam stability. Oscillatory rheological experiments demonstrated solid-like viscoelastic properties in concentrated cationic surfactant solutions after shear. Polarized optical light imaging rheology shed further light on this phenomenon, and this experimental technique revealed the formation of birefringent structures in solution. This shear-induced alignment of cationic surfactant self-assemblies provided foams with more solid like properties compared to zwitterionic surfactants which did not form higher order assemblies under shear. This knowledge informed a previously unknown, but critical feature of surfactant self-assemblies in fire-fighting applications.

Key Takeaways:

- 4,4’ dimethyloxybisbenzoate provided predictable control over polyester glass transition temperatures and crystallinity.
- Solubility tests in solvents with varied polarity in addition to dynamic light scattering afforded analytical methodology to validate polyurethane extrusion performance.

- Acid catalyzed vinyl ether hydroxyl polymerization provided acetal functionalized, selectively degradable, and photo processable oligomers for radical thiol-ene gelation.
- Binary thiol-acrylate polymerization of acetal functionalized telechelic acrylate precursors provided hydrogels with controlled network architecture, which predicted degradation behavior.
- Photoacid generators enabled in-*situ* acetal functionalization during network formation from multifunctional vinyl ether and hydroxyl monomers. These gels required base stabilization to prevent unwanted acetal degradation.
- Current photobase generator technologies proved insufficient for photocatalyzed carbon-Michael addition of acetoacetate to acrylate functionalities due to the generation of a radical species during base generation.
- Triethylsilyl-containing surfactants did not lower solution surface tension as effectively as siloxane surfactants.
- Oscillatory and polarized light imaging rheology revealed the impact of shear-aligned surfactant self-assemblies on foam stability. Cationic surfactants formed stable alignments under shear and zwitterionic surfactants did not.

REFERENCES

Chapter 1

1. Nunes, R. W.; Martin, J. R.; Johnson, J. F. Influence of Molecular Weight and Molecular Weight Distribution on Mechanical Properties of Polymers. *Polym Eng Sci* **1982**, *22* (4), 205–228. https://doi.org/10.1002/PEN.760220402.

2. Wilts, E. M.; Herzberger, J.; Long, T. E. Addressing Water Scarcity: Cationic Polyelectrolytes in Water Treatment and Purification. *Polym Int* **2018**, *67* (7), 799–814. https://doi.org/10.1002/PI.5569.

3. Rabnawaz, M.; Wyman, I.; Auras, R.; Cheng, S. A Roadmap towards Green Packaging: The Current Status and Future Outlook for Polyesters in the Packaging Industry. *Green Chemistry* **2017**, *19* (20), 4737–4753. https://doi.org/10.1039/C7GC02521A.

4. Mapari, S.; Mestry, S.; Mhaske, S. T. Developments in Pressure-Sensitive Adhesives: A Review. *Polymer Bulletin 2020 78:7* **2020**, *78* (7), 4075–4108. https://doi.org/10.1007/S00289-020-03305-1.

5. Li, T.; Senesi, A. J.; Lee, B. Small Angle X-Ray Scattering for Nanoparticle Research. *Chem Rev* **2016**, *116* (18), 11128–11180. https://doi.org/10.1021/ACS.CHEMREV.5B00690/ASSET/IMAGES/CR-2015-00690Z_M061.GIF.

6. Carvalho, P. M.; Felício, M. R.; Santos, N. C.; Gonçalves, S.; Domingues, M. M. Application of Light Scattering Techniques to Nanoparticle Characterization and Development. *Front Chem* **2018**, *6*, 237. https://doi.org/10.3389/FCHEM.2018.00237/BIBTEX.

7. Saba, N.; Jawaid, M. A Review on Thermomechanical Properties of Polymers and Fibers Reinforced Polymer Composites. *Journal of Industrial and Engineering Chemistry* **2018**, *67*, 1–11. https://doi.org/10.1016/J.JIEC.2018.06.018.

8. Tjong, S. C. Structure, Morphology, Mechanical and Thermal Characteristics of the in Situ Composites Based on Liquid Crystalline Polymers and Thermoplastics. *Materials Science and Engineering: R: Reports* **2003**, *41* (1–2), 1–60. https://doi.org/10.1016/S0927-796X(03)00035-4.

9. Wang, W.; Lu, W.; Goodwin, A.; Wang, H.; Yin, P.; Kang, N. G.; Hong, K.; Mays, J. W. Recent Advances in Thermoplastic Elastomers from Living Polymerizations: Macromolecular Architectures and Supramolecular Chemistry. *Prog Polym Sci* **2019**, *95*, 1–31. https://doi.org/10.1016/J.PROGPOLYMSCI.2019.04.002.

10. Rizwan, M.; Baker, A. E. G.; Shoichet, M. S. Designing Hydrogels for 3D Cell Culture Using Dynamic Covalent Crosslinking. *Adv Healthc Mater* **2021**, *10* (12), 2100234. https://doi.org/10.1002/ADHM.202100234.

11. Rodin, M.; Li, J.; Kuckling, D. Dually Cross-Linked Single Networks: Structures and Applications. *Chem Soc Rev* **2021**, *50* (14), 8147–8177. https://doi.org/10.1039/D0CS01585G.

12. Svenson, S. Controlling Surfactant Self-Assembly. *Curr Opin Colloid Interface Sci* **2004**, *9* (3–4), 201–212. https://doi.org/10.1016/J.COCIS.2004.06.008.

13. Romsted, L. S. Introduction to Surfactant Self-Assembly. *Supramol Chem* **2012**. https://doi.org/10.1002/9780470661345.SMC013.

Chapter 2

1. *Sustainable chemistry – OECD*. https://www.oecd.org/chemicalsafety/risk-management/sustainable-chemistry/ (accessed 2023-04-12).

2. Geng, Y.; Doberstein, B. Developing the Circular Economy in China: Challenges and Opportunities for Achieving "Leapfrog Development." *International Journal of Sustainable Development & World Ecology* **2008**, *15* (3), 231–239. https://doi.org/10.3843/SusDev.15.3:6.

3. Webster, K. *The Circular Economy: A Wealth of Flows*; Ellen MacArthur Foundation Publishing, 2017.

4. *Global Adhesives And Sealants Market Size Report, 2023-2030*. https://www.grandviewresearch.com/industry-analysis/adhesives-and-sealants-market (accessed 2023-04-12).

5. Dahlbo, H.; Poliakova, V.; Mylläri, V.; Sahimaa, O.; Anderson, R. Recycling Potential of Post-Consumer Plastic Packaging Waste in Finland. *Waste management* **2018**, *71*, 52–61.

6. Klein, J. D.; Blount, M. A.; Sands, J. M. Urea Transport in the Kidney. *Compr Physiol* **2011**, *1*, 699–729. https://doi.org/10.1002/cphy.c100030.

7. Loeser, E.; Delacruz, M.; Madappalli, V. Solubility of Urea in Acetonitrile-Water Mixtures and Liquid-Liquid Phase Separation of Urea-Saturated Acetonitrile-Water Mixtures. *J Chem Eng Data* **2011**, *56*, 2909–2913. https://doi.org/10.1021/je200122b.

8. Greenan, N. S.; Mulvaney, R. L.; Sims, G. K. A Microscale Method for Colorimetric Determination of Urea in Soil Extracts. *Commun Soil Sci Plant Anal* **1995**, *26*, 2519–2529. https://doi.org/10.1080/00103629509369465.

9. Marsh, K. L.; Sims, G. K.; Mulvaney, R. L. Availability of Urea to Autotrophic Ammonia-Oxidizing Bacteria as Related to the Fate of 14C- and 15N-Labeled Urea Added to Soil. *Biol Fertil Soils* **2005**, *42*, 137–145. https://doi.org/10.1007/s00374-005-0004-2.

10. Dunky, M. Urea-Formaldehyde (UF) Adhesive Resins for Wood. *Int J Adhes Adhes* **1998**, *18*, 95–107. https://doi.org/10.1016/S0143-7496(97)00054-7.

11. Zhou, J.; Yue, K.; Lu, W.; Chen, Z.; Cheng, X.; Liu, W.; Jia, C.; Tang, L. Bonding Performance of Melamine-Urea-Formaldehyde and Phenol-Resorcinol-Formaldehyde Adhesives in Interior Grade Glulam. *J Adhes Sci Technol* **2017**, *31*, 2630–2639. https://doi.org/10.1080/01694243.2017.1313185.

12. Paiva, N. T.; Ferra, J. M.; Pereira, J.; Martins, J.; Carvalho, L.; Magalhães, F. D. Production of Water Tolerant Melamine–Urea–Formaldehyde Resin by Incorporation of Sodium Metabisulphite. *Int J Adhes Adhes* **2016**, *70*, 160–166. https://doi.org/10.1016/j.ijadhadh.2016.06.005.

13. Jeong, B.; Park, B.-D. Practical Relationship between Apparent Viscosity and Molecular Weight of Urea-Formaldehyde Resin Adhesives. *J Adhes Sci Technol* **2019**, *33*, 209–216. https://doi.org/10.1080/01694243.2018.1529282.

14. Rollinson, A. N.; Jones, J.; Dupont, V.; Twigg, M. V. Urea as a Hydrogen Carrier: A Perspective on Its Potential for Safe, Sustainable and Long-Term Energy Supply. *Energy Environ Sci* **2011**, *4*, 1216–1224. https://doi.org/10.1039/c0ee00705f.

15. Macpherson, G. Black’s Student Medical Dictionary. **2004**.

16. Maurer, M.; Muncke, J.; … T. A. L.-R. and R.; 2002, undefined. Technologies for Nitrogen Recovery and Reuse. *IWA Publishing London*.

17. Udert, K. M.; Larsen, T. A.; Biebow, M.; Gujer, W. Urea Hydrolysis and Precipitation Dynamics in a Urine-Collecting System. *Water Res* **2003**, *37*, 2571–2582. https://doi.org/10.1016/S0043-1354(03)00065-4.

18. Hellström, D.; Johansson, E.; Grennberg, K. Storage of Human Urine: Acidification as a Method to Inhibit Decomposition of Urea. *Ecol Eng* **1999**, *12*, 253–269. https://doi.org/10.1016/S0925-8574(98)00074-3.

19. Montarnal, D.; Cordier, P.; Soulié-Ziakovic, C.; Tournilhac, F.; Leibler, L. Synthesis of Self-Healing Supramolecular Rubbers from Fatty Acid Derivatives, Diethylene Triamine, and Urea. *J Polym Sci A Polym Chem* **2008**, *46*, 7925–7936. https://doi.org/10.1002/pola.23094.

20. Wang, P.; Ma, X.; Li, Q.; Yang, B.; Shang, J.; Deng, Y. Green Synthesis of Polyureas from CO2 and Diamines with a Functional Ionic Liquid as the Catalyst. *RSC Adv* **2016**, *6*, 54013–54019. https://doi.org/10.1039/c6ra07452a.

21. Redlich, C. A.; Karol, M. H. Diisocyanate Asthma: Clinical Aspects and Immunopathogenesis. *Int Immunopharmacol* **2002**, *2*, 213–224. https://doi.org/10.1016/S1567-5769(01)00174-6.

22. Ma, S.; Liu, C.; Sablong, R. J.; Noordover, B. A. J.; Hensen, E. J. M.; Van Benthem, R. A. T. M.; Koning, C. E. Catalysts for Isocyanate-Free Polyurea Synthesis: Mechanism and Application. *ACS Catal* **2016**, *6*, 6883–6891. https://doi.org/10.1021/acscatal.6b01673.

23. Sintas, J. I.; Wolfgang, J. D.; Long, T. E. Carbamate Thermal Decarboxylation for the Design of Non-Isocyanate Polyurethane Foams. *Polym Chem* **2023**, *14* (13), 1497–1506. https://doi.org/10.1039/D3PY00096F.

24. Wolfgang, J. D.; White, B. T.; Long, T. E. Non-Isocyanate Polyurethanes from 1,1′-Carbonyldiimidazole: A Polycondensation Approach. *Macromol Rapid Commun* **2021**, *42* (13), 2100163. https://doi.org/10.1002/MARC.202100163.

25. Sirrine, J. M.; Schexnayder, S. A.; Dennis, J. M.; Long, T. E. Urea as a Monomer for Isocyanate-Free Synthesis of Segmented Poly(Dimethyl Siloxane) Polyureas. *Polymer (Guildf)* **2018**, *154*, 225–232. https://doi.org/https://doi.org/10.1016/j.polymer.2018.09.003.

26. Dennis, J. M.; Steinberg, L. I.; Pekkanen, A. M.; Maiz, J.; Hegde, M.; Müller, A. J.; Long, T. E. Synthesis and Characterization of Isocyanate-Free Polyureas. *Green Chemistry* **2018**, *20* (1), 243–249. https://doi.org/10.1039/C7GC02996A.

27. White, B. T.; Migliore, J. M.; Mapesa, E. U.; Wolfgang, J. D.; Sangoro, J.; Long, T. E. Isocyanate- and Solvent-Free Synthesis of Melt Processible Polyurea Elastomers Derived from Urea as a Monomer. *RSC Adv* **2020**, *10*, 18760–18768. https://doi.org/10.1039/D0RA02369H.

28. Dlugokencky, E. J. Atmospheric Composition [in State of the Climate in 2018, Chapter 2: Global Climate]. *Bull Am Meteorol Soc* **2019**, *100* (9), S48–S50.

29. Scharfenberg, M.; Hilf, J.; Frey, H. Functional Polycarbonates from Carbon Dioxide and Tailored Epoxide Monomers: Degradable Materials and Their Application Potential. *Adv Funct Mater* **2018**, *28* (10), 1704302. https://doi.org/10.1002/adfm.201704302.

30. Orgilés-Calpena, E.; Arán-Aís, F.; Torró-Palau, A. M.; Orgilés-Barceló, C. Novel Polyurethane Reactive Hot Melt Adhesives Based on Polycarbonate Polyols Derived from CO2 for the Footwear Industry. *Int J Adhes Adhes* **2016**, *70*, 218–224. https://doi.org/https://doi.org/10.1016/j.ijadhadh.2016.07.009.

31. Samanta, S.; Selvakumar, S.; Bahr, J.; Wickramaratne, D. S.; Sibi, M.; Chisholm, B. J. Synthesis and Characterization of Polyurethane Networks Derived from Soybean-Oil-Based Cyclic Carbonates and Bioderivable Diamines. *ACS Sustain Chem Eng* **2016**, *4* (12), 6551–6561. https://doi.org/10.1021/acssuschemeng.6b01409.

32. Poussard, L.; Mariage, J.; Grignard, B.; Detrembleur, C.; Jérôme, C.; Calberg, C.; Heinrichs, B.; De Winter, J.; Gerbaux, P.; Raquez, J. M.; Bonnaud, L.; Dubois, P. Non-

Isocyanate Polyurethanes from Carbonated Soybean Oil Using Monomeric or Oligomeric Diamines To Achieve Thermosets or Thermoplastics. *Macromolecules* **2016**, *49* (6), 2162–2171. https://doi.org/10.1021/acs.macromol.5b02467.

33. Wang, Y.; Darensbourg, D. J. Carbon Dioxide-Based Functional Polycarbonates: Metal Catalyzed Copolymerization of CO2 and Epoxides. *Coord Chem Rev* **2018**, *372*, 85–100. https://doi.org/https://doi.org/10.1016/j.ccr.2018.06.004.

34. Aida, T.; Ishikawa, M.; Inoue, S. Alternating Copolymerization of Carbon Dioxide and Epoxide Catalyzed by the Aluminum Porphyrin-Quaternary Organic Salt or -Triphenylphosphine System. Synthesis of Polycarbonate with Well-Controlled Molecular Weight. *Macromolecules* **1986**, *19* (1), 8–13. https://doi.org/10.1021/ma00155a002.

35. Trott, G.; Saini, P. K.; Williams, C. K. Catalysts for CO2/Epoxide Ring-Opening Copolymerization. *Philosophical Transactions of the Royal Society A: Mathematical, Physical and Engineering Sciences* **2016**, *374* (2061), 20150085. https://doi.org/doi:10.1098/rsta.2015.0085.

36. Kember, M. R.; Copley, J.; Buchard, A.; Williams, C. K. Triblock Copolymers from Lactide and Telechelic Poly(Cyclohexene Carbonate). *Polym Chem* **2012**, *3* (5), 1196–1201. https://doi.org/10.1039/C2PY00543C.

37. Ren, G.; Sheng, X.; Qin, Y.; Chen, X.; Wang, X.; Wang, F. Toughening of Poly(Propylene Carbonate) Using Rubbery Non-Isocyanate Polyurethane: Transition from Brittle to Marginally Tough. *Polymer (Guildf)* **2014**, *55* (21), 5460–5468. https://doi.org/https://doi.org/10.1016/j.polymer.2014.08.052.

38. Han, D.; Chen, G.; Xiao, M.; Wang, S.; Chen, S.; Peng, X.; Meng, Y. Biodegradable and Toughened Composite of Poly(Propylene Carbonate)/Thermoplastic Polyurethane (PPC/TPU): Effect of Hydrogen Bonding. *Int J Mol Sci* **2018**, *19* (7), 2032.

39. Ma, L.; Song, L.; Wang, H.; Fan, L.; Liu, B. Synthesis and Characterization of Poly(Propylene Carbonate) Glycol-Based Waterborne Polyurethane with a High Solid Content. *Prog Org Coat* **2018**, *122*, 38–44. https://doi.org/https://doi.org/10.1016/j.porgcoat.2018.05.003.

40. Sulley, G. S.; Gregory, G. L.; Chen, T. T. D.; Peña Carrodeguas, L.; Trott, G.; Santmarti, A.; Lee, K.-Y.; Terrill, N. J.; Williams, C. K. Switchable Catalysis Improves the Properties of CO2-Derived Polymers: Poly(Cyclohexene Carbonate-b-ε-Decalactone-b-Cyclohexene Carbonate) Adhesives, Elastomers, and Toughened Plastics. *J Am Chem Soc* **2020**, *142* (9), 4367–4378. https://doi.org/10.1021/jacs.9b13106.

41. Jenkins, C. L.; Siebert, H. M.; Wilker, J. J. Integrating Mussel Chemistry into a Bio-Based Polymer to Create Degradable Adhesives. *Macromolecules* **2017**, *50* (2), 561–568. https://doi.org/10.1021/acs.macromol.6b02213.

42. Chung, H. U.; Kim, B. H.; Lee, J. Y.; Lee, J.; Xie, Z.; Ibler, E. M.; Lee, K.; Banks, A.; Jeong, J. Y.; Kim, J.; Ogle, C.; Grande, D.; Yu, Y.; Jang, H.; Assem, P.; Ryu, D.; Kwak, J. W.; Namkoong, M.; Park, J. Bin; Lee, Y.; Kim, D. H.; Ryu, A.; Jeong, J.; You, K.; Ji, B.; Liu, Z.; Huo, Q.; Feng, X.; Deng, Y.; Xu, Y.; Jang, K.-I.; Kim, J.; Zhang, Y.; Ghaffari, R.; Rand, C. M.; Schau, M.; Hamvas, A.; Weese-Mayer, D. E.; Huang, Y.; Lee, S. M.; Lee, C. H.; Shanbhag, N. R.; Paller, A. S.; Xu, S.; Rogers, J. A. Binodal, Wireless Epidermal Electronic Systems with in-Sensor Analytics for Neonatal Intensive Care. *Science* **2019**, *363* (6430), eaau0780–eaau0780. https://doi.org/10.1126/science.aau0780.

43. Shukla, K.; Srivastava, V. C. Synthesis of Organic Carbonates from Alcoholysis of Urea: A Review. *Catalysis Reviews* **2017**, *59* (1), 1–43. https://doi.org/10.1080/01614940.2016.1263088.

44. Beharaj, A.; McCaslin, E. Z.; Blessing, W. A.; Grinstaff, M. W. Sustainable Polycarbonate Adhesives for Dry and Aqueous Conditions with Thermoresponsive Properties. *Nat Commun* **2019**, *10* (1), 5478. https://doi.org/10.1038/s41467-019-13449-y.

45. Krase, N. W.; Gaddy, V. L. Synthesis of Urea from Ammonia and Carbon Dioxide. *Journal of Industrial & Engineering Chemistry* **1922**, *14* (7), 611–615. https://doi.org/10.1021/ie50151a009.

46. Du, Z.; Chen, F.; Lin, Z.; Li, X.; Yuan, H.; Wu, Y. Effect of MgO on the Catalytic Performance of MgTiO3 in Urea Alcoholysis to Propylene Carbonate. *Chemical Engineering Journal* **2015**, *278*, 79–84. https://doi.org/https://doi.org/10.1016/j.cej.2014.12.033.

47. Woodcock, J. W.; Wright, R. A. E.; Jiang, X.; O'Lenick, T. G.; Zhao, B. Dually Responsive Aqueous Gels from Thermo- and Light-Sensitive Hydrophilic ABA Triblock Copolymers. *Soft Matter* **2010**, *6* (14), 3325–3336. https://doi.org/10.1039/C000450B.

48. Bender, T. A.; Dabrowski, J. A.; Gagné, M. R. Homogeneous Catalysis for the Production of Low-Volume, High-Value Chemicals from Biomass. *Nat Rev Chem* **2018**, *2* (5), 35–46. https://doi.org/10.1038/s41570-018-0005-y.

49. Stemmelen, M.; Lapinte, V.; Habas, J.-P.; Robin, J.-J. Plant Oil-Based Epoxy Resins from Fatty Diamines and Epoxidized Vegetable Oil. *Eur Polym J* **2015**, *68*, 536–545. https://doi.org/https://doi.org/10.1016/j.eurpolymj.2015.03.062.

50. Farhadian, A.; Gol Afshani, M. B.; Babaei Miyardan, A.; Nabid, M. R.; Safari, N. A Facile and Green Route for Conversion of Bifunctional Epoxide and Vegetable Oils to Cyclic Carbonate: A Green Route to CO2 Fixation. *ChemistrySelect* **2017**, *2* (4), 1431–1435. https://doi.org/10.1002/slct.201601891.

51. Orgilés-Calpena, E.; Arán-Aís, F.; Torró-Palau, A. M.; Montiel-Parreño, E.; Orgilés-

Barceló, C. Synthesis of Polyurethanes from CO2-Based Polyols: A Challenge for Sustainable Adhesives. *Int J Adhes Adhes* **2016**, *67*, 63–68. https://doi.org/https://doi.org/10.1016/j.ijadhadh.2015.12.027.

52. Delebecq, E.; Pascault, J.-P.; Boutevin, B.; Ganachaud, F. On the Versatility of Urethane/Urea Bonds: Reversibility, Blocked Isocyanate, and Non-Isocyanate Polyurethane. *Chem Rev* **2013**, *113* (1), 80–118. https://doi.org/10.1021/cr300195n.

53. Heinrich, L. A. Future Opportunities for Bio-Based Adhesives – Advantages beyond Renewability. *Green Chemistry* **2019**, *21* (8), 1866–1888. https://doi.org/10.1039/C8GC03746A.

54. Janvier, M.; Ducrot, P.-H.; Allais, F. Isocyanate-Free Synthesis and Characterization of Renewable Poly(Hydroxy)Urethanes from Syringaresinol. *ACS Sustain Chem Eng* **2017**, *5* (10), 8648–8656. https://doi.org/10.1021/acssuschemeng.7b01271.

55. Wai, P. T.; Jiang, P.; Shen, Y.; Zhang, P.; Gu, Q.; Leng, Y. Catalytic Developments in the Epoxidation of Vegetable Oils and the Analysis Methods of Epoxidized Products. *RSC Adv* **2019**, *9* (65), 38119–38136. https://doi.org/10.1039/C9RA05943A.

56. Li, Y.; Sun, X. S. Polyols from Epoxidized Soybean Oil and Alpha Hydroxyl Acids and Their Adhesion Properties from UV Polymerization. *Int J Adhes Adhes* **2015**, *63*, 1–8. https://doi.org/https://doi.org/10.1016/j.ijadhadh.2015.07.013.

57. Li, Y.; Chou, S.-H.; Qian, W.; Sung, J.; Chang, S. I.; Sun, X. S. Optimization of Soybean Oil Based Pressure-Sensitive Adhesives Using a Full Factorial Design. *J Am Oil Chem Soc* **2017**, *94* (5), 713–721. https://doi.org/10.1007/s11746-017-2966-2.

58. Liu, X. Synthesis and Properties of Bio-Based Adhesives Derived from Plant Oil Residues. *American Journal of Modern Energy* **2019**, *5* (6), 94–99. https://doi.org/10.11648/j.ajme.20190506.12.

59. Sawpan, M. A. Polyurethanes from Vegetable Oils and Applications: A Review. *Journal of Polymer Research* **2018**, *25* (8), 184. https://doi.org/10.1007/s10965-018-1578-3.

60. Vanags, E.; Kirpluks, M.; Cabulis, U.; Walterova, Z. Highly Functional Polyol Synthesis from Epoxidized Tall Oil Fatty Acids. *J Renew Mater* **2018**, *6* (7), 764–771. https://doi.org/10.7569/JRM.2018.634111.

61. Kurańska, M.; Banaś, J.; Polaczek, K.; Banaś, M.; Prociak, A.; Kuc, J.; Uram, K.; Lubera, T. Evaluation of Application Potential of Used Cooking Oils in the Synthesis of Polyol Compounds. *J Environ Chem Eng* **2019**, *7* (6), 103506. https://doi.org/https://doi.org/10.1016/j.jece.2019.103506.

62. Goudarzi, F.; Izadbakhsh, A. Evaluation of K/SnO2 Performance as a Solid Catalyst in the Trans-Esterification of a Mixed Plant Oil. *Reaction Kinetics, Mechanisms and*

Catalysis **2017**, *121* (2), 539–553. https://doi.org/10.1007/s11144-017-1176-0.

63. Li, C.; Wang, W.; Yan, L.; Ding, Y. A Mini Review on Strategies for Heterogenization of Rhodium-Based Hydroformylation Catalysts. *Front Chem Sci Eng* **2018**, *12* (1), 113–123. https://doi.org/10.1007/S11705-017-1672-9/METRICS.

64. Pandey, S.; Chikkali, S. H. Highly Regioselective Isomerizing Hydroformylation of Long-Chain Internal Olefins Catalyzed by a Rhodium Bis(Phosphite) Complex. *ChemCatChem* **2015**, *7* (21), 3468–3471. https://doi.org/10.1002/cctc.201500743.

65. Alagi, P.; Ghorpade, R.; Jang, J. H.; Patil, C.; Jirimali, H.; Gite, V.; Hong, S. C. Functional Soybean Oil-Based Polyols as Sustainable Feedstocks for Polyurethane Coatings. *Ind Crops Prod* **2018**, *113*, 249–258. https://doi.org/https://doi.org/10.1016/j.indcrop.2018.01.041.

66. Pechar, T. W.; Sohn, S.; Wilkes, G. L.; Ghosh, S.; Frazier, C. E.; Fornof, A.; Long, T. E. Characterization and Comparison of Polyurethane Networks Prepared Using Soybean-Based Polyols with Varying Hydroxyl Content and Their Blends with Petroleum-Based Polyols. *J Appl Polym Sci* **2006**, *101* (3), 1432–1443. https://doi.org/10.1002/app.23625.

67. Alagi, P.; Choi, Y. J.; Seog, J.; Hong, S. C. Efficient and Quantitative Chemical Transformation of Vegetable Oils to Polyols through a Thiol-Ene Reaction for Thermoplastic Polyurethanes. *Ind Crops Prod* **2016**, *87*, 78–88. https://doi.org/https://doi.org/10.1016/j.indcrop.2016.04.027.

68. Teacă, C.-A.; Roşu, D.; Tanasă, F.; Zănoagă, M.; Mustaţă, F. Epoxidized Vegetable Oils for Thermosetting Resins and Their Potential Applications. In *Functional Biopolymers*; Thakur, V. K., Thakur, M. K., Eds.; Springer International Publishing: Cham, 2018; pp 217–238. https://doi.org/10.1007/978-3-319-66417-0_8.

69. Wang, X.-L.; Chen, L.; Wu, J.-N.; Fu, T.; Wang, Y.-Z. Flame-Retardant Pressure-Sensitive Adhesives Derived from Epoxidized Soybean Oil and Phosphorus-Containing Dicarboxylic Acids. *ACS Sustain Chem Eng* **2017**, *5* (4), 3353–3361. https://doi.org/10.1021/acssuschemeng.6b03201.

70. Tenorio-Alfonso, A.; Sánchez, M. C.; Franco, J. M. A Review of the Sustainable Approaches in the Production of Bio-Based Polyurethanes and Their Applications in the Adhesive Field. *J Polym Environ* **2020**, *28* (3), 749–774. https://doi.org/10.1007/s10924-020-01659-1.

71. Hong, J.; Radojčić, D.; Yang, X.-Q.; Wan, X.; Petrović, Z. S. Tough Thermosetting Polyurethanes and Adhesives from Rubber Seed Oil by Hydroformylation. *J Appl Polym Sci* **2020**, *137* (13), 48509. https://doi.org/10.1002/app.48509.

72. Gama, N.; Ferreira, A.; Barros-Timmons, A. Cure and Performance of Castor Oil Polyurethane Adhesive. *Int J Adhes Adhes* **2019**, *95*, 102413.

https://doi.org/https://doi.org/10.1016/j.ijadhadh.2019.102413.

73. Faria, D. L.; Lopes, T. A.; Scatolino, M. V.; Protásio, T. D. P.; Nascimento, M. F. do; Lahr, F. A. R.; Mendes, L. M.; Guimarães Júnior, J. B. STUDYING THE GRAMMAGE IN LVL PANELS GLUED WITH CASTOR OIL-BASED POLYURETHANE ADHESIVE: A POSSIBLE ALTERNATIVE TO FORMALDEHYDE RELEASING ADHESIVES. *CERNE* **2020**, No. 1, 140-149%V 26.

74. Mapari, S.; Mestry, S.; Mhaske, S. T. Developments in Pressure-Sensitive Adhesives: A Review. *Polymer Bulletin 2020 78:7* **2020**, *78* (7), 4075–4108. https://doi.org/10.1007/S00289-020-03305-1.

75. Ewert, T. R.; Mannion, A. M.; Coughlin, M. L.; Macosko, C. W.; Bates, F. S. Influence of Rheology on Renewable Pressure-Sensitive Adhesives from a Triblock Copolymer. *J Rheol (N Y N Y)* **2018**, *62* (1), 161–170. https://doi.org/10.1122/1.5009194.

76. Sodergard, A.; Stolt, M. Properties of Lactic Acid Based Polymers and Their Correlation with Composition. *Progress in Polymer Science – PROG POLYM SCI* **2002**, *27*, 1123–1163. https://doi.org/10.1016/S0079-6700(02)00012-6.

77. De Hoe, G. X.; Zumstein, M. T.; Tiegs, B. J.; Brutman, J. P.; McNeill, K.; Sander, M.; Coates, G. W.; Hillmyer, M. A. Sustainable Polyester Elastomers from Lactones: Synthesis, Properties, and Enzymatic Hydrolyzability. *J Am Chem Soc* **2018**, *140* (3), 963–973. https://doi.org/10.1021/jacs.7b10173.

78. Martello, M. T.; Schneiderman, D. K.; Hillmyer, M. A. Synthesis and Melt Processing of Sustainable Poly(ε-Decalactone)-Block-Poly(Lactide) Multiblock Thermoplastic Elastomers. *ACS Sustain Chem Eng* **2014**, *2* (11), 2519–2526. https://doi.org/10.1021/sc500412a.

79. Wu, S. Chain Structure and Entanglement. *J Polym Sci B Polym Phys* **1989**, *27* (4), 723–741. https://doi.org/10.1002/polb.1989.090270401.

80. Nasiri, M.; Reineke, T. M. Sustainable Glucose-Based Block Copolymers Exhibit Elastomeric and Adhesive Behavior. *Polym Chem* **2016**, *7* (33), 5233–5240. https://doi.org/10.1039/C6PY00700G.

81. Kim, H. J.; Jin, K.; Shim, J.; Dean, W.; Hillmyer, M. A.; Ellison, C. J. Sustainable Triblock Copolymers as Tunable and Degradable Pressure Sensitive Adhesives. *ACS Sustain Chem Eng* **2020**. https://doi.org/10.1021/acssuschemeng.0c03158.

82. Kim, H. J. Sustainable Triblock Copolymers as Tunable and Degradable Pressure Sensitive Adhesives. *ACS Sustain Chem Eng* **2020**.

83. Dastjerdi, Z.; Cranston, E. D.; Dubé, M. A. Pressure Sensitive Adhesive Property Modification Using Cellulose Nanocrystals. *Int J Adhes Adhes* **2018**, *81*, 36–42.

https://doi.org/https://doi.org/10.1016/j.ijadhadh.2017.11.009.

84. Yang, X.; Li, N.; Constantinesco, I.; Yu, K.; Kizhakkedathu, J. N.; Brooks, D. E. Choline Phosphate Functionalized Cellulose Membrane: A Potential Hemostatic Dressing Based on a Unique Bioadhesion Mechanism. *Acta Biomater* **2016**, *40*, 212–225. https://doi.org/https://doi.org/10.1016/j.actbio.2016.06.030.

85. Abd el-sayed, E.; El-Sakhawy, M.; Kamel, S.; El-Gendy, A.; Abouzeid, R. Eco-Friendly Mimosa Tannin Adhesive System for Bagasse Particleboard Fabrication. *Egypt J Chem* **2018**. https://doi.org/10.21608/ejchem.2018.5413.1479.

86. Patel, A. K.; Mathias, J.-D.; Michaud, P. Polysaccharides as Adhesives. *Reviews of Adhesion and Adhesives* **2013**, *1* (3), 312–345. https://doi.org/10.7569/RAA.2013.097310.

87. Zhao, X.; Peng, L.; Wang, H.; Wang, Y.; Zhang, H. Environment-Friendly Urea-Oxidized Starch Adhesive with Zero Formaldehyde-Emission. *Carbohydr Polym* **2018**, *181*, 1112–1118. https://doi.org/https://doi.org/10.1016/j.carbpol.2017.11.035.

88. Chen, L.; Wang, Y.; Zia ud, D.; Fei, P.; Jin, W.; Xiong, H.; Wang, Z. Enhancing the Performance of Starch-Based Wood Adhesive by Silane Coupling Agent(KH570). *Int J Biol Macromol* **2017**, *104*, 137–144. https://doi.org/https://doi.org/10.1016/j.ijbiomac.2017.05.182.

89. Umemura, K.; Mihara, A.; Kawai, S. Development of New Natural Polymer-Based Wood Adhesives III: Effects of Glucose Addition on Properties of Chitosan. *Journal of Wood Science* **2010**, *56* (5), 387–394. https://doi.org/10.1007/s10086-010-1117-2.

90. Park, E.; Lee, J.; Huh, K. M.; Lee, S. H.; Lee, H. Toxicity-Attenuated Glycol Chitosan Adhesive Inspired by Mussel Adhesion Mechanisms. *Adv Healthc Mater* **2019**, *8* (14), 1900275. https://doi.org/10.1002/adhm.201900275.

91. Nourmohammadi, J.; Ghaee, A.; Liavali, S. H. Preparation and Characterization of Bioactive Composite Scaffolds from Polycaprolactone Nanofibers-Chitosan-Oxidized Starch for Bone Regeneration. *Carbohydr Polym* **2016**, *138*, 172–179. https://doi.org/https://doi.org/10.1016/j.carbpol.2015.11.055.

92. Benedek, I. *Pressure-Sensitive Adhesives and Applications*; CRC Press, 2004.

93. Griehl, W.; Ruestem, D. Nylon-12-Preparation, Properties, and Applications. *Ind Eng Chem* **1970**, *62* (3), 16–22.

94. Lundberg, R. D. Structure and Properties of Ionomers'(Eds M. Pineri and A. Eisenberg), D. Reidel Publishing Company, Boston 1987.

95. Boval'dinova, K. A.; Sherstneva, N. E.; Fel'dshtein, M. M.; Moskalets, A. P.; Khokhlov, A. R. Pressure-Sensitive Adhesives with Tunable Tackiness. *Polymer*

Science, Series B **2019**, *61* (4), 458–470.

96. Wang, W.; Liu, S.; Chen, B.; Yan, X.; Li, S.; Ma, X.; Yu, X. DNA-Inspired Adhesive Hydrogels Based on the Biodegradable Polyphosphoesters Tackified by a Nucleobase. *Biomacromolecules* **2019**, *20* (10), 3672–3683. https://doi.org/10.1021/acs.biomac.9b00642.

97. Zhang, K.; Fahs, G. B.; Margaretta, E.; Hudson, A. G.; Moore, R. B.; Long, T. E. Acetyl-Protected Cytosine and Guanine Containing Acrylics as Supramolecular Adhesives. *J Adhes* **2019**, *95* (2), 146–167.

98. Chen, X.; Zhang, K.; Talley, S. J.; Orsino, C. M.; Moore, R. B.; Long, T. E. Quadruple Hydrogen Bonding Containing Supramolecular Thermoplastic Elastomers: Mechanical and Morphological Correlations. *J. Polym. Sci. Part A: Polym. Chem.* **2019**, *57* (1), 13–23. https://doi.org/doi:10.1002/pola.29272.

99. Tamami, M.; Zhang, K.; Dixit, N.; Moore, R. B.; Long, T. E. Association of Nucleobase-Containing Ammonium Ionenes. *Macromol Chem Phys* **2014**, *215* (23), 2337–2344.

100. Zhang, K.; Fahs, G. B.; Aiba, M.; Moore, R. B.; Long, T. E. Nucleobase-Functionalized ABC Triblock Copolymers: Self-Assembly of Supramolecular Architectures. *Chemical Communications* **2014**, *50* (65), 9145–9148. https://doi.org/10.1039/C4CC03363A.

101. Tamami, M.; Hemp, S. T.; Zhang, K.; Zhang, M.; Moore, R. B.; Long, T. E. Poly(Ethylene Glycol)-Based Ammonium Ionenes Containing Nucleobases. *Polymer (Guildf)* **2013**, *54* (6), 1588–1595. https://doi.org/10.1016/J.POLYMER.2013.01.040.

102. Zhang, K.; Chen, M.; Drummey, K. J.; Talley, S. J.; Anderson, L. J.; Moore, R. B.; Long, T. E. Ureido Cytosine and Cytosine-Containing Acrylic Copolymers. *Polym. Chem.* **2016**, *7* (43), 6671–6681.

103. Zhang, K.; Aiba, M.; Fahs, G. B.; Hudson, A. G.; Chiang, W. D.; Moore, R. B.; Ueda, M.; Long, T. E. Nucleobase-Functionalized Acrylic ABA Triblock Copolymers and Supramolecular Blends. *Polym Chem* **2015**, *6* (13), 2434–2444.

104. Cashion, M. P.; Park, T.; Long, T. E. Influence of Hydrogen Bonding on the Adhesive Properties of Photo-Curable Acrylics. *J Adhes* **2009**, *85* (1), 1–17.

105. Karikari, A. S.; Mather, B. D.; Long, T. E. Association of Star-Shaped Poly (D, L-Lactide) s Containing Nucleobase Multiple Hydrogen Bonding. *Biomacromolecules* **2007**, *8* (1), 302–308.

106. Yamauchi, K.; Lizotte, J. R.; Long, T. E. Thermoreversible Poly (Alkyl Acrylates) Consisting of Self-Complementary Multiple Hydrogen Bonding. *Macromolecules* **2003**, *36* (4), 1083–1088.

107. Chen, X.; Zawaski, C. E.; Spiering, G. A.; Liu, B.; Orsino, C. M.; Moore, R. B.; Williams, C. B.; Long, T. E. Quadruple Hydrogen Bonding Supramolecular Elastomers for Melt Extrusion Additive Manufacturing. *ACS Appl Mater Interfaces* **2020**, *12* (28), 32006–32016. https://doi.org/10.1021/acsami.0c08958.

108. Liu, B.; Chen, X.; Spiering, G. A.; Moore, R. B.; Long, T. E. Quadruple Hydrogen Bond-Containing A-AB-A Triblock Copolymers: Probing the Influence of Hydrogen Bonding in the Central Block. *Molecules 2021, Vol. 26, Page 4705* **2021**, *26* (15), 4705. https://doi.org/10.3390/MOLECULES26154705.

109. Domb, A. J.; Kost, J.; Wiseman, D. *Handbook of Biodegradable Polymers*; CRC press, 1998.

110. Du, X.; Liu, Y.; Yan, H.; Rafique, M.; Li, S.; Shan, X.; Wu, L.; Qiao, M.; Kong, D.; Wang, L. Anti-Infective and Pro-Coagulant Chitosan-Based Hydrogel Tissue Adhesive for Sutureless Wound Closure. *Biomacromolecules* **2020**, *21* (3), 1243–1253. https://doi.org/10.1021/acs.biomac.9b01707.

111. Takeoka, Y.; Yurube, T.; Morimoto, K.; Kunii, S.; Kanda, Y.; Tsujimoto, R.; Kawakami, Y.; Fukase, N.; Takemori, T.; Omae, K.; Kakiuchi, Y.; Miyazaki, S.; Kakutani, K.; Takada, T.; Nishida, K.; Fukushima, M.; Kuroda, R. Reduced Nucleotomy-Induced Intervertebral Disc Disruption through Spontaneous Spheroid Formation by the Low Adhesive Scaffold Collagen (LASCol). *Biomaterials* **2020**, *235*, 119781. https://doi.org/https://doi.org/10.1016/j.biomaterials.2020.119781.

112. Ushimaru, K.; Morita, T.; Fukuoka, T. A Bio-Based Adhesive Composed of Polyelectrolyte Complexes of Lignosulfonate and Cationic Polyelectrolytes. *Journal of Wood Chemistry and Technology* **2020**, *40* (3), 172–177. https://doi.org/10.1080/02773813.2020.1722701.

113. Vargas Villanueva, J. G.; Sarmiento Huertas, P. A.; Galan, F. S.; Esteban Rueda, R. J.; Briceño Triana, J. C.; Casas Rodriguez, J. P. Bio-Adhesion Evaluation of a Chitosan-Based Bone Bio-Adhesive. *Int J Adhes Adhes* **2019**, *92*, 80–88. https://doi.org/https://doi.org/10.1016/j.ijadhadh.2019.04.009.

114. Giroto, J. A.; Teixeira, A. C. S. C.; Nascimento, C. A. O.; Guardani, R. Degradation of Poly(Ethylene Glycol) in Aqueous Solution by Photo-Fenton and H2O2/UV Processes. *Ind Eng Chem Res* **2010**, *49* (7), 3200–3206. https://doi.org/10.1021/ie9015792.

115. Banerjee, A.; Chatterjee, K.; Madras, G. Enzymatic Degradation of Polymers: A Brief Review. *Materials Science and Technology* **2014**, *30* (5), 567–573.

116. Kawai, F.; Moriya, F. Bacterial Assimilation of Polytetramethylene Glycol. *J Ferment Bioeng* **1991**, *71* (1), 1–5. https://doi.org/https://doi.org/10.1016/0922-338X(91)90294-Q.

117. Kawai, F. Biodegradation of Polyethers (Polyethylene Glycol, Polypropylene Glycol, Polytetramethylene Glycol, and Others). *Biopolymers Online: Biology• Chemistry• Biotechnology• Applications* **2005**, *9*.

118. Cernadas, T. M.; Gonçalves, F. A. M. M.; Alves, P.; Miguel, S. P.; Cabral, C.; Correia, I. J.; Ferreira, P. Preparation of Biodegradable Functionalized Polyesters Aimed to Be Used as Surgical Adhesives. *Eur Polym J* **2019**, *117*, 442–454. https://doi.org/https://doi.org/10.1016/j.eurpolymj.2019.05.019.

119. Daristotle, J. L.; Zaki, S. T.; Lau, L. W.; Ayyub, O. B.; Djouini, M.; Srinivasan, P.; Erdi, M.; Sandler, A. D.; Kofinas, P. Pressure-Sensitive Tissue Adhesion and Biodegradation of Viscoelastic Polymer Blends. *ACS Appl Mater Interfaces* **2020**, *12* (14), 16050–16057. https://doi.org/10.1021/acsami.0c00497.

120. Daristotle, J. L.; Lau, L. W.; Erdi, M.; Hunter, J.; Djoum Jr., A.; Srinivasan, P.; Wu, X.; Basu, M.; Ayyub, O. B.; Sandler, A. D.; Kofinas, P. Sprayable and Biodegradable, Intrinsically Adhesive Wound Dressing with Antimicrobial Properties. *Bioeng Transl Med* **2020**, *5* (1), e10149. https://doi.org/10.1002/btm2.10149.

121. Yang, Z.; Wang, F.; Liu, H. Dual Responsive Spiropyran-Ended Poly(N-Vinyl Caprolactam) for Reversible Complexation with Metal Ions. *Journal of Polymer Research* **2019**, *26* (4). https://doi.org/10.1007/s10965-019-1747-z.

122. Wang, X.; Chen, D.; Zhang, M.; Hu, H. Biodegradable Polylactide/TiO2 Composite Fiber Scaffolds with Superhydrophobic and Superadhesive Porous Surfaces for Water Immobilization, Antibacterial Performance, and Deodorization. *Polymers (Basel)* **2019**, *11* (11), 1860.

123. Bou-Francis, A.; Piercey, M.; Al-Qatami, O.; Mazzanti, G.; Khattab, R.; Ghanem, A. Polycaprolactone Blends for Fracture Fixation in Low Load-Bearing Applications. *J Appl Polym Sci* **2020**, *137* (32), 48940. https://doi.org/10.1002/app.48940.

124. Orgilés-Calpena, E.; Arán-Aís, F.; Torró-Palau, A.; Orgilés-Barceló, C. Biodegradable Polyurethane Adhesives Based on Polyols Derived from Renewable Resources. *Proceedings of the Institution of Mechanical Engineers, Part L: Journal of Materials: Design and Applications* **2014**, *228* (2), 125–136. https://doi.org/10.1177/1464420713517674.

125. Tous, L.; Ruseckaite, R. A.; Ciannamea, E. M. Sustainable Hot-Melt Adhesives Based on Soybean Protein Isolate and Polycaprolactone. *Ind Crops Prod* **2019**, *135*, 153–158. https://doi.org/https://doi.org/10.1016/j.indcrop.2019.04.043.

126. Cernadas, T.; Morgado, S.; Alves, P.; Gonçalves, F. A. M. M.; Correia, T. R.; Correia, I. J.; Ferreira, P. Preparation of Functionalized Poly(Caprolactone Diol)/Castor Oils Blends to Be Applied as Photocrosslinkable Tissue Adhesives. *J Appl Polym Sci* **2020**, *n/a* (n/a), 49092. https://doi.org/10.1002/app.49092.

127. Gu, Y.; Cheng, L.; Gu, Z.; Hong, Y.; Li, Z.; Li, C. Preparation, Characterization and Properties of Starch-Based Adhesive for Wood-Based Panels. *Int J Biol Macromol* **2019**, *134*, 247–254. https://doi.org/https://doi.org/10.1016/j.ijbiomac.2019.04.088.

Chapter 3

1. Chen, T. T. D.; Carrodeguas, L. P.; Sulley, G. S.; Gregory, G. L.; Williams, C. K. Bio-Based and Degradable Block Polyester Pressure-Sensitive Adhesives. *Angewandte Chemie* **2020**, *132* (52), 23656–23661. https://doi.org/10.1002/ANGE.202006807.

2. Kausar, A. High Performance Epoxy/Polyester-Based Nanocomposite Coatings for Multipurpose Applications: A Review. *Journal of Plastic Film & Sheeting* **2020**, *36* (4), 391–408. https://doi.org/10.1177/8756087920910481.

3. Snyder, R. L.; Lidston, C. A. L.; De Hoe, G. X.; Parvulescu, M. J. S.; Hillmyer, M. A.; Coates, G. W. Mechanically Robust and Reprocessable Imine Exchange Networks from Modular Polyester Pre-Polymers. *Polym Chem* **2020**, *11* (33), 5346–5355. https://doi.org/10.1039/C9PY01957J.

4. Self, J. L.; Sample, C. S.; Levi, A. E.; Li, K.; Xie, R.; De Alaniz, J. R.; Bates, C. M. Dynamic Bottlebrush Polymer Networks: Self-Healing in Super-Soft Materials. *J Am Chem Soc* **2020**, *142* (16), 7567–7573. https://doi.org/10.1021/JACS.0C01467/ASSET/IMAGES/LARGE/JA0C01467_0005.JPEG.

5. Bartoli, M.; Frediani, M.; Dehcheshmeh, I. M.; Poursattar Marjani, A.; Moghadam, P. N. Historical Aspects of Polyesters. *Applications of Unsaturated Polyester Resins* **2023**, 1–16. https://doi.org/10.1016/B978-0-323-99466-8.00004-6.

6. Allen, R. D.; James, M. I. Chemical Recycling of PET. *ACS Symposium Series* **2021**, *1391*, 61–80. https://doi.org/10.1021/BK-2021-1391.CH004/ASSET/IMAGES/LARGE/BK-2021-00150M_G010.JPEG.

7. Zhang, S.; Hu, Q.; Zhang, Y.-X.; Guo, H.; Wu, Y.; Sun, M.; Zhu, X.; Zhang, J.; Gong, S.; Liu, P.; Niu, Z. Depolymerization of Polyesters by a Binuclear Catalyst for Plastic Recycling. *Nature Sustainability 2023* **2023**, 1–9. https://doi.org/10.1038/s41893-023-01118-4.

8. Arrington, A. S.; Brown, J. R.; Win, M. S.; Winey, K. I.; Long, T. E. Melt Polycondensation of Carboxytelechelic Polyethylene for the Design of Degradable Segmented Copolyester Polyolefins †. **2022**. https://doi.org/10.1039/d2py00394e.

9. Ojha, U. P.; Kumar, A. Design, Synthesis, and Characterization of Main-Chain, Aromatic Polyesters Based on 3,4-Ethylenedioxythiophene. *J Polym Sci A Polym Chem* **2006**, *44* (11), 3479–3486. https://doi.org/10.1002/POLA.21414.

10. Chang, S.; Han, C. D. Effect of Flexible Spacer Length on the Phase Transitions and Mesophase Structures of Main-Chain Thermotropic Liquid-Crystalline Polyesters Having Bulky Pendent Side Groups. *Macromolecules* **1997**, *30* (6), 1670–1684. https://doi.org/10.1021/MA961730N/ASSET/IMAGES/LARGE/MA961730NFB15B.JPEG.

11. Mondschein, R. J.; Dennis, J. M.; Liu, H.; Ramakrishnan, R. K.; Sirrine, J. M.; Weiseman, T.; Colby, R. H.; Nazarenko, S.; Turner, S. R.; Long, T. E. Influence of Bibenzoate Regioisomers on Cyclohexanedimethanol-Based (Co)Polyester Structure-Property Relationships. *Macromolecules* **2019**, *52* (3), 835–843. https://doi.org/10.1021/ACS.MACROMOL.8B02411/SUPPL_FILE/MA8B02411_SI_002.PDF.

12. Light, R. R.; Seymour, R. W. Effect of Sub-Tg Relaxations on the Gas Transport Properties of Polyesters. *Polym Eng Sci* **1982**, *22* (14), 857–864. https://doi.org/10.1002/PEN.760221402.

13. Bhowmik, P. K.; Molla, A. H.; Han, H.; Gangoda, M. E.; Bose, R. N. Lyotropic Liquid Crystalline Main-Chain Viologen Polymers: Homopolymer of 4,4′-Bipyridyl with the Ditosylate of Trans-1,4-Cyclohexanedimethanol and Its Copolymers with the Ditosylate of 1,8-Octanediol. *Macromolecules* **1998**, *31* (3), 621–630. https://doi.org/10.1021/MA971115Z/ASSET/IMAGES/LARGE/MA971115ZF00012.JPEG.

14. Eliot Edling, H.; Mondschein, R. J.; Davis, M. K.; Long, T. E.; Richard Turner, S. Amorphous Copolyesters Based on Bibenzoic Acids and Neopentyl Glycol. *J Polym Sci A Polym Chem* **2019**, *57* (5), 579–587. https://doi.org/10.1002/POLA.29296.

15. Wang, G.; Liang, Y.; Jiang, M.; Zhang, Q.; Wang, R.; Wang, H.; Zhou, G. High Tg and Tough Poly(Butylene 2,5-Thiophenedicarboxylate-Co-1,4-Cyclohexanedimethylene 2,5-Thiophenedicarboxylate)s: Synthesis and Characterization. *J Appl Polym Sci* **2020**, *137* (18), 48634. https://doi.org/10.1002/APP.48634.

16. Porter, R. S.; Jonza, J. M.; Kimura, M.; Desper, C. R.; George, E. R. Polyesters II: A Review of Phase Behavior in Binary Blends: Amorphous, Crystalline, Liquid Crystalline, and on Transreaction. *Polym Eng Sci* **1989**, *29* (1), 55–62. https://doi.org/10.1002/PEN.760290110.

17. Pan, P.; Inoue, Y. Polymorphism and Isomorphism in Biodegradable Polyesters. *Prog Polym Sci* **2009**, *34* (7), 605–640. https://doi.org/10.1016/J.PROGPOLYMSCI.2009.01.003.

18. Akhmetshina, A. I.; Ignat’eva, E. K.; Deberdeev, T. R.; Karimova, L. K.; Yuminova, Y. N.; Berlin, A. A.; Deberdeev, R. Y. Thermotropic Liquid Crystalline Polyesters with Mesogenic Fragments Based on the P-Oxybenzoate Unit. *Polymer Science – Series D* **2019**, *12* (4), 427–434. https://doi.org/10.1134/S1995421219040026/TABLES/1.

19. G., F. T. Influence of Diluent and of Copolymer Composition on the Glass Temperature of a Polymer System. *Bull. Am. Phs. Soc.* **1952**, *1*, 123-.

20. Hamza, A. A.; Sokkar, T. Z. N.; El-Bakary, M. A. Interferometric Determination of the Birefringence of Thermo-Tropic Polyester Fibers and Its Copolymers of Structure (PCPT-Co-CPO). *J Appl Polym Sci* **2012**, *125* (3), 1814–1821. https://doi.org/10.1002/APP.36267.

21. McIntyre, J. E.; Maj, P. E. P.; Tomka, J. G. Thermotropic Polyesters: Synthesis and Properties of Poly(Chloro-1,4-Phenylene Terephthalate-Co-4,4′-Hexamethylenedioxy-Bisbenzoate)s. *Polymer (Guildf)* **1989**, *30* (4), 732–738. https://doi.org/10.1016/0032-3861(89)90164-X.

22. Heifferon, K. V.; Spiering, G. A.; Talley, S. J.; Hegde, M.; Moore, R. B.; Turner, S. R.; Long, T. E. Synthesis and Characterization of a Nematic Fully Aromatic Polyester Based on Biphenyl 3,4′-Dicarboxylic Acid. *Polym Chem* **2019**, *10* (31), 4287–4296. https://doi.org/10.1039/C9PY00683D.

23. Collins, S.; Peace, S. K.; Richards, R. W.; Macdonald, W. A.; Mills, P.; King, S. M. Transesterification in Poly(Ethylene Terephthalate). Molecular Weight and End Group Effects. **2000**. https://doi.org/10.1021/MA991637.

24. George Socrates. *Infrared and Raman Characteristic Group Frequencies: Tables and Charts*; John Wiley & sons, 2004.

25. Mondschein, R. J.; Hostetler, J.; Arrington, C. B.; Long, T. E. Hydroxyethylresorcinol- and Hydroxyethylhydroquinone-Containing Poly(Ethylene Terephthalate) Copolymers. *Polymer (Guildf)* **2021**, *228*, 123890. https://doi.org/10.1016/J.POLYMER.2021.123890.

26. Shukla, S.; Lochab, B. Role of Higher Aromatic Content in Modulating Properties of Cardanol Based Benzoxazines. *Polymer (Guildf)* **2016**, *99*, 684–694. https://doi.org/10.1016/J.POLYMER.2016.07.074.

27. Sarasua, J.-R.; Zuza, E.; Imaz, N.; Meaurio, E. Crystallinity and Crystalline Confinement of the Amorphous Phase in Polylactides. https://doi.org/10.1002/masy.200851211.

Chapter 4

1. D. Nichetti, S. Cossar, N. Grizzuti, Effects of molecular weight and chemical structure on phase transition of thermoplastic polyurethanes, J. Rheol. 49(6) (2005) 1361-1376. https://doi.org/10.1122/1.2071987.

2. A. Kumar, R.K. Gupta, Fundamentals of Polymers, McGraw-Hill 1998.

3. J. Guo, T. Chai, Y. Liu, J. Cui, H. Ma, S. Jing, L. Zhong, S. Qin, G. Wang, X. Ren, Kinetic research on the curing reaction of hydroxyl-terminated polybutadiene based polyurethane binder system via FT-IR measurements, Coatings 8(5) (2018) 175. https://doi.org/10.3390/coatings8050175.

4. C. Korah Bina, K. Kannan, K. Ninan, DSC study on the effect of isocyanates and catalysts on the HTPB cure reaction, J. Therm. Anal. Calorim. 78(3) (2004) 753-760. https://doi.org/10.1007/s10973-005-0442-0.

5. V. Sekkar, S. Venkatachalam, K.N. Ninan, Rheokinetic studies on the formation of urethane networks based on hydroxyl terminated polybutadiene, Eur. Polym. J. 38(1) (2002) 169-178. https://doi.org/10.1016/S0014-3057(01)00106-9.

6. M.A. Pérez-Limiñana, F. Arán-Aís, A.M. Torró-Palau, C. Orgilés-Barcel, J.M. Martín-Martínez, Influence of the hard-to-soft segment ratio on the adhesion of water-borne polyurethane adhesive, J. Adhes. Sci. Technol. 21(8) (2007) 755-773. https://doi.org/10.1163/156856107781362635.

7. J. Silva, D. Meltzer, J. Liu, M. Cox, J. Maia, The influence of thermo-mechanical history on structure development of elastomeric and amorphous glass thermoplastic polyurethanes, Polymer Engineering & Science 54(6) (2014) 1383-1393. https://doi.org/10.1002/pen.23673.

8. A. Frick, A. Rochman, Characterization of TPU-elastomers by thermal analysis (DSC), Polym. Test. 23(4) (2004) 413-417. https://doi.org/10.1016/j.polymertesting.2003.09.013.

9. G. Kim, E. Barocio, R.B. Pipes, R. Sterkenburg, 3D printed thermoplastic polyurethane bladder for manufacturing of fiber reinforced composites, Addit. Manuf. 29 (2019) 100809. https://doi.org/10.1016/j.addma.2019.100809.

10. T. Xu, W. Shen, X. Lin, Y.M. Xie, Mechanical properties of additively manufactured thermoplastic polyurethane (TPU) material affected by various processing parameters, Polymers 12(12) (2020) 3010. https://doi.org/10.3390/polym12123010.[11] X. Lin, P. Coates, M. Hebda, R. Wang, Y. Lu, L. Zhang, Experimental analysis of the tensile property of FFF-printed elastomers, Polym. Test. 90 (2020) 106687. https://doi.org/10.1016/j.polymertesting.2020.106687.

11. H.Y. Mi, X. Jing, M.R. Salick, W.C. Crone, X.F. Peng, L.S. Turng, Approach to fabricating thermoplastic polyurethane blends and foams with tunable properties by twin-screw extrusion and microcellular injection molding, Adv. Polym. Tech. 33(1) (2014). https://doi.org/10.1002/adv.21380.

12. G. Lu, D.M. Kalyon, I. Yilgör, E. Yilgör, Rheology and extrusion of medical-grade thermoplastic polyurethane, Polymer Engineering & Science 43(12) (2003) 1863-1877. https://doi.org/10.1002/pen.10158.

13. M.J. Bortner, V. Bhanu, J.E. McGrath, D.G. Baird, Shear rheological properties of acrylic copolymers and terpolymers suitable for potentially melt processable carbon fiber precursors, J. Appl. Polym. Sci. 93(6) (2004) 2856-2865. https://doi.org/10.1002/app.20833.

14. B. Lucio, J.L. de la Fuente, Kinetic and chemorheological modelling of the polymerization of 2, 4-Toluenediisocyanate and ferrocene-functionalized hydroxyl-terminated polybutadiene, Polymer 140 (2018) 290-303. https://doi.org/10.1016/j.polymer.2018.02.058.

15. G. Santhosh, S. Reshmi, C.R. Nair, Rheokinetic characterization of polyurethane formation in a highly filled composite solid propellant, J. Therm. Anal. Calorim. 140(1) (2020) 213-223. https://doi.org/10.1007/s10973-019-08793-6.

16. M. Špírková, M. Kubin, K. Dušek, Side reactions in the formation of polyurethanes: Stability of reaction products of phenyl isocyanate, Journal of Macromolecular Science-Chemistry 27(4) (1990) 509-522. https://doi.org/10.1080/00222339009349572.

17. M. Špírková, M. Kubin, K. Dušek, Side reactions in the formation of polyurethanes: Model reactions between phenylisocyanate and 1-butanol, Journal of Macromolecular Science—Chemistry 24(10) (1987) 1151-1166. https://doi.org/10.1080/00222338708076935.

18. E. Sacher, A re-examination of the polyurethane reaction, Journal of Macromolecular Science, Part B: Physics 16(4) (1979) 525-538. https://doi.org/doi.org/10.1080/00222347908215180.

19. A.M. Heintz, D.J. Duffy, S.L. Hsu, W. Suen, W. Chu, C.W. Paul, Effects of reaction temperature on the formation of polyurethane prepolymer structures, Macromolecules 36(8) (2003) 2695-2704. https://doi.org/10.1021/MA021559H.

20. Y. Suryawanshi, P. Sanap, V. Wani, Advances in the synthesis of non-isocyanate polyurethanes, Polym. Bull. 76 (2019) 3233-3246. https://doi.org/doi.org/10.1007/S00289-018-2531-7.

21. E. Delebecq, J.-P. Pascault, B. Boutevin, F. Ganachaud, On the versatility of urethane/urea bonds: reversibility, blocked isocyanate, and non-isocyanate polyurethane, Chem. Rev. 113(1) (2013) 80-118. https://doi.org/10.1021/cr300195n.

22. K. Dušek, Theory of network formation by additional crosslinking of polyurethanes due to biuret and allophanate formation, Polym. Bull. 17 (1987) 481-488. https://doi.org/10.1007/BF00255622.

23. J.N. Gibb, J.M. Goodman, The formation of high-purity isocyanurate through proazaphosphatrane-catalysed isocyanate cyclo-trimerisation: computational insights,

Organic & Biomolecular Chemistry 11(1) (2013) 90-97. https://doi.org/10.1039/C2OB26547H.

24. M.G. McKee, S. Unal, G.L. Wilkes, T.E. Long, Branched polyesters: recent advances in synthesis and performance, Prog. Polym. Sci. 30(5) (2005) 507-539. https://doi.org/10.1016/j.progpolymsci.2005.01.009.

25. J.M. Dennis, R.J. Mondschein, J.D. Wolfgang, M. Hegde, R. Odle, T.E. Long, Synthesis and characterization of long-chain branched poly (ether imide) s with A3 comonomers, ACS Applied Polymer Materials 2(2) (2020) 958-965. https://doi.org/10.1021/acsapm.9b01148.

26. J.D. Wolfgang, K.J. Reynolds, C.B. Arrington, R.R. Odle, S.I. Nazarenko, T.E. Long, Influence of dianhydride regiochemistry on thermomechanical and rheological properties of 3, 3′-and 4, 4′-polyetherimides, Polymer 212 (2021) 123277. https://doi.org/10.1016/j.polymer.2020.123277.

27. D.J. Martin, G.F. Meijs, P.A. Gunatillake, S.P. Yozghatlian, G.M. Renwick, The influence of composition ratio on the morphology of biomedical polyurethanes, J. Appl. Polym. Sci. 71(6) (1999) 937-952. https://doi.org/10.1002/(sici)1097-4628(19990207)71:6<937::aid-app9>3.0.co;2-0.

28. Q. Tang, K. Gao, Structure analysis of polyether-based thermoplastic polyurethane elastomers by FTIR, 1H NMR and 13C NMR, Int. J. Polym. Anal. Charact. 22(7) (2017) 569-574. https://doi.org/10.1080/1023666X.2017.1312754.

29. L. Zeng, X. Lin, P. Li, F.-Q. Liu, H. Guo, W.-H. Li, Recent advances of organogels: From fabrications and functions to applications, Prog. Org. Coat. 159 (2021) 106417. https://doi.org/10.1016/J.PORGCOAT.2021.106417.

30. J.F. Douglas, J. Roovers, K.F. Freed, Characterization of branching architecture through" universal" ratios of polymer solution properties, Macromolecules 23(18) (1990) 4168-4180. https://doi.org/10.1021/ma00220a022.

Chapter 5

1. Lin, C. C.; Anseth, K. S., PEG hydrogels for the controlled release of biomolecules in regenerative medicine. *Pharm Res* **2009,** *26* (3), 631-43.

2. Peppas, N. A.; Hilt, J. Z.; Khademhosseini, A.; Langer, R., Hydrogels in Biology and Medicine: From Molecular Principles to Bionanotechnology. *Advanced Materials* **2006,** *18* (11), 1345-1360.

3. Herzberger, J.; Niederer, K.; Pohlit, H.; Seiwert, J.; Worm, M.; Wurm, F. R.; Frey, H., Polymerization of Ethylene Oxide, Propylene Oxide, and Other Alkylene Oxides: Synthesis, Novel Polymer Architectures, and Bioconjugation. *Chem Rev* **2016,** *116* (4), 2170-243.

4. Palombo, M.; Deshmukh, M.; Myers, D.; Gao, J.; Szekely, Z.; Sinko, P. J., Pharmaceutical and toxicological properties of engineered nanomaterials for drug delivery. *Annu Rev Pharmacol Toxicol* **2014,** *54*, 581-98.

5. Caliceti, P., Pharmacokinetic and biodistribution properties of poly(ethylene glycol)–protein conjugates. *Advanced Drug Delivery Reviews* **2003,** *55* (10), 1261-1277.

6. Zustiak, S. P.; Leach, J. B., Hydrolytically degradable poly(ethylene glycol) hydrogel scaffolds with tunable degradation and mechanical properties. *Biomacromolecules* **2010,** *11* (5), 1348-57.

7. Rydholm, A. E.; Anseth, K. S.; Bowman, C. N., Effects of neighboring sulfides and pH on ester hydrolysis in thiol-acrylate photopolymers. *Acta Biomater* **2007,** *3* (4), 449-55.

8. Rizzi, S. C.; Ehrbar, M.; Halstenberg, S.; Raeber, G. P.; Schmoekel, H. G.; Hagenmuller, H.; Muller, R.; Weber, F. E.; Hubbell, J. A., Recombinant protein-co-PEG networks as cell-adhesive and proteolytically degradable hydrogel matrixes. Part II: biofunctional characteristics. *Biomacromolecules* **2006,** *7* (11), 3019-29.

9. Metters, A.; Hubbell, J., Network formation and degradation behavior of hydrogels formed by Michael-type addition reactions. *Biomacromolecules* **2005,** *6* (1), 290-301.

10. Mason, M. N.; Metters, A. T.; Bowman, C. N.; Anseth, K. S., Predicting Controlled-Release Behavior of Degradable PLA-b-PEG-b-PLA Hydrogels. *Macromolecules* **2001,** *34* (13), 4630-4635.

11. Worm, M.; Leibig, D.; Dingels, C.; Frey, H., Cleavable Polyethylene Glycol: 3,4-Epoxy-1-butene as a Comonomer to Establish Degradability at Physiologically Relevant pH. *ACS Macro Letters* **2016,** *5* (12), 1357-1363.

12. Dingels, C.; Frey, H., From Biocompatible to Biodegradable: Poly(Ethylene Glycol)s with Predetermined Breaking Points. In *Hierarchical Macromolecular Structures: 60 Years after the Staudinger Nobel Prize II*, 2013; pp 167-190.

13. Lundberg, P.; Lee, B. F.; van den Berg, S. A.; Pressly, E. D.; Lee, A.; Hawker, C. J.; Lynd, N. A., Poly[(ethylene oxide)-co-(methylene ethylene oxide)]: A hydrolytically-degradable poly(ethylene oxide) platform. *ACS Macro Lett* **2012,** *1* (11), 1240-1243.

14. Schmaljohann, D., Thermo- and pH-responsive polymers in drug delivery. *Adv Drug Deliv Rev* **2006,** *58* (15), 1655-70.

15. Gupta, P.; Vermani, K.; Garg, S., Hydrogels: from controlled release to pH-responsive drug delivery. *Drug Discovery Today* **2002,** *7* (10), 569-579.

16. Brocchini, S. C. S., Polyacetals. *Natural and Synthetic Biomedical Polymers* **2014**, 219-233.

17. Samanta, S.; Bogdanowicz, D. R.; Lu, H. H.; Koberstein, J. T., Polyacetals: Water-Soluble, pH-Degradable Polymers with Extraordinary Temperature Response. *Macromolecules* **2016,** *49* (5), 1858-1864.

18. Pohlit, H.; Bellinghausen, I.; Schomer, M.; Heydenreich, B.; Saloga, J.; Frey, H., Biodegradable pH-Sensitive Poly(ethylene glycol) Nanocarriers for Allergen Encapsulation and Controlled Release. *Biomacromolecules* **2015,** *16* (10), 3103-11.

19. Wang, Y.; Morinaga, H.; Sudo, A.; Endo, T., Synthesis of amphiphilic polyacetal by polycondensation of aldehyde and polyethylene glycol as an acid-labile polymer for controlled release of aldehyde. *Journal of Polymer Science Part A: Polymer Chemistry* **2011,** *49* (3), 596-602.

20. Plyduang, T.; Arminan, A.; Movellan, J.; England, R. M.; Wiwattanapatapee, R.; Vicent, M. J., Polyacetal-Based Combination Therapy for the Treatment of Prostate Cancer. *Macromol Rapid Commun* **2018**, e1800265.

21. Tomlinson, R.; Klee, M.; Garrett, S.; Heller, J.; Duncan, R.; Brocchini, S., Pendent Chain Functionalized Polyacetals That Display pH-Dependent Degradation: A Platform for the Development of Novel Polymer Therapeutics. *Macromolecules* **2002,** *35* (2), 473-480.

22. Samanta, S.; De Silva, C. C.; Leophairatana, P.; Koberstein, J. T., Main-chain polyacetal conjugates with HIF-1 inhibitors: temperature-responsive, pH-degradable drug delivery vehicles. *Journal of Materials Chemistry B* **2018,** *6* (4), 666-674.

23. Pritchard, C. D.; O'Shea, T. M.; Siegwart, D. J.; Calo, E.; Anderson, D. G.; Reynolds, F. M.; Thomas, J. A.; Slotkin, J. R.; Woodard, E. J.; Langer, R., An injectable thiol-acrylate poly(ethylene glycol) hydrogel for sustained release of methylprednisolone sodium succinate. *Biomaterials* **2011,** *32* (2), 587-97.

24. Moon, N. G.; Pekkanen, A. M.; Long, T. E.; Showalter, T. N.; Libby, B., Thiol-Michael ‘click’ hydrogels as an imageable packing material for cancer therapy. *Polymer* **2017,** *125*, 66-75.

25. Peach, M. S.; Moore, J.; Long, T. E.; Moon, N.; Showalter, T.; Libby, B., Preclinical Testing of a Novel Biodegradable Hydrogel Based Intravaginal Spacer for HDR Gynecologic Brachytherapy. *Brachytherapy* **2018,** *17* (4), S15-S16.

26. Fairbanks, B. D.; Schwartz, M. P.; Bowman, C. N.; Anseth, K. S., Photoinitiated polymerization of PEG-diacrylate with lithium phenyl-2,4,6-trimethylbenzoylphosphinate: polymerization rate and cytocompatibility. *Biomaterials* **2009,** *30* (35), 6702-7.

27. Christopher Kielbassa, L. R., Bernd Epe, Wavelength dependence of oxyidative DNA damage induced by UV and visible light. *Carcinogenesis* **1997,** *18* (4), 811-816.

28. Kielbassa, C.; Epe, B., [39] DNA damage induced by ultraviolet and visible light and its wavelength dependence. In *Singlet Oxygen, UV-A, and Ozone*, 2000; pp 436-445.

29. O'Shea, T. M.; Aimetti, A. A.; Kim, E.; Yesilyurt, V.; Langer, R., Synthesis and characterization of a library of in-situ curing, nonswelling ethoxylated polyol thiol-ene hydrogels for tailorable macromolecule delivery. *Adv Mater* **2015,** *27* (1), 65-72.

30. Rydholm, A. E.; Reddy, S. K.; Anseth, K. S.; Bowman, C. N., Development and Characterization of Degradable Thiol-Allyl Ether Photopolymers. *Polymer (Guildf)* **2007,** *48* (15), 4589-4600.

31. Marchitti, S. A.; Brocker, C.; Stagos, D.; Vasiliou, V., Non-P450 aldehyde oxidizing enzymes: the aldehyde dehydrogenase superfamily. *Expert Opin Drug Metab Toxicol* **2008,** *4* (6), 697-720.

32. Crabb, D. W.; Matsumoto, M.; Chang, D.; You, M., Overview of the role of alcohol dehydrogenase and aldehyde dehydrogenase and their variants in the genesis of alcohol-related pathology. *Proceedings of the Nutrition Society* **2007,** *63* (01), 49-63.

33. Drury, J. L.; Mooney, D. J., Hydrogels for tissue engineering: scaffold design variables and applications. *Biomaterials* **2003,** *24* (24), 4337-4351.

34. Moon, N. G.; Mazzini, F.; Pekkanen, A. M.; Wilts, E. M.; Long, T. E., Sugar-Derived Poly(β-thioester)s as a Biomedical Scaffold. *Macromolecular Chemistry and Physics* **2018**.

Chapter 6

1. Jothimani, B.; Venkatachalapathy, B.; Karthikeyan, N.; Ravichandran, C., A review on versatile applications of degradable polymers. *Green Biopolymers and their Nanocomposites* **2019**, 403-422.

2. Binauld, S.; Stenzel, M. H., Acid-degradable polymers for drug delivery: a decade of innovation. *Chemical communications* **2013,** *49* (21), 2082-2102.

3. Mohanty, S.; Larsen, L. B.; Trifol, J.; Szabo, P.; Burri, H. V. R.; Canali, C.; Dufva, M.; Emnéus, J.; Wolff, A., Fabrication of scalable and structured tissue engineering scaffolds using water dissolvable sacrificial 3D printed moulds. *Materials science and engineering: C* **2015,** *55*, 569-578.

4. Tetsuka, H.; Shin, S. R., Materials and technical innovations in 3D printing in biomedical applications. *Journal of materials chemistry B* **2020,** *8* (15), 2930-2950.

5. Herzberger, J.; Sirrine, J. M.; Williams, C. B.; Long, T. E., Polymer Design for 3D Printing Elastomers: Recent Advances in Structure, Properties, and Printing. *Progress in Polymer Science* **2019,** *97*, 101144.

6. Weyhrich, C. W.; Long, T. E., Additive manufacturing of high-performance engineering polymers: present and future. *Polymer International* **2022,** *71* (5), 532-536.

7. Mondschein, R. J.; Kanitkar, A.; Williams, C. B.; Verbridge, S. S.; Long, T. E., Polymer structure-property requirements for stereolithographic 3D printing of soft tissue engineering scaffolds. *Biomaterials* **2017,** *140*, 170-188.

8. Cucciniello, R.; Anastas, P. T., Design for degradation or recycling for reuse? *Current Opinion in Green and Sustainable Chemistry* **2021,** *31*, 100528.

9. Schelhaas, M.; Waldmann, H., Protecting group strategies in organic synthesis. *Angewandte Chemie International Edition in English* **1996,** *35* (18), 2056-2083.

10. Brocchini, S. C. S., Polyacetals. *Natural and Synthetic Biomedical Polymers* **2014**, 219-233.

11. Kasprzak, C.; Brown, J. R.; Feller, K.; Scott, P. J.; Meenakshisundaram, V.; Williams, C.; Long, T., Vat Photopolymerization of Reinforced Styrene–Butadiene Elastomers: A Degradable Scaffold Approach. *ACS Applied Materials & Interfaces* **2022,** *14* (16), 18965-18973.

12. Lin, C. C.; Anseth, K. S., PEG hydrogels for the controlled release of biomolecules in regenerative medicine. *Pharm Res* **2009,** *26* (3), 631-43.

13. Peppas, N. A.; Hilt, J. Z.; Khademhosseini, A.; Langer, R., Hydrogels in biology and medicine: from molecular principles to bionanotechnology. *Advanced materials* **2006,** *18* (11), 1345-1360.

14. Pritchard, C. D.; O'Shea, T. M.; Siegwart, D. J.; Calo, E.; Anderson, D. G.; Reynolds, F. M.; Thomas, J. A.; Slotkin, J. R.; Woodard, E. J.; Langer, R., An injectable thiol-acrylate poly (ethylene glycol) hydrogel for sustained release of methylprednisolone sodium succinate. *Biomaterials* **2011,** *32* (2), 587-597.

15. Lin, C.-C.; Anseth, K. S., PEG hydrogels for the controlled release of biomolecules in regenerative medicine. *Pharmaceutical research* **2009,** *26* (3), 631-643.

16. Moon, N. G.; Pekkanen, A. M.; Long, T. E.; Showalter, T. N.; Libby, B., Thiol-Michael 'click'hydrogels as an imageable packing material for cancer therapy. *Polymer* **2017,** *125*, 66-75.

17. Mason, M. N.; Metters, A. T.; Bowman, C. N.; Anseth, K. S., Predicting controlled-release behavior of degradable PLA-b-PEG-b-PLA hydrogels. *Macromolecules* **2001,** *34* (13), 4630-4635.

18. Metters, A.; Hubbell, J., Network formation and degradation behavior of hydrogels formed by Michael-type addition reactions. *Biomacromolecules* **2005,** *6* (1), 290-301.

19. Worm, M.; Leibig, D.; Dingels, C.; Frey, H., Cleavable polyethylene glycol: 3, 4-epoxy-1-butene as a comonomer to establish degradability at physiologically relevant pH. *ACS Macro Letters* **2016,** *5* (12), 1357-1363.

20. Samanta, S.; Bogdanowicz, D. R.; Lu, H. H.; Koberstein, J. T., Polyacetals: Water-Soluble, pH-Degradable Polymers with Extraordinary Temperature Response. *Macromolecules* **2016,** *49* (5), 1858-1864.

21. Marchitti, S. A.; Brocker, C.; Stagos, D.; Vasiliou, V., Non-P450 aldehyde oxidizing enzymes: the aldehyde dehydrogenase superfamily. *Expert Opin Drug Metab Toxicol* **2008,** *4* (6), 697-720.

22. Crabb, D. W.; Matsumoto, M.; Chang, D.; You, M., Overview of the role of alcohol dehydrogenase and aldehyde dehydrogenase and their variants in the genesis of alcohol-related pathology. *Proceedings of the Nutrition Society* **2007,** *63* (01), 49-63.

23. Cai, Z.; Wan, Y.; Becker, M. L.; Long, Y.-Z.; Dean, D., Poly (propylene fumarate)-based materials: Synthesis, functionalization, properties, device fabrication and biomedical applications. *Biomaterials* **2019,** *208*, 45-71.

24. Zhang, J.; Xiao, P., 3D printing of photopolymers. *Polymer Chemistry* **2018,** *9* (13), 1530-1540.

25. Scott, P. J.; Meenakshisundaram, V.; Hegde, M.; Kasprzak, C. R.; Winkler, C. R.; Feller, K. D.; Williams, C. B.; Long, T. E., 3D printing latex: a route to complex geometries of high molecular weight polymers. *ACS applied materials & interfaces* **2020,** *12* (9), 10918-10928.

26. Leonards, H.; Engelhardt, S.; Hoffmann, A.; Pongratz, L.; Schriever, S.; Bläsius, J.; Wehner, M. M.; Gillner, A. In *Advantages and drawbacks of Thiol-ene based resins for 3D-printing*, Laser 3D Manufacturing II, SPIE: 2015; pp 52-58.

27. Cook, C. C.; Fong, E. J.; Schwartz, J. J.; Porcincula, D. H.; Kaczmarek, A. C.; Oakdale, J. S.; Moran, B. D.; Champley, K. M.; Rackson, C. M.; Muralidharan, A., Highly tunable thiol-ene photoresins for volumetric additive manufacturing. *Advanced Materials* **2020,** *32* (47), 2003376.

28. Rydholm, A. E.; Reddy, S. K.; Anseth, K. S.; Bowman, C. N., Controlling network structure in degradable thiol− acrylate biomaterials to tune mass loss behavior. *Biomacromolecules* **2006,** *7* (10), 2827-2836.

29. Hoyle, C. E.; Bowman, C. N., Thiol–ene click chemistry. *Angewandte Chemie International Edition* **2010,** *49* (9), 1540-1573.

30. Rydholm, A. E.; Anseth, K. S.; Bowman, C. N., Effects of neighboring sulfides and pH on ester hydrolysis in thiol-acrylate photopolymers. *Acta Biomater* **2007,** *3* (4), 449-55.

31. Rydholm, A. E.; Reddy, S. K.; Anseth, K. S.; Bowman, C. N., Development and Characterization of Degradable Thiol-Allyl Ether Photopolymers. *Polymer (Guildf)* **2007,** *48* (15), 4589-4600.

32. Jiang, T.; He, Y.; Jian, Y.; Nie, J., Exploration for decreasing the volume shrinkage for photopolymerization. *Progress in Organic Coatings* **2012,** *75* (4), 398-403.

33. Tierney, C. M.; Haugh, M. G.; Liedl, J.; Mulcahy, F.; Hayes, B.; O'Brien, F. J., The effects of collagen concentration and crosslink density on the biological, structural and mechanical properties of collagen-GAG scaffolds for bone tissue engineering. *Journal of the mechanical behavior of biomedical materials* **2009,** *2* (2), 202-209.

34. Krongauz, V. V., Crosslink density dependence of polymer degradation kinetics: photocrosslinked acrylates. *Thermochimica Acta* **2010,** *503,* 70-84.

35. Khalfa, A. L.; Becker, M. L.; Dove, A. P., Stereochemistry-controlled mechanical properties and degradation in 3D-printable photosets. *Journal of the American Chemical Society* **2021,** *143* (42), 17510-17516.

36. Hoti, G.; Caldera, F.; Cecone, C.; Rubin Pedrazzo, A.; Anceschi, A.; Appleton, S. L.; Khazaei Monfared, Y.; Trotta, F., Effect of the cross-linking density on the swelling and rheological behavior of Ester-bridged β-cyclodextrin nanosponges. *Materials* **2021,** *14* (3), 478.

37. D'souza, A. A.; Shegokar, R., Polyethylene glycol (PEG): a versatile polymer for pharmaceutical applications. *Expert opinion on drug delivery* **2016,** *13* (9), 1257-1275.

38. Sirrine, J. M.; Meenakshisundaram, V.; Moon, N. G.; Scott, P. J.; Mondschein, R. J.; Weiseman, T. F.; Williams, C. B.; Long, T. E., Functional siloxanes with photo-activated, simultaneous chain extension and crosslinking for lithography-based 3D printing. *Polymer* **2018,** *152*, 25-34.

39. Jones, B. H.; Alam, T. M.; Lee, S.; Celina, M. C.; Allers, J. P.; Park, S.; Chen, L.; Martinez, E. J.; Unangst, J. L., Curing behavior, chain dynamics, and microstructure of high Tg thiol-acrylate networks with systematically varied network heterogeneity. *Polymer* **2020,** *205*, 122783.

40. Martens, P.; Metters, A. T.; Anseth, K. S.; Bowman, C. N., A Generalized Bulk-Degradation Model for Hydrogel Networks Formed from Multivinyl Cross-linking Molecules. *The Journal of Physical Chemistry B* **2001,** *105* (22), 5131-5138.

Chapter 7

1. Manouras, T.; Argitis, P. High Sensitivity Resists for EUV Lithography: A Review of Material Design Strategies and Performance Results. *Nanomaterials 2020, Vol. 10, Page 1593* **2020**, *10* (8), 1593. https://doi.org/10.3390/NANO10081593.

2. Bratton, D.; Yang, D.; Dai, J.; Ober, C. K. Recent Progress in High Resolution Lithography. *Polym Adv Technol* **2006**, *17* (2), 94–103. https://doi.org/10.1002/PAT.662.

3. Luo, C.; Xu, C.; Lv, L.; Li, H.; Huang, X.; Liu, W. Review of Recent Advances in Inorganic Photoresists. *RSC Adv* **2020**, *10* (14), 8385–8395. https://doi.org/10.1039/C9RA08977B.

4. Baek, J.; Kim, M.; Park, Y.; Kim, B. S. Acetal-Based Functional Epoxide Monomers: Polymerizations and Applications. *Macromol Biosci* **2021**, *21* (11), 2100251. https://doi.org/10.1002/MABI.202100251.

5. Kisla, M. M.; Hassan, M. A.-K.; Osman, H. M.; Aydin, A. S.; Sen, H. T.; Khazei, S.; Kul, P.; Kuş, C. Incorporation of Protecting Groups in Organic Chemistry: A Mini-Review. *Curr Org Synth* **2022**, *20* (5), 491–503. https://doi.org/10.2174/1570179419666220820152723.

6. Brown, J. R.; Herzberger, J.; Spiering, G. A.; Wilts, E.; Moore, R. B.; Long, T. E. Binary Thiol-Acrylate Photopolymerization for the Design of Degradable Acetal-Functionalized Hydrogels. *ACS Appl Polym Mater* **2022**, *5*, 1030–1036. https://doi.org/10.1021/ACSAPM.2C01978/ASSET/IMAGES/LARGE/AP2C01978_0006.JPEG.

7. Dingels, C.; Müller, S. S.; Steinbach, T.; Tonhauser, C.; Frey, H. Universal Concept for the Implementation of a Single Cleavable Unit at Tunable Position in Functional Poly(Ethylene Glycol)s. *Biomacromolecules* **2013**, *14* (2), 448–459. https://doi.org/10.1021/BM3016797/SUPPL_FILE/BM3016797_SI_001.PDF.

8. Kottisch, V.; Michaudel, Q.; Fors, B. P. Cationic Polymerization of Vinyl Ethers Controlled by Visible Light. *J Am Chem Soc* **2016**, *138* (48), 15535–15538. https://doi.org/10.1021/JACS.6B10150/ASSET/IMAGES/LARGE/JA-2016-10150B_0004.JPEG.

9. Decker, C.; Bianchi, C.; Decker, D.; Morel, F. Photoinitiated Polymerization of Vinyl Ether-Based Systems. *Prog Org Coat* **2001**, *42* (3–4), 253–266. https://doi.org/10.1016/S0300-9440(01)00203-X.

10. K Rajaraman, S. S.; Mowers, W. A.; Crivello, J. V. Interaction of Epoxy and Vinyl Ethers During Photoinitiated Cationic Polymerization. *J Polym Sci A: Polym Chem* **1999**, *37*, 4007–4018. https://doi.org/10.1002/(SICI)1099-0518(19991101)37:21.

11. Michaudel, Q.; Kottisch, V.; Fors, B. P. Cationic Polymerization: From Photoinitiation to Photocontrol. *Angewandte Chemie International Edition* **2017**, *56* (33), 9670–9679. https://doi.org/10.1002/ANIE.201701425.

12. Shen, J.; Lin, X.; Liu, J.; Li, X. Effects of Cross-Link Density and Distribution on Static and Dynamic Properties of Chemically Cross-Linked Polymers. *Macromolecules* **2019**,

52 (1), 121–134. https://doi.org/10.1021/ACS.MACROMOL.8B01389/ASSET/IMAGES/LARGE/MA-2018-01389Y_0010.JPEG.

13. Shih, H.; Lin, C. C. Cross-Linking and Degradation of Step-Growth Hydrogels Formed by Thiol-Ene Photoclick Chemistry. *Biomacromolecules* **2012**, *13* (7), 2003–2012. https://doi.org/10.1021/BM300752J/ASSET/IMAGES/LARGE/BM-2012-00752J_0011.JPEG.

14. George Socrates. *Infrared and Raman Characteristic Group Frequencies: Tables and Charts*; John Wiley & sons, 2004.

Chapter 8

1. Rau, D. A.; Herzberger, J.; Long, T. E.; Williams, C. B. Ultraviolet-Assisted Direct Ink Write to Additively Manufacture All-Aromatic Polyimides. *ACS Appl Mater Interfaces* **2018**, *10* (41), 34828–34833. https://doi.org/10.1021/ACSAMI.8B14584/ASSET/IMAGES/LARGE/AM-2018-145849_0003.JPEG.

2. Beaman, J. J.; Bourell, D. L.; Seepersad, C. C.; Kovar, D. Additive Manufacturing Review: Early Past to Current Practice. *Journal of Manufacturing Science and Engineering, Transactions of the ASME* **2020**, *142* (11). https://doi.org/10.1115/1.4048193/1086507.

3. Behera, D.; Cullinan, M. Current Challenges and Potential Directions towards Precision Microscale Additive Manufacturing – Part I: Direct Ink Writing/Jetting Processes. *Precis Eng* **2021**, *68*, 326–337. https://doi.org/10.1016/J.PRECISIONENG.2020.12.009.

4. Manuel De Lardizabal, P. Development of Polythiourethane Based Resins for 3D Printing Applications Using Photobase Generators. **2022**.

5. Zivic, N.; Kuroishi, P. K.; Dumur, F.; Gigmes, D.; Dove, A. P.; Sardon, H. Recent Advances and Challenges in the Design of Organic Photoacid and Photobase Generators for Polymerizations. *Angewandte Chemie International Edition* **2019**, *58* (31), 10410–10422. https://doi.org/10.1002/ANIE.201810118.

6. Lopez De Pariza, X.; Cordero Jara, E.; Zivic, N.; Ruipérez, F.; Long, T. E.; Sardon, H. Novel Imino- and Aryl-Sulfonate Based Photoacid Generators for the Cationic Ring-Opening Polymerization of ε-Caprolactone. *Polym Chem* **2021**, *12* (28), 4035–4042. https://doi.org/10.1039/D1PY00734C.

7. Sun, X.; Gao, J. P.; Wang, Z. Y. Bicyclic Guanidinium Tetraphenylborate: A Photobase Generator and a Photocatalyst for Living Anionic Ring-Opening Polymerization and Cross-Linking of Polymeric Materials Containing Ester and Hydroxy Groups. *J Am*

Chem Soc **2008**, *130* (26), 8130–8131. https://doi.org/10.1021/JA802816G/SUPPL_FILE/JA802816G-FILE001.PDF.

8. Zivic, N.; Sadaba, N.; Almandoz, N.; Ruipérez, F.; Mecerreyes, D.; Sardon, H. Thioxanthone-Based Photobase Generators for the Synthesis of Polyurethanes via the Photopolymerization of Polyols and Polyisocyanates. *Macromolecules* **2020**, *53* (6), 2069–2076. https://doi.org/10.1021/ACS.MACROMOL.9B02648/ASSET/IMAGES/LARGE/MA9B02648_0004.JPEG.

9. Williams, S. R.; Miller, K. M.; Long, T. E. Michael Addition Reaction Kinetics of Acetoacetates and Acrylates for the Formation of Polymeric Networks. *Progress in Reaction Kinetics and Mechanism* **2007**, *32* (4). https://doi.org/10.3184/146867807X247730.

10. Mather, B. D.; Viswanathan, K.; Miller, K. M.; Long, T. E. Michael Addition Reactions in Macromolecular Design for Emerging Technologies. *Prog Polym Sci* **2006**, *31* (5), 487–531. https://doi.org/10.1016/J.PROGPOLYMSCI.2006.03.001.

11. Chatani, S.; Gong, T.; Earle, B. A.; Podgorski, M.; Bowman, C. N. Visible-Light Initiated Thiol-Michael Addition Photopolymerization Reactions. *ACS Macro Lett* **2014**, *3* (4), 315–318. https://doi.org/10.1021/MZ500132J/SUPPL_FILE/MZ500132J_SI_001.PDF.

12. Hoyle, C. E.; Bowman, C. N. Thiol-Ene Click Chemistry. *Angewandte Chemie - International Edition*. 2010. https://doi.org/10.1002/anie.200903924.

13. Wutzel, H.; Jarvid, M.; Bjuggren, J. M.; Johansson, A.; Englund, V.; Gubanski, S.; Andersson, M. R. Thioxanthone Derivatives as Stabilizers against Electrical Breakdown in Cross-Linked Polyethylene for High Voltage Cable Applications. *Polym Degrad Stab* **2015**, *112*, 63–69. https://doi.org/10.1016/J.POLYMDEGRADSTAB.2014.12.002.

14. George Socrates. *Infrared and Raman Characteristic Group Frequencies: Tables and Charts*; John Wiley & sons, 2004.

15. Nunes, R. W.; Martin, J. R.; Johnson, J. F. Influence of Molecular Weight and Molecular Weight Distribution on Mechanical Properties of Polymers. *Polym Eng Sci* **1982**, *22* (4), 205–228. https://doi.org/10.1002/PEN.760220402.

Chapter 9

1. Lehmler, H. J. Synthesis of Environmentally Relevant Fluorinated Surfactants—a Review. *Chemosphere* **2005**, *58* (11), 1471–1496. https://doi.org/10.1016/J.CHEMOSPHERE.2004.11.078.

2. Hussain, S. M. S.; Adewunmi, A. A.; Mahboob, A.; Murtaza, M.; Zhou, X.; Kamal, M. S. Fluorinated Surfactants: A Review on Recent Progress on Synthesis and Oilfield Applications. *Adv Colloid Interface Sci* **2022**, *303*, 102634. https://doi.org/10.1016/J.CIS.2022.102634.

3. Filipovic, M.; Woldegiorgis, A.; Norström, K.; Bibi, M.; Lindberg, M.; Österås, A. H. Historical Usage of Aqueous Film Forming Foam: A Case Study of the Widespread Distribution of Perfluoroalkyl Acids from a Military Airport to Groundwater, Lakes, Soils and Fish. *Chemosphere* **2015**, *129*, 39–45. https://doi.org/10.1016/J.CHEMOSPHERE.2014.09.005.

4. Place, B. J.; Field, J. A. Identification of Novel Fluorochemicals in Aqueous Film-Forming Foams Used by the US Military. *Environ Sci Technol* **2012**, *46* (13), 7120–7127. https://doi.org/10.1021/ES301465N/SUPPL_FILE/ES301465N_SI_001.PDF.

5. Guenthner, F. A.; Vietor, M. L. SURFACE ACTIVE MATERIALS FROM PERFLUOROCARBOXYLIC AND PERFLUOROSULFONIC ACIDS.

6. Gao, S.; Cao, Z.; Niu, Q.; Zong, W.; Liu, R. Probing the Toxicity of Long-Chain Fluorinated Surfactants: Interaction Mechanism between Perfluorodecanoic Acid and Lysozyme. *J Mol Liq* **2019**, *285*, 607–615. https://doi.org/10.1016/J.MOLLIQ.2019.04.134.

7. Moody, C. A.; Field, J. A. Perfluorinated Surfactants and the Environmental Implications of Their Use in Fire-Fighting Foams. *Environ Sci Technol* **2000**, *34* (18), 3864–3870. https://doi.org/10.1021/ES991359U/ASSET/IMAGES/LARGE/ES991359UF00003.JPEG.

8. Hinnant, K. M.; Giles, S. L.; Smith, E. P.; Snow, A. W.; Ananth, R. Characterizing the Role of Fluorocarbon and Hydrocarbon Surfactants in Firefighting-Foam Formulations for Fire-Suppression. *Fire Technol* **2020**, *56*, 1413–1441. https://doi.org/10.1007/s10694-019-00932-7.

9. Sheng, Y.; Jiang, N.; Lu, S.; Li, C. Fluorinated and Fluorine-Free Firefighting Foams Spread on Heptane Surface. *Colloids Surf A Physicochem Eng Asp* **2018**, *552*, 1–8. https://doi.org/10.1016/J.COLSURFA.2018.05.004.

10. Kovalchuk, N. M.; Trybala, A.; Starov, V.; Matar, O.; Ivanova, N. Fluoro- vs Hydrocarbon Surfactants: Why Do They Differ in Wetting Performance? *Adv Colloid Interface Sci* **2014**, *210*, 65–71. https://doi.org/10.1016/J.CIS.2014.04.003.

11. Kunieda, H.; Shinoda, K. Solubilizing Power of Aqueous Solutions of Fluorinated Surfactants.

12. Hetzer, R. H.; Kümmerlen, F.; Wirz, K.; Blunk, D. Fire Testing a New Fluorine-Free AFFF Based on a Novel Class of Environmentally Sound High Performance Siloxane Surfactants. **2014**. https://doi.org/10.3801/IAFSS.FSS.11-1261.

13. Ananth, R.; Snow, A. W.; Hinnant, K. M.; Giles, S. L.; Farley, J. P. Synergisms between Siloxane-Polyoxyethylene and Alkyl Polyglycoside Surfactants in Foam Stability and Pool Fire Extinction. *Colloids Surf A Physicochem Eng Asp* **2019**, *579*. https://doi.org/10.1016/j.colsurfa.2019.123686.

14. Moradighadi, N.; Lewis, S.; Dominguez Olivo, J.; Young, D.; Brown, B.; Neši´c, S. N. Determining Critical Micelle Concentration of Organic Corrosion Inhibitors and Its Effectiveness in Corrosion Mitigation. **2021**. https://doi.org/10.5006/3679.

15. Meyer, E. E.; Rosenberg, K. J.; Israelachvili, J. Recent Progress in Understanding Hydrophobic Interactions. *Proceedings of the National Academy of Sciences* **2006**, *103* (43), 15739–15746. https://doi.org/10.1073/PNAS.0606422103.

16. Romsted, L. S. Introduction to Surfactant Self-Assembly. *Supramol Chem* **2012**. https://doi.org/10.1002/9780470661345.SMC013.

17. Fan, H.; Yan, Y.; Li, Z.; Xu, Y.; Jiang, L.; Xu, L.; Zhang, B.; Huang, J. General Rules for the Scaling Behavior of Linear Wormlike Micelles Formed in Catanionic Surfactant Systems. *J Colloid Interface Sci* **2010**, *348* (2), 491–497. https://doi.org/10.1016/J.JCIS.2010.04.065.

18. Molchanov, V. S.; Kuklin, A. I.; Orekhov, A. S.; Arkharova, N. A.; Philippova, O. E. Temporally Persistent Networks of Long-Lived Mixed Wormlike Micelles of Zwitterionic and Anionic Surfactants. *J Mol Liq* **2021**, *342*, 116955. https://doi.org/10.1016/J.MOLLIQ.2021.116955.

19. Hemp, S. T.; Hudson, A. G.; Allen, M. H.; Pole, S. S.; Moore, R. B.; Long, T. E. Solution Properties and Electrospinning of Phosphonium Gemini Surfactants. *Soft Matter* **2014**, *10* (22), 3970–3977. https://doi.org/10.1039/C4SM00271G.

20. Weissman, S.; Mason, E. A. Determination of Gaseous-Diffusion Coefficients from Viscosity Measurements. *J Chem Phys* **2004**, *37* (6), 1289. https://doi.org/10.1063/1.1733277.

21. Ronteltap, A. D.; Damsté, B. R.; De Gee, M.; Prins, A. The Role of Surface Viscosity in Gas Diffusion in Aqueous Foams. I. Theoretical. *Colloids and Surfaces* **1990**, *47* I, 269–283. https://doi.org/10.1016/0166-6622(90)80078-I.

22. Cashion, M. P.; Li, X.; Geng, Y.; Hunley, M. T.; Long, T. E. Gemini Surfactant Electrospun Membranes. *Langmuir* **2010**, *26* (2), 678–683. https://doi.org/10.1021/LA902287B/ASSET/IMAGES/LARGE/LA-2009-02287B_0007.JPEG.

23. Svenson, S. Controlling Surfactant Self-Assembly. *Curr Opin Colloid Interface Sci* **2004**, *9* (3–4), 201–212. https://doi.org/10.1016/J.COCIS.2004.06.008.

24. Nagarajan, R. Molecular Packing Parameter and Surfactant Self-Assembly: The Neglected Role of the Surfactant Tail. *Langmuir* **2002**, *18* (1), 31–38. https://doi.org/10.1021/LA010831Y/ASSET/IMAGES/MEDIUM/LA010831YE00021.GIF.

25. McKee, M. G.; Layman, J. M.; Cashion, M. P.; Long, T. E. Phospholipid Nonwoven Electrospun Membranes. *Science (1979)* **2006**, *311* (5759), 353–355. https://doi.org/10.1126/SCIENCE.1119790/SUPPL_FILE/MCKEE.SOM.PDF.

26. Kume, G.; Gallotti, M.; Nunes, G. Review on Anionic/Cationic Surfactant Mixtures. *J Surfactants Deterg* **2008**, *11* (1), 1–11. https://doi.org/10.1007/S11743-007-1047-1/FIGURES/17.

27. Nagarajan, R.; Ruckenstein, E. Theory of Surfactant Self-Assembly: A Predictive Molecular Thermodynamic Approach. *Langmuir* **1991**, *7*, 2934–2969.

28. *Critical Micelle Concentrations of Aqueous Surfactant Systems,*. https://apps.dtic.mil/sti/citations/ADD095344 (accessed 2023-03-16).

29. The Preparation Method and Aldehyde-Free Colour Stabilizer of DMAA. **2017**.

30. Abraham, M. J.; Murtola, T.; Schulz, R.; Páll, S.; Smith, J. C.; Hess, B.; Lindah, E. GROMACS: High Performance Molecular Simulations through Multi-Level Parallelism from Laptops to Supercomputers. *SoftwareX* **2015**, *1–2*, 19–25. https://doi.org/10.1016/J.SOFTX.2015.06.001.

31. Humphrey, W.; Dalke, A.; Schulten, K. VMD: Visual Molecular Dynamics. *J Mol Graph* **1996**, *14* (1), 33–38. https://doi.org/10.1016/0263-7855(96)00018-5.

32. Dodda, L. S.; De Vaca, I. C.; Tirado-Rives, J.; Jorgensen, W. L. LigParGen Web Server: An Automatic OPLS-AA Parameter Generator for Organic Ligands. *Nucleic Acids Res* **2017**, *45* (W1), W331–W336. https://doi.org/10.1093/NAR/GKX312.

33. Mark, P.; Nilsson, L. Structure and Dynamics of the TIP3P, SPC, and SPC/E Water Models at 298 K. *Journal of Physical Chemistry A* **2001**, *105* (43), 9954–9960. https://doi.org/10.1021/JP003020W/ASSET/IMAGES/LARGE/JP003020WF00004.JPEG.

34. Joung, I. S.; Cheatham, T. E. Determination of Alkali and Halide Monovalent Ion Parameters for Use in Explicitly Solvated Biomolecular Simulations. *Journal of Physical Chemistry B* **2008**, *112* (30), 9020–9041. https://doi.org/10.1021/JP8001614/SUPPL_FILE/JP8001614-FILE003.PDF.

35. Martinez, L.; Andrade, R.; Birgin, E. G.; Martínez, J. M. PACKMOL: A Package for Building Initial Configurations for Molecular Dynamics Simulations. *J Comput Chem* **2009**, *30* (13), 2157–2164. https://doi.org/10.1002/JCC.21224.

36. Pan, Y.; Tong, K.; Lin, M.; Zhuang, W.; Zhu, W.; Chen, X.; Li, Q. Aggregation Behaviours of Sulfobetaine Zwitterionic Surfactants in EAN. *J Mol Liq* **2022**, *368*, 120608. https://doi.org/10.1016/J.MOLLIQ.2022.120608.

37. Liu, Q.; Lv, D.; Zhang, J.; Huang, C.; Yin, B.; Wei, X.; Li, J. Triple-Responsive Wormlike Micelles Based on Cationic Surfactant and Sodium Trans-o-Methoxycinnamic Acid. *J Mol Liq* **2021**, *324*, 114680. https://doi.org/10.1016/J.MOLLIQ.2020.114680.

38. Hinnant, K. M.; Ananth, R.; Farley, J. P.; Whitehurst, C. L.; Giles, S. L.; Maza, W. A.; Snow, A. W.; Karwosky, S.; Hughes Jensen. *Extinction Performance Summary of Commercial Fluorine-Free Firefighting Foams over a 28 Ft2 Pool Fire Detailed by MIL-PRF-24385*; 2019. https://apps.dtic.mil/sti/citations/AD1100426 (accessed 2023-03-13).

39. Snow, S. A.; Fenton, W. N.; Owen, M. J. Synthesis and Characterization of Zwitterionic Silicone Sulfobetaine Surfactants. *Langmuir* **1990**, *6*, 385–391.

40. Hill, R. M. Silicone Surfactants—New Developments. *Curr Opin Colloid Interface Sci* **2002**, *7* (5–6), 255–261. https://doi.org/10.1016/S1359-0294(02)00068-7.

41. Ananth. Zwitterionic and Glucoside Surfactant Formulations for Fire-Fighting Foam Applications. **2022**, *444*.

42. Yu, X.; Li, F.; Fang, H.; Miao, X.; Wang, J.; Zong, R.; Lu, S. Foaming Behavior of Fluorocarbon Surfactant Used in Fire-Fighting: The Importance of Viscosity and Self-Assembly Structure. *J Mol Liq* **2021**, *327*, 114811. https://doi.org/10.1016/J.MOLLIQ.2020.114811.

43. Carnicer, V.; Alcázar, C.; Orts, M. J.; Sánchez, E.; Moreno, R. Microfluidic Rheology: A New Approach to Measure Viscosity of Ceramic Suspensions at Extremely High Shear Rates. *Open Ceramics* **2021**, *5*, 100052. https://doi.org/10.1016/J.OCERAM.2020.100052.

44. Zhou, J.; Ranjith, P. G. Self-Assembly and Viscosity Changes of Binary Surfactant Solutions: A Molecular Dynamics Study. *J Colloid Interface Sci* **2021**, *585*, 250–257. https://doi.org/10.1016/J.JCIS.2020.11.022.

45. Liu, B.; Brown, J. R.; Zeng, C.; Rajput, H.; McDonough, R. K.; Westerhoff, P.; Long, T. E. Spiropyran-Containing Water-Soluble and Photoreversible Copolymers. *Polymer (Guildf)* **2023**, *272*, 125827. https://doi.org/10.1016/J.POLYMER.2023.125827.

46. Lopez, C. G.; Colby, R. H.; Graham, P.; Cabral, J. T. Viscosity and Scaling of Semiflexible Polyelectrolyte NaCMC in Aqueous Salt Solutions. *Macromolecules* **2017**, *50* (1), 332–338. https://doi.org/10.1021/ACS.MACROMOL.6B02261/ASSET/IMAGES/LARGE/MA-2016-022618_0005.JPEG.

47. Magrabi, S. A.; Dlugogorski, B. Z.; Jameson, G. J. A Comparative Study of Drainage Characteristics in AFFF and FFFP Compressed-Air Fire-Fighting Foams. *Fire Saf J* **2002**, *37* (1), 21–52. https://doi.org/10.1016/S0379-7112(01)00024-8.

48. Yekeen, N.; Idris, A. K.; Manan, M. A.; Samin, A. M.; Risal, A. R.; Kun, T. X. Bulk and Bubble-Scale Experimental Studies of Influence of Nanoparticles on Foam Stability. *Chin J Chem Eng* **2017**, *25* (3), 347–357. https://doi.org/10.1016/J.CJCHE.2016.08.012.

49. Dhasindrakrishna, K.; Pasupathy, K.; Ramakrishnan, S.; Sanjayan, J. Effect of Yield Stress Development on the Foam-Stability of Aerated Geopolymer Concrete. *Cem Concr Res* **2020**, *138*, 106233. https://doi.org/10.1016/J.CEMCONRES.2020.106233.

50. Stone, H. A.; Koehler, S. A.; Hilgenfeldt, S.; Durand, M. Perspectives on Foam Drainage and the Influence of Interfacial Rheology. *Journal of Physics: Condensed Matter* **2002**, *15* (1), S283. https://doi.org/10.1088/0953-8984/15/1/338.

51. Mykhaylyk, O. O.; Warren, N. J.; Parnell, A. J.; Pfeifer, G.; Laeuger, J. Applications of Shear-Induced Polarized Light Imaging (SIPLI) Technique for Mechano-Optical Rheology of Polymers and Soft Matter Materials. *J Polym Sci B Polym Phys* **2016**, *54* (21), 2151–2170. https://doi.org/10.1002/POLB.24111.

52. Bragg, W. L.; Pippard, A. B.; IUCr. The Form Birefringence of Macromolecules. *Urn:issn:0365-110X* **1953**, *6* (11–12), 865–867. https://doi.org/10.1107/S0365110X53002519.

Chapter 10

1. Ananth, R.; Snow, A. W.; Hinnant, K. M.; Giles, S. L.; Farley, J. P. Synergisms between Siloxane-Polyoxyethylene and Alkyl Polyglycoside Surfactants in Foam Stability and Pool Fire Extinction. *Colloids Surf A Physicochem Eng Asp* **2019**, *579*. https://doi.org/10.1016/j.colsurfa.2019.123686.

2. Hetzer, R. H.; Kümmerlen, F.; Wirz, K.; Blunk, D. Fire Testing a New Fluorine-Free AFFF Based on a Novel Class of Environmentally Sound High Performance Siloxane Surfactants. **2014**. https://doi.org/10.3801/IAFSS.FSS.11-1261.

3. Snow, S. A.; Fenton, W. N.; Owen, M. J. Synthesis and Characterization of Zwitterionic Silicone Sulfobetaine Surfactants. *Langmuir* **1990**, *6*, 385–391.

4. Mykhaylyk, O. O.; Warren, N. J.; Parnell, A. J.; Pfeifer, G.; Laeuger, J. Applications of Shear-Induced Polarized Light Imaging (SIPLI) Technique for Mechano-Optical

Rheology of Polymers and Soft Matter Materials. *J Polym Sci B Polym Phys* **2016**, *54* (21), 2151–2170. https://doi.org/10.1002/POLB.24110.

5. Lowry, G. V.; Hill, R. J.; Harper, S.; Rawle, A. F.; Hendren, C. O.; Klaessig, F.; Nobbmann, U.; Sayre, P.; Rumble, J. Guidance to Improve the Scientific Value of Zeta-Potential Measurements in NanoEHS. *Environ Sci Nano* **2016**, *3* (5), 953–965. https://doi.org/10.1039/C6EN00136J.

6. Wettig, S. D.; Verrall, R. E. Thermodynamic Studies of Aqueous m–s–m Gemini Surfactant Systems. *J Colloid Interface Sci* **2001**, *235* (2), 310–316. https://doi.org/10.1006/JCIS.2000.7348.

7. Svenson, S. Controlling Surfactant Self-Assembly. *Curr Opin Colloid Interface Sci* **2004**, *9* (3–4), 201–212. https://doi.org/10.1016/J.COCIS.2004.06.008.

8. Nagarajan, R. Molecular Packing Parameter and Surfactant Self-Assembly: The Neglected Role of the Surfactant Tail. *Langmuir* **2002**, *18* (1), 31–38. https://doi.org/10.1021/LA010831Y/ASSET/IMAGES/MEDIUM/LA010831YE00021.GIF.

9. Hill, R. M. Silicone Surfactants—New Developments. *Curr Opin Colloid Interface Sci* **2002**, *7* (5–6), 255–261. https://doi.org/10.1016/S1359-0294(02)00068-7.

10. Rakowska, J. Best Practices for Selection and Application of Firefighting Foam. https://doi.org/10.1051/matecconf/201824700014.

11. Lu, J.; Pu, W.; He, W.; Zou, B.; Li, B.; Liu, R. Progress in Research of Sulfobetaine Surfactants Used in Tertiary Oil Recovery. *J Surfactants Deterg* **2022**. https://doi.org/10.1002/JSDE.12651.

12. Chukhajian, E. O.; Ayrapetyan, L. V.; Mkrtchyan, H. S.; Panosyan, H. A. Synthesis of Mixed Secondary and Tertiary Amines. *Russian Journal of Organic Chemistry* **2020**, *56* (2), 353–355. https://doi.org/10.1134/S1070428020010311/SCHEMES/2.

13. Kunz, W.; Testard, F.; Zemb, T. Correspondence between Curvature, Packing Parameter, and Hydrophilic-Lipophilic Deviation Scales around the Phase-Inversion Temperature. https://doi.org/10.1021/la8028879.

14. McKee, M. G.; Layman, J. M.; Cashion, M. P.; Long, T. E. Phospholipid Nonwoven Electrospun Membranes. *Science (1979)* **2006**, *311* (5759), 353–355. https://doi.org/10.1126/SCIENCE.1119790/SUPPL_FILE/MCKEE.SOM.PDF.

15. Cashion, M. P.; Li, X.; Geng, Y.; Hunley, M. T.; Long, T. E. Gemini Surfactant Electrospun Membranes. *Langmuir* **2010**, *26* (2), 678–683. https://doi.org/10.1021/LA902287B/ASSET/IMAGES/LARGE/LA-2009-02287B_0007.JPEG.

16. Hemp, S. T.; Hudson, A. G.; Allen, M. H.; Pole, S. S.; Moore, R. B.; Long, T. E. Solution Properties and Electrospinning of Phosphonium Gemini Surfactants. *Soft Matter* **2014**, *10* (22), 3970–3977. https://doi.org/10.1039/C4SM00271G.

17. Rudert, R.; Schmaucks, G. Crystal and Molecular Structure of 1-Ethyl-3-[Tris(Trimethylsiloxanyl)Silyl]Pyrrolinium Hydrochloride. *Crystal Research and Technology* **1997**, *32* (2), 347–352. https://doi.org/10.1002/CRAT.2170320219.

18. Laschewsky, A.; Touillaux, R.; Hendlinger, P.; Vierengel, A. Characterization of Sulfobetaine Monomers by Nuclear Magnetic Resonance Spectroscopy: A Note. *Polymer (Guildf)* **1995**, *36* (15), 3045–3049. https://doi.org/10.1016/0032-3861(95)94357-Y.

19. Goubet, N.; Albouy, P. A.; Thompson, A.; Pileni, M. P. Polymorphism in Nanoparticle-Based Crystals Depending upon Their Single or Polycrystalline Character. *CrystEngComm* **2016**, *18* (33), 6166–6175. https://doi.org/10.1039/C6CE01006G.

20. Gonçalves, R. A.; Holmberg, K.; Lindman, B. Cationic Surfactants: A Review. *J Mol Liq* **2023**, *375*, 121335. https://doi.org/10.1016/J.MOLLIQ.2023.121335.

21. Williams, S. R.; Long, T. E. Recent Advances in the Synthesis and Structure–Property Relationships of Ammonium Ionenes. *Prog Polym Sci* **2009**, *34* (8), 762–782. https://doi.org/10.1016/J.PROGPOLYMSCI.2009.04.004.

22. Holmberg, K. Polymerizable Surfactants. *Prog Org Coat* **1992**, *20* (3–4), 325–337. https://doi.org/10.1016/0033-0655(92)80022-O.

23. Yager, P.; Schoen, P. E. Molecular Crystals and Liquid Crystals Formation of Tubules by a Polymerizable Surfactant. https://doi.org/10.1080/00268948408071454.

24. Arrington, C. B.; Rau, D. A.; Vandenbrande, J. A.; Hegde, M.; Williams, C. B.; Long, T. E. 3D Printing Carbonaceous Objects from Polyimide Pyrolysis. *ACS Macro Lett* **2021**, *10* (4), 412–418. https://doi.org/10.1021/ACSMACROLETT.1C00032/ASSET/IMAGES/LARGE/MZ1C00032_0004.JPEG.

25. Rau, D. A.; Herzberger, J.; Long, T. E.; Williams, C. B. Ultraviolet-Assisted Direct Ink Write to Additively Manufacture All-Aromatic Polyimides. *ACS Appl Mater Interfaces* **2018**, *10* (41), 34828–34833. https://doi.org/10.1021/ACSAMI.8B14584/ASSET/IMAGES/LARGE/AM-2018-145849_0003.JPEG.

26. Herzberger, J.; Meenakshisundaram, V.; Williams, C. B.; Long, T. E. 3D Printing All-Aromatic Polyimides Using Stereolithographic 3D Printing of Polyamic Acid Salts. **2018**. https://doi.org/10.1021/acsmacrolett.8b00126.

APPENDIX A

PUBLISHED PORTIONS

Portions of the data presented in this dissertation have been previously published, submitted for publication, or will be submitted for publication in the following journals. The published materials were included with permission from all co-authors.

CHAPTER 4

Brown, J. R.; Reynolds, J. P.; Das, A.; Long, T. E.; Bortner, M. J. Characterization methods to predict extrusion performance in thermoplastic polyurethane batches. (Prepared for submission to *Polym. Degrad. Stab.* **2023)**

CHAPTER 6

Brown, J. R.; Herzberger, J.; Spiering, G. A.; Wilts, E.; Moore, R. B.; Long, T. E.. Binary Thiol-Acrylate Photopolymerization for the Design of Degradable Acetal-Functionalized Hydrogels. *ACS Appl. Polym. Mater.* **2022**.

CHAPTER 9

Brown, J. R.; Madsen M. D, Ateş A.; Isla, R.; Ham S.; Agbo, B.; Karimi Nikoo, K.; Lattimer, B. Y.; Qiau, R.; Xie, R.; Long, T. E. Revealing Foam Stability for Cationic and Zwitterionic Triethylsilyl-containing Surfactants. *Phys. Fluids* **2023** (*Submitted March 2023*)